

The use of patient-specific modelling in the assessment of a clinical indicator for arteriovenous fistula failure

Author:

Ng, Olivia

Publication Date:

2021

DOI:

<https://doi.org/10.26190/unsworks/23902>

License:

<https://creativecommons.org/licenses/by/4.0/>

Link to license to see what you are allowed to do with this resource.

Downloaded from <http://hdl.handle.net/1959.4/100212> in <https://unsworks.unsw.edu.au> on 2024-04-24



The use of patient-specific modelling in the assessment of a clinical indicator for arteriovenous fistula failure

Olivia X. W. Ng

A thesis in fulfilment of the requirements for the degree of
Doctor of Philosophy

School of Mechanical and Manufacturing Engineering
Faculty of Engineering
University of New South Wales

December 2021

Originality statement, Copyright and Authenticity statements

Thesis Title and Abstract

Declarations

Inclusion of Publications
Statement

Corrected Thesis and
Responses

ORIGINALITY STATEMENT

☒ I hereby declare that this submission is my own work and to the best of my knowledge it contains no materials previously published or written by another person, or substantial proportions of material which have been accepted for the award of any other degree or diploma at UNSW or any other educational institution, except where due acknowledgement is made in the thesis. Any contribution made to the research by others, with whom I have worked at UNSW or elsewhere, is explicitly acknowledged in the thesis. I also declare that the intellectual content of this thesis is the product of my own work, except to the extent that assistance from others in the project's design and conception or in style, presentation and linguistic expression is acknowledged.

COPYRIGHT STATEMENT

☒ I hereby grant the University of New South Wales or its agents a non-exclusive licence to archive and to make available (including to members of the public) my thesis or dissertation in whole or part in the University libraries in all forms of media, now or here after known. I acknowledge that I retain all intellectual property rights which subsist in my thesis or dissertation, such as copyright and patent rights, subject to applicable law. I also retain the right to use all or part of my thesis or dissertation in future works (such as articles or books).

For any substantial portions of copyright material used in this thesis, written permission for use has been obtained, or the copyright material is removed from the final public version of the thesis.

AUTHENTICITY STATEMENT

☒ I certify that the Library deposit digital copy is a direct equivalent of the final officially approved version of my thesis.

Inclusion of Publications Statement

Thesis Title and Abstract

Declarations

Inclusion of Publications
Statement

Corrected Thesis and
Responses

UNSW is supportive of candidates publishing their research results during their candidature as detailed in the UNSW Thesis Examination Procedure.

Publications can be used in the candidate's thesis in lieu of a Chapter provided:

- The candidate contributed **greater than 50%** of the content in the publication and are the "primary author", i.e. they were responsible primarily for the planning, execution and preparation of the work for publication.
- The candidate has obtained approval to include the publication in their thesis in lieu of a Chapter from their Supervisor and Postgraduate Coordinator.
- The publication is not subject to any obligations or contractual agreements with a third party that would constrain its inclusion in the thesis.

☒ The candidate has declared that **some of the work described in their thesis has been published and has been documented in the relevant Chapters with acknowledgement.**

A short statement on where this work appears in the thesis and how this work is acknowledged within chapter/s:

Chapter 2 is partially comprised of a review paper that I contributed and submitted to Computer and Programs of Biomedicine Update.

Chapter 3 contains work that I contributed, published and presented at the Australian Biomedical Engineering Conference 2019. Acknowledgement of work of other authors has been made at the beginning of the chapter.

Chapter 4 is partially comprised of a manuscript that I contributed, submitted and currently under review with the Computer Methods in Biomechanics and Biomedical Engineering: Imaging & Visualization.

Chapter 5 is partially comprised of a manuscript that I contributed and submitted to the Computer Methods and Programs in Biomedicine Update. Some work in this chapter has also been presented in the 22nd Australasian Fluid Mechanics Conference. Acknowledgement of work of other authors has been made at the beginning of the chapter.

Chapter 6 contains work that I contributed and presented at the 26th Congress of Biomechanics at Milan, Italy in July 2021.

Candidate's Declaration



I declare that I have complied with the Thesis Examination Procedure.

Relevant Publications

Journal Articles

O. Ng, S D. Gunasekera, S D. Thomas, R L. Varcoe, and T J. Barber, “A review of the predictive methods for arteriovenous fistula (AVF) failure identification”, *Comput. Methods Biomech. Biomed. Eng. Imaging Vis*, 2022 [*Under Review*]

O. Ng, S D. Thomas, S D. Gunasekera, R L. Varcoe, and T J. Barber, “The use of patient-specific modelling for CFD-derived resistance to identify problematic arteriovenous fistula”, *Computer Methods and Programs in Biomedicine Update*, 2021 [*Under Review*]

O. Ng, S. D. Gunasekera, S. D. Thomas, R. L. Varcoe, and T. J. Barber, “The effect of assumed boundary conditions on the accuracy of patient-specific CFD arteriovenous fistula model,” *Comput. Methods Biomech. Biomed. Eng. Imaging Vis.*, vol. 0, no. 0, pp. 1–13, 2022, doi: 10.1080/21681163.2022.2040054.

S D. Gunasekera, **O. Ng**, S D. Thomas, R L. Varcoe, de Silva, Charitha and T J. Barber, “Impact of juxta-anastomotic stent implantation on the haemodynamics within a single representative patient AVF”, *Int. J. Heat Fluid Flow*, vol. 92, p. 108874, 2021.

S D. Gunasekera, **O. Ng**, S D. Thomas, R L. Varcoe, de Silva, Charitha and T J. Barber, “Tomographic PIV analysis of physiological flow conditions in a patient-specific arteriovenous fistula”, *Exp. Fluids*, vol. 61, no. 12, pp. 1–14, 2020.

Conference proceedings and presentations

O. Ng, S. Gunasekera, S. Thomas, R. Varcoe, and T. Barber, “CFD-Derived Resistance as a clinical indicator for problematic AVF,” in 26th Congress of Biomechanics, 2021, vol. 65, no. 8, p. 2021.

S. Gunasekera, **O. Ng**, S D. Thomas, R L. Varcoe, de Silva, Charitha and T J. Barber, “Flow through a malapposed flexible stent within an arteriovenous fistula”, 26th Congress of the European Society of Biomechanics, Milan, Italy, 2021

O. Ng, S. Gunasekera, S. Thomas, R. Varcoe, and T Barber, “A clinical predictive tool for arteriovenous fistula (AVF) failure”, Proceedings of the 22nd Australasian Fluid Mechanics Conference AFMC2020, Brisbane, Australia, 2020. DOI: <https://doi.org/10.14264/d3dc63e>

S G. Mallinson, G D. McBain, **O. Ng**, S D. Gunasekera and T J. Barber, “Hydraulic resistance and inertance of multi-port vessels”, Proceedings of the 22nd Australasian Fluid Mechanics Conference AFMC2020, Brisbane, Australia, 2020. DOI: <https://doi.org/10.14264/e9afca2>

S. Gunasekera, **O. Ng**, S. Thomas, R. Varcoe, CM. De Silva, and T. Barber, “A numerical investigation of a stented arteriovenous fistula”, Proceedings of the 22nd Australasian Fluid Mechanics Conference AFMC2020, Brisbane, Australia, 2020. DOI: <https://doi.org/10.14264/160df47>

O. Ng, S Gunasekera, S Thomas, R Varcoe, T Barber, “Arteriovenous Fistula (AVF) failure prediction through patient-specific (PS) modelling”, Australian Biomedical Engineering Conference 2019 (ABEC 2019): Technology & Research in Australian Medical Science. Melbourne: Engineers Australia, 2019: 3. ISBN: 9781925627435

O. Ng, S. Gunasekera, S. Thomas, R. Varcoe, and T Barber, “Regular Non-Invasive Surveillance of Arteriovenous Fistula (AVF)”, presented at the 5th Annual 3DMed Australia Conference, Melbourne, Australia, 2019

S. Gunasekera, **O. Ng**, S. Thomas, R. Varcoe, CM. De Silva, and T. Barber, “Flow analysis in a patient-specific arteriovenous fistula”, Australian Biomedical Engineering Conference 2019 (ABEC 2019): Technology & Research in Australian Medical Science. Melbourne: Engineers Australia, 2019: 86. ISBN: 9781925627435

S. Gunasekera, **O. Ng**, S. Thomas, R. Varcoe, CM. De Silva, and T. Barber, “Towards 3D PIV measurements of patient-specific arteriovenous fistula”, IX Australian Conference on Laser Diagnostics, Adelaide, Australia, 2019. ISBN: 978-0-646-81267-0

Acknowledgment

Pursuing a PhD can feel lonely and isolating, especially when half of it is completed during a global pandemic. That said, I am very thankful for the support I received throughout this wild journey and would like to acknowledge key individuals who have helped me overcome countless hurdles along the way. Some say that completing a PhD is like running a marathon – what matters is perseverance. Yet, reflecting on this year's 2020ne Tokyo Olympics, I'd say completing a PhD is more like a competitive swimming event (200m, 400m, 800m etc) – it's not just about persevering through the first 100m, but also the final sprint. The key to success is to not give up halfway through the race (or towards the end) but to keep swimming!

I would like to express my deepest gratitude to the Australian government for their financial support provided through the Research Training Scholarship, without which I would not be able to pursue this Doctorate degree.

I am very thankful for a supervisor like Prof. Tracie Barber – Thank you for your guidance and support, and the numerous opportunities you afforded me even prior to my PhD, helping me understand the vastly complex yet fascinating field of vascular fluid dynamics. Thank you also for making research feel less stressful with jokes, chocolates, plants, and fun activities along the way.

I would also like to thank my amazing co-supervisors, Dr. Shannon Thomas and Dr. Ramon Varcoe. Thank you, Ramon, for your clinical advice and expertise, which helped me see how my research translates to practical applications in a clinical setting. Thank you, Shannon, for your patience and advice throughout this journey – I really appreciate how you *squeeze* time out from your busy schedule and sit down with me to do the less exciting work. Of course, a shoutout to Gaye, for your patience and effort in slotting me into Shannon's calendar!

Completing this work would not have been possible without the help of the incredible nurses and patients from the dialysis unit of Sydney's Prince of Wales Hospital, Sydney, Australia. Thank you so much for providing us access to the research centre and assisting us throughout the entire process.

A shoutout to other people who have helped us with this research along the way in different ways – thank you Dr. Mark Donoghoe, Dr. Sam Mallinson, Dr. Charitha de Silva, Dr. Zoran Vulovic, Associate Prof. Victoria Timchenko, Associate Prof. Rob Taylor, Prof. Guan Yeoh and Associate Prof. Garth Pearce for your excellent help and encouragement throughout this journey. It is because of your critical and sharp feedback that I can carry out fruitful research.

To my PhD comrades – Sanjiv, PJ, Bac, Yoka, Ranita, Joseph, Jackie, Michael, Mark, Xinxing, Yani, Andre, Jie Yi, Alex B, Amin – I am grateful that we have kept each other sane! I will miss the random coffee and lunch catch ups. I wish you all the best with your research and future endeavours. I am already missing our banters in Ainsworth (or on Teams)! John and Eammon, thank you for your help and for sharing your knowledge when I first began the PhD. You guys have been incredible, and I believe you will continue to do great things in this field, impacting many lives. Vivian L, it has been great to see your work flourish into an AR application. Good luck with your future endeavours.

Thank you to the amazing FIC crew – Zoe, Kevin P, Christa, Bih Hua, Sheina, Alex C, Josh C, Josh W, Josh N, Ming, Alison, Karen, and everyone in my growth groups over the years for your constant support and prayer. Words cannot describe how grateful I am. You have been more important than you could ever imagine – not just in this PhD journey, but also being my family away from home, and for reminding me of important things in life.

Nanda, Amy and Yilyn, thank you for being with me throughout some of the toughest times in my life, and for praying and checking up on me from time to time to make sure that I am doing

alright. Thanks for keeping me well-fed, well-cafeinated, and for listening to my rambles. On a side note, I am also very glad that you (finally!) understand what an AVF is after more than 3.5 years (still counting...) of explaining. Thank you all for reading, proofreading, reading, and reading and reading again.

Josh T, thank you for steering me back to the goal whenever I lose sight of things, and for being the calmer one between the two of us. And yes, of course, the jokes (at the appropriate time).

Thank you, Mum and Dad, for the sacrifices you made for our family – I am indeed grateful for the chance to receive proper education. The trust you have in me gave me the confidence to keep going when it was hard. Thank you for the unconditional love and support all along. Jack, *yes you*, you've been a great support too – the best little (not so little now) brother one could ever ask for.

Shoutout to Peanut – thanks for being a great company to Mum and Dad!

Being away from home has never been easy, especially in these last couple of years of this PhD, with looming uncertainty and immense emotional pressures due to COVID-19. However, I am grateful for the hope I see in Christ, in whom I find ultimate identify, security, and strength to keep persevering, to keep myself grounded, and to push through hard times.

Finally, I thank God for His grace, sovereignty, and provision.

Abstract

The arteriovenous fistula (AVF) is a surgically-made vascular structure connecting an artery to a vein. It is the optimal form of vascular access for haemodialysis-dependent end-stage renal disease patients. However, AVF are prone to access dysfunction through the formation of stenoses, which compromise the structure's utility. To date, a plethora of clinical models are used to predict AVF formation failure based on patient factors and other models predicting late AVF failure by assessing haemodynamics and quantifying disturbed flow behaviours and wall shear stress metrics with stenosis formation. That said, inconsistencies were identified in the correlation between these metrics and diseased AVFs.

This thesis aims to assess the suitability of another haemodynamic-related metric, resistance, derived from pressure drop and flow rates through patient-specific CFD modelling, for diagnosing and predicting AVF failure. A three-dimensional ultrasound scanning system was used to obtain patient-specific geometry and flow profiles, used for CFD models which were then analysed, with resistance calculated for each patient.

The significance of patient-specific CFD modelling was demonstrated in its usefulness to generate a patient-targeted indicator of diseased AVF. To study the effectiveness of resistance as a metric, the relationship between CFD-derived resistance and the potential for AVF failure was evaluated, starting with classification of resistance results among patients who had undergone treatment for stenosis. An exploratory study into the suitability of CFD-derived resistance and its association with patients' AVF conditions was further conducted by classifying data from a larger patient dataset and fitting the classified data to a multilevel regression model.

CFD-derived resistance was found to be higher at the proximal vein of problematic AVF, however this figure was 76% lower among patients who had undergone stenosis treatment. Meanwhile, no correlation was found between resistance at the proximal artery and patency status. An area under curve of 92.1% was found from the receiver operating characteristic analysis, noting an outstanding discrimination of the classification. CFD-derived resistance appears to be a promising metric in the assessment of a suitable diagnostic marker for AVF failure. This research concludes with aspirations for clinical implementation of a related system, alongside routine surveillance of AVF.

Table of Content

Abstract.....	IX
List of Tables	XVII
List of Figures.....	XIX
List of Abbreviations	XXVIII
<i>Chapter 1</i>	1
<i>Introduction</i>	1
1.1 Haemodialysis.....	2
1.2 Vascular access.....	4
1.3 Arteriovenous fistula (AVF).....	5
1.4 AVF failure	9
1.5 Summary	10
1.6 Thesis Scope.....	11
<i>Chapter 2</i>	12
<i>Literature Review.....</i>	12
2.1 Overview	13
2.2 Predictive model for AVF failure	16
2.3 Clinical AVF “fail to mature” predictive model	18

2.4 Vascular computer network model	22
2.5 Haemodynamic predictors for AVF failure.....	25
2.6 AVF condition indication based on pressure changes	35
2.7 Blood flow sound frequency to measure AVF patency.....	38
2.8 Other emerging technologies to assist with AVF failure prediction	40
2.9 Summary.....	41
 <i>Chapter 3</i>	 43
 <i>Patient-specific computational fluid dynamics modelling of an AVF</i>	 43
3.1 Overview	44
3.2 Patient selection.....	46
3.3 Patient-specific model.....	47
3.3.1 Geometry acquisition.....	47
3.3.2 Flow profiles.....	51
3.4 Patient-specific CFD model.....	54
3.4.1 Boundary conditions.....	57
3.4.2 Mesh strategy.....	59
3.5 CFD results post-processing.....	65
3.6 CFD-derived resistance calculation.....	66
3.7 Validation.....	67
3.7.1 Validation with experimental data.....	67

3.7.2 Validation of pressure drop	71
3.8 Summary	71
<i>Chapter 4</i>	<i>72</i>
<i>The effect of boundary conditions on the accuracy of CFD predictions in patient-specific AVFs</i>	<i>72</i>
4.1 Background.....	73
4.2 Methods.....	76
4.3 Haemodynamic parameters	81
4.4 CFD-derived resistance	85
4.5 Geometrical influence on blood flow behaviour.....	87
4.6 Comparison with the Hagen-Poiseuille mathematical model	90
4.7 Limitation	93
4.8 Clinical relevance	94
4.9 Conclusion.....	96
<i>Chapter 5</i>	<i>97</i>
<i>The use of CFD-derived resistance to identify problematic AVFs</i>	<i>97</i>
5.1 Background.....	98
5.2 Patient selection.....	100
5.3 Statistical analysis	102

5.4 CFD-derived resistance	103
5.5 Resistance at different AVF segment	104
5.5.1 Vein segment (PV)	105
5.5.2 Artery segment (PA).....	107
5.6 Patients' clinical observation	108
5.7 Identifying stenosis region at the PV segment.....	111
5.7.1 Case Study I: Patient 1.....	111
5.7.2 Case Study II: Patient 4	113
5.8 Using resistance to predict the need for surgical intervention.....	116
5.9 Clinical relevance	118
5.9.1 Incorporating other technologies to complement the current model.....	120
5.10 Limitation	123
5.11 Conclusion.....	124
<i>Chapter 6</i>	125
<i>Assessment of the suitability of CFD-derived resistance as a clinical indicator for AVF failure</i> <i>.....</i>	125
6.1 Background.....	126
6.2 Methods.....	127
6.2.1 Data Selection.....	127
6.2.2 Patients' AVF geometry acquisition and data processing	127

6.2.3 Definitions	129
6.3 Statistical Analysis	130
6.3.1 The multilevel logistic regression model.....	130
6.3.2 Receiver operating characteristic (ROC) analysis.....	133
6.4 Resistance range.....	135
6.4.1 Vein segment (PV)	136
6.4.2 Artery segment (PA).....	137
6.4.3 Outliers	138
6.5 Association of resistance with an outcome (intervention)	139
6.5.1 AVF geometrical configuration.....	144
6.6 Diagnostic ability of the model.....	148
6.7 Clinical relevance	151
6.7.1 Comparison of individualised resistance values and the effect of different individuals	151
6.7.2 Other comorbidities	154
6.8 Limitation and future recommendations.....	156
6.9 Conclusion.....	157
<i>Chapter 7</i>	158
<i>Conclusion</i>	158
7.1 Discussion.....	159
7.2 Key findings	163

7.3 Future directions	165
Bibliography	166
Appendices	A
Appendix 3A.....	A
Appendix 6A.....	C
Appendix 6B.....	D

List of Tables

Table 1: AVF patency definitions [13]	13
Table 2: Flow condition exposed by endothelial cells, that is unidirectional flow, flow reversal and multidirectional flow. Black arrows represent the instantaneous WSS vectors at an arbitrary point in time within the cardiac cycle, where the progression of it. Reprinted with permission [39].....	28
Table 3: Boundary condition for the CFD model	58
Table 4: Discretisation error of the WSS.....	63
Table 5: Percentage difference for mesh independence study	63
Table 6: Average, maximum and minimum difference at four different locations. The points where the maximum and minimum difference identified are indicated in the brackets of column 3 and 4.....	70
Table 7: Boundary conditions (BC) used for Patient A, B and C.....	77
Table 8: Pressure difference and flow rate data of Patient C for the three different boundary conditions at PA and PV	85
Table 9: Resistance values at the PA segment and the discrepancies from the patient specific condition (BC 1)	86
Table 10: Resistance values at the PV segment from and the patient specific condition (BC 1)	86
Table 11: Baseline clinical characteristic. Continuous data are presented as mean with standard deviation (\pm) (range). Categorical data are presented as the number (percentage).....	101
Table 12: Interpretation of correlation coefficient [211]	102
Table 13: Changes in resistance pre- and post-intervention at the PV	105
Table 14: Changes in diameter pre- and post-intervention at the PV	106
Table 15: Post intervention resistance values	106

Table 16: Baseline clinical characteristic for all patients examined.....	128
Table 17: General guideline in assessing the diagnostic ability of a test based on the AUC values in a ROC graph	134
Table 18: Descriptive statistics of the resistance data at the PA and PV for the two different groups (intervention and no intervention). Units: mmHg/l/min	136
Table 19: Estimates from the multilevel logistic regression model, the effects of the fixed effect on the multilevel logistic regression model. Odds ratio is represented in exponential term.	141
Table 20: Summary results from the multilevel binary logistic regression model	143
Table 21: Outliers- AVF that had an intervention and have a resistance in the range of 0 -10 mmHg/l/min.....	145
Table 22: Outliers: AVF that had no intervention and are in the range of 10- 20 mmHg/l/min	146
Table 23: AVF that had an intervention and are within the resistance range of 10-20 mmHg/l/min.....	147
Table 24: True positive rates (sensitivity), true negative rates (specificity), false negative rates (1- sensitivity) and false positive rates (1- specificity) of different resistance with confidence interval in bracket if applicable.....	150
Table 25: Relationship of other variables and the probability of an intervention	154

List of Figures

Figure 1: Haemodialysis extracorporeal circuit: Blood removed from the body was pumped to the dialyzer (filter). Then, filtration happens at the dialyser before filtered blood returns to the body. Pressure was being monitored before and after blood was removed and entered the body, as well as before entering the dialyser. Heparin was infused to the stream to prevent blood clot. The arrows represent the direction of blood flow.....	3
Figure 2: The three different types of vascular access: (a) Arteriovenous fistula (AVF) (b) Arteriovenous graft (c) Central venous catheter. Reprinted with permission [4].....	4
Figure 3: (left to right) Radiocephalic AVF, Branchiocephalic AVF, Brachiobasilic transposition AVF. Reprinted with permission [9].....	6
Figure 4: AVF maturation process: (top) Preoperative flow rate of the radial artery and cephalic vein (middle) An increase in flow rate at the artery and vein segment of the AVF day 1 after creation (bottom) Examples of successful and unsuccessful cases of AVF maturation where an insufficient increase in flow rate usually result to an unsuccessful vascular remodelling. The other mode of early fistula failure is the development of stenosis as shown in the middle image. Reprinted with permission [21].	8
Figure 5: Common site of stenosis in an AVF. Reprinted with permission [42].....	14
Figure 6: Histology of AVF tissue specimen. (top three) represents the section of mature AVF, (bottom three) represents section of failed AVF with maximal intimal thickening (indicated with the yellow dotted arrow) that result in AVF failure due to intimal hyperplasia. Reprinted with permission [46].	14
Figure 7: (top) Vascular remodelling response after creation of AVF where a series of response and structure changes occurred in the vasculature due to the altered haemodynamic environment. (bottom) The different vascular remodelling modalities: outward remodelling for adequately matured AVF, optimal net balance achieved between outward remodelling and	

intimal hyperplasia, that is sufficient outward remodelled achieved, leaving the AVF patent despite intimal hyperplasia and intimal hyperplasia that is when the fistula fails due to stenosis or thrombosis. Reprinted with permission [20].	15
Figure 8: Velocity needle jet visualisation for (a-c) blood flow rate of 200 ml/min, 300 ml/min and 400 ml/min (d-f) needle angle of 10°, 20°, and 30° (g-i) needle position of bottom, central and top. Reprinted with permission [55].	17
Figure 9: Vascular network model from [99] based on a 0D/1F pulse wave propagation model where the blue segment represents the venous network and the red segment represents the arterial network. Reprinted with permission [99].	23
Figure 10: Site susceptible to the intimal thickening within an AVF of (a) antegrade flow where blood flows towards the palmar arch and (b) retrograde flow where blood is going against the palmar arch into the AVF vein segment. The thick black arrow shows the direction of blood flow, while the recirculating zones are indicated with the thin black dotted arrow. Reprinted with permission [39].	29
Figure 11: Region of low and oscillating shear stress/flow coincides with the region prone to stenosis development for end-to-side and end-to-end type AVF. Reprinted with permission [102].	30
Figure 12: Presence of transitional and multidirectional disturbed flow on inner wall of vein segment for two separate study of patient-specific radial-cephalic AVF. Reprinted and adapted with permission [35], [136].	32
Figure 13: Presence of helical flow for different AVF idealised models with varying configuration and anastomotic angle. The helical content of the flow are represented with the averaged localised normalised helicity (LNH), where clockwise helical structures are represented in red and anticlockwise helical structure are represented in yellow. Reprinted with permission [38].	33

Figure 14: (top) Relationship between average pressure drop and flow rate of experimental and CFD results. (bottom) Relationship of pressure drop and pulsatile flow conditions. Figure reprinted with permission [88].	36
Figure 15: (a) In-vivo pressure measurements environment and schematic from [34] (b) the pressure drop at the PA (-6 to 0 cm) and PV (0 – 6cm). Reprinted and adapted with permission [34].	37
Figure 16: Pipeline analysis performed for each patient: Processing of geometry and flow profile were done in parallel and take about 2 hours and 15 minutes respectively. This was followed by setting up of patient-specific CFD model with the mesh and patient-specific boundary conditions. CFD results were processed, and resistance calculated after each simulation.	45
Figure 17: Set-up for the clinical patient scans performed for data collection with two personnel, one to perform the ultrasound scan of a patient and the other tasked at the workstation. (a) The workstation laptop (b) Mindray, TE7 Ultrasound machine, (c) Optitrack V120: Trio camera and (d) Mindray L14-6NS, 14MHz, 38mm FOV linear ultrasound transducer, with a rigid body attached to it [152].	47
Figure 18: (a) Example two-dimensional ultrasound image that shows the identifiable vessel lumen based on the grey-scale contrast with the surrounding tissues (b) Volume recreated from the stack of two-dimensional ultrasound images. (c) Overlay of the three-dimensional AVF geometry before and after interpolation within the image slices	50
Figure 19: (a) Example ECG waves of a healthy patient, with QRS complex labelled in red. Reprinted with permission from [168] (b) Doppler ultrasound measurements of velocity profile from different vessel of the AVF. The ECG information is indicated with the arrow in grey (c) Extracted profile from the Doppler data	53

Figure 20: (a) An example patient-specific AVF with retrograde flow (flow traveling from the PA and DA) towards the PV. The anastomosis is the connection between the three vessels (indicated with the red arrow). (b) Inlet transient velocity waveforms are set at the boundary areas of the extended cylindrical of PA and DA, while the PV is set as a non-tractive pressure outlet, with relative pressure held at zero	58
Figure 21: (a) Polyhedral elements on each CFD models, and a zoom out of elements at the anastomotic region were shown (b) Elements and prism layer at the boundary areas	60
Figure 22: Discretisation error was estimated in four location - Point 1: PA segment before the anastomosis, Point 2: PV segment after the anastomosis, Point 3: downstream of the PV segment and Point 4: downstream of the PA segment.....	61
Figure 23: Resistance calculation in an AVF, represented by the ratio of pressure difference from the anastomosis, d_0 to a certain distance (d_1 at PA and d_2 at PV) along the AVF and the average flow rates of respective vessels	66
Figure 24: Experimental (Exp) and CFD results comparison at the four location indicated in the AVF geometry on the right at Location 1 (blue), Location 2 (green), Location 3 (red) and Location 4 (black) at 0.141s, peak systole of the cardiac cycle.....	69
Figure 25: (a) Retrograde flow (b) Antegrade flow; Direction of blood flow from the DA, represented with the yellow arrow varies for the different flow types.	73
Figure 26: The flow type in Patient A's AVF is the retrograde flow condition where flow from PA and DA contributes to the total flow in PV. The black arrow represents the direction of blood flow. Approximately 94% of the flow from the PA and 6% flow from the DA contributes to the PV of Patient A's AVF (BC 1) . A flow split condition is employed for the retrograde condition with 70% of the total flow at the PA and 30% from the DA (BC 2) . The antegrade flow was modelled by using the patient-specific flow profile at the PA, and an outflow of 2:8 ratio of flow at the DA and the PV respectively (BC 3)	78

Figure 27: The flow type in Patient B's AVF is antegrade where most of the flow from PA diverts to the DA and PV at the anastomosis. The black arrow represents the direction of blood flow. Approximately 99.7% of the measured flow exits the PV and 0.3 % of the total flow measured exits the DA. Flow profile at the DA shares a similar shape with the patient-specific condition. Due to the low velocity, it is barely distinguishable from the zero line in this figure **(BC 1)**. A flow split condition is employed with 70% of the total flow modelled at the PA and 30% from the DA to mimic the retrograde flow condition **(BC 2)**. The antegrade flow was modelled by using the patient-specific flow profile at the PA, and an outflow of 2:8 ratio of flow at the DA and the PV respectively **(BC 3)**.79

Figure 28: The flow type in Patient C's AVF is the retrograde flow condition where flow from PA and DA contributes to the total flow in PV. The black arrow represents the direction of blood flow. Approximately 0.8% of blood flow from the DA and 99.2% of the flow from the PA. A majority of the blood feeding into the PV is from the PA **(BC 1)**. A flow split condition is employed with 70% of the total flow modelled at the PA and 30% from the DA to mimic the retrograde flow condition **(BC 2)**. The antegrade flow was modelled by using the patient-specific flow profile at the PA, and an outflow of 2:8 ratio of flow at the DA and the PV respectively **(BC 3)**.80

Figure 29: Streamline velocity of blood flow for the three different cases of patient A (a) BC 1(b) BC 2 and (c) BC 3 at peak systole of the fourth cardiac cycle. All cases share the same legend.....81

Figure 30: TAWSS and transWSS at the PV of Patient A82

Figure 31: Streamline velocity of blood flow for the three different cases of patient B **(a)** BC 1**(b)** BC 2 and **(c)** BC 3 at peak systole of the fourth cardiac cycle. Separate legends were used for each cases due to the wide range of velocity.83

Figure 32: (top) Circumferential average calculated at the surface of the wall with a 1mm increment along the centreline of Patient B's AVF (left) TAWSS and (middle) transWSS (right) OSI of the PV and PA.....	84
Figure 33: Streamlines of blood flow for another patient-specific model, Patient C (a) BC 1 (b) BC 2 and (c) BC 3 at peak systole of the fourth cardiac cycle. All cases share the same legend.	87
Figure 34: (top to bottom) Anastomotic angle for Patient A, B and C, where $\theta_A \approx 107^\circ$, $\theta_B \approx 132^\circ$ and $\theta_C \approx 48^\circ$ and $\theta_B > \theta_A > \theta_C$	89
Figure 35: Comparison of CFD-derived resistance with the Hagen Poiseuille estimation at the PA segment	91
Figure 36: Comparison of CFD-derived resistance with the Hagen Poiseuille estimation at the PV segment	91
Figure 37: Change of $1/r^4$ along the anastomosis ($L = 0$ to 75mm) of (a) Patient A and (b) Patient B.....	92
Figure 38: Boxplot representation and comparison of resistance range for the six patients with a pre- and post-intervention scan. Shadowed (grey) squared points represent mean values. Outliers are represented with blue circles.....	104
Figure 39: Changes of resistance at the PA pre- and post- intervention.....	107
Figure 40: (a) Changes of R at 1mm interval along the PV of the AVF. Red circles represents the maximum change in R, coinciding with the stenosis region observed in each scan.(b) Scan 1a was taken 684 days post creation, (c) Scan 1b was taken 726 days post creation, and approximately 42 days from Scan 1a, (d) Scan 1c, 1160 days post creation, and approximately 434 days from the Scan 1b, e) Scan 1d, 42 months post creation, and approximately 112 days from Scan 1c. There was also an intervention between Scan 1b and 1c. (f) Angiography image before stent deployment, comparable to Scan 1b, (g) Angiography image after stent	

deployment, comparable to scan 1c. The three-dimensional geometry for these two scans are shown in the bottom right of the angiography images.....	112
Figure 41:(right) Angiography images of Scan 4a, Scan 4b and Scan 4c that are comparable to the (left) three-dimensional AVF geometries.	114
Figure 42: (a) Changes of R at 1mm interval along the PV of the AVF. The red circle shows the maximum change in R, that correlates with the stenosis region shown in respective geometries. Scan 4a was taken before the interwoven nitinol stent was deployed. Scan 4b was taken 4.5 month after the mentioned intervention. Scan 4c was taken one week after Scan 4b was taken.....	115
Figure 43: (a) R in the PA and PV of Patient 8. The geometry that associates to the pre- (Scan 8a) and post- intervention (Scan 8b) scans are shown below respective bar charts. (b) Angiography image that is comparable to Scan 8a and (c) Scan 8b.....	117
Figure 44: The relationship of resistance and average diameter of PV for the six patients pre- and post-intervention. Pt represents “patient” ID. Overlap labels for post-intervention scans are Pt 1, Pt 2, Pt 3; Overlap labels for pre-intervention scans is Pt 1.	118
Figure 45: (top) Web database for the FistulaFlow application, accessible at https://www.vfdunsw.com/fistula-scans (bottom). Example patient scan, information, CFD results and QR code for the FistulaFlow mobile application.....	121
Figure 46: The user interface of the FistulaFlow mobile application platform in augmented reality: (top right) one can select or deselect any data of interest available; (bottom left) the patient ID, geometry and blood flow pattern specific to the AVF; (bottom right) Legend of blood flow velocity and wall shear stress [217].....	122
Figure 47: Illustration of the relationship between Level 1 predictor (fixed effect), that is resistance and the cluster (random effect), that is the different patient. A patient can have	

multiple resistance values based on the scan taken. Graphical illustration reproduced from [230].	131
Figure 48: The range of resistance with patients of with intervention (labelled as "1") and without an intervention (labelled as "0") at PA and PV of the AVF. Shadowed (grey) squared points represent mean values. Outliers are labelled as blue circles outside of the range of the boxplot.	135
Figure 49: Marginal distribution plot of resistance calculated for eligible patient data. The intervention group are distinguished by colour: with an intervention denoted as "1", and without intervention denoted as "0". The histogram on the top corresponds to the frequency distribution of resistance at the PA, while the histogram on the right corresponds to the frequency distribution of resistance at the PV.	139
Figure 50: The logistic regression fitted curves the represents the fitted probability of an intervention for a given resistance of a mixed-effects logistic regression model. The shaded area depicts the uncertainty in that prediction based on the confidence interval limit. The rugs represents the dataset collected, and intervention, "1" and no intervention "0" group are distinguished by colour, per the legend.	142
Figure 51: The ROC graph used to illustrate the diagnostic ability of the multilevel regression model. The AUC of this ROC curve is 92.1%, with a 95% confidence interval of sensitivity of 84.4 % to 99.9%. The threshold that has optimum sensitivity (90%) and specificity (83%) is when resistance is at 6.7 mmHg/l/min (labelled with the black cross).	149
Figure 52: Association of resistance and the fitted probability curve for randomly generated variance of hypothetical individuals. Blue lines represent the fitted curve produced from the randomly generated hypothetical patients, and the black lines represent the average fitted prediction curve from our dataset.	153

Figure 53: ROC graphs of continuous variables such as resistance at the artery segment and age of the patient.....	155
Figure 54: Connection of different parts of the system, distinguishable by the coloured boxes: AVF data acquisition, CFD modelling and post-processing (yellow) along with clinical database validation (blue) and regular communication with clinicians (green). This is followed by the visualisation of data to identify disease sites and likelihood of an intervention (red), which is the outcome of this thesis. The future direction toward a predictive clinical model will be achievable with more dataset and by incorporating emerging technologies (purple).....	165
Figure 55: The confusion matrix, visualising the performance algorithm used for the ROC analysis. Reprinted and adapted with permission [232].	D

List of Abbreviations

AVF	Arteriovenous fistula
ESRD	End-stage renal disease
CKD	Chronic kidney disease
IH	Intimal hyperplasia
WSS	Wall shear stress
TAWSS	Time-averaged wall shear stress
TransWSS	Transverse wall shear stress
OSI	Oscillatory shear index
R	Resistance
CFD	Computational fluid dynamics
FSI	Fluid structure interaction
PA	Proximal artery
PV	Proximal vein
DA	Distal artery
JXA	Juxta-anastomotic
HTN	Hypertension
CVA	Cerebral vascular accident
PVD	Peripheral vascular disease
ROC	Receiver operating characteristic
AUC	Area under curve
PIV	Particle image velocimetry
CI	Confidence interval

Chapter 1

Introduction

1.1 Haemodialysis

Kidneys are central to the body's waste filtration system, removing waste products and excess fluid from the body through urination. This process removes toxins from the blood stream, maintains the body's delicate balance between water, salt and other minerals, and releases hormones that regulate blood pressure. When kidney function is compromised, a person will be diagnosed with chronic kidney disease (CKD). In the final stage of CKD, known as end-stage renal disease (ESRD), a person's kidneys will lose their function completely.

To maintain the body's waste filtration system, ESRD patients will require kidney transplants, to replace their malfunctioning kidney. However, long waiting lists for kidney transplants can result in the need for patients to undergo dialysis instead. Dialysis is a process of artificially cleaning a person's blood using an external machine, thereby maintaining the function of the kidney.

There are three types of dialysis available: peritoneal dialysis, in-centre haemodialysis and home haemodialysis. Among these, haemodialysis (in-centre or home-based) is most common, due to favourable long-term outcomes [1]. Each haemodialysis session generally lasts for approximately four to five hours, where patients typically require three sessions per week [2]. Blood from the arteries side is drawn through a cannulation needle as it passes through the extracorporeal system to the dialysis machine. The dialyser filters blood with treated water, and waste from the blood is drained before the blood is re-introduced to the body [3]. Blood pressure was monitored before and after being removed and entered the body, as well as before entering the dialyser. The haemodialysis extracorporeal circuit is illustrated in Figure 1.

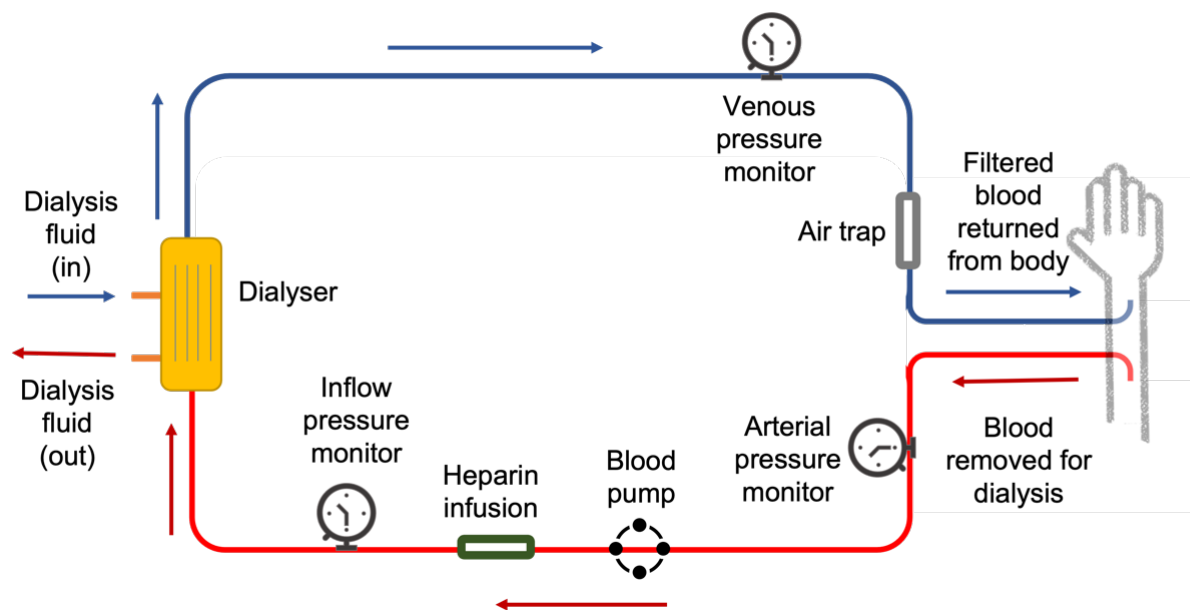


Figure 1: Haemodialysis extracorporeal circuit: Blood removed from the body was pumped to the dialyser (filter). Then, filtration happens at the dialyser before filtered blood returns to the body. Pressure was being monitored before and after blood was removed and entered the body, as well as before entering the dialyser. Heparin was infused to the stream to prevent blood clot. The arrows represent the direction of blood flow.

1.2 Vascular access

Vascular access refers to quick and direct access to the body's venous and arterial circulation. Types of vascular access include arteriovenous fistula (AVF), arteriovenous graft (AVG) and central venous catheter (CVC), shown in Figure 2 [4]. CVC is usually used for the short-term, as well as when immediate vascular access is required, such as in the case of an acute ESRD. However, with CVC there is a high risk of complications such as infections which lower a patient's quality-of-life, thus making it both AVF and AVG more desirable choices for vascular access, compared to CVC [5], especially for elderly patients [6].

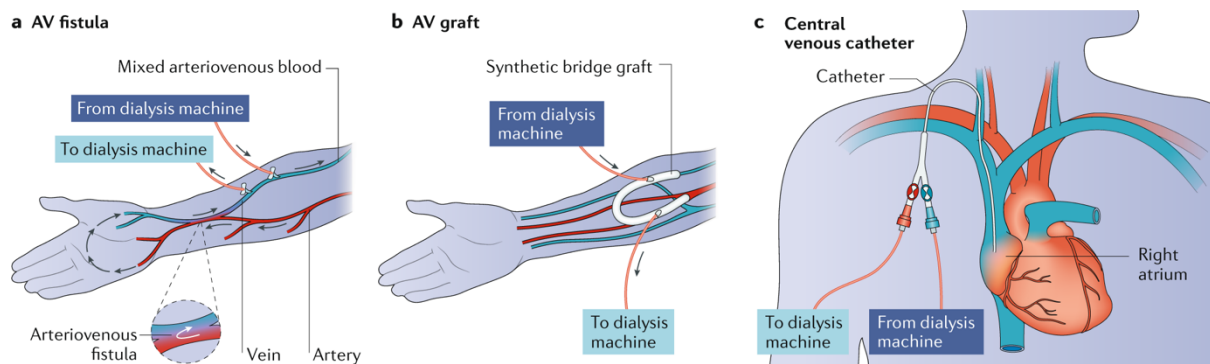


Figure 2: The three different types of vascular access: (a) Arteriovenous fistula (AVF) (b) Arteriovenous graft (c) Central venous catheter. Reprinted with permission [4].

To create an AVF or AVG as an access point from a blood vessel to the dialysis machine, surgical processes are required. The artery and vein of an AVG are connected through the placement of a synthetic tube, made from materials such as polytetrafluoroethylene [7]. Although the AVG has a simpler surgical technique and can be used for haemodialysis quicker than an AVF, it is more prone to failure due to infection [5] and has yielded a higher all-cause mortality rate among patients [5], [8].

1.3 Arteriovenous fistula (AVF)

The AVF is a surgically-created autologous vasculature, connecting the native artery and vein of a patient, where the vein serves as the accessible conduit for haemodialysis. The AVF has greater longevity, lower frequency of thrombosis and lower infection rates, as compared to the AVG [5], [9]. The AVF, however, requires a period of maturation of about 6 weeks to allow sufficient blood flow along it before starting the dialysis process [10]. This also means that AVF needs to be created a few months prior to ensure that the blood flow is sufficient for the patient to undergo haemodialysis [4].

The long-term patency and lower complication rates of an AVF make it the preferred vascular access type [10], [11]. AVF placement is dependent on the patient's ESRD plan for haemodialysis, where patients considering undergoing haemodialysis for a prolonged period are recommended to first consider a forearm AVF placement, that is the radiocephalic AVF, before opting for the upper arm such as brachiocephalic and brachiobasilic transposition AVF (Figure 3) [9], [10], [12], [13]. The radiocephalic AVF is created by connecting the radial artery and the cephalic vein, where the point of connecting both vessels on is called the anastomosis, bypassing peripheral capillaries [14]. Radiocephalic AVF are reported to have better long-term survival than other AVF, although with high primary failure rate [15]. The four types of anastomoses are end artery to end vein anastomosis, end artery to side vein anastomosis, side artery to end vein anastomosis and side artery to side vein anastomosis [14]. The AVF configuration influences blood flow distribution which subsequently affects the patency rate of an AVF, with end-to-side AVF configuration being the preferred AVF type [16].

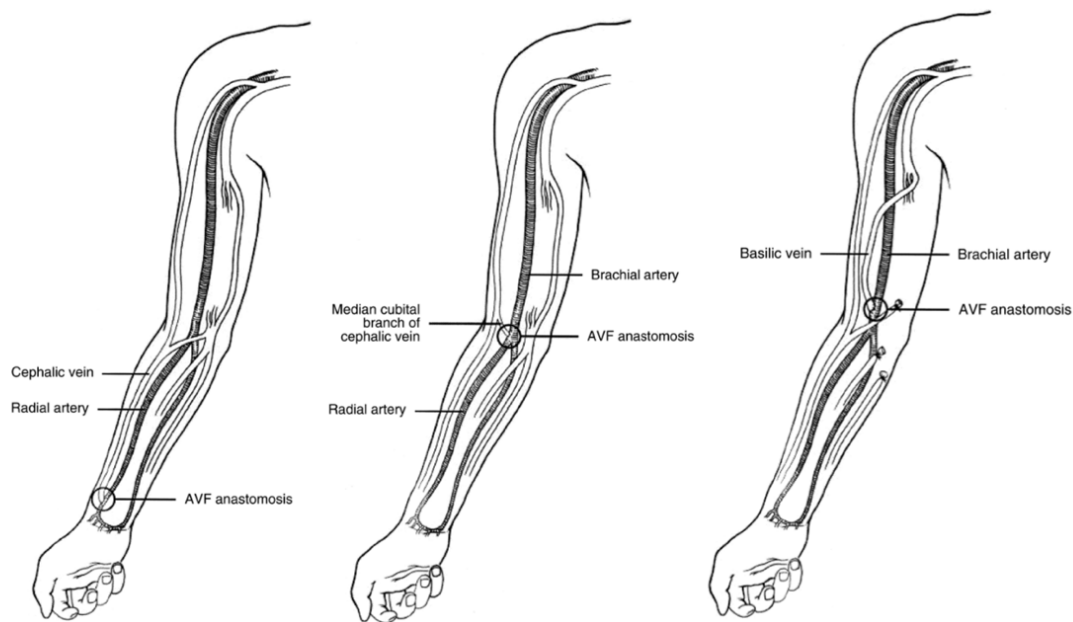


Figure 3: (left to right) Radiocephalic AVF, Branchiocephalic AVF, Brachiocephalic transposition AVF. Reprinted with permission [9].

Once surgically created, AVF vessel walls take at least 6 weeks, and up to 3.5 months, to adapt to the new environment as a result of increased blood flow, a phenomena called vascular remodelling, before the AVF is suitable to be used for dialysis [17]. A matured AVF attains a high blood flow rate, with the ability to achieve a rate as high as 1000-2000 ml/min [14], [18] for effective haemodialysis process. The National Kidney Foundation's Kidney Dialysis Outcome Quality Initiative (KDOQI) guidelines advise on maturation determinations based on the rule of 6s: typically 6 weeks after surgery, an AVF with blood flow greater than 600 ml/min, and diameter greater than 6mm can be used [10].

Within the early stages of AVF formation (the first 2 months), the AVF is closely observed to ensure sufficient blood flow for haemodialysis. The possible failure mode during this time includes limited outward remodelling and inward remodelling induced by intimal hyperplasia (IH) development [19]. The connection of the low-pressure venous system and high pressure arterial system results in a low-resistance circuit, hence causing an increase in blood flow in

the venous segment of the AVF [20]. As a response, the vessel lumen will dilate to cope with the increased flow rate based on Poiseuille's law (Eq. 1).

$$Q = \frac{(\pi \Delta P r^4)}{8nl} \quad \text{Eq. 1}$$

where Q depicts the flow rate, ΔP depicts the pressure gradient, n depicts viscosity, r depicts radius of the vessel and l depicts the length of the vessel.

The overview of the vascular maturation process is illustrated in Figure 4. The flow rates of the cephalic vein and radial artery increase by 60% and 20% respectively after day 1 and increase further by 150% and 50% respectively within 4 to 8 weeks, for a successful maturation. An inadequate increase in flow rates (limited outward remodelling) results in an unsuccessful maturation process, where AVF is not suitable for haemodialysis due to insufficient flow [21].

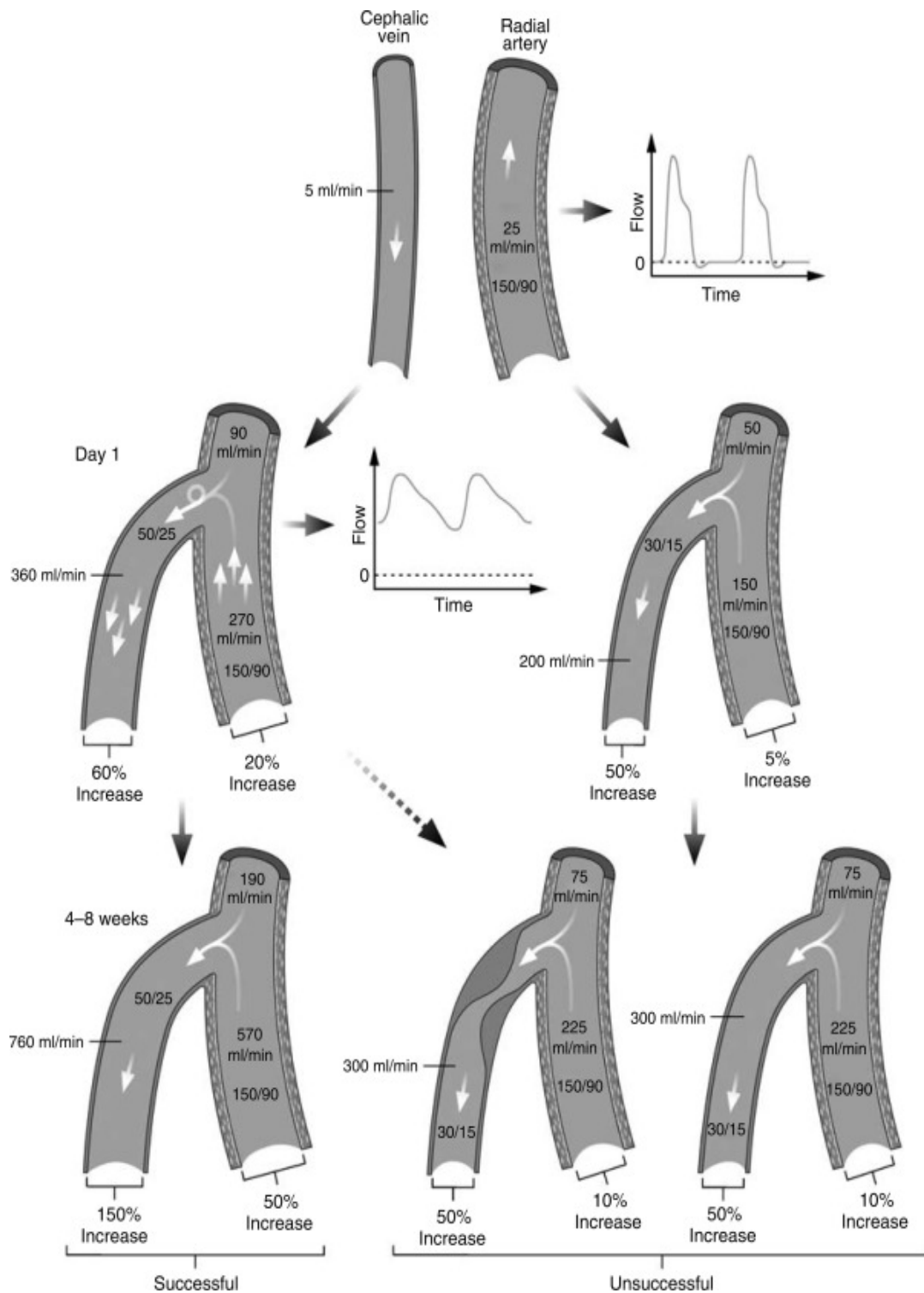


Figure 4: AVF maturation process: **(top)** Preoperative flow rate of the radial artery and cephalic vein **(middle)** An increase in flow rate at the artery and vein segment of the AVF day 1 after creation **(bottom)** Examples of successful and unsuccessful cases of AVF maturation where an insufficient increase in flow rate usually result to an unsuccessful vascular remodelling. The other mode of early fistula failure is the development of stenosis as shown in the middle image. Reprinted with permission [21].

1.4 AVF failure

The introduction of a “fistula first” policy may have resulted in an increase in AVF failure, with AVF creation proposed even for patients of high clinical risks and disadvantaged anatomies (e.g. small vessels) [11], [22]. Bylsma et al. performed a meta-analysis of 62712 AVFs reported in literature, finding that 25% to 33% of created AVFs failed, and hence were never used for their intended purpose [17]. In the same meta-analysis, 73% of mature AVFs were found to require interventions to maintain patency in the first year after formation [17]. In a multi-centre longitudinal study in four European centres, following 93 AVFs from creation, 21% failed to mature, with average patency at 66% one year after creation, and 56% two years from creation [23]. On the other side of the globe, a retrospective study among the Asian population, following 436 radiocephalic AVFs revealed a secondary patency rate of 72% within a year from creation and 69% in the second year, followed by a decreasing trend of patency rates in subsequent years [24].

1.5 Summary

CKD is life threatening, and continues to be, with data from the Australian Institute of Health and Welfare identifying CKD as an underlying cause for more than 1 of every 10 Australian deaths in 2018 [25]. Despite AVF being the optimal form of vascular access for haemodialysis dependent ESRD patients, significant problems remain which hinder the successful and timely maturation of AVF and cause other post-formation issues. Post-maturation, AVF are frequently affected by the formation of IH, which can cause stenotic lesions resulting in clinical dialysis dysfunction and/or circuit thrombosis [26]. IH causes the inner cross-sectional area of the vessel to narrow, causing a reduction in the blood flow rate and pressure through the AVF, which may lead to arterial insufficiency [27], [28].

Given high failure rates, it is imperative to explore current clinical approaches to monitoring AVF patency. Current clinical strategies for monitoring AVF patency include considerations of demographics, age, other comorbidities, pre-operative diameter of the vessels, and pre- or intra-operative flow rates [29], [30]. The dynamic development of diseases in an AVF [31], [32] poses the need to identify different indicators of failure, to make clinical monitoring more strategic. Lower costs associated with computational fluid dynamics (CFD) modelling have encouraged the use of this tool for regular surveillance of diseased vessels by assessing blood flow behaviours. Furthermore, haemodynamic variations in an AVF are inherent to blood vessel geometry, with a body of evidence [33]–[39] supporting the need for a patient-specific modelling approach to closely monitor and predict localised diseased development.

1.6 Thesis Scope

The objective of this thesis is to examine the use of CFD-derived resistance as a clinical indicator for AVF failure through patient-specific modelling. The thesis is outlined as such:

Chapter 2 covers a review of current work in the field of AVF failure prediction during maturation and post-maturation. Current retrospective clinical predictive models for AVF maturation prediction, computational modelling (0D, 1D and 3D modelling) and other emerging technologies used in AVF failure prediction were assessed.

Chapter 3 describes the methodology for patient-specific CFD modelling. Patient-specific geometry and flow profile acquisition, the CFD modelling approach, the CFD-derived resistance calculations for AVF and validation strategies are included in this chapter.

Chapter 4 details the significance of using patient-specific boundary conditions, rather than an assumed flow split ratio in AVF CFD models, especially towards targeted patient care and recommendation.

Chapter 5 introduces and describes the relationship between CFD-derived resistance and the identification of problematic AVF in a group of patients who have undergone juxta-anastomotic stent deployment to treat juxta-anastomotic stenosis. CFD-derived resistance was also used to identify regions with stenosis, in real patient cases.

Chapter 6 details overall trends observed in CFD-derived resistance and the likelihood that intervention is required for all patients, regardless of intervention status and types through a systematic review of patient data.

Chapter 7 elaborates key findings of the thesis and recommendations for future research directions, contributing to more effective and targeted identification of problematic AVF.

Chapter 2

Literature Review

This chapter is a review of literature on clinical predictive models for AVF maturation and ongoing efforts to predict late failure (post-maturation period) based on the haemodynamics of an AVF. Different approaches in assessing risk factors and haemodynamic quantifiers for AVF failure prediction will be discussed. Some parts of this chapter are based on the paper “A review of the predictive methods for arteriovenous fistula (AVF) failure identification”, which is currently under review with the Computer Methods in Biomechanics and Biomedical Engineering: Imaging & Visualization.

2.1 Overview

The high prevalence of diseased AVF leading to subsequent failure is evident, regardless of demographic and population. The definitions used for time-dependent AVF patency are as shown in Table 1 [13].

Table 1: AVF patency definitions [13]

Terminology	Definition
Primary failure	New AVF that fails to mature (Not applicable for AVF that have been used for more than 6 months)
Primary unassisted patency	The time from AVF creation until any first intervention to maintain blood flow
Secondary patency	The time from AVF creation until abandonment or achievement of a censored event e.g. death
Post-intervention primary patency	The time from the previous surgical procedure until the next intervention

A matured AVF means the vasculature has sufficient outward remodelling, leading to an increase in lumen diameter, enabling sufficient blood flow in the draining vein segment for efficient haemodialysis. However, there is still a possibility of secondary failure for matured AVF, affected by the formation of IH as a biological response of the endothelial cells to haemodynamic changes, resulting in the development of stenosis, that is a narrowing of blood vessels which leads to access dysfunction and circuit thrombosis [26], [40], [41]. The common sites of stenosis are at the anastomosis (Type 1), the inner wall of the vein segment (Type 2),

and upstream of the vein segment (Type 3), as illustrated in Figure 5, from an early study by Sivanesan et al. [42].

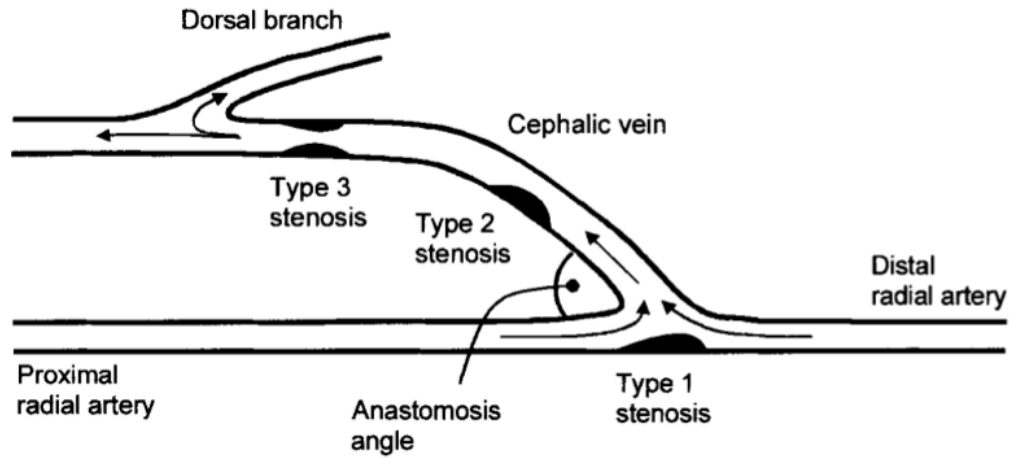


Figure 5: Common site of stenosis in an AVF. Reprinted with permission [42].

Endothelial denudation, vascular smooth muscle cell proliferation and migration are among the other factors that impede outward remodelling and contribute to the formation of IH [20], [43]. Although IH has been associated with anatomical failure of an AVF [44], [45], postoperative histological samples of 56 patients' AVFs suggest that there is a lack of association of IH and

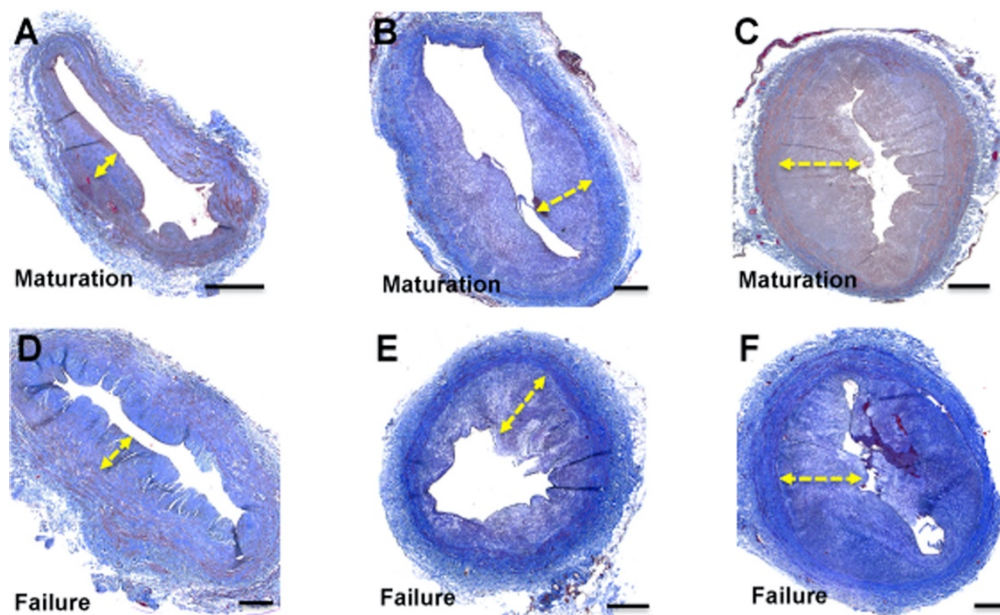


Figure 6: Histology of AVF tissue specimen. (top three) represents the section of mature AVF, (bottom three) represents section of failed AVF with maximal intimal thickening (indicated with the yellow dotted arrow) that result in AVF failure due to intimal hyperplasia. Reprinted with permission [46].

AVF failure with similar intimal thickness (more than 0.62mm) observed in the group with matured and failed AVFs, as shown in Figure 6 [46]. This supports findings that suggest a balance between outward expansion and luminal narrowing due to IH determines stenosis formation [19], [20]. Maturation of AVF can be hindered by CKD-associated venous pathology such as IH, while a healthy vein has the potential to successfully mature. The biology of AVF remodelling that leads to IH and subsequent failure is illustrated in Figure 7.

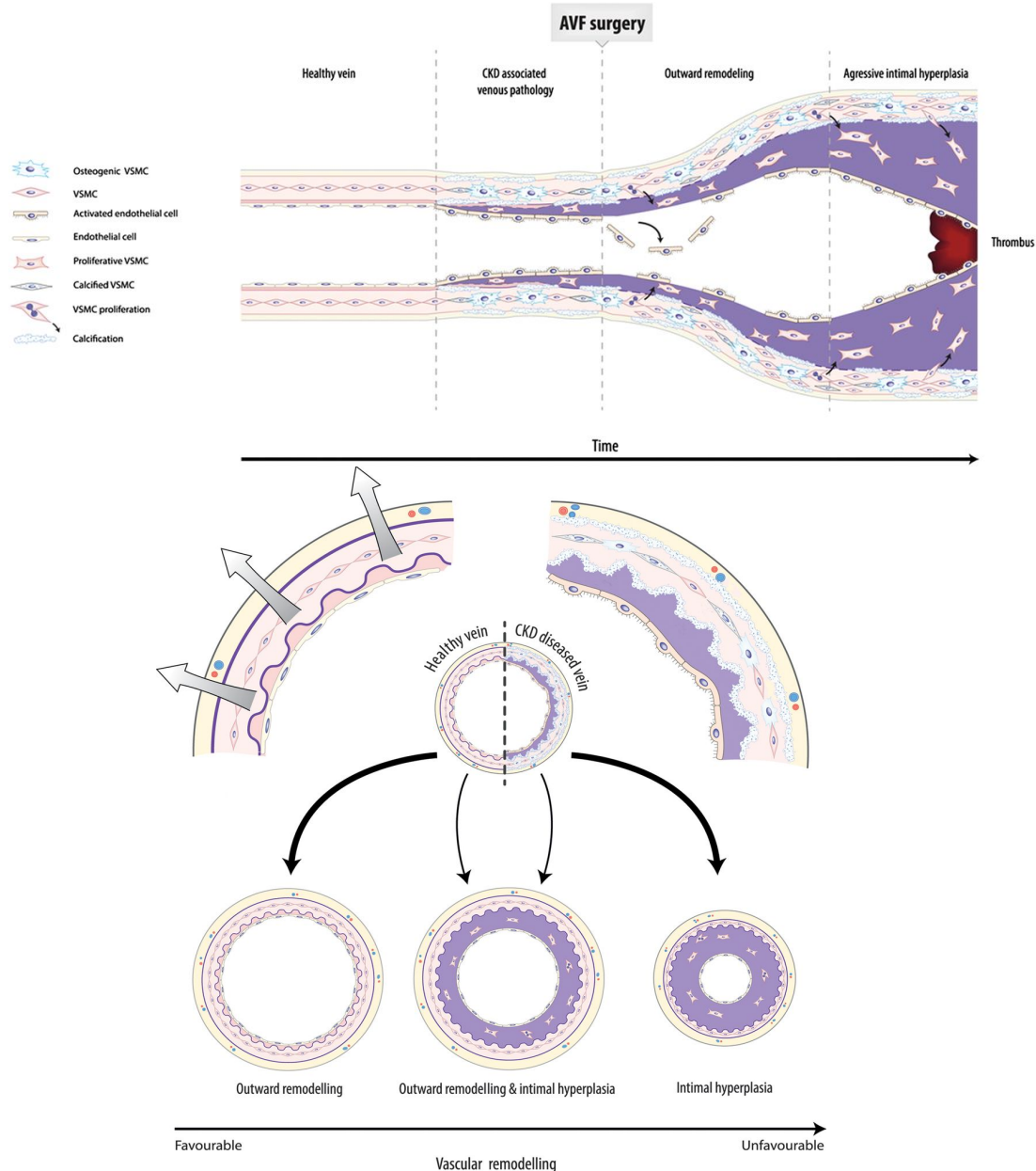


Figure 7: **(top)** Vascular remodelling response after creation of AVF where a series of response and structure changes occurred in the vasculature due to the altered haemodynamic environment. **(bottom)** The different vascular remodelling modalities: outward remodelling for adequately matured AVF, optimal net balance achieved between outward remodelling and intimal hyperplasia, that is sufficient outward remodelled achieved, leaving the AVF patent despite intimal hyperplasia and intimal hyperplasia that is when the fistula fails due to stenosis or thrombosis. Reprinted with permission [20].

2.2 Predictive model for AVF failure

AVF patency depends on a range of factors, including patient, clinical, anatomical, and biochemical factors [17], [29], [47], [48]. Patient factors such as age and presence of other comorbidities (diabetes, smoking, peripheral vascular disease, pre-dialysis hypotension) are risk factors that were found to affect AVF patency rates [47], [49]. There was also an increased risk of AVF failure reported among elderly patients [50], owing to other significant comorbidities resulting in poor vessels [6]. On a molecular level, factors associated with AVF failure include inflammation, uremia, hypoxia, shear stress, hypoxic injury and thrombosis [51].

Another factor found to be associated with patency rates was cannulation time and technique, where a rope-ladder or buttonhole cannulation technique was shown to yield favourable patency rates, as opposed to area cannulation, according to a cross-sectional survey of 171 dialysis units [52]. In a prospective observational study of 3674 patients in 309 centres around the world (France, Germany, Italy, Japan, Spain, the United Kingdom, and the United States), Rayner et al. pointed out that cannulation within the first 14 days post-creation leads to a higher risk of AVF failure [53]. Furthermore, AVF cannulation techniques and cannulation day from creation were reported to be more superior than patient-related factors [53]. This finding complements a multi-centre randomised trial conducted by Hussain et al. of 914 subjects which reported that patient's dialysis when AVF was created to have increased risk of primary patency loss ($P = 0.004$); and the use of haemodialysis catheters in primary and primary assisted patency prediction ($P < 0.001$) [54]. Needle position such as location at the arterial and venous vessel or cannulation angle at site of impingement can produce a high speed jet that gives rise to high wall shear stress, affecting the endothelial structures [55], [56]. The haemodynamics vary for different cannulation needle position, technique and location, as illustrated in Figure 8. Jet dissipation occurs directly after exiting the needle with an increase

of flow rate. The needle angle and needle position has little effect on the venous needle jet [55].

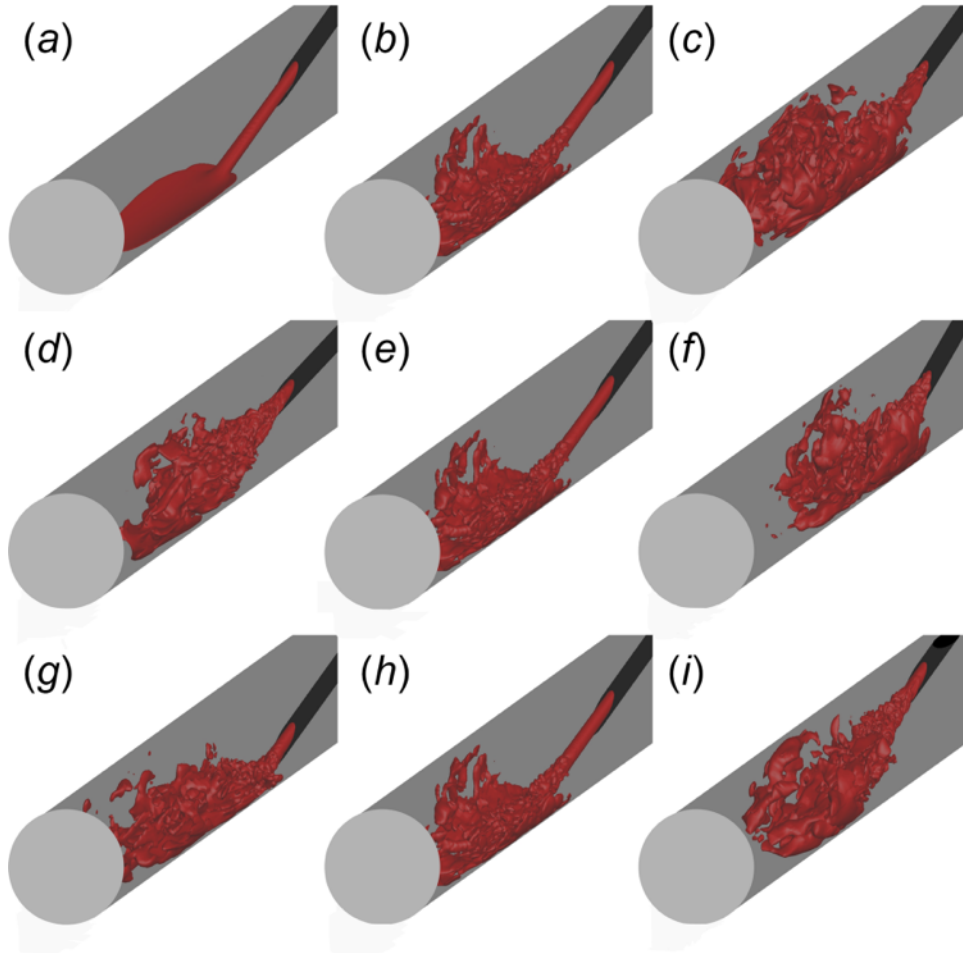


Figure 8: Velocity needle jet visualisation for (a-c) blood flow rate of 200 ml/min, 300 ml/min and 400 ml/min (d-f) needle angle of 10°, 20°, and 30° (g-i) needle position of bottom, central and top. Reprinted with permission [55].

2.3 Clinical AVF “fail to mature” predictive model

According to an early study assessing predictors for AVF maturation (N = 101), only 47% of AVF successfully matured, becoming suitable for dialysis [29]. Older patients ($P = 0.03$) with diabetes ($P = 0.061$) were found to be at greater risk of achieving inadequate AVF maturation. Furthermore, forearm AVF performed particularly poorly in female patients [29].

The common approach to predicting AVF maturation is by reviewing retrospective clinical data to classify risk factors and scoring systems to develop predictive models [57]–[62]. Lok et al. developed a failure to mature (FTM) prediction model that consists of a scoring system with different risk factors to identify patients with a high risk of AVF maturation failure in a study of 422 patients across five dialysis centres in North America [57]. The study drew findings paralleling with a study by Miller et al. on trend observed in older patients and AVF maturation rate [29]. The predictive risk factors include age, coronary artery disease, peripheral vascular disease, and race. Primary failure increased significantly within certain demographics, including female gender ($P = 0.03$), age over 65 years old ($P < 0.01$), pre-existing peripheral vascular disease ($P < 0.01$), coronary artery disease ($P < 0.01$) and diabetes ($P = 0.05$). The scoring system was proposed and designed to be used alongside vascular access surgical planning, as it classifies patients to different risk groups (score < 2.0 , low risk; $2.0 < \text{score} < 3.0$, moderate risk; $3.1 < \text{score} < 7.0$, high risk; Score > 8.0 very high risk), and this determines if surgical intervention is required to salvage the AVF. The model is however only applicable to patients with their first AVF, as it does not account for previously failed AVF. Another multivariate study (CMS 2728) with 195,756 patients also reported that clinical risk factors identified by Lok et al. failed to predict incident use AVF for haemodialysis [59]. Furthermore, they reported that even patients with the highest factor based on the scoring system can have successful AVF for initiation of haemodialysis [59]. This study therefore suggest that a similar

outcome will be observed even if a more intricate model with currently available parameters is used [59].

A prospective study with a total of 525 European patients assessed the model in a wider population [58], compared to the Canadian and American cohort used previously [57]. The model revealed similar trends across the European cohorts, with high risk AVF FTM patients being of older age and has existing co-morbidities. The model, however, does not predict non-maturation [58]. Although additional risk factors were considered, both models failed to predict ongoing AVF status and were therefore found inadequate to increase AVF functional patency rate [57], [59]. Voorzaat et al. also suggested that the failure to mature AVF observed were not limited to demographical or comorbidities parameters (N = 1383) [63].

Twine et al. proposed the use of DISTAL scoring to predict failure in snuffbox fistula – that is, fistula created with an advantage of proximal vessel preservation [64]. Factors reported to show significant influence over predictive ability, which were included in the scoring system (DISTAL maximum score of 6) include age > 70 years old ($P = 0.034$), venous diameter < 2.0 mm ($P = 0.032$), arterial diameter < 2.5 mm ($P = 0.029$), undergoing two procedures, and presence of pre-existing conditions such as diabetes, ischaemic heart disease, or cerebrovascular accident. This predictive scoring system was proposed to be extended to other AVF types such as radiocephalic AVF [64] given that similar risk factors were reported [49].

More recently, studies have cited the CaVeA₂T₂ scoring system [60] which is a model used to predict fistula patency rates after AVF creation, by identifying a number of risk factors. The system predicts the outcome of forearm radio-cephalic fistulae survival for both pre- and post-fistula creation based on significant risk factors, namely age > 73 years old ($P = 0.040$), anastomosed vein < than 2.2 mm ($P = 0.025$), history of lower limb angioplasty ($P = 0.007$), no peri-operative thrill ($P = 0.004$) and ipsilateral central venous catheters (CVC) access ($P =$

0.019). Validation of this scoring system was conducted in a single-centre retrospective study to measure primary, assisted primary and secondary patency rates which supported the scoring system for VA surgical planning, with a decrease in survival rate when primary and secondary patency are observed [61].

Kordzadeh et al. conducted a large prospective cohort study of 324 patients, concluding that a cephalic vein diameter of more than 1.5 mm and radial artery diameter of more than 1.6mm have independent association with AVF maturation [65]. However, Kakkos et al. [66] argued that the reported study by Kordzadeh et al. [65] ought to be evaluated and assessed clinically with additional duplex ultrasonography evidence to support the reported patency rate.

A prognostic model for AVF clinical maturation was proposed based on different ultrasound measurements of 602 patients' data in a multicentre observational cohort [62]. The predictive model indicates the likelihood of AVF maturation based on different variables, which include AVF blood flow, diameter and depth of vessels provided from ultrasound values from 1 day, 2 weeks or 6 weeks after creation. AVF blood flow is the most significant predictor, with $P < 0.001$ for the three assessment rounds [62]. A larger cephalic vein diameter, of more than or equal to 3.0mm was reported to increase patency rate shown in data from a recent multicentre randomised controlled trial of 914 patients [54].

There is increasing evidence linking an increase of patency rate with the use of duplex ultrasound techniques for pre-surgical assessment planning, and to determine anatomical information such as artery and vein diameters [67]–[70]. Patient radial artery and cephalic vein diameter were the main anatomy factors linked to primary functional maturation of AVF [65], [71]. Although preoperative assessments suggest vein diameter to be the major predictor for AVF maturation, surgeons' overall judgment remained crucial [72]. That said, in terms of vessel wall characteristics, venous distensibility was proposed to be a predictor for AVF

maturation over vessel diameters, and low arterial elasticity was reported to result in poor lumen dilation, thus contributing to AVF maturation failure [73], [74]. Besides, intra-operative information, such as blood flow measured immediately after AVF creation, were suggested to differentiate successful and unsuccessful AVF creation [30], [75].

Resistive index (RI) can be estimated by calculating the ratio of the difference between peak systolic velocity and end diastolic velocity and end diastolic velocity, from Doppler ultrasound [76]. RI values were lower in non-stenotic patients [76] in agreement with Malvorch study [77] that reported a 95.3% patency rate of a group of patients with resistance index of less than 0.7 at reactive hyperaemia, and 38.7% patency rate of a group of patients with resistance index of more than 0.7. Furthermore, a study performed on 48 patients undergoing haemodialysis reported that an increased in resistance index values were detected in patients with reduced pumped flow during dialysis [78]. Whilst RI has been used for AVF assessment and morphological data characteristic with Doppler ultrasound, it provides insufficient information regarding the effects of haemodynamic on the AVF condition, especially when blood flow has turbulent-like features [79]. It was also worth noting that these studies were conducted only during the AVF maturation (remodelling) phase.

2.4 Vascular computer network model

The classic Hagen-Poiseuille law, in the form of a linear equation, was used in 0D models to predict AVF blood flow in patient-specific models [80], [81]. Despite reducing the time required to solve the equation, the use of this simplified method on patient-specific models that have turbulent-like flow features raises questions about the reliability of the results. Non-Newtonian properties, which are not modelled here, also reportedly had an effect on WSS estimation [82], [83]. Besides the application of blood flow model prediction in a 0D vascular computer model [81], the Hagen-Poiseuille WSS estimation has also been used in idealised [84]–[87] or patient-specific 3D models [88] with some studies attempting to apply a correction factor in order, to minimise errors in WSS estimation [89], [90]. Similarly, Remuzzi et al. developed a method to calculate WSS for AVF models based on Womersley’s theory of pulsatile flow, noting the simplification of the assumptions in the Hagen-Poiseuille equations [90], and applying it in a study aimed to examine the relationship between vascular remodelling and shear stresses [91].

Noordergraaf et al. [92] proposed a model with inertance in series with resistance, in addition to the fundamental work of Frank’s two-element Windkessel model [93]. The aforementioned Windkessel model consists of a capacitor that represents the arterial compliance and resistance accounting for outflow and fluid pressure [93]. Gemert et al. [94], [95] introduced an analytically-solvable resistance model to model systematic vascular circulation with an AVF. A computer network (pulse wave propagation) model of the arm circulation was proposed more recently by Hubert et al. [96]–[98], followed by Manini et al. [99], [100] (Figure 9). The algorithm of the pulse wave propagation approach adopted predicts the haemodynamic behaviour after vascular access surgery based on vessel wall remodelling and changes of blood flow [97]. The vascular model of an arterial network in the lower arm was segmented, and the relationships between pressure and volumetric flow rate were derived from the conservation of

mass and momentum at each segment. Different factors affecting remodelling, including pressure, volumetric flow rate and wall shear-stress distribution over the entire vascular system, were incorporated in the mathematical algorithm. The model receives input parameters such as vessel diameters, using these to predict post-operative blood flow volume at anastomosis prior to the surgery, in efforts to avoid unsuccessful procedures [99], [100]. Simulated and measured data correlated well both 40 days post creation ($p < 0.05$) and 100 days post remodelling ($p < 0.01$). The model was limited to post-operative blood flow volume [99], [100].

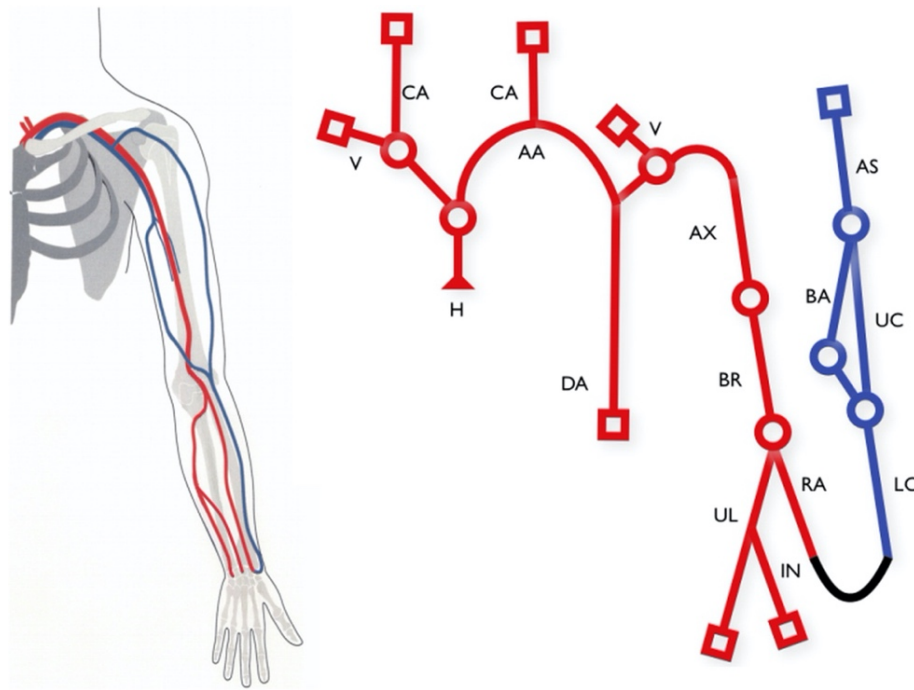


Figure 9: Vascular network model from [99] based on a 0D/1F pulse wave propagation model where the blue segment represents the venous network and the red segment represents the arterial network. Reprinted with permission [99].

The AVF.SIM system [101] was developed in conjunction with the computational vascular network model [23] to integrate computational model with clinical information for surgical planning. Geometrical information including vessel diameter and length, as well as body weight, height, age and gender of individual patients were defined as inputs in the algorithm [99]–[101]. The system also allows data from the simulation to be collected and stored in the feedback system. Clinical tests showed good agreement of blood flow volume upstream of the distal artery, away from the anastomosis, but less accurately at the proximal artery [101]. Disturbed flow at the anastomosis [37], [102] was suggested to be the reason for this inaccuracy at the proximal artery [101]. Although the AVF.SIM system allowed blood flow volume prediction for surgical planning, the limitation of the model to accurately predict blood flow volume at locations closer to the anastomosis becomes problematic, as the anastomosis is a common region for disease development [23], [103]. Moreover, whilst the model showed potential in blood flow prediction post creation during AVF maturation, long-term care throughout the patency of an AVF and the need of a clinical predictor for AVF failure remain of top priority [104].

2.5 Haemodynamic predictors for AVF failure

A different type of predictive approach considers haemodynamic factors in the AVF such as the effect of blood flow, usually making use of a computational fluid dynamics (CFD) model of the AVF (side-to-side [105], end-to-end [33], [102] and side-to-end [37], [106], [107]) to determine the necessary detail of the flow [105], [108]–[110]. CFD is a non-invasive approach to allow insights on the flow field by using computer-based simulations, and has been useful for optimising the AVF shape based on flow patterns of the blood [37], [38], [102], [106], [107], [111]–[114]. The different flow patterns contribute to hemodynamic complexity in an AVF, such as transitional flow found at the venous region of the AVF, with high-frequency fluctuations of velocity observed [35] as well as the simulation of distensible walls [115]. Longitudinal studies were conducted to understand the correlation between WSS and the maturation of AVFs [116]–[119]. Outward remodelling of AVF during maturation is affected by the overall change in WSS [118], [119]. Additionally, disturbed flow in the recirculation zone of an AVF contributes to non-uniform remodelling, initiating the development of IH along the wall of the AVF.

Wall shear stress (WSS), τ_w , calculated on the vessel walls, is directly proportional to the gradient of velocity in the direction perpendicular to the flow and blood viscosity (Eq. 2) [120].

$$\tau_w = \mu \left(\frac{\partial u}{\partial y} \right) \quad \text{Eq. 2}$$

where μ depicts blood dynamic viscosity, u depicts the blood velocity parallel to the wall, and y depicts the distance to the wall

During AVF maturation, vasculature will dilate in response to increased WSS, and the vessel wall responds by attempting to return the shear stress level to the baseline [22], [31], [121], [122]. High WSS promotes outward remodelling where blood vessels expand to reduce high velocities and correlates with aneurysm formation [123], atherosclerotic plaque instability

[124] and endothelial cell damage [113]. High shear stress in the anastomotic and juxta-anastomotic (JXA) venous segment suggests an incomplete remodelling in these regions, even in matured AVF [125]. Low and oscillatory WSS promotes inward remodelling, correlated with intimal thickening, where the blood vessel wall thickens due to IH [113], [116], [126]. Nevertheless, both high and low WSS have been associated with IH formation, and 50% of the literature supports the statement that low and oscillating shear leads to the development of IH in a review by Cunnane et al. [39].

The time-averaged wall shear stress (TAWSS) (Eq. 3), that is the average of the WSS magnitude over the cardiac cycle allows prediction of intimal thickening, based on an early study of a carotid bifurcation model [127]. This can be calculated with Eq. 3, where $\vec{\tau}_w$ depicts the WSS vector and T depicts the time for one complete cardiac cycle.

$$TAWSS = \frac{1}{T} \int_0^T |\vec{\tau}_w| dt \quad \text{Eq. 3}$$

Peiffer et al. [128] outlined the inconsistency in WSS characteristics for low and oscillatory flows. Other time-varying studies show that low TAWSS was observed with diseased vessels [129]–[131], although, in some cases, no correlation was observed with studies that show intimal thickening [132]. Due to the multidirectional flow frequently found in situations such as the anastomosis, TAWSS was not able to accurately capture the flow behaviour [103], [133]. Another metric, the transverse WSS (transWSS) (Eq. 4) was proposed by Peiffer et al. [103] to overcome this limitation. It is calculated as the time-average magnitude of the WSS components which are perpendicular to the mean flow direction. This was followed up by Mohamied et al. [134] who suggested that the pattern of transWSS was strongly dependent on the geometry of the vessel, although the pulsatile nature of blood flow also mediates multidirectional flow.

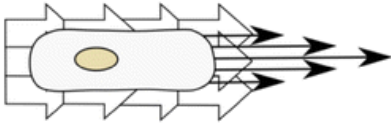
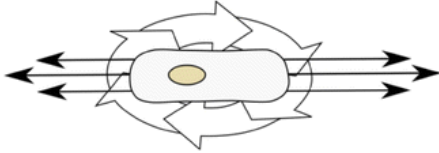
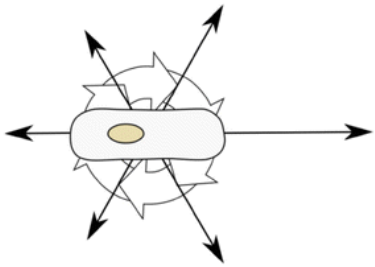
$$transWSS = \frac{1}{T} \int_0^T \left| \vec{\tau}_w \cdot \left(\vec{n} \times \frac{\int_0^T \vec{\tau}_w dt}{\left| \int_0^T \vec{\tau}_w dt \right|} \right) \right| dt \quad Eq. 4$$

Oscillatory shear index (OSI) (Eq. 5) is a metric that specify shear stress acting in directions apart from the direction of the temporal mean shear stress vector in a cardiac cycle [135]. In other word, it is a dimensionless parameter that characterises whether wall shear stress vectors align with the TAWSS vector in a pulsatile flow and can characterise blood moving in the reverse direction (which commonly occurs in the near vicinity of anastomosis). OSI values fall in the range of 0-0.5, where 0 represents unidirectional flow with no oscillations and 0.5 indicates pure oscillatory flow with no net forward motion [133].

$$OSI = 0.5 \left(1 - \frac{\left| \int_0^T \vec{\tau}_w dt \right|}{\int_0^T |\vec{\tau}_w| dt} \right) \quad Eq. 5$$

The described metrics based on flow conditions were summarised in Table 2.

Table 2: Flow condition exposed by endothelial cells, that is unidirectional flow, flow reversal and multidirectional flow. Black arrows represent the instantaneous WSS vectors at an arbitrary point in time within the cardiac cycle, where the progression of it. Reprinted with permission [39].

	TAWSS	OSI	transWSS
<p>Unidirectional Flow</p> 	2.5	0	0
<p>Flow Reversal</p> 	2.5	0.367	0
<p>Multidirectional Flow</p> 	2.5	0.367	1.1547

The aforementioned WSS metrics were adopted for AVF CFD models, and Ene-Iordache et al. showed the possibility of characterising flow configuration with different WSS metrics, by identifying zones with low and oscillating WSS [102], or multidirectional and reciprocating near wall flow patterns [136]. Disturbed flow most commonly occurs on the artery floor and inner wall of the vein, for end-to-side and end-to-end AVF configurations [102], [111]; both are regions where stenosis was often localised [39], [137], as illustrated in Figure 11. Results from Remuzzi et al. [138] showed similarities with previous studies [102] on prime locations that were prone to stenosis. These localised sites of disturbed flow and recirculation zones that correlates with IH development were also shown to be dependent on the blood flow distribution in the AVF (retrograde and antegrade flow) [39], [138], [139], as shown in Figure 10.

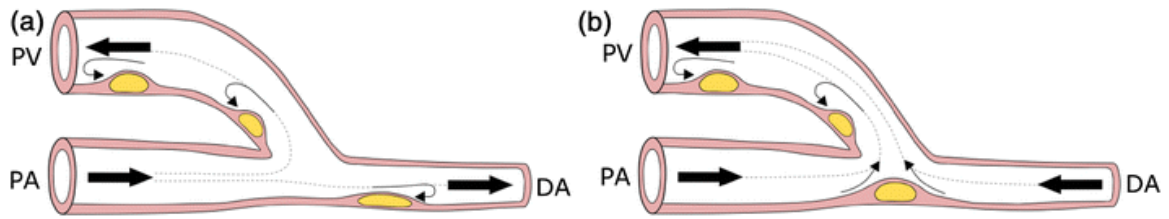


Figure 10: Site susceptible to the intimal thickening within an AVF of (a) antegrade flow where blood flows towards the palmar arch and (b) retrograde flow where blood is going against the palmar arch into the AVF vein segment. The thick black arrow shows the direction of blood flow, while the recirculating zones are indicated with the thin black dotted arrow. Reprinted with permission [39].

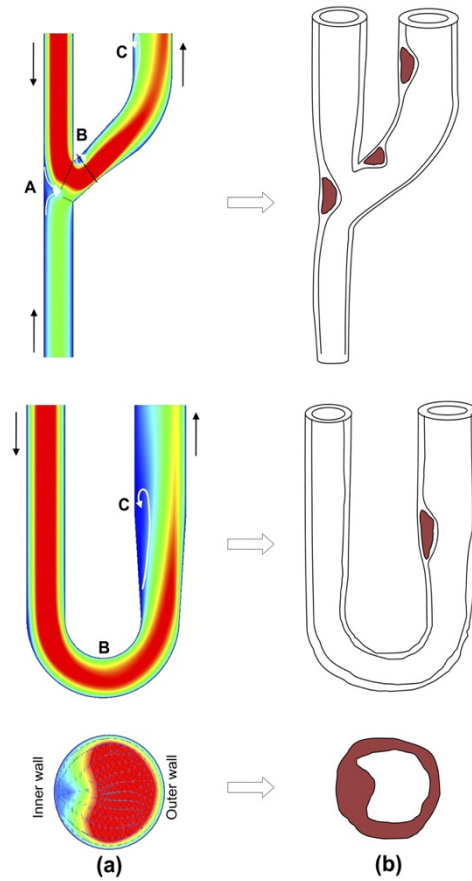


Figure 11: Region of low and oscillating shear stress/flow coincides with the region prone to stenosis development for end-to-side and end-to-end type AVF. Reprinted with permission [102].

The anastomotic flow disturbance can be minimised by slightly modifying the angle of the anastomotic configuration, as reported in an idealised end-to-side AVF [37], [38] and shown in an experiment conducted in an animal model [122]. Geometrical configurations were shown to influence blood flow distribution and haemodynamic parameters with several studies reporting on the benefit of AVF with obtuse-angled anastomosis for more gradual flow transitions [112], [140], minimising the likelihood of failure due to disturbed flow. Disturbed flow was also reported at different locations of a parametrised study of idealised AVF models; low and oscillating shear presence in the anastomotic floor of all models (10° , 35° , 50° and 70°), and high and multidirectional shear stress present in the anastomotic floor of the model smaller anastomotic angle (10° and 35°) [38].

Wang et al. quantify the pro-inflammatory effects of flow acting perpendicular to the predominant axial direction, reporting that inflammatory activation is a result of the inability of cells to align at low and oscillatory flow, suggesting the presence of multidirectional disturbed flow patterns [141], [142]. A large amount of multidirectional flow, indicated by the transWSS metric in addition to the reciprocal flow patterns was found specifically at the juxta-anastomotic region and the anastomotic floor [35], [136], [138], as illustrated in Figure 12. Multidirectional flow investigation with transWSS in relation to IH development, especially in the juxta-anastomotic region may be a key characteristic to look out for to assess the status of AVF.

Cunnane et al. suggested that helical flow be used as a marker to identify exposure sites with low and oscillatory flow [38], previously reported to trigger the onset of IH [39]. Models with the highest helical intensity correlate with the models that had the lowest distribution of low and oscillating shear, in a study of idealised AVF of four different geometrical and angle configurations, as shown in Figure 13 [38]. These regions of high helical intensity, however, coincide with regions with the largest amount of other shear stress metrics such as TAWSS and transWSS. In other words, the presence of helical flow was shown to suppress low and oscillating shear stress except when it comes to high, multidirectional or gradient shear stress [38]. Although the use of metrics based on shear stress may provide a good indicator of disease progression and AVF failure [39], [41], [137], [138], it is still difficult to ascertain the capability of onset disease prediction based on a single WSS metric [38], [39].

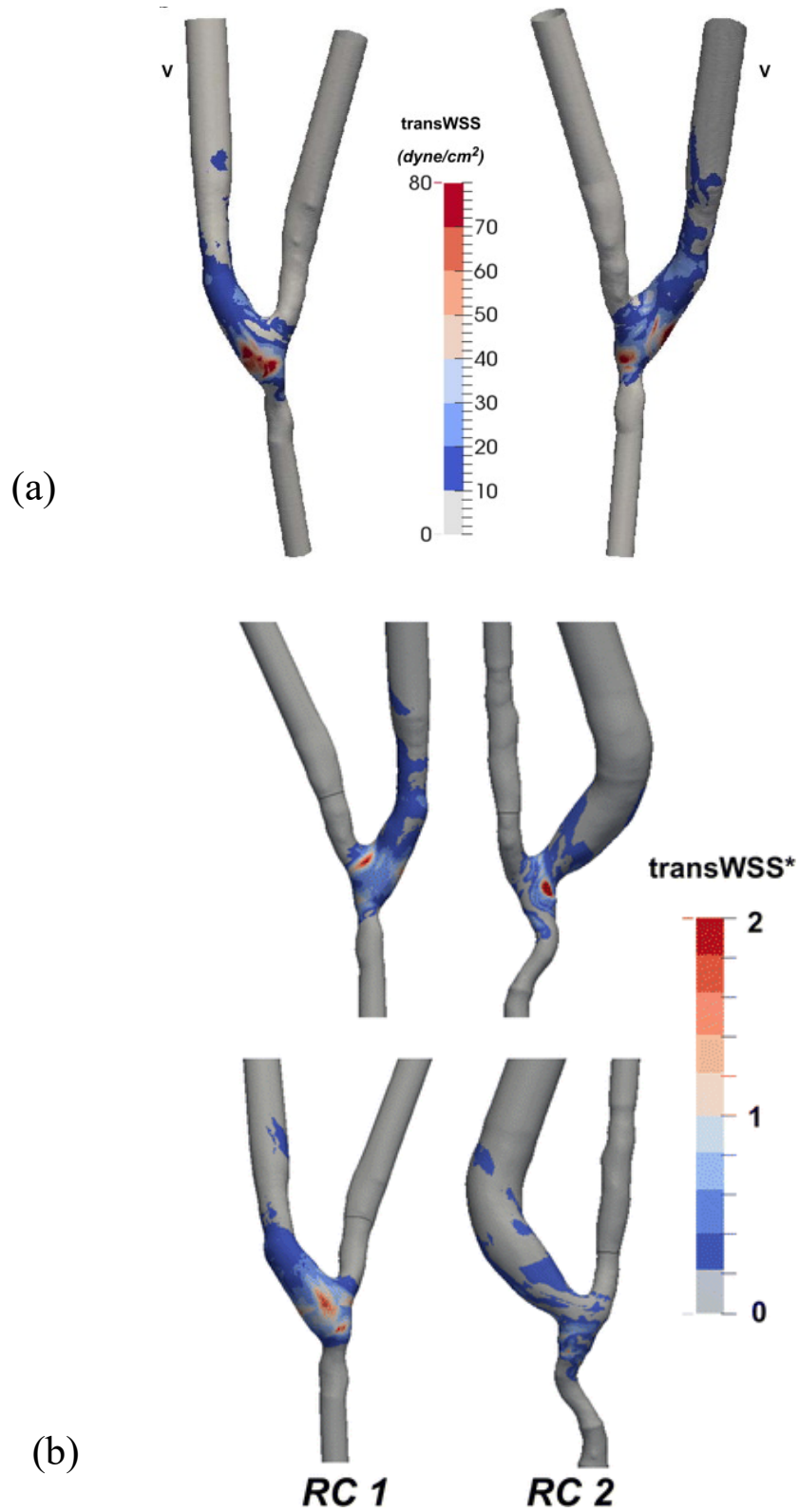


Figure 12: Presence of transitional and multidirectional disturbed flow on inner wall of vein segment for two separate study of patient-specific radial-cephalic AVF. Reprinted and adapted with permission [35], [136].

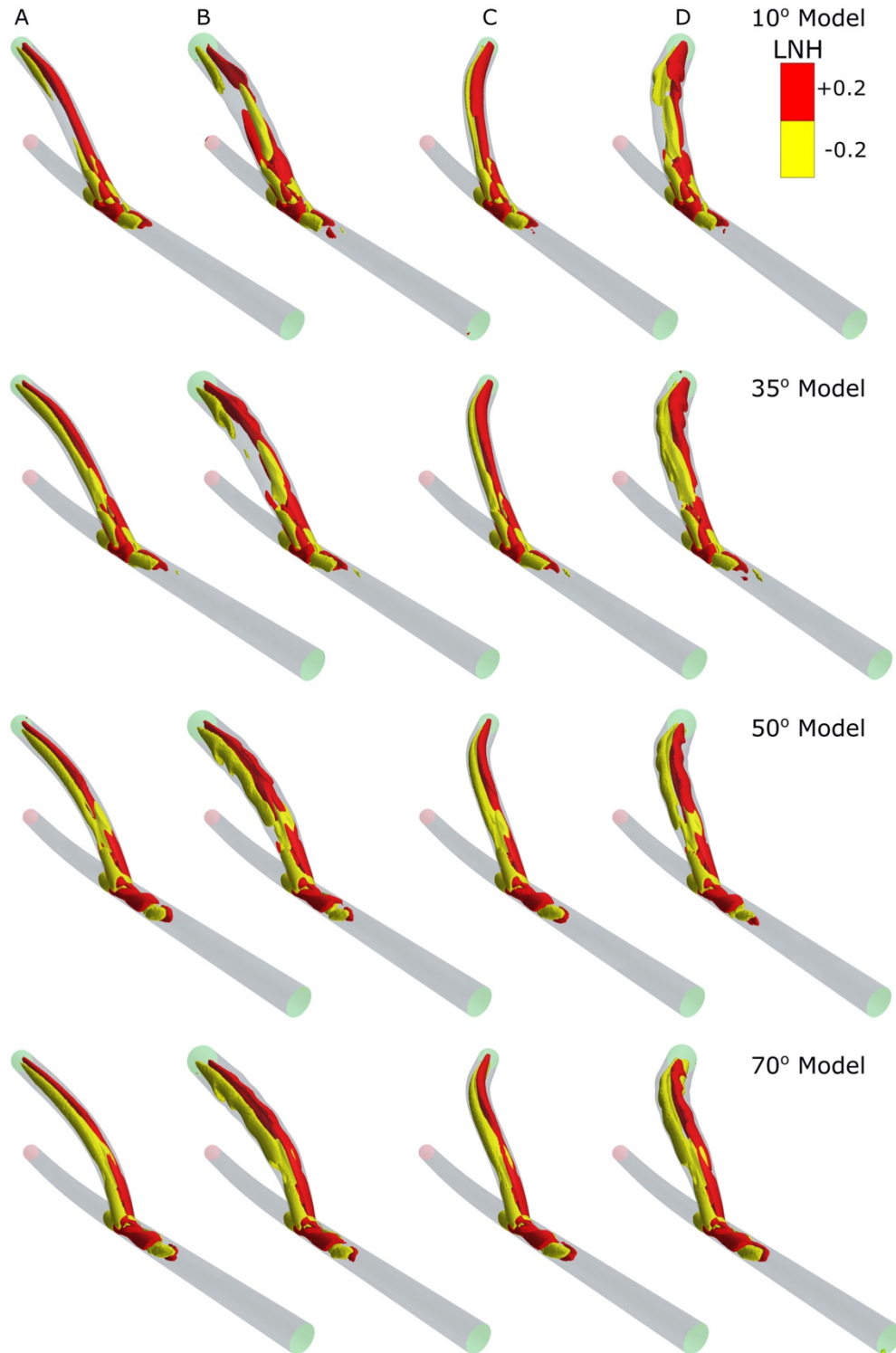


Figure 13: Presence of helical flow for different AVF idealised models with varying configuration and anastomotic angle. The helical content of the flow are represented with the averaged localised normalised helicity (LNH), where clockwise helical structures are represented in red and anticlockwise helical structure are represented in yellow. Reprinted with permission [38].

Effects of the wall compliance on a numerical simulation can be further evaluated through fluid structure interaction (FSI) CFD modelling. In the FSI study carried out on one of the end-to-side geometries, TAWSS showed a lower value in the FSI model as compared to the rigid wall model, but its value in the JXA region remained high, indicating that the high value was not a result of the rigid wall assumption [115]. Decorato et al.[143] conducted a further patient-specific FSI model which supports previous findings [115], and suggests that vessel wall deformability has limited influence on wall shear stresses. Both studies demonstrated an agreement for TAWSS at mid to low magnitude [115], [143].

2.6 AVF condition indication based on pressure changes

The pressure drop has been shown to be closely linked to the instabilities that arise at the anastomosis and the overall resistance of the AVF, with studies reporting its role as an indicator for the global haemodynamics of an AVF [34], [88], [107]. Botti et al. studied the potential to predict pressure drop of a patient-specific AVF models, which showed good correlation with the experimental results for the in-vitro particle velocimetry (PIV) experimental data [88], as shown in Figure 14 (top). The pressure drop and flow rate exhibit a non-linear, quadratic relationship, seen in Figure 14. This non-linear relationship, especially at the anastomosis deem the need of patient-specific models to properly estimate pressure drops based on geometrical configurations [88]. The effects of pulsatility appear to be more dominant at higher flow rates, with a higher frequency of pressure drop observed, although, the relationship of pressure drop and flow rate remains unchanged, as shown in Figure 14 (bottom).

An idealised end-to-side computational model to predict pressure drop across the anastomosis has also been studied, along with *in vivo* pressure catheter measurements to validate the CFD results [34]. Non-linear behaviours of these flow instabilities from turbulent-like flow types around the anastomosis led to pressure and velocity fluctuations around these regions [107]. This lead to significant pressure drops across the anastomosis (Figure 15), at regions of the proximal vein that coincides with the presence of thrill [34]. Flow rate predictions were also conducted on idealised models of AVF with a range of different stenosis diameters, using CFD models with varying pressure differences between the inlet and outlet, validated with ultrasound data with less than 20% average variation [144].

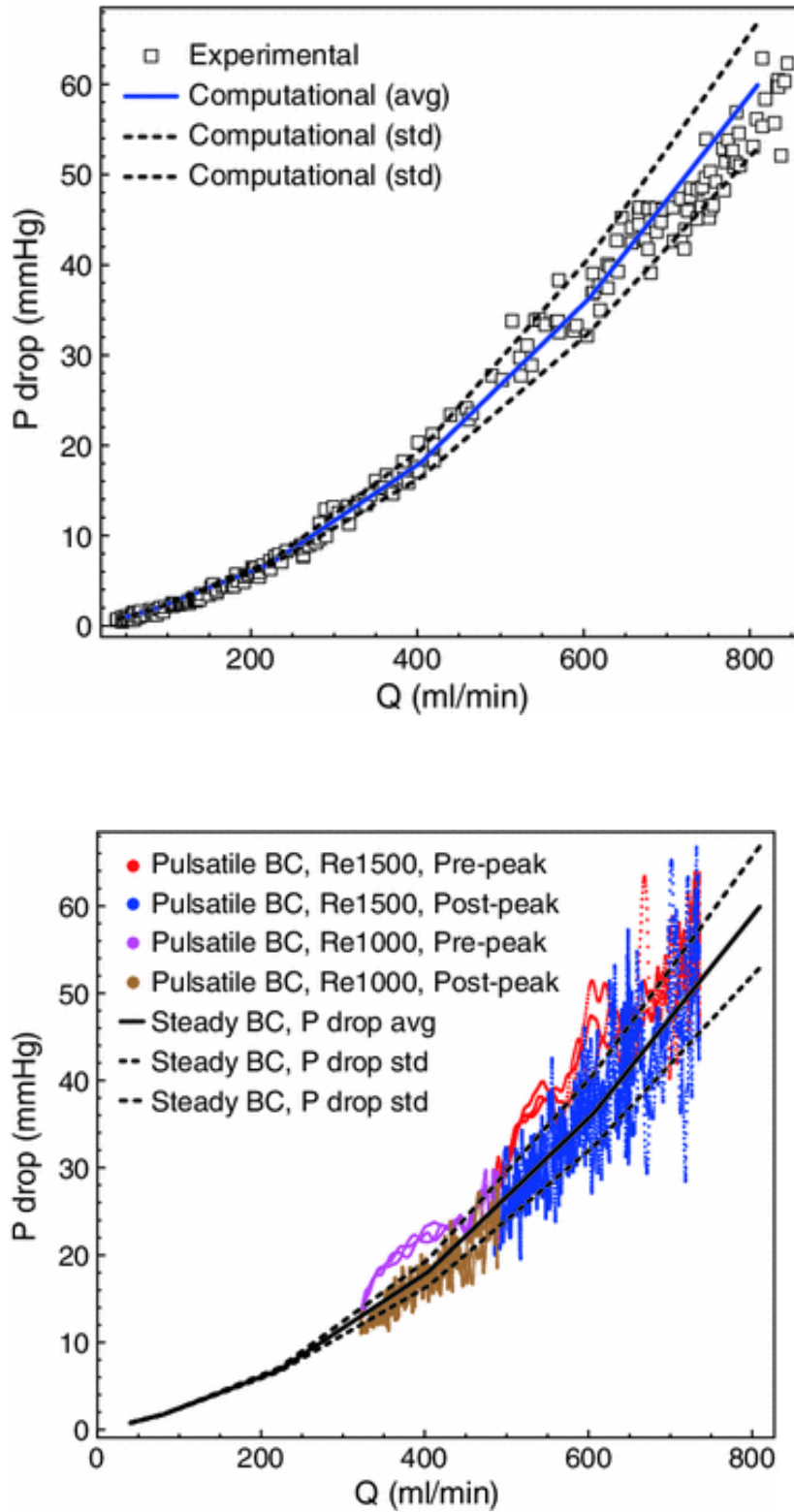


Figure 14: **(top)** Relationship between average pressure drop and flow rate of experimental and CFD results. **(bottom)** Relationship of pressure drop and pulsatile flow conditions. Figure reprinted with permission [88].

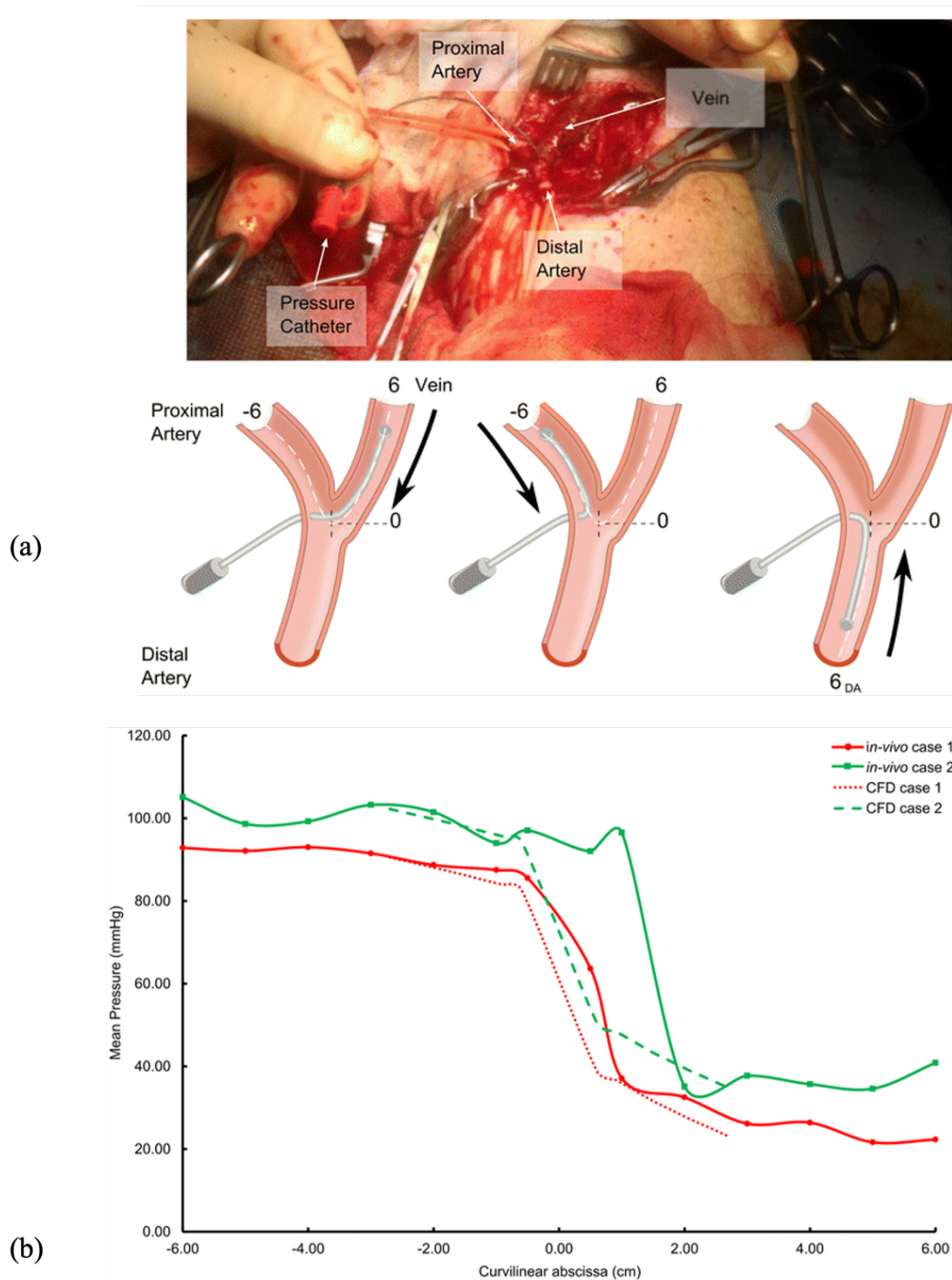


Figure 15: (a) In-vivo pressure measurements environment and schematic from [34] (b) the pressure drop at the PA (-6 to 0 cm) and PV (0 – 6cm). Reprinted and adapted with permission [34].

2.7 Blood flow sound frequency to measure AVF patency

Frequency spectrum characterisation was reported to correlate with endothelial cell activation and inflammatory phenotypes in a study based on experimental Fourier Transform analysis and *in-vitro* human carotid bifurcation, where harmonic changes in the blood vessel were reported to affect inflammatory phenotypes [145]. A linear relationship between the NF-kB activity (a regulator for inflammatory activity) and a change was observed in the 0th and 1st frequency harmonics spectrum. Furthermore, a significant correlation was also noted ($P < 0.05$) between the mean the NF-kB activity and haemodynamic WSS parameters such as OSI [145].

Acoustic signals and sound patterns generated from the AVF have been used to monitor the vasculature condition with a non-invasive approach [146]. Wang et al. also took advantage of the transitional turbulent-like blood flow that causes oscillation and varied frequency sound waves generated around the narrowed region. This was used in their non-invasive technique to detect stenosis with a stethoscope auscultation system [147]. Another similar approach is using auscultation sounds in the AVF with a deep learning technique to assess the degree of stenosis [148]. This was coupled with physical examination of the AVF and was reported with a mean accuracy of 82.1% [148].

More recently, Chen et al. proposed a system based on vessel wall motion, capturing the pulse wave generated as a result of the AVF vessel wall movement to predict access dysfunction, and having the information transfer to mobile phone in real time [149]. Results from the pilot clinical trial showed a maximum sensitivity of 95.2%, with a cut-off threshold of 750 ml/min in the receiver operating characteristic (ROC) analysis. High discrimination ability was also noted in the ROC analysis, with an area under curve of 0.994 reported, suggesting good correlation between the ultrasound dilution flow monitor and the monitoring system. The drawback is however the lack of conceptualisation of the AVF geometry and haemodynamics

of AVF that in turn benefits vascular surgeons and improve nurses' cannulation techniques. Critical assumptions made in the scattered pulses equation such as the radius of AVF estimation may reduce the individualisation power of classifier and algorithm [149].

2.8 Other emerging technologies to assist with AVF failure prediction

The use of medical imaging has been promising in regular monitoring and surveillance. Apart from the conventional Doppler ultrasound, emerging techniques with magnetic resonance imaging (MRI) for 4D flow visualisation have been assessed for regular monitoring of AVFs. Li et al. assessed the feasibility of 4D flow MRI in determining the haemodynamics of the AVF for 50 patients in a single-centre study [150]. Although there were haemodynamic parameters that showed good consistency across the two different radiologists, the turbulent-type flow behaviour, especially at the anastomotic region showed assessment of haemodynamic parameters to be challenging [150]. Comparisons made between blood flow rates measurement of Doppler ultrasound (DUS) and phase-contrast magnetic resonance imaging (MRI) reported comparable findings between the two techniques [150], [151].

Several studies have proposed three-dimensional geometry acquisition from conventional ultrasound two-dimensional images to [152], [153], coupled with neural networks [152]. Such convenient geometry acquisition techniques enabled further geometrical visualisation such as 3D-printed patient specific geometries [154]–[156], virtual reality (VR) and augmented reality (AR) tools [157], [158] for educational and training purposes. These 3D models also allowed better visualisation of anatomies with the ability to view them in a realistically scaled context, increasing the ability to accurately identify diseased lesions for surgical planning, besides improving educational experiences. The application of AR has also been used to successfully enhance procedures in a neurosurgical operating room [158]. There is therefore ample potential for these tools to be used along with standard approaches in different clinical settings (such as renal and dialysis clinics) to yield better visualisation of geometries.

2.9 Summary

Kidney failure is a global health issue, although remedied by dialysis, treatment-related complications often occur [159]. Patients whose AVF fails during dialysis treatment will need surgical interventions, and these are usually immediate. Patients may at times need to relocate to major cities and undergo surgical revision which can be burdensome and costly especially for the indigenous communities in Australia given the high number of dialysis patients in the Northern Territories, 13 times more likely to require dialysis [160].

There are many clinical models that classify different risk factors to predict vascular remodelling and AVF maturation, including scoring systems based on patient factors [161] and AVF.SIM which builds on a 0D/1D pulse wave propagation network model [101]. However, issues are also often recorded in the post-maturation period which therefore poses a need for an indicator that can identify the condition of an AVF at any time. The nature of blood flow that is turbulent [79] has left doubt in the ability of one-dimensional vascular networks to assess AVF condition.

Techniques for stenosis detection and diagnosis for post maturation remains sparse, with ongoing efforts to classify haemodynamic parameters such as WSS to the condition of an AVF and susceptible disease regions [39], [102], [136]–[138]. Disturbed blood flow causes a non-uniform shear stress along the endothelial cells in the direction of the flow, promoting the onset of IH [22], [39]. Furthermore, three-dimensional CFD computational modelling have been used to characterise haemodynamic stresses that causes IH formation [35], [102], [136]. However, the diverse findings from a review by Cunnane et al. in correlating shear stress metrics with IH development suggest that the physiological responses that cause IH remain unclear [39].

Carroll et al. introduces a concept of using resistance, derived from the ratio of pressure drop and flow in an AVF to classify the AVF condition post creation (during maturation or past

maturation and ready to be used for dialysis) [36], [162]. In general, high resistance values were found in patients with high risk AVFs and low resistance values were found in well-performing AVFs [36]. The haemodynamics remain to be the driving factor of VA dysfunction and hence should be closely monitored with accessible tools such as CFD modelling. On top of that, clinical and patient factors should also be taken into consideration in identifying issues arise from VA complication.

This thesis aims to address gaps in AVF failure and to assess the suitability of resistance as a diagnostic marker for AVF failure through real-patient data.

Chapter 3

Patient-specific computational fluid dynamics modelling of an AVF

This chapter outlines the structured process to obtain patient-specific geometry, which are then used to build the computational fluid dynamic (CFD) models. A non-invasive, portable and freehand ultrasound system developed by Colley et al. [153] was used to obtain patient-specific three-dimensional scans of the AVF. Doppler anemometry of flow profiles was obtained during the same scanning session. These scans were segmented with a segmentation software to obtain realistic 3D geometry from a volume of 2D ultrasound images. Then, CFD simulations were performed, and the results analysed to develop a new CFD-based metric for disease diagnosis and prediction, namely flow resistance, R . This approach was also designed with a view towards effective repetition, to efficiently process multiple patients' scans. CFD results were validated with experimental data [163] and verified to quantify numerical errors. This chapter contains work that has been previously presented and published in the Australian Biomedical Engineering Conference 2019.

3.1 Overview

AVF can have complex geometrical configuration that makes visualising the vasculature challenging. 3D visualisation of the AVF is hence important to envision any geometrical irregularities of the AVF. An ultrasound based medical imaging method was preferred over computed tomography (CT) scans or magnetic resonance imaging (MRI) due to its practicality for the purpose of this study. The high costs, extensive protocols, comfort of patient during the scan, loud noise and exposure to contrast and radiation were among the other concerns in using MRI and CT imaging for regular monitoring of patients within a clinical environment.

Regular monitoring of dialysis patients was conducted at the Prince of Wales Hospital Sydney, Australia approved by the South Eastern Sydney Local Health District Human Research Ethics Committee (2018/ETH00577) [164]. The AVF patient-specific modelling pipelines starts with the AVF free-hand scanning system, where real-patient AVF geometry (Section 3.3.1) and flow profiles (Section 3.3.2) of respective patients was acquired (Figure 16). These were obtained in parallel during the same clinic monitoring session. The geometry and flow profile datasets are important elements of the CFD model (Section 3.4). In particular, the geometry is used to create the mesh and the flow profiles provide the boundary conditions. The CFD results were post-processed for the calculation of resistance, R (Section 3.6).

3. Patient-specific computational fluid dynamics modelling of an AVF

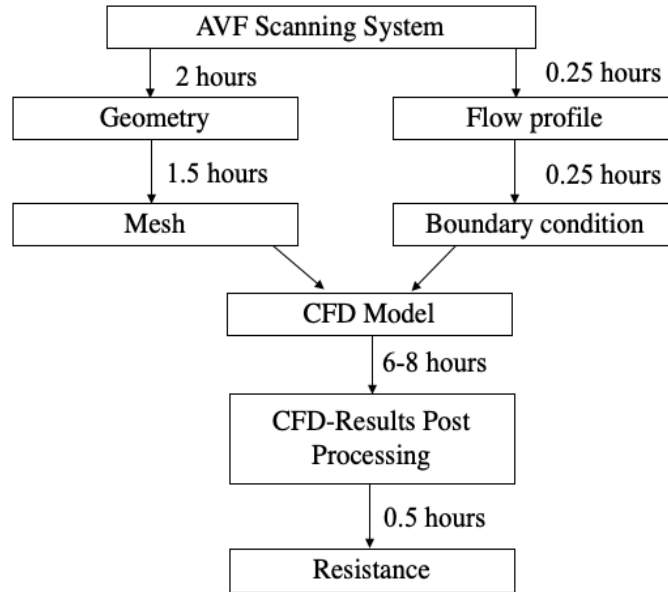


Figure 16: Pipeline analysis performed for each patient: Processing of geometry and flow profile were done in parallel and take about 2 hours and 15 minutes respectively. This was followed by setting up of patient-specific CFD model with the mesh and patient-specific boundary conditions. CFD results were processed, and resistance calculated after each simulation.

3.2 Patient selection

Patients with a forearm radiocephalic AVF were assessed at a renal vascular access clinic at the Prince of Wales Hospital, Sydney, Australia. A total of 106 patient examinations (henceforth referred to as 'scans') are included in this thesis - half the scans were obtained prior to 2018 [165], the remainder were collected from June 2018 to January 2020. That is, prior to the global COVID-19 pandemic, which halted further in-person clinical examinations after March 2020. Consent was obtained for all patients in accordance with the ethical standards prior to the study participation. Clinical data were retrieved from the electronic medical records of the hospital database.

Patients with any of the following conditions were excluded: brachial-cephalic AVF; arteriovenous graft; missing clinical information; unused fistula; poor ultrasound visibility of non-superficial vessels; or vessel size that exceeds the limit of the ultrasound transducer (maximum 38 mm field of view). This equates to a total of 83 patient scans being used.

3.3 Patient-specific model

3.3.1 Geometry acquisition

The novel freehand ultrasound system utilises features of ultrasound imaging, enabling geometry and flow profiles to be captured in real time non-invasively. Ultrasound frequency waves were emitted from the ultrasound transducer and received the reflected signals from the organ boundaries, generating grey-scale B-mode ultrasound images [166]. Highly reflective regions such as organ boundaries are often brighter in these grey-scale images as compared to less reflective ones such as blood, an example B-mode image shown in Figure 18 (a) [166]. These two-dimensional B-mode image slices can form a volume of images that can be recreated by assigning a global position and orientation to them.

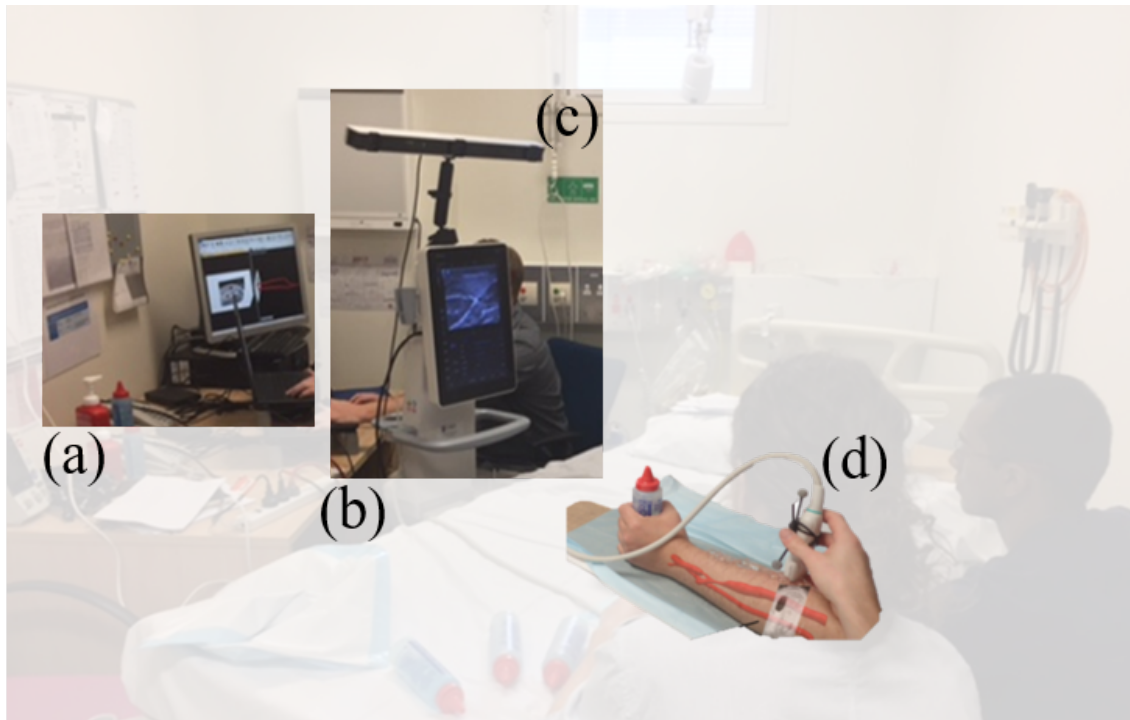


Figure 17: Set-up for the clinical patient scans performed for data collection with two personnel, one to perform the ultrasound scan of a patient and the other tasked at the workstation. (a) The workstation laptop (b) Mindray, TE7 Ultrasound machine, (c) Optitrack V120: Trio camera and (d) Mindray L14-6NS, 14MHz, 38mm FOV linear ultrasound transducer, with a rigid body attached to it [153].

3. Patient-specific computational fluid dynamics modelling of an AVF

The novel freehand ultrasound scanning system developed by Colley et al. [153] consists of an ultrasound machine (Mindray, TE7) (Figure 17 (b)), a linear ultrasound transducer (Mindray L14-6NS, 14MHz, 38mm FOV) (Figure 17 (d)), an infrared optical tracking camera (Optitrack V120:Trio) (Figure 17(c)) and a workstation laptop with graphic user interface (GUI) (Figure 17 (a)). The rigid body tracking with passive reflective markers that enabled detection by the motion-tracking camera was attached to the ultrasound transducer (Figure 17 (d)).

The linear ultrasound transducer was swept slowly and steadily, avoiding any sudden change in direction or rotation along the forearm of the patients where the AVF is located, shown in Figure 17 (d) to ensure that the images are evenly distributed. Ultrasound settings such as gains, and depth of 35 mm were adjusted accordingly to ensure clear contrast of the vessel and the surrounding tissues. The infrared camera tracks the transducer by locating the rigid body attached to the transducer. Hence, it is important to ensure that the rigid bodies are always within the camera frame during the scanning session. The location and orientation of the rigid body were transfer from the tracking camera to the workstation through the Motive 1.9 software (Optitrack).

In order to capture the right representation of diameter and without any deformation of the vessels, a thick layer of ultrasound gel was applied to the region of interest on the patient forearm. The software records the two-dimensional B-mode ultrasound images that form a three-dimensional bounding volume of constant spacing of 0.05 mm, with a pixel size of 0.05 mm x 0.05 mm in the direction of the sagittal plane. Real-time verification of scan quality was performed in the software, ensuring the ultrasound images, and bounding volume were coherent and no plane intersected another. Each scan takes approximately 15 to 20 minutes, depending on the complexity of the AVF. A total error of 2.5% was found with the use of a cross-wire calibration phantom [153].

3. Patient-specific computational fluid dynamics modelling of an AVF

A volume, formed from the stack of image slices were processed with the ScanIP segmentation image processing software (Synopsys Inc., CA, USA). Due to the low-contrast ultrasound images, the segmentation process required manual identification of the lumen of the three main AVF vessels (PA, PV, and DA). These vessels have a higher greyscale density compared to the surrounding tissue, enabling the surrounding tissues to be removed (Figure 18 (a) & Figure 18 (b)). A mask around the lumen was created to distinguish the vessels and the surrounding tissues. This was followed by an interpolation between slices in the axial direction and smoothing of the vessel surface with the recursive Gaussian smoothing method (Figure 18 (c)). Flow distribution in the AVF is dependant to the geometrical configuration at the anastomosis. Therefore, extra masks were placed between the image slices in this region due to its geometrical complexity. The final geometry was examined closely with the final mask for verification. This segmentation process takes approximately 1-2 hours dependent on the ultrasound images for respective scans.

3. Patient-specific computational fluid dynamics modelling of an AVF

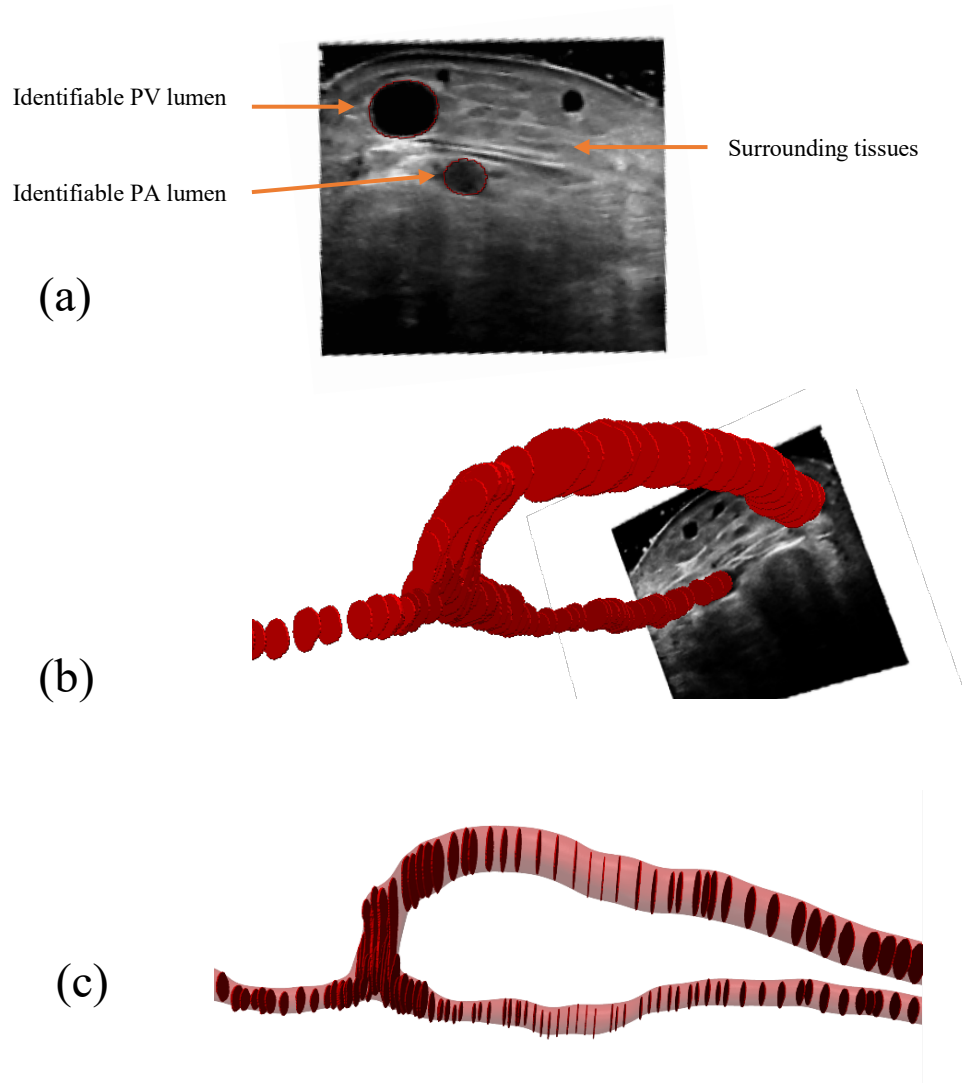


Figure 18: (a) Example two-dimensional ultrasound image that shows the identifiable vessel lumen based on the grey-scale contrast with the surrounding tissues (b) Volume recreated from the stack of two-dimensional ultrasound images. (c) Overlay of the three-dimensional AVF geometry before and after interpolation within the image slices

3.3.2 Flow profiles

At the same time as capturing the patient geometry, flow velocity profiles in the three vessels were obtained during the scanning session via Spectral Doppler Ultrasound (DUS) using the same ultrasound machine. The pulsed-wave Doppler measurements consider the shift in Doppler frequency between the incident and the receiving ultrasound beam from the transducers and reflecting particles in the blood. This method is adopted as it shows comparable flow rates with phase-contrast MRI [151].

$$f_{doppler} = \frac{2 f_o V \cos \theta}{c} \quad \text{Eq. 6}$$

where $f_{doppler}$ = Doppler shift, f_o = transmitted beam, V = blood velocity, c = sound speed in tissue and θ = the incident angle between ultrasound beam and axis of flow

Based on Eq. 6, an angle, θ of 90° will give zero Doppler shift. For this reason, the incidence angle is essential for appropriate estimation of Doppler shift and blood flow velocity, and was kept below 60° to minimise errors [167], [168]. Velocity was measured at the centre of each vessel, with a small gate size, and maximum intensity point, with at least five samples per period obtained.

The configuration of the AVF, where the ulnar and radial artery are joined at the palmar arch, means that there is a slight delay of blood flow to the DA of the AVF as compared to the PA. This challenge was overcome by synchronising the peaks of the blood velocity with the waveform of the cardiac contraction using a three-lead electrocardiography (ECG) device (Figure 19 (b)), connected to the same ultrasound machine. The R peak of the QRS complex, representing ventricular depolarisation [169], was used as the global reference for synchronisation as an endpoint of each period of waveform (Figure 19 (a)). This allowed the Doppler spectral waveform to be reproduced and normalized with the cardiac cycle by measuring the heart rate of the patient.

3. Patient-specific computational fluid dynamics modelling of an AVF

Multiple periods were captured for each patient and realigned with the ECG waveform. These waveforms were extracted by processing the ultrasound transducer signal with an in-house MATLAB (Mathworks Inc.) algorithm (Figure 19 (c)). Each segment was combined before noise removal with a median filter, followed by column-wise Gaussian smoothing [36]. Velocity and average vessel area from the ultrasound data were used to convert to flow rate with Eq. 7 and Eq. 8.

$$Q(t) = V(t)A \quad \text{Eq. 7}$$

$$A = \frac{\pi D^2}{8} \quad \text{Eq. 8}$$

where $V(t)$ = velocity of blood flow, A is the area of the vessel and D is the diameter of the vessel

3. Patient-specific computational fluid dynamics modelling of an AVF

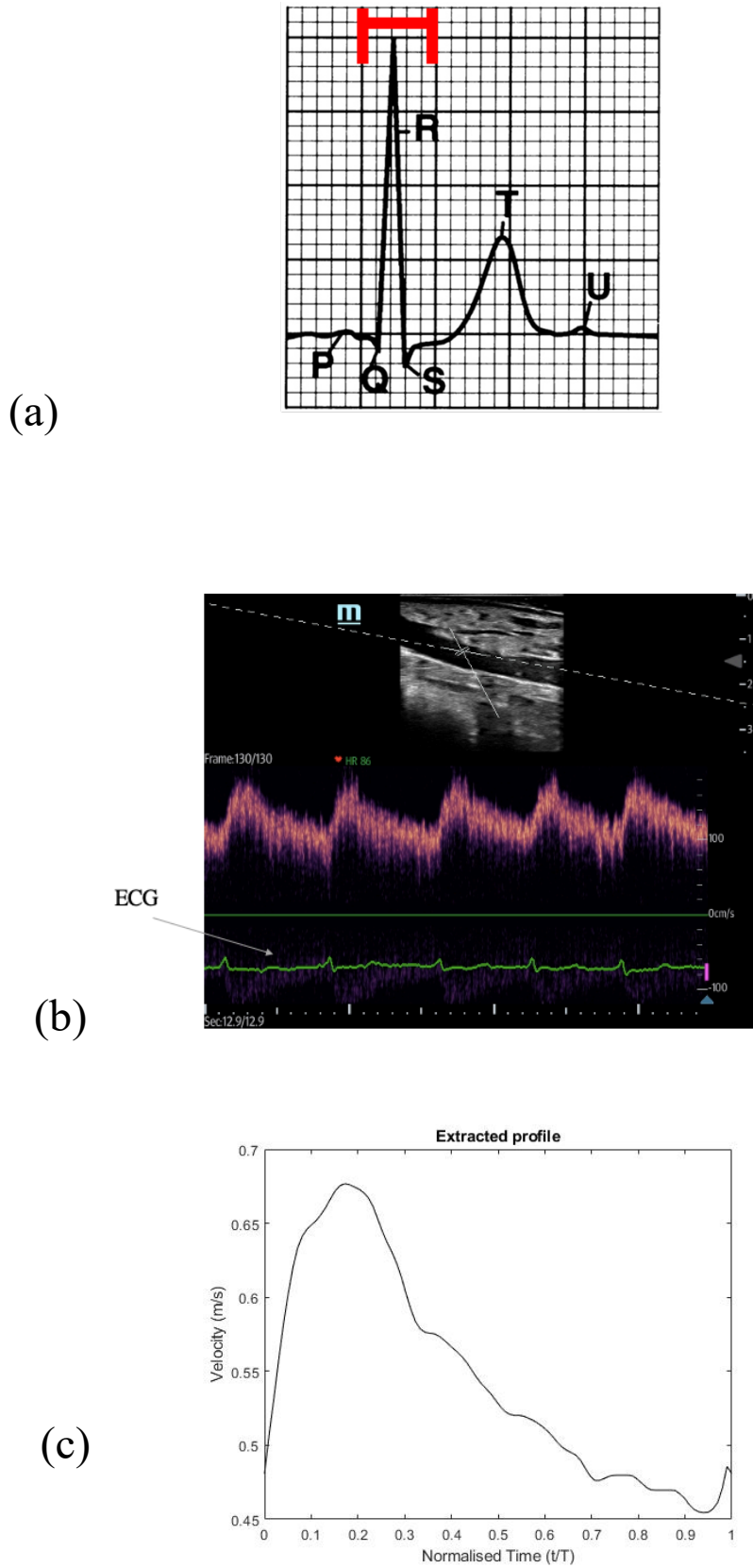


Figure 19: (a) Example ECG waves of a healthy patient, with QRS complex labelled in red. Reprinted with permission from [169] (b) Doppler ultrasound measurements of velocity profile from different vessel of the AVF. The ECG information is indicated with the arrow in grey (c) Extracted profile from the Doppler data

3.4 Patient-specific CFD model

CFD simulations were performed with the high performing computing facilities of the National Computational Infrastructure (NCI) Australia. Simulation performed with 48 cores took approximately 6-8 hours to compute. The Reynolds-averaged Navier Stokes (RANS) equations [170] were solved with the finite volume method in discretised form using FLUENT software package (ANSYS® FLUENT, Release 19.2, ANSYS, Inc.). Pressure-velocity coupling was achieved with the SIMPLE algorithm. Momentum and pressure variables were spatially discretised with a second order upwind scheme, while turbulent kinetic energy and specific dissipation rate with first order upwind. The second order implicit scheme was used for temporal discretisation.

Since the conservation of mass and momentum are satisfied for incompressible flow, these equations can be reduced to Eq. 9 and Eq. 10. RANS modelling was selected over other more high-fidelity methods of capturing turbulence due to the large number of patient-specific CFD models requiring computing.

$$\nabla \cdot \mathbf{u} = 0 \quad \text{Eq. 9}$$

$$\rho \left(\frac{\partial \mathbf{u}}{\partial t} + \mathbf{u} \cdot \nabla \mathbf{u} \right) = -\nabla p + \mu \nabla^2 \mathbf{u} - \tau_{ij} \quad \text{Eq. 10}$$

where ρ is the density, \mathbf{u} is the velocity vector, μ is the viscosity, p is pressure and τ_{ij} is the Reynolds-stress tensor.

The Reynolds number, Re was calculated with Eq. 11,

$$Re = \frac{\rho u D}{\mu} \quad \text{Eq. 11}$$

where u depicts the flow speed and D depicts the diameter of the vessel.

Although the local Reynolds number at peak cycle velocity at the venous outflow ranges approximately between 150 to 2000, transitional to turbulent flow was previously reported in

physiological blood flow studies [79], for an AVF in particular, around the anastomotic region and stenosed region, despite the low Reynold number [35], [163], [171].

The $k-\omega$ shear stress transport (SST) turbulence model [172] was chosen for all the CFD models to capture a meaningful description of the turbulent flow conditions. This model has also been shown to perform well in vasculature with transitional flows and flows near the wall in carotid artery bifurcations [173] and blood damage modelling [174], which have similar analyses as AVFs. The governing equations of the $k - \omega$ SST model used in this thesis can be found in Appendix 3A. The standard $k-\omega$ model does not involve a damping function and is known to perform well near wall and at sublayer of viscous internal flow. $k-\omega$ model, however, is very sensitive to the freestream values outside of the viscous internal flow, making the $k-\epsilon$ model a better option at wake region of the viscous internal flow. The two-equation $k-\omega$ SST model combines the superior elements of both models, having applied $k-\omega$ at the near wall region through the viscous sub-layer, and $k-\epsilon$ model in the free-stream flow. The major enhancement of this model is the modification of the eddy viscosity to account for the transport of the principle turbulent shear stress [172]. Additionally, this model has also shown to have better overall agreement with experimental results of a stenosed carotid artery [175]. Blood density was set at $1060\text{kg}/\text{m}^3$ to replicate the average blood physical properties [176]. Blood is a non-Newtonian fluid with the time-dependent shear thinning and viscoelastic properties [177]. Blood rheology have been reported to affect the numerical results, with varying recirculation length reported in a comparison study of non-Newtonian rheological models [178]. The Carreau model [179], [180] predicts the shear-thinning effect, achieving a maximum value of absolute strain rate approaches zero [178], [181], and have been previously used in blood flow numerical studies [182], [183]. This model was hence chosen to model the non-Newtonian rheology of blood, for which the viscosity is dependent on the fluid shear rate (Eq. 12):

3. Patient-specific computational fluid dynamics modelling of an AVF

$$\mu = \mu_{\infty} + (\mu_0 - \mu_{\infty})(1 + (\lambda\dot{\gamma})^2)^{\frac{n-1}{2}} \quad \text{Eq. 12}$$

The parameters in the model are taken from Cho et al [180]: $\lambda = 3.313s$, $n = 0.3568$, $\mu_0 = 0.056 Pa.s$, $\mu_{\infty} = 0.00345 Pa.s$ where μ_0 represents viscosity at zero shear, μ_{∞} represents viscosity at infinity shear, λ represents characteristic time, n represents the power law index, $\dot{\gamma}$ represents the shear rate.

3.4.1 Boundary conditions

Following from Section 3.3.2, the flow profiles that were obtained during the scanning session serves as pulsatile inlet flow waveforms for the CFD model, prescribed at the DA and PA (Figure 20). The PV is set as a non-tractive pressure outlet, with relative pressure held at zero. The vessel walls are set as no-slip and are not compliant and instead are held rigid. Although vessel walls may be inherently compliant, the rigid wall assumption has been deemed acceptable in identifying key features in an AVF [184]. The flow profile is normalised with the cardiac cycle of each patient. For example, the period of the inlet waveform is 1s if the heart rate of the patient is 60 beats per minute. For this reason, the number of timesteps for each patient will be different and set based on the specific heart rate. The direction of blood from or to the DA is dependent on the types of blood flow, namely retrograde or antegrade flow of the patients.

In order to ensure consistency across all the patient cases, it is important that blood flow is fully developed before entering the actual AVF geometrical domain of interest. For that reason all vessel ends were extended by twenty times the diameter of the relevant vessel with the Vascular Modelling Toolkit (VMTK) [185], as this entrance length was sufficient for the varying patient-specific geometry [186]. A cylindrical extension in the direction normal to the vessel face is created after selecting and clipping the midpoint of the boundaries. The patient-specific STL geometry, including the extensions, are then used in the CFD model (Figure 20). The boundary condition used for each CFD model is tabulated in Table 3. A comprehensive study of using a patient-specific boundary condition, rather than the conventional flow split in an AVF will be discussed in Chapter 4.

3. Patient-specific computational fluid dynamics modelling of an AVF

Table 3: Boundary condition for the CFD model

Location	Boundary conditions
Proximal Artery (PA)	Pulsatile inlet flow profiles
Distal Artery (DA)	Pulsatile inlet flow profiles
Proximal Vein (PV)	Non-tractive pressure outlet, relative pressure held at zero
Wall	No slip wall and without compliance condition

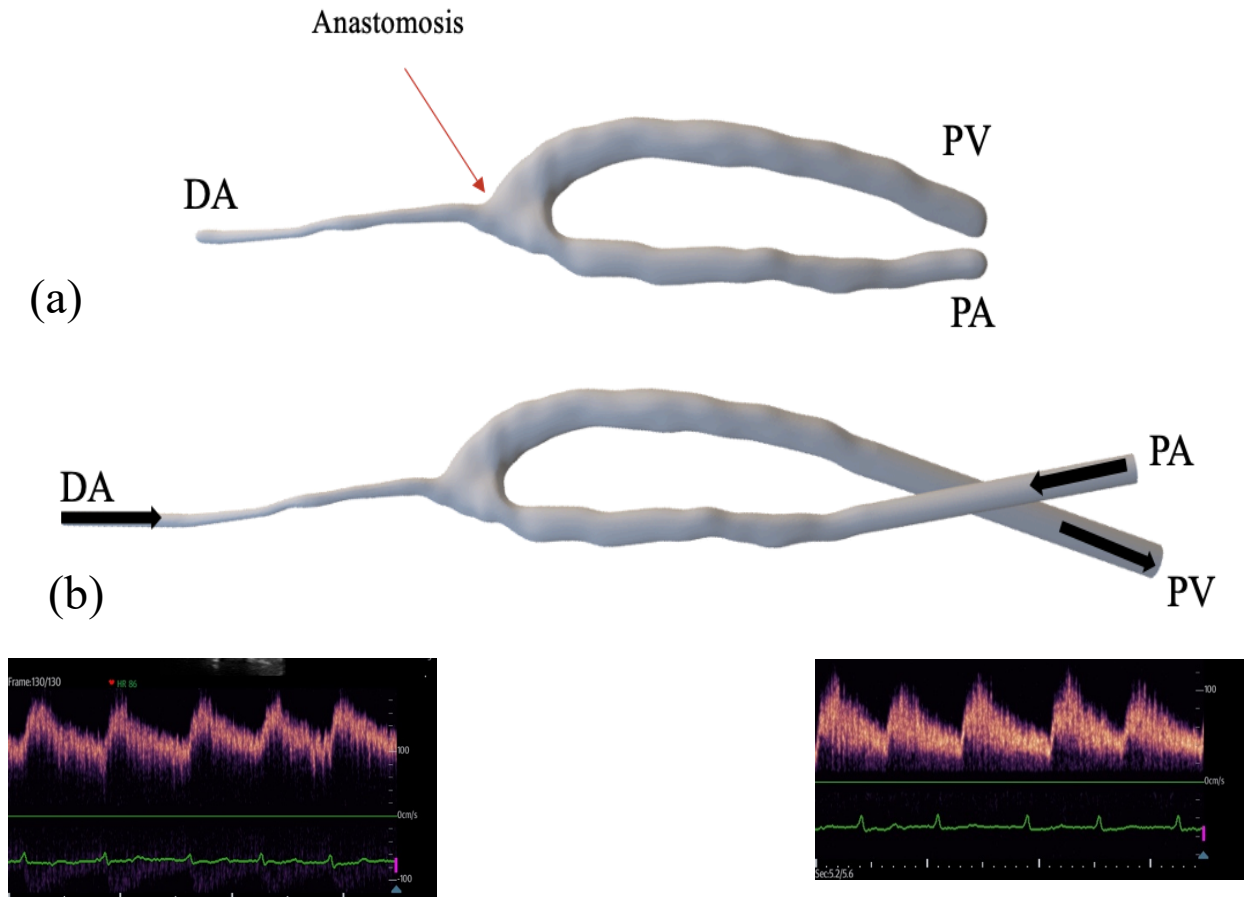


Figure 20: (a) An example patient-specific AVF with retrograde flow (flow traveling from the PA and DA) towards the PV. The anastomosis is the connection between the three vessels (indicated with the red arrow). (b) Inlet transient velocity waveforms are set at the boundary areas of the extended cylindrical of PA and DA, while the PV is set as a non-tractive pressure outlet, with relative pressure held at zero

3.4.2 Mesh strategy

ANSYS ICEM (Ansys ICEM CFD, Release 18.1) is used to create the mesh for each geometry. The patient-specific STL geometry, including the extensions are imported to the ANSYS ICEM software. Boundary faces, wall boundaries and fluid domain are defined. An unstructured tetrahedral and prism mesh was generated for all cases (Figure 21). The global element scale factor is set at 0.3, a multiple of other mesh parameters set globally for the model. The largest possible element size is set at 0.8, and the smallest minimum size with curvature and proximity-based refinement is 0.3. This allows the creation of smaller size elements and is essential for complex patient geometry. Elements will be created based on the multiplication of the scale factor and the set criteria.

The $k-\omega$ SST model capture flow in the viscous sub-layer and near-wall requires a high mesh resolution near the geometry wall [175]. To better capture the near-wall effect, twelve high density prism layers are extruded from the surface with an exponential growth ratio of 1.2 inwards, and a total height of 0.6. The first cell height was set to yield y^+ values below 1 [187], thereby ensuring accurate near wall effects. Quality checks and subsequent mesh cell smoothing are performed to maximize the quality of the mesh and avoid possible errors and problems of mesh such as unconnected vertices, duplicate elements, multiple edges, poor volume and surface orientation and so on. Tetrahedral and prism meshes are converted to polyhedral elements in ANSYS FLUENT as the computations with the polyhedral mesh have sufficient accuracy whilst requiring less computational power [188].

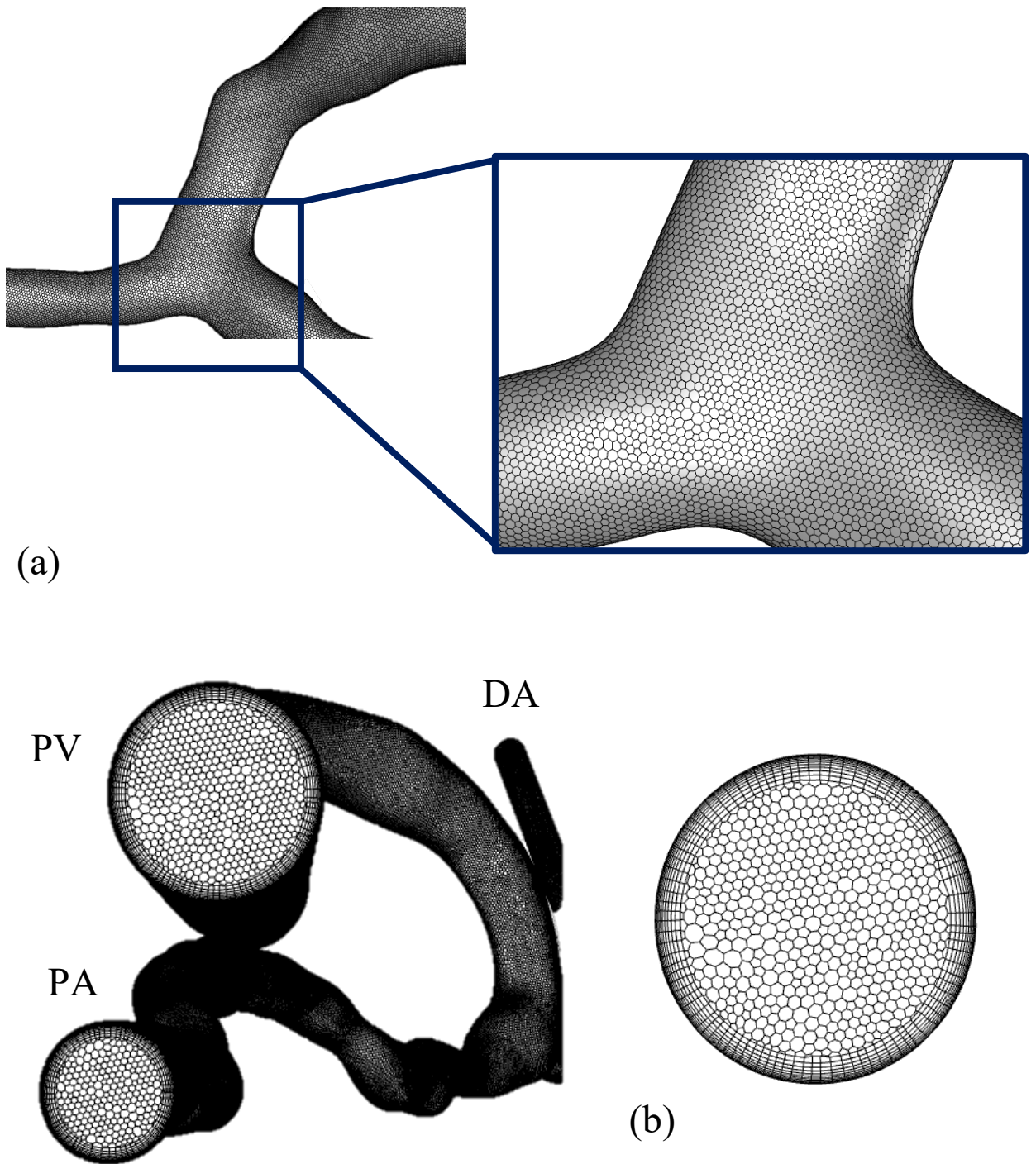


Figure 21: (a) Polyhedral elements on each CFD models, and a zoom out of elements at the anastomotic region were shown (b) Elements and prism layer at the boundary areas

3.4.2.1 Mesh convergence

The grid convergence index (GCI), derived from the generalised Richardson extrapolation [189] was calculated on the mesh generated for a particular patient (Eq. 7). This is to verify grid independence and quantify sensitivity by estimating the numerical error due to the mesh size. Discretisation errors were estimated for the average wall shear stress (WSS) at four different locations (Figure 22) of a patient-specific model for the final cycle (fourth cycle) of the simulation.

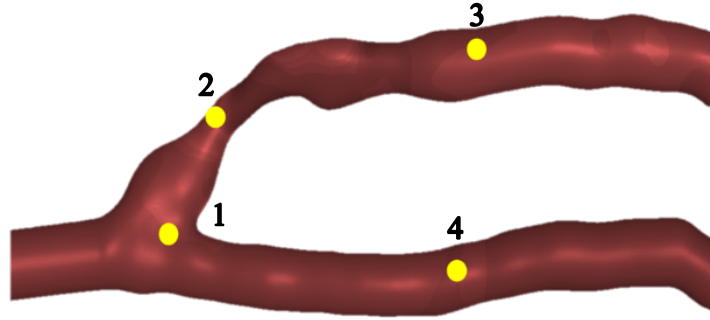


Figure 22: Discretisation error was estimated in four location - Point 1: PA segment before the anastomosis, Point 2: PV segment after the anastomosis, Point 3: downstream of the PV segment and Point 4: downstream of the PA segment

Three different meshes, denoted coarse (1,515,016 cells), medium (3,739,057 cells) and fine (6, 233,651 cells) were generated based on different grid scale factor. Grid refinement ratio, r_{ij} is defined as $\left(\frac{N_j}{N_i}\right)^{\frac{1}{3}}$, for a three-dimensional problem, where $r > 1$ [189]. The apparent order, p was calculated using Eq. 13 and 14. Eq. 13 was calculated with fixed point iteration, where $q(p)=0$ as an initial guess since the grid refinement ratio is not constant (Eq. 14).

$$p = \frac{1}{\ln(r_{21})} \left| \ln \left| \frac{\epsilon_{32}}{\epsilon_{21}} \right| + q(p) \right| \quad \text{Eq. 13}$$

$$q(p) = \ln \left(\frac{(r_{21}^p - s)}{(r_{32}^p - s)} \right), s = 1. \text{sign} \left(\frac{\epsilon_{32}}{\epsilon_{21}} \right) \quad \text{Eq. 14}$$

where $\phi_3 - \phi_2 = \epsilon_{32}$ and $\phi_2 - \phi_1 = \epsilon_{21}$, and ϕ_3 denotes a coarse-grid numerical solution, ϕ_2 denotes a medium-grid numerical solution and ϕ_1 denotes a fine-grid numerical solution.

3. Patient-specific computational fluid dynamics modelling of an AVF

The extrapolated values were calculated using Eq. 15. Estimated errors along with respective apparent order were computed with approximate relative error, e^{21} and extrapolated relative error e_{ext}^{21} (Eq. 16 and Eq. 17).

$$\phi_{ext}^{21} = \frac{r_{21}^p \phi_1 - \phi_2}{r_{21}^p - 1} \quad \text{Eq. 15}$$

$$e^{21} = \left| \frac{\phi_1 - \phi_2}{\phi_1} \right| \quad \text{Eq. 16}$$

$$e_{ext}^{21} = \left| \frac{\phi_{ext}^{21} - \phi_1}{\phi_{ext}^{21}} \right| \quad \text{Eq. 17}$$

The discretization errors can be estimated with Eq. 18,

$$GCI_{fine} = \frac{1.25e}{r_{21}^p - 1} \quad \text{Eq. 18}$$

At point 1 to 4 to be $GCI_{fine} = 0.06\%, 0.09\%, 1.03\%, 1.55\%$.

These grids were also verified to ensure that they were in the asymptotic range of convergence, using Eq. 19,

$$\frac{GCI_{fine}^{21}}{r^p \times GCI_{fine}^{32}} \cong 1 \quad \text{Eq. 19}$$

At points 1 to 4, the values were 0.98, 1.00, 0.94, 1.08.

Parameters that were used for the GCI calculations are summarised in Table 4. The mesh independence study was also evaluated for resistance (ratio of pressure difference and flow rate). There was less than 2% difference recorded for the calculated resistance values for two subsequent number of elements (N1, N2 and N3) after mesh refinement, as shown Table 5. The fine grid was chosen to ensure that the numerical results were at a sufficient level of spatial discretisation. The same meshing strategy was subsequently assumed to be suitable for all patient model used in this thesis.

3. Patient-specific computational fluid dynamics modelling of an AVF

Table 4: Discretisation error of the WSS

	Point 1	Point 2	Point 3	Point 4
N1	4,288,635	4,288,635	4,288,635	4,288,635
N2	2,127,489	2,127,489	2,127,489	2,127,489
N3	1,583,782	1,583,782	1,583,782	1,583,782
r_{21}	1.26	1.26	1.26	1.26
r_{32}	1.10	1.10	1.10	1.10
ϕ_1	14.07	53.95	23.92	2.64
ϕ_2	14.35	54.21	25.43	2.45
ϕ_3	13.22	54.63	27.95	2.72
p	16.26	8.86	9.24	8.12
ϕ_{ext}^{21}	14.07	53.91	23.72	2.67
e^{21}	2.00%	0.49%	6.3%	7.01%
e_{ext}^{21}	0.05%	0.07%	0.83%	1.22%
GCI_{fine}^{21}	0.06%	0.09%	1.03%	1.55%
GCI_{fine}^{32}	2.50%	0.70%	8.38%	11.09%

Table 5: Percentage difference for mesh independence study

	Number of elements	Resistance (mmHg/l/min)	Percentage difference (%)
N1	4,288,635	18.6	-
N2	2,127,489	18.7	1.4
N3	1,583,782	18.5	0.4

3.4.2.2 Time-step sensitivity analysis

A time-step sensitivity and independence analysis were carried out with a patient-specific CFD model in the final cycle (fourth cycle) of the simulation to quantify the sensitivity of the simulation to the magnitude of the time-step. A similar CFD set up outlined in Section 3.4 was adopted for this analysis, with time-steps of 0.001s and 0.0005s used as timestep is independent of Courant number for an implicit time integration scheme [175]. Average WSS values at four different locations (Figure 7) showed an average of 2.8% (3.3%, 1.7%, 6.3% and 0.1% at Point 1 to 4) differences in both results. The maximum discrepancy is observed at point 3, similar to the location reported for the mesh convergence study (Section 3.4.2.1). A timestep of 0.001s was deemed to be an acceptable range for all cases, as it requires less computational power to approximate the transient flow behaviours and minimise the effect of the initial transient motion building in the fluid.

3.5 CFD results post-processing

All simulations ran for four cardiac cycles and the results from the fourth cardiac cycle were exported and post-processed in MATLAB (MathWorks Inc.). Centrelines from each geometry were generated and voxel edges sampled at 1 mm distance by adopting the skeletonization algorithm, to reduce the 3-D binary volume to a single line, followed by a smooth curve fitting algorithm in Simpleware SCANIP (Synopsis Inc., CA, USA).

Cycle-averaged pressure and wall shear stress values were processed in MATLAB (MathWorks Inc.). The circumferential average of the time-averaged WSS (TAWSS), transverse WSS (transWSS) and oscillatory shear index (OSI) were calculated at the surface area of the wall with a 1 mm increment along the centreline at each timestep. The time-averaged WSS (TAWSS) shows the averaged value of wall shear stress over the entire cardiac cycle, the transverse WSS (transWSS) captures the presence of multi-directional flows [103] and oscillatory shear index (OSI) characterizes reciprocal flow [190].

3.6 CFD-derived resistance calculation

Pressures of each face on the wall were averaged to the closest nodes along the centrelines for each timestep, allowing a circumferential averaged pressure to be obtained in 1mm increments from the anastomosis. Resistance, R of the P and PA were calculated with were calculated with Eq. 20 (see also Figure 23) to determine the geometrical resistance of the vessel [191], [192].

$$R_{vessel} = \left| \frac{\Delta P_{vessel}}{\bar{Q}_{vessel}} \right| \quad \text{Eq. 20}$$

$$\Delta R_{spatial} = \left| \frac{P_{vessel\ i} - P_{vessel\ i-1}}{\bar{Q}_{vessel}} \right| \quad \text{Eq. 21}$$

where R_{vessel} represents resistance, ΔP_{vessel} represents pressure difference and \bar{Q} represent the mean flow rate of the respective vessel. Depending on the vessel branch, ΔP_{vessel} can be represented as $(\bar{P}_1 - \bar{P}_0)$, which represents the pressure difference from PA, \bar{P}_1 to the anastomosis, \bar{P}_0 , and $(\bar{P}_0 - \bar{P}_2)$ represent the pressure difference from the anastomosis to PV, \bar{P}_2 . $\Delta R_{spatial}$ represents the changes in resistance spatially, $P_{vessel\ i} - P_{vessel\ i-1}$ represents pressure difference at two consecutive nodes that are sampled 1mm apart.

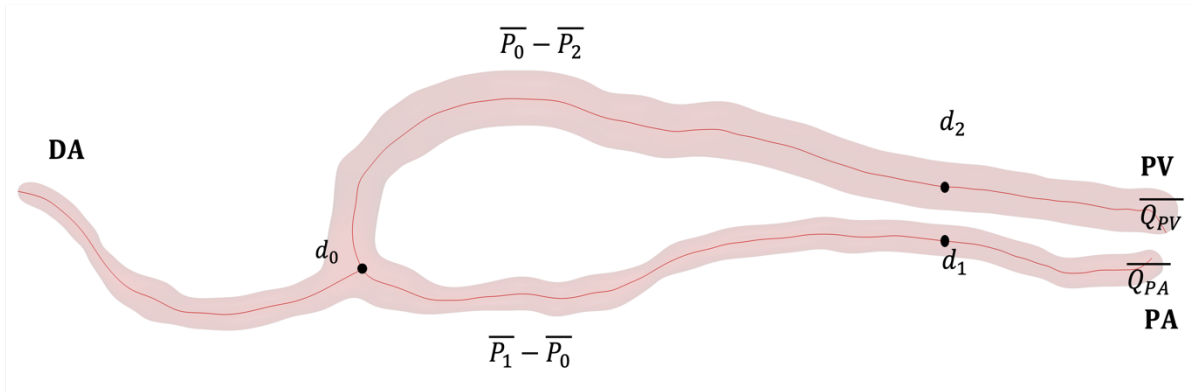


Figure 23: Resistance calculation in an AVF, represented by the ratio of pressure difference from the anastomosis, d_0 to a certain distance (d_1 at PA and d_2 at PV) along the AVF and the average flow rates of respective vessels

3. Patient-specific computational fluid dynamics modelling of an AVF

Three different approaches (1) - (3) were used to examine the effects of resistance in different contexts based on Eq. 20 and Eq. 21, which will be further explained in Chapters 5 and 6:

(1) to quantify the effects of resistance associated with the juxta-anastomotic treatment in an AVF, pressure differences were calculated at the vein segment (PV) and the main inflow artery segment (PA), from the anastomosis, d_0 to $d_2 = 50$ mm of the PV segment and $d_1 = 35$ mm of the PA segment, as this is the common region for juxta-anastomotic stent deployment of the AVF. Approach (1) will be further elaborate in Chapter 5, Section 5.4.

(2) to have consistently examined resistance for all patients (with or without juxta-anastomotic treatment), pressure differences were calculated at the same distance, $d_1 = d_2 = 75$ mm from the anastomosis of both vein segment (PV) and the main inflow artery segment (PA). Approach (2) will be further elaborate in Chapter 6, Section 6.2.2.

(3) to visualise the effect of resistance throughout the AVF spatially, pressure differences from each node were calculated at the vein segment (PV) and the main inflow artery segment (PA).

3.7 Validation

3.7.1 Validation with experimental data

Validation was performed by comparing the CFD results with tomographic PIV data from an in-vitro experiment using a patient-specific AVF geometry [163]. The benchtop experimental model consists of a patient-specific geometry obtained through the same system described in Section 3.3.1. This model was created by casting silicone around the soluble 3D printed AVF geometry. The model was connected, via a tubing network, to a pulsatile pump that drives the working fluid to replicates the patient-specific boundary condition via a tubing network. A double-pulsed laser was used to illuminate the seeded working fluid. Four high-speed cameras

3. Patient-specific computational fluid dynamics modelling of an AVF

were placed at optimised location to capture the particle images. These particle images were then processed using the commercial PIV software, Davis 8.4.0 (LaVision GmbH).

The geometry of the CFD model used for this validation was identical to the experimental model. The meshing strategy was the same as the ones outlined in Section 3.4.2. However, other properties were set to match the experimental condition. These include the fluid properties of working fluid, with density set at 1202.7kg/m^3 and the dynamic viscosity set at 9.21 mPa.s . It is worth noting that the blood viscosity in the experimental model was set as a Newtonian fluid whereas the CFD model of all the patient-specific cases in this thesis were modelled as non-Newtonian fluid. Despite shear-thinning effects in blood, the relative difference between pressure distribution in these models were small with a maximum difference of only less than 0.5% [186]. Hence, this validation was deemed suitable to validate the CFD set up for patient-specific models in this thesis.

The experimental velocity magnitude profiles are compared with the CFD results in Figure 24, at the four locations indicated in blue, green, red and black. The average difference in velocity between CFD and experiment is 0.0956 m/s , with the highest absolute error observed in Location 4. After the anastomosis and further downstream at the PV, the variation becomes more apparent, observed in Location 3 and Location 4 (Figure 24 and Table 6). This also coincides with the region where recirculating flow is often observed in an AVF [35], [163].

3. Patient-specific computational fluid dynamics modelling of an AVF

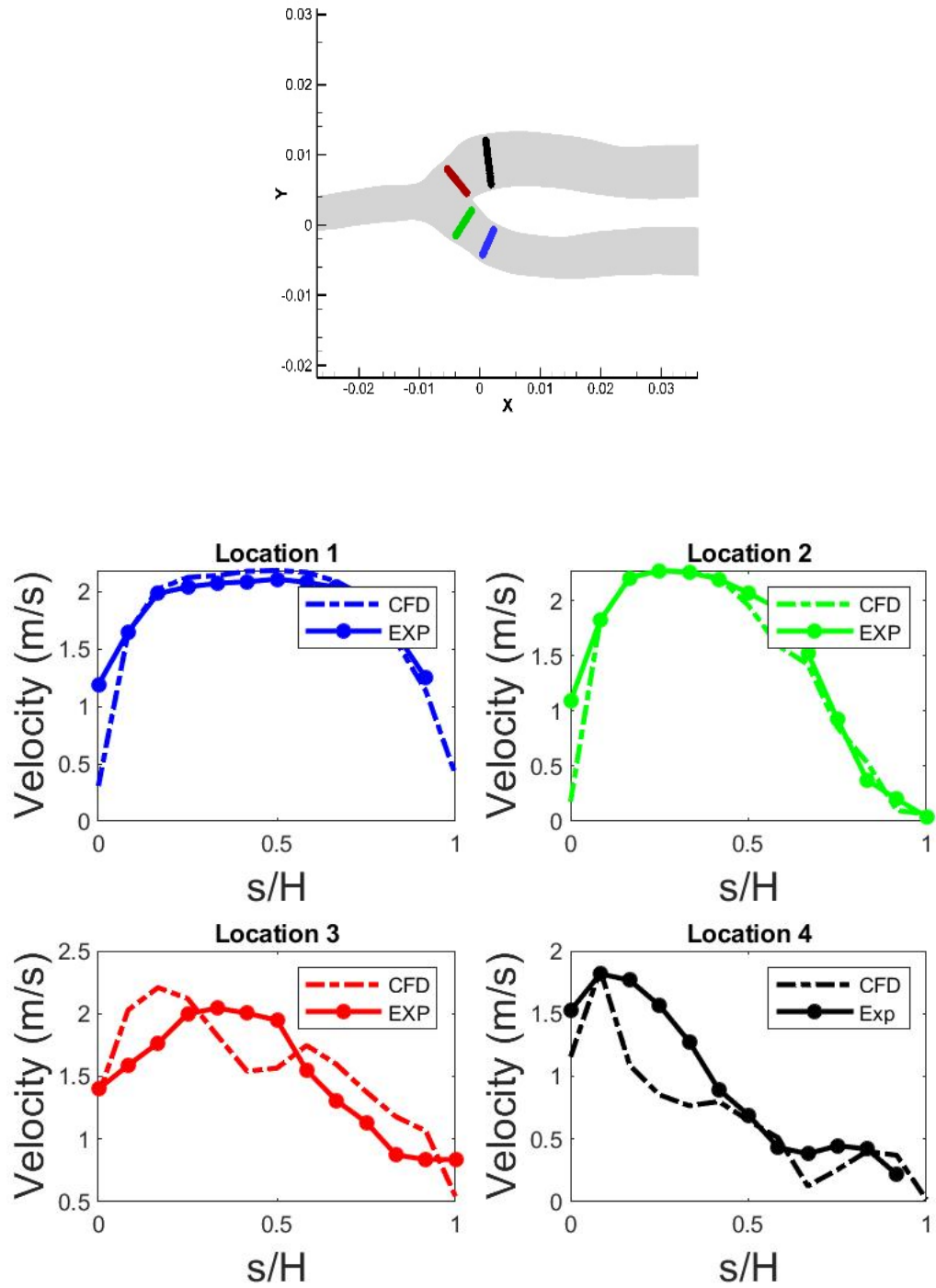


Figure 24: Experimental (Exp) and CFD results comparison at the four location indicated in the AVF geometry on the right at Location 1(blue), Location 2 (green), Location 3 (red) and Location 4(black) at 0.141s, peak systole of the cardiac cycle

3. Patient-specific computational fluid dynamics modelling of an AVF

Table 6: Average, maximum and minimum difference at four different locations. The points where the maximum and minimum difference identified are indicated in the brackets of column 3 and 4.

Location	Average Absolute error in velocity (m/s)	Maximum difference in velocity (m/s) (point)	Minimum difference in velocity (m/s) (point)
1	0.0056	0.8848 (1)	0.0096 (2)
2	0.1108	0.9119 (1)	0.0012 (4)
3	0.0659	0.4632 (6)	0.0514 (1)
4	0.2001	0.7123 (4)	0.0174 (13)

3.7.2 Validation of pressure drop

Flow impinges on the PV which commonly causes a recirculating flow at the heel of an AVF as blood travels from the PA towards the anastomosis [35]. The pressure drop is an important parameter as it directly links overall resistance and haemodynamics of the AVF. The transfer or loss of energy in highly pulsatile blood flow, as blood transitions from laminar to turbulent behaviour, leads to the non-linear relationship between pressure drop and flow rate [34], [88]. The pressure drop and flow rates values for CFD cases included in this thesis ranges from 0.25 – 18.4 mmHg for flow rates of 78.2 – 1038.6 ml/min at the PA and 0.13 – 15.4 mmHg for flow rates ranged from 53.2 – 1240 ml/min at the PV. The maximum flow rate of AVF used in this thesis is 1240 ml/min, hence all flow rates are within the range of those in the reported pressure validation study [34], [88].

3.8 Summary

This chapter includes the methodology of obtaining patient-specific geometry and flow profiles of real patients with a freehand ultrasound scanning system. The set-up of the patient-specific CFD simulation models was also outlined. Verification of grid independence and sensitivity analysis of the numerical models were quantified by calculating the GCI values and performing mesh independence and time sensitivity test. GCI_{fine} at the four selected locations were reported to be an average of 0.7% (0.06%, 0.09%, 1.03%, 1.55% at the four different locations), while the mesh independence study was reported to have an average of less than 1.5%. Time sensitivity analysis was reported to be an average of 2.8%. Besides, validation of CFD models was conducted by comparing results of an experimental model with a similar set up, in which both results showed similar trends.

Chapter 4

The effect of boundary conditions on the accuracy of CFD predictions in patient-specific AVFs

The geometry and flow rate distribution in an AVF – regardless of antegrade or retrograde flow – varies considerably among patients, based on observations made during regular monitoring of ESRD patients. Therefore, the use of a patient-specific models is essential for modelling the AVF flow under physiological conditions that are as close as possible to those of each patient. This chapter details the significance of modelling appropriate boundary conditions for an AVF CFD model, with flow distribution comparison made between models of patient-specific and assumed boundary conditions (retrograde and antegrade flow), and resistance estimation with models of patient-specific and the Hagen-Poiseuille assumption. Some parts of this chapter are based on the paper “The effect of assumed boundary conditions on the accuracy of patient-specific CFD arteriovenous fistula model”, which is published with the Computer Methods in Biomechanics and Biomedical Engineering: Imaging & Visualization.

4.1 Background

Despite being the gold standard of vascular access for haemodialysis treatment [193], AVFs induce complications such as stenosis caused by the formation of intimal hyperplasia, ischemia or dialysis-associated steal syndrome [194], [195]. Access dysfunction due to IH formation, causing narrowing in a vessel that eventually leads to AVF failure, is the most common complication observed. 45% of AVFs succumbed to either primary or secondary failure [196]. The definition of failure mode is shown in Table 1 in Chapter 2.

To assist with AVF disease prediction, CFD modelling has been used widely as a non-invasive tool to provide more information on blood flow behaviour in AVFs [35], [102], [136], [191]. The two common flow distribution types in an AVF are the antegrade and retrograde flow conditions. For retrograde flow, blood moves from the radial distal artery (DA) and radial proximal artery (PA) to the cephalic proximal vein (PV), and conversely for antegrade flow, where blood moves from the PA to the PV and the palmar arch through the DA, illustrated in Figure 25 [197].

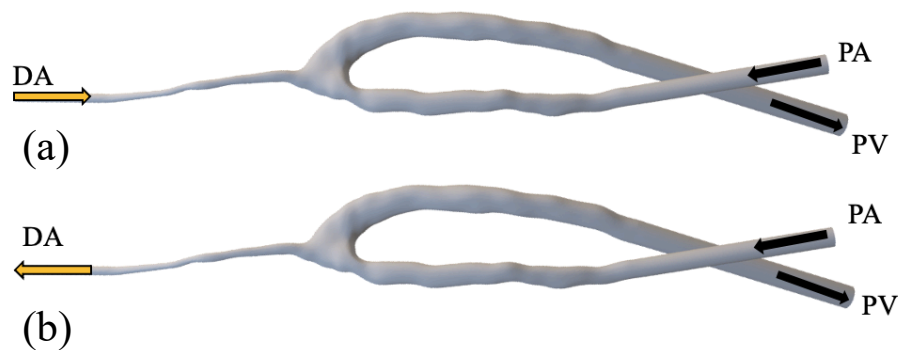


Figure 25: (a) Retrograde flow (b) Antegrade flow; Direction of blood flow from the DA, represented with the yellow arrow varies for the different flow types.

4. The effect of boundary conditions on the accuracy of CFD predictions

Studies with idealised AVF geometries have previously addressed the differences in flow due to anastomosis configuration [112], namely side-to-side [105], end-to-end [33], [102] and side-to-end [37], [106], [107]. The anastomosis region is of high significance when modelling flow patterns in an AVF, which subsequently affects the spatial WSS distribution, pressure drop and velocity [112]. Sivanesan et al. suggested a common flow split ratio [197] that has been adopted in idealised AVF computational models as boundary conditions [102], [111]. Specifically, the flow split assumption used for a retrograde flow is that PA and the DA are assumed to contribute 70% and 30% respectively to the total flow at the PV. The flow split assumption made for an antegrade flow is that the flow is assumed to divert from the PA, with 20% of the flow going to the DA and 80% to the PV [197]. Another set of assumed flow split ratio used for modelling in studies to examine changes in anastomosis angle effect was a ratio of 8:92 or 10:90 outflow at the PA and PV outflow boundary [38], [112]. An assumed flow split ratio used in a patient-specific model is unlikely to replicate a patient's exact physiological conditions since fluid resistance and vascular compliance are unlikely to remain the same across all three vessels [198], [199].

Patient-specific modelling is essential for realistic AVF simulations as AVF geometries and flow types vary considerably for different patients. The boundary conditions at each AVF vessel determine how the flow patterns develop in each vessel, impacting the results produced from the patient-specific studies. Kharboutly et al. reproduced the physiological flow profile of a measured patient waveform via a computer-controlled pump, which later served as the boundary condition for the CFD model of an end-to-end AVF [33]. Similarly, we previously adopted pulsatile waveforms produced by a peristaltic pump with a controlled flow split at the PA and DA as boundary conditions [56]. Synchronising boundary condition becomes a challenge in an end-to-side or side-to-end AVF geometry due to the multiple boundaries. To overcome this, McGah et al. [125] matched the measured Doppler ultrasound (DUS) velocity

4. The effect of boundary conditions on the accuracy of CFD predictions

with a Womersley velocity profile [200] at the feeding artery (PA) and assumed an outflow at the DA and the PV with a fixed pressure value prescribed. Flow rates determined through DUS measurement enabled real-time measurements of patients' flow waveforms to be taken. En-Iordache et al. reported studies on patient-specific AVF modelling adopting volumetric flow measurements derived from DUS examinations [35], [136], [201].

In this chapter, the effects of different boundary conditions on patient-specific AVF CFD models are examined. Three different boundary conditions, namely patient specific flow profiles and the assumed flow split assumption for flow profiles for retrograde and antegrade flow condition were modelled, to determine the effect of using these different types of flow specifications.

4.2 Methods

This chapter adopts the same assessment pipeline as outlined in Chapter 3, where patients' AVF geometry was obtained with the freehand ultrasound scanning system [153] before examining blood flow behaviour through CFD simulation. The CFD modelling strategy was the same as in Section 3.4. Here, we delve into the effects of different boundary conditions on different haemodynamic parameters.

Three different patients who have existing radiocephalic AVF were chosen to represent the common flow types in an AVF. Patient A (Figure 26) and Patient C (Figure 28) have retrograde flow, while Patient B (Figure 27) has antegrade flow. All information was taken with consent from patients. Three different sets of boundary conditions - patient specific flow which was measured from respective patients (BC 1) (outlined in Section 3.3.2) and the assumed flow split profiles of retrograde (BC 2) and antegrade flow types (BC 3) were modelled in the three different patient models (Patient A, B and C). Vessel walls were assumed to be rigid and set up with a no-slip condition. A description of the boundary conditions applied are outlined in Table 7.

The simulations ran for four cardiac cycles and the results from the fourth cardiac cycle were exported and post-processed. WSS metrics were processed in MATLAB (MathWorks Inc.), with the circumferential average calculated at the surface area of the wall with a 1 mm increment along the centreline (Figure 32 (top)).

4. The effect of boundary conditions on the accuracy of CFD predictions

Table 7: Boundary conditions (BC) used for Patient A, B and C.

Boundary condition	Description
BC 1	Patient-specific condition: The PA and the DA were set as transient velocity inlets taken from the measured patient data with PV set as zero-pressure outlet (relative pressure of zero).
BC 2	Assumed flow split condition for retrograde flow: 70% and 30% of the total flow was approximated to flow towards the PV from PA and DA respectively. The approximated flow at the PA and DA were derived from the patient-specific waveform of the same cardiac cycle with Eq. 7. Similarly, the PA and DA were set as transient velocity inlets, while PV was set as zero-pressure outlet (relative pressure of zero).
BC 3	Assumed flow split condition for antegrade flow: 20% of the total flow directed to the palm via the DA and 80% of the total flow flows into the PV from the PA. These approximations were made from the patient-specific waveform of the same cardiac cycle with Eq. 7. The PA was set as transient velocity inlet, while DA and PV are set as outflow with a weighting of 0.2 and 0.8 respectively.

4. The effect of boundary conditions on the accuracy of CFD predictions

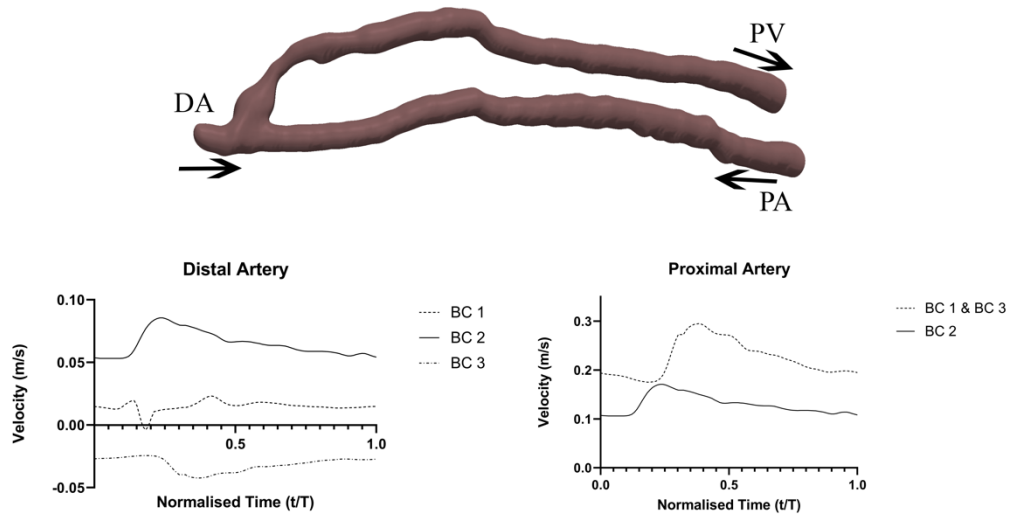


Figure 26: The flow type in Patient A's AVF is the retrograde flow condition where flow from PA and DA contributes to the total flow in PV. The black arrow represents the direction of blood flow. Approximately 94% of the flow from the PA and 6% flow from the DA contributes to the PV of Patient A's AVF (**BC 1**). A flow split condition is employed for the retrograde condition with 70% of the total flow at the PA and 30% from the DA (**BC 2**). The antegrade flow was modelled by using the patient-specific flow profile at the PA, and an outflow of 2:8 ratio of flow at the DA and the PV respectively (**BC 3**).

4. The effect of boundary conditions on the accuracy of CFD predictions

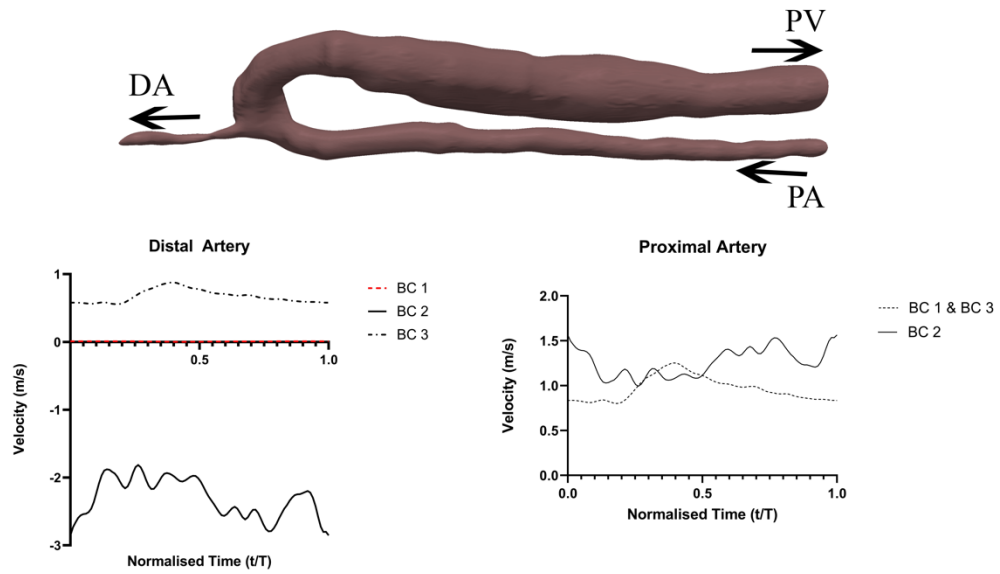


Figure 27: The flow type in Patient B's AVF is antegrade where most of the flow from PA diverts to the DA and PV at the anastomosis. The black arrow represents the direction of blood flow. Approximately 99.7% of the measured flow exits the PV and 0.3 % of the total flow measured exits the DA. Flow profile at the DA shares a similar shape with the patient-specific condition. Due to the low velocity, it is barely distinguishable from the zero line in this figure (**BC 1**). A flow split condition is employed with 70% of the total flow modelled at the PA and 30% from the DA to mimic the retrograde flow condition (**BC 2**). The antegrade flow was modelled by using the patient-specific flow profile at the PA, and an outflow of 2:8 ratio of flow at the DA and the PV respectively (**BC 3**).

4. The effect of boundary conditions on the accuracy of CFD predictions

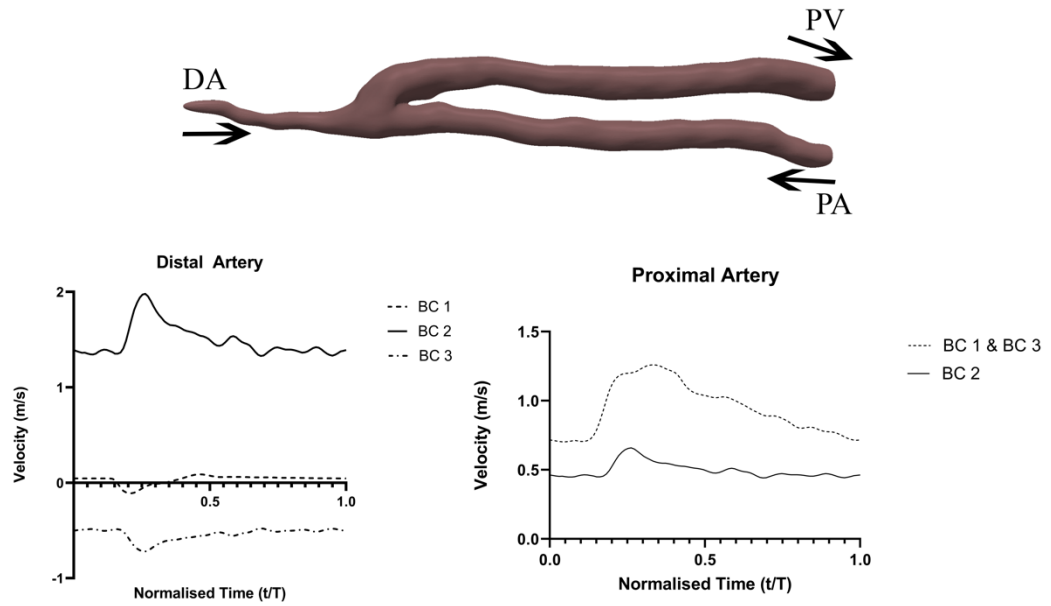


Figure 28: The flow type in Patient C's AVF is the retrograde flow condition where flow from PA and DA contributes to the total flow in PV. The black arrow represents the direction of blood flow. Approximately 0.8% of blood flow from the DA and 99.2% of the flow from the PA. A majority of the blood feeding into the PV is from the PA (**BC 1**). A flow split condition is employed with 70% of the total flow modelled at the PA and 30% from the DA to mimic the retrograde flow condition (**BC 2**). The antegrade flow was modelled by using the patient-specific flow profile at the PA, and an outflow of 2:8 ratio of flow at the DA and the PV respectively (**BC 3**).

4.3 Haemodynamic parameters

The results of the CFD simulation of Patient A for BC 1 showed that the majority of the blood was directed from the PA, with maximum velocity observed at the narrowing of the PV (Figure 29 (a)) at peak systole. Since BC 2 modelled the retrograde flow, flow distribution was similar to the case of BC 1 but blood flowed at a lower speed with the majority of the flow from the PA. Similarly, a maximum velocity of about 1.6 m/s was observed at the narrowing at the PV Figure 29 ((b)). The low velocity region at the floor of the anastomosis for the case of BC 3, towards the DA and the PV (Figure 29 (c)) resulted in recirculating flow, as flow was diverted at the anastomosis from the PA. TAWSS and transWSS were the highest for the three conditions at the narrowed segment (10 – 20mm from the anastomosis) in the PV (Figure 30). OSI remained low (less than 0.2) at both PA and PV.

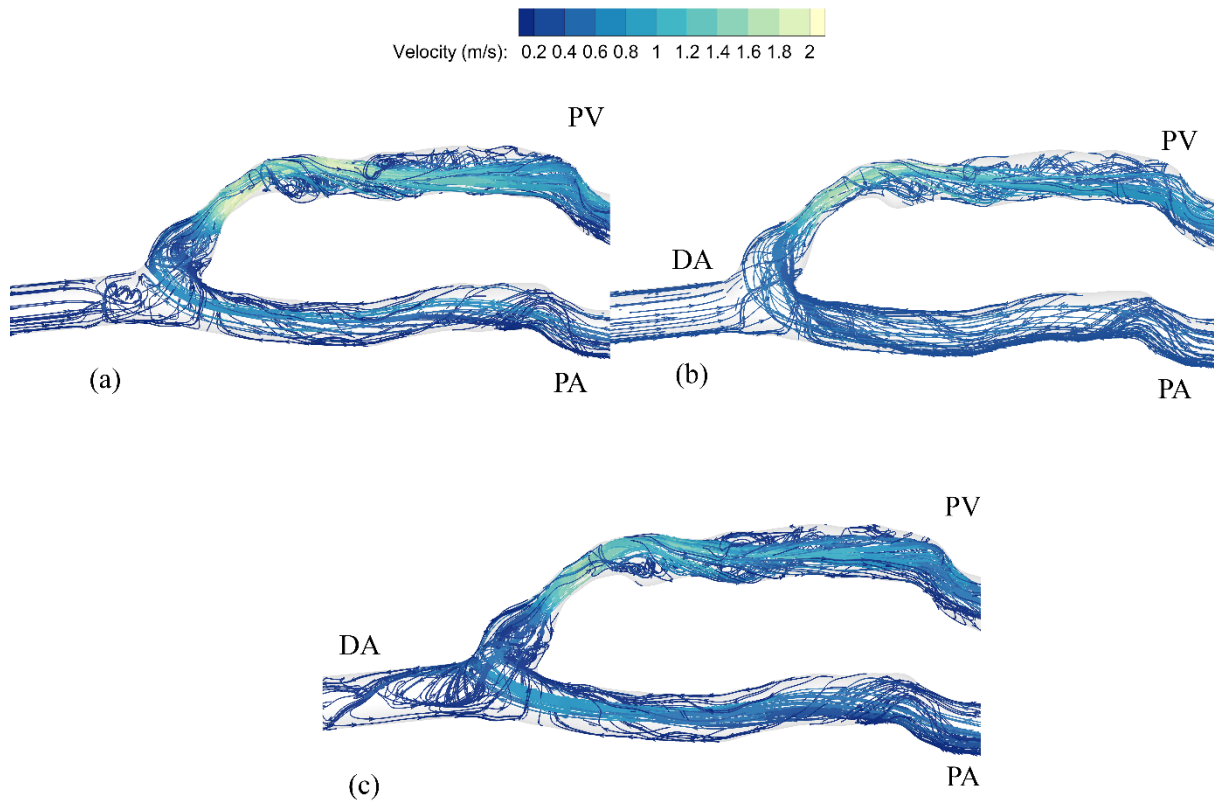


Figure 29: Streamline velocity of blood flow for the three different cases of patient A (a) BC 1 (b) BC 2 and (c) BC 3 at peak systole of the fourth cardiac cycle. All cases share the same legend

Patient A

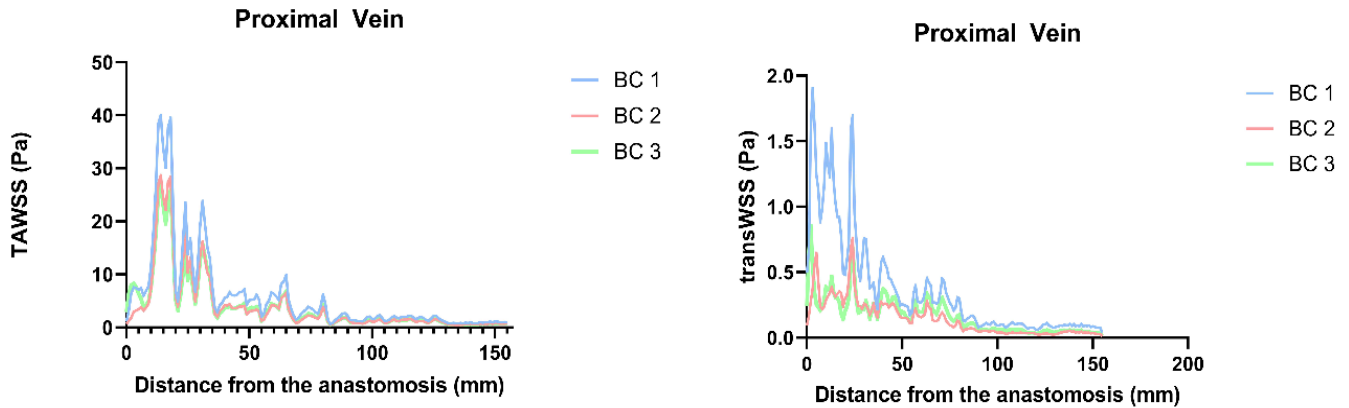


Figure 30: TAWSS and transWSS at the PV of Patient A

The results of the CFD simulation of Patient B for BC 1 showed that velocity drops after entering the PV, as a result of the increase in blood vessel diameter (Figure 31 (a)). In the case of BC 2, we noted that the maximum velocity is 8.7 m/s at the DA. This was due to the smaller diameter in the DA relative to the PA and PV. The high velocity of blood flow that entered from the DA resulted in a maximum flow towards the wall of the AVF at close proximity to the anastomosis (Figure 31 (b)). Although BC 1 and BC 3 are modelled as the antegrade flow type, a higher maximum blood flow velocity of 2.4 m/s observed in BC 3 was found at the DA, as opposed to the maximum blood flow observed at the PA for BC 1 (Figure 31 (c)). Further, this patient had a relatively negligible amount of blood directed to the DA (Figure 27), however the flow split assumption of an antegrade flow type assumes 20% of the total flow will enter the DA. A similar trend of flow diversion was observed in BC 1 of Patient B and Patient A at the anastomosis, towards the DA.

Maximum TAWSS and transWSS was located at the PA, near to the anastomosis of BC 2 (Figure 32). These values were also found to be located at the high velocity region for BC 2 (Figure 31). OSI was also noted to be higher (0.3-0.5) downstream of the PV segment where multidirectional flows were present, but remained low at the PA. High transWSS were

4. The effect of boundary conditions on the accuracy of CFD predictions

observed close to the anastomosis for all three boundary conditions of all three patients (Figure 30 and Figure 32) suggesting a common multi-directional flow around the anastomosis region of the AVF.

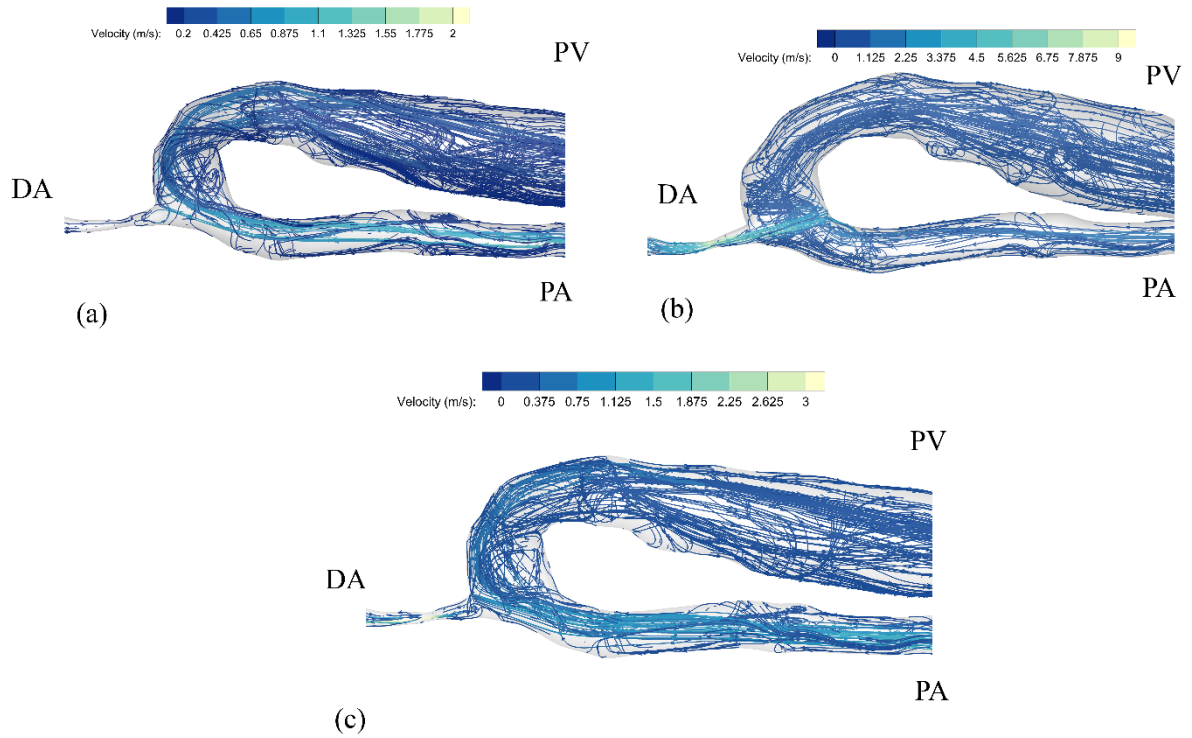


Figure 31: Streamline velocity of blood flow for the three different cases of patient B **(a)** BC 1 **(b)** BC 2 and **(c)** BC 3 at peak systole of the fourth cardiac cycle. Separate legends were used for each cases due to the wide range of velocity.

4. The effect of boundary conditions on the accuracy of CFD predictions

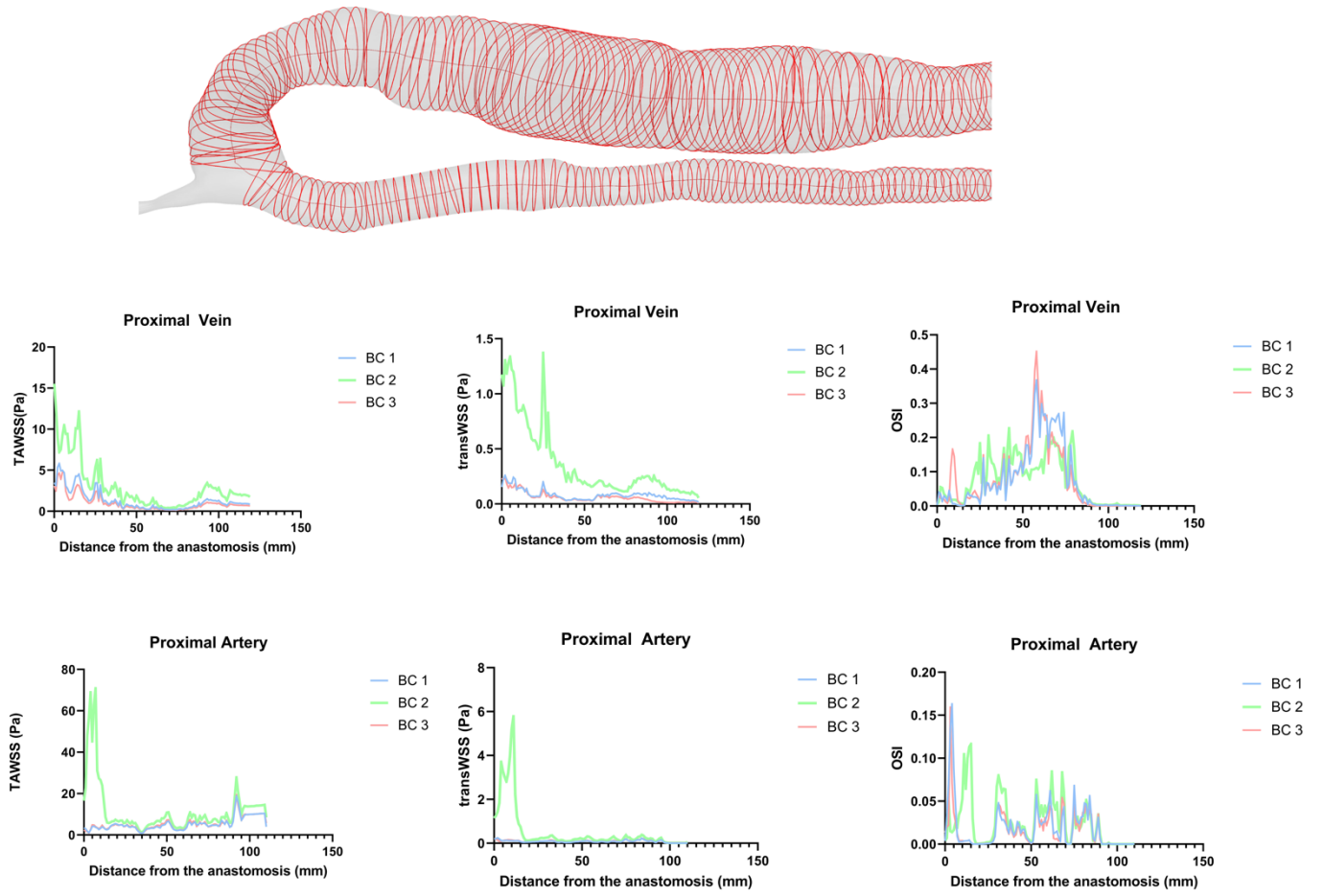


Figure 32: **(top)** Circumferential average calculated at the surface of the wall with a 1mm increment along the centreline of Patient B's AVF **(left)** TAWSS and **(middle)** transWSS **(right)** OSI of the PV and PA.

4.4 CFD-derived resistance

BC 2 and BC 3 underestimate the flow rate in the AVF (of Patient C), as observed in Table 8, with a difference of 48% (BC 2 and BC 3) at the PA and 26% (BC 2) and 58% (BC 3) in the PV relative to BC 1. A higher drop in pressure was also observed at the PA and PV of BC 1 at high flow regime. Flow instabilities across the anastomosis resulted in a significant pressure drop across the anastomosis, with greater pressure drop at the PA and PV, as compared to the DA [107], [137].

Table 8: Pressure difference and flow rate data of Patient C for the three different boundary conditions at PA and PV

PA			PV	
	Pressure difference (mmHg)	Flow rate (ml/min)	Pressure difference (mmHg)	Flow rate (ml/min)
BC 1	5.19	1067.80	9.36	1053.50
BC 2	2.12	559.10	4.12	777.60
BC 3	2.05	559.20	2.65	439.80

Average resistance, calculated as a ratio of pressure difference and flow rate of the fourth simulation (cardiac) cycle (Section 3.6) was examined for the three patients' cases, along with the different boundary conditions modelled. Patient A and Patient C were patients with retrograde flow, while Patient B had antegrade flow; hence, the discrepancies were expected to be smaller between BC 2 and BC 1 for Patients A and C, and BC 3 and BC 1 for Patient B. The resistance values showed no discernible pattern for all three patients, with no particular pattern observed at the PA, shown in Table 9. In the PV, resistance was lower for Patient A and C (for both conditions, BC 2 and BC 3) relative to BC 1 due to a lower pressure difference to drive lower blood flow. Furthermore, it is less erroneous to assume the split boundary condition to model a patient with antegrade flow as compared to retrograde flow. When a split

4. The effect of boundary conditions on the accuracy of CFD predictions

retrograde flow boundary condition was applied to a patient such as Patient B, blood flow that was expected to flow away from the usable PV segment (for cannulation) was forced to flow towards the PV, causing a large difference in the expected blood flow rate of the PV. This is evident where large discrepancies were observed for BC 2 and BC 1 in the resistance value for both segment in Patient B, seen in Table 9 and Table 10. The changes of flow rate due to the varying diameter and boundary conditions were the contributing factor of the variation in resistance.

Table 9: Resistance values at the PA segment and the discrepancies from the patient specific condition (BC 1)

Resistance (mmHg/l/min)						
	Patient A	Differences from BC 1 (%)	Patient B	Differences from BC 1 (%)	Patient C	Differences from BC 1 (%)
BC 1	2.5	-	0.5	-	4.9	-
BC 2	1.9	24	4.9	881	3.8	22
BC 3	2.5	2	0.4	30	3.7	24

Table 10: Resistance values at the PV segment from and the patient specific condition (BC 1)

Resistance (mmHg/l/min)						
	Patient A	Differences from BC 1 (%)	Patient B	Differences from BC 1 (%)	Patient C	Differences from BC 1 (%)
BC 1	18.6	-	0.8	-	8.9	-
BC 2	15.8	15	1.9	133	5.3	40
BC 3	15.4	17	0.5	42	6.0	32

4.5 Geometrical influence on blood flow behaviour

The geometry of the AVF plays a significant role in influencing the blood flow distribution along the AVF, observed in Patient A (Figure 29) and Patient B (Figure 31). This is especially important at the anastomosis where flow where flow is diverted via the DA. Although Patients A and B have anastomoses with less acute angles than Patient C, the latter had a more abrupt change in diameter between vessels, resulting in different flow behaviour. For this reason, another patient-specific model, Patient C, which has an AVF with a more acute angle than Patients A and B, but more gradual change in diameter was analysed. Patient C's AVF had a retrograde flow type, but the CFD results showed a different trend compared to Patient A as higher velocity was observed along the PA and PV for BC 1 and BC 2, as opposed to BC 3 where low flow was noted at the DA at peak systole (Figure 33). Recirculating flow was observed at similar locations (at the floor of the anastomosis) in Patients A and C.

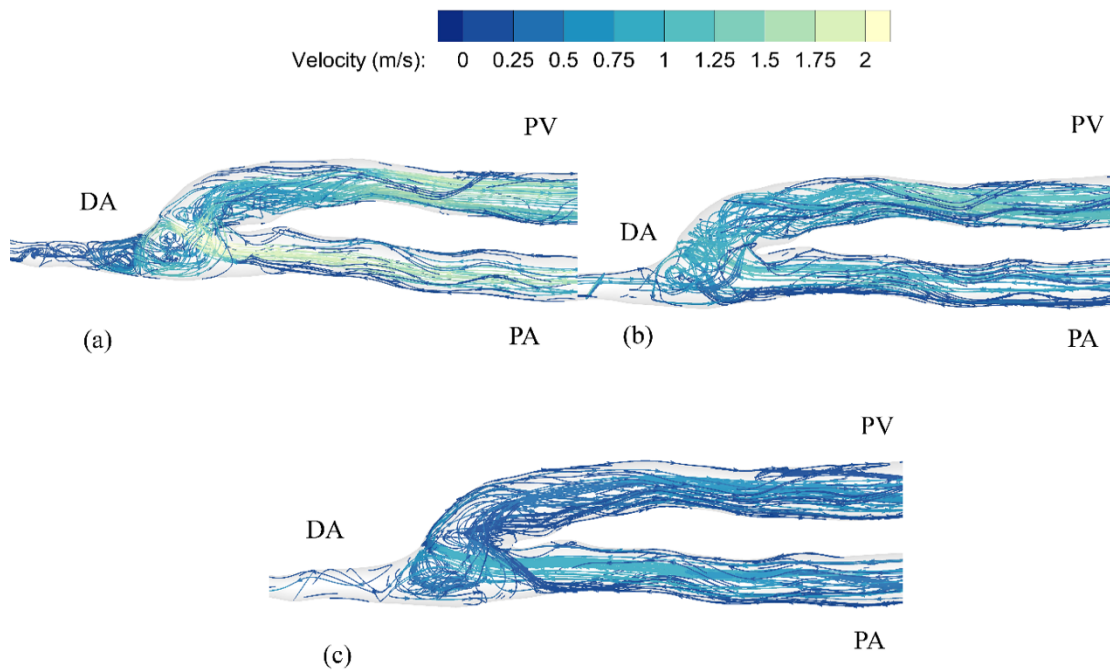


Figure 33: Streamlines of blood flow for another patient-specific model, Patient C (a) BC 1 (b) BC 2 and (c) BC 3 at peak systole of the fourth cardiac cycle. All cases share the same legend.

4. The effect of boundary conditions on the accuracy of CFD predictions

The ratio of the diameter of DA to PV for Patients A, B and C was 0.89, 0.19 and 0.49 respectively. The change in vessel diameter of the DA to PV was smaller in Patients A and C, explaining the similar trends observed in streamline velocity for the three cases. Changes in area of the blood vessel affects the velocity and flow distribution in the AVF which was particularly evident in Patient B. The decrease in diameter of the DA resulted in an increase in velocity, given the same inlet flow conditions.

The anastomotic angle for Patient A, B and C are illustrated in Figure 34. A larger anastomotic angle was observed in Patient A as compared to Patient C, explaining the diminished flow disturbance observed in Patient A. The level of recirculating flow was seen to be less for a more gradual change of geometry, especially at the anastomotic region as seen in Patient A, similar to reported trend by Carroll et al. [140]. Flow direction was not only affected by the contraction of the heart during systole or diastole [202] but also the geometry of the AVF as the direction of blood flow in the DA was shown to change from antegrade to retrograde when the anastomosis angle exceeds 58° [106]. Flow disturbance in an idealised end-to-side AVF has also shown to reduce when the angle of the anastomotic configuration is modified [37].

4. The effect of boundary conditions on the accuracy of CFD predictions

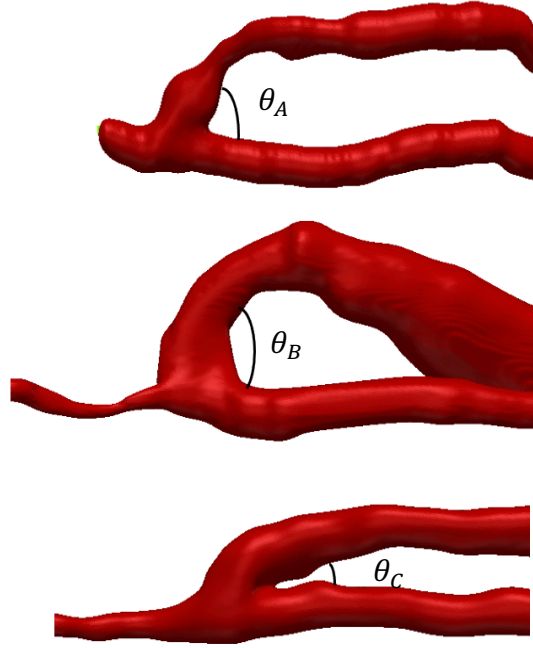


Figure 34: (top to bottom) Anastomotic angle for Patient A, B and C, where $\theta_A \approx 107^\circ$, $\theta_B \approx 132^\circ$ and $\theta_C \approx 48^\circ$ and $\theta_B > \theta_A > \theta_C$

4.6 Comparison with the Hagen-Poiseuille mathematical model

The classic Hagen-Poiseuille law has been used to predict blood flow in arteries based on the relationship between pressure, flow rate and resistance [80], [81] in incompressible flow. It is worth noting that blood was modelled as a non-Newtonian fluid in this thesis. The non-Newtonian properties were found to have an effect on WSS estimation [82], [83]. That being said, the Hagen-Poiseuille WSS estimation has previously been used in blood flow prediction and WSS estimation [81], [84], [89]. Therefore, it is of our interest to evaluate the validity of the Hagen-Poiseuille model in resistance calculation for patient-specific AVF, where the mathematical model involves less computationally intensive processes to estimate resistance as compared to CFD calculation.

The Hagen-Poiseuille equation [80] (Eq. 22) is given as:

$$R = \frac{\Delta P}{Q} = \frac{8\mu L}{\pi r^4} \quad \text{Eq. 22}$$

where ΔP is the change in pressure, Q is the mean flow rate, L is the length of the vessel, r is the radius of the vessel and μ is the dynamic viscosity of blood.

Given that the diameter of the AVF changes along the z -direction for respective patients, an estimation of the average resistance corresponding to the radius and length of the AVF in the z -direction can be estimated by the following integral (Eq. 23):

$$R = \frac{8\mu}{\pi} \int_0^L \frac{1}{r(z)^4} dz \quad \text{Eq. 23}$$

4. The effect of boundary conditions on the accuracy of CFD predictions

The comparison of resistance obtained from the Hagen-Poiseuille law and CFD calculation at the PA and PV are shown in Figure 35 and Figure 36. A more prominent difference is observed at the PV segment as compared to the PA.

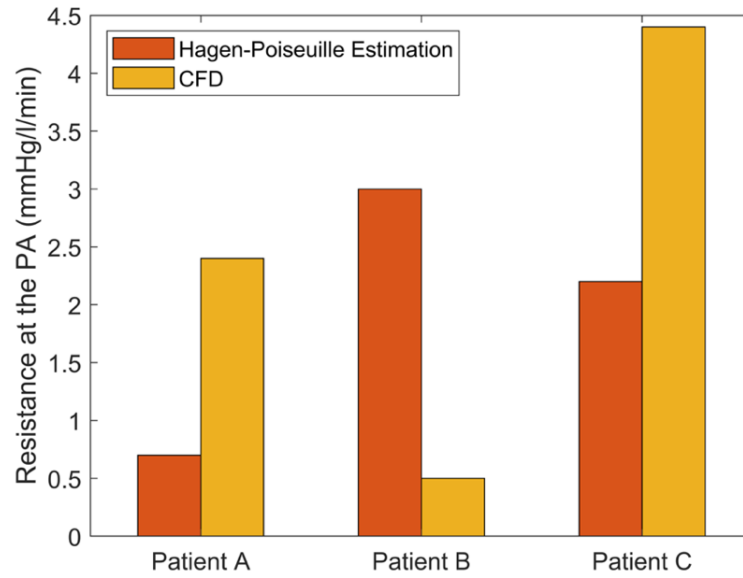


Figure 35: Comparison of CFD-derived resistance with the Hagen Poiseuille estimation at the PA segment

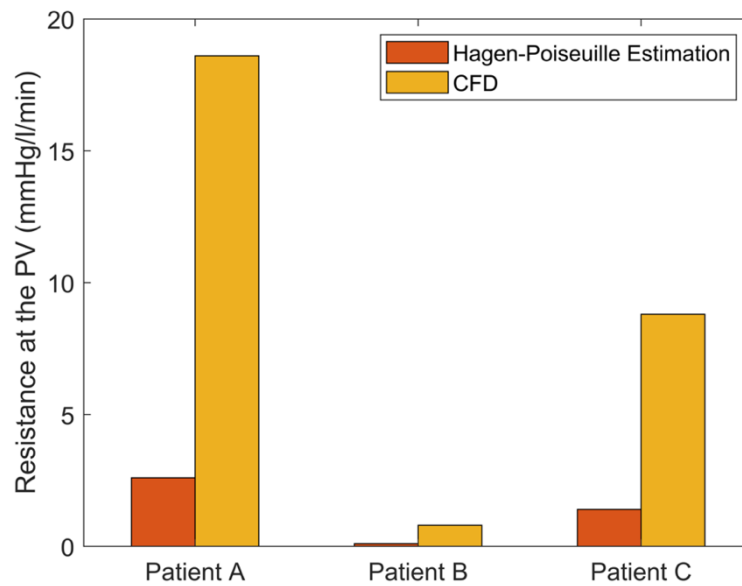


Figure 36: Comparison of CFD-derived resistance with the Hagen Poiseuille estimation at the PV segment

4. The effect of boundary conditions on the accuracy of CFD predictions

The Hagen-Poiseuille calculation assumes that flow is laminar and the cross-sectional area of the tube (vessel) is perfectly cylindrical, in which for most patient-specific cases, an equivalent radius was estimated instead. The former was especially significant given that unsteady flow is often observed at the anastomotic region of the AVF [35], [163]. Moreover, blood viscosity was assumed to be constant based on the Hagen-Poiseuille law, which is not the case for blood viscosity that are affected by haematocrit and different composition of blood [203].

CFD modelling was also able to capture the effects caused by stenosis better than the Hagen-Poiseuille model, seen in Patient A, where a higher change in pressure was observed as a result of the stenosis at the heel of the PV segment (Figure 29), which was also the main contributor to high resistance (Figure 36). Due to the fourth-power radius, $1/r^4$ calculation in Eq. 23, a small change in vessel radius results in a large difference in resistance calculation. The sudden increase observed in inverse r^4 (Figure 37 (a)) is a result of the stenosis (narrowing) at the PV segment of Patient A. On the contrary, the diameter of the PA segment of Patient A remained constant as a result of the somewhat constant diameter of the vessel. Conversely, the diameter of PV is larger than the PA in Patient B, with a small inverse r^4 value (Figure 37 (b)). The effect of these flow behaviours, as shown by the CFD simulation appear to be more notable over the assumptions made for the mathematical model.

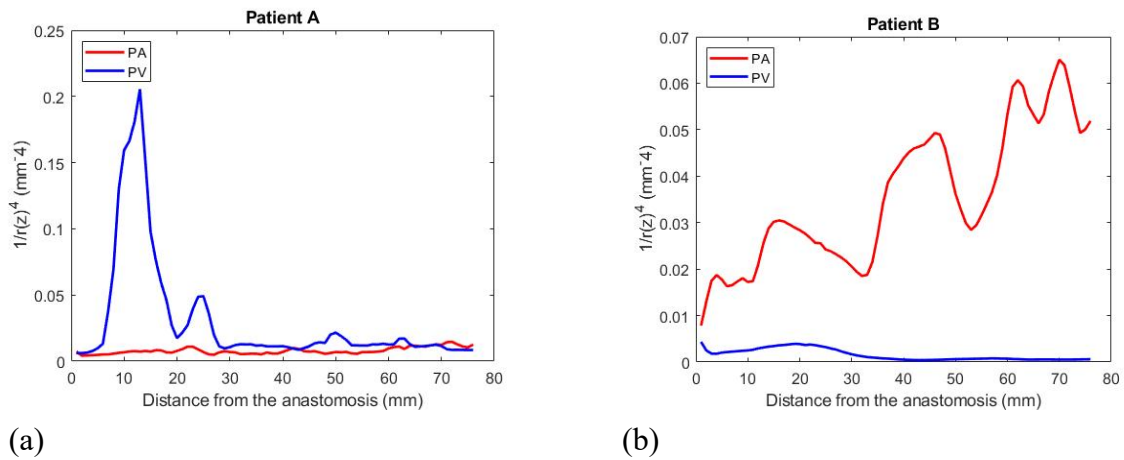


Figure 37: Change of $1/r^4$ along the anastomosis ($L = 0$ to 75mm) of (a) Patient A and (b) Patient B

4.7 Limitation

A previous study showed comparable flow rates in DUS and phase-contrast magnetic resonance imaging (MRI) [151], however with the lack of portability of MRI, DUS appears to be the better choice for regular non-invasive surveillance. Nonetheless, the results from this study had some limitations such as the lack of compliance of the vessel walls. Although an FSI study is able to model the wall compliance, it requires more computational power and time, and is less feasible for regular surveillance of the AVF. Rigid wall effects were also reported to have limited impact on blood flow dynamics [184], [204].

4.8 Clinical relevance

Based on presented patient case studies, an inappropriate boundary condition can lead to a significantly different simulation outcome. The boundary conditions were reported to affect the temporal development of flow and spatial variations in WSS in a numerical study performed with different sets of inlet and outflow boundary conditions for blood vessels [199], [205]. Here, we identified varying patient AVF blood flow distributions during our clinical assessment with regular monitoring of dialysis patients with AVF [164]. No specific ratio of blood distribution was found to be suitable for all kinds of patients. An assumed flow split distribution was a poor representation of blood flow in an AVF, outlined in the case of Patient B. Here, we found the assumption made for antegrade flow to be unreasonable, given that assumed flow rates differed significantly to measured flow rate. The haemodynamic effects are prominent, especially at the anastomosis and dependent on the geometry of the AVF. It is therefore critical that haemodynamic boundary conditions are properly modelled in order to accurately predict AVF outcomes. Patient-specific conditions need to be as close as possible to the patient's measured physiological condition to gain a high fidelity representation of the AVF flow [35], [136], [153], [191], [201].

Different blood flow distributions lead to varying locality where the AVF is susceptible to the development of intimal hyperplasia [39]. The locality of the low velocity regions where flow stagnation occurred in Patients A, B and C varied for the three sets of boundary conditions (BC 1, BC 2, and BC 3), suggesting that an inaccurate site of IH development within an AVF will be predicted if the boundary condition is not modelled correctly. Swirling and recirculating flows were observed at the anastomosis for the three datasets of Patient C, and these were seen to settle farther. Conversely, recirculating flow was observed along the PV of Patient B. A likely disease initiation site is the inner curvature of the vein segment adjacent to the anastomosis, based on the results of BC 1 in Patient B. However, if the retrograde flow split

4. The effect of boundary conditions on the accuracy of CFD predictions

assumption was made in the model (BC 2), the clinical approach to salvage the AVF might be to ligate the DA due to high blood flow drawing from the palm, as the patient would be at risk of steal syndrome [206]. Clinical studies that simplified flow and WSS assumptions based on the equation may also lead to a mismatch in clinical diagnostic [84], [207].

4.9 Conclusion

AVF computational results are showed to be heavily dependent on geometric factors, and inaccurate assumptions can lead to incorrect clinical recommendations. Geometry and boundary conditions both have an impact in the simulation of biomechanical forces such as velocity, wall shear stress and hydraulic resistance in an AVF, which subsequently highlights the importance of appropriate patient-specific CFD modelling. The velocity distribution demonstrated disturbed and recirculating flows, observed at different locations for the three patient datasets, with different sets of boundary conditions, highlighting the discrepancies of using assumed rather than measured boundary conditions. Inappropriate specification of inlet boundary conditions leads to an incorrect prediction of blood flow patterns and velocity prediction. Whilst assumptions made on blood flow distribution simplify the computational modelling processes and reduce the computational time, they compromise the accuracy of results.

Although the Hagen-Poiseuille law is a good representation between vessel diameter and resistance for long straight channels of uniform section, the blood flow and vessel in the AVF or any diseased vessels do not conform to assumptions for Hagen-Poiseuille flow. The mathematical model underestimated the resistance of a stenosed AVF (Patient A).

In summary, CFD modelling is still a notable non-invasive tool in capturing three-dimensional blood flow behaviour and is useful for predicting the likelihood of diseased vessels. It is recommended that to properly predict and examine diseased vessel occurrence, appropriate patient-specific computational modelling should be conducted with realistic physiologically appropriate cardiac waveforms at the boundaries of the vasculature.

Chapter 5

The use of CFD-derived resistance to identify problematic AVFs

Inconsistencies have been found between the correlation of wall shear stress (WSS) and diseased AVFs. This chapter aims to address the relationship between resistance, derived from CFD solutions and the patency rate of an AVF. Seventeen cases of patients with juxta-anastomotic stenoses were examined, each with different examinations (scans) at different time points – six patients were examined before and after treatment, while eleven patients were examined after treatment. The calculation of resistance enabled the detection of problematic AVFs and regions of stenosis. Part of the findings in this chapter have been submitted to Computer Methods and Programs in Biomedicine Update and presented in the 22nd Australasian Fluid Mechanics Conference [192]. The development of an augmented reality (AR) model for training was completed in collaboration with an Honours student, Vivian Lun.

5.1 Background

AVF failure may be attributed to IH formation [51] where intimal vascular smooth muscle cell proliferation induces vascular negative remodelling leading to the formation of flow limiting stenoses [22], [51]. Whilst there are many factors influencing the development of these stenoses, pathological flow-related phenomenon may also incite the formation of intimal hyperplasia, and hence a stenosis. The formation of stenoses compromises the utility and longevity of the AVF. These stenoses form before any clinical sequelae and are thus difficult to detect using regular clinical tools. Our research group have previously demonstrated the use of a three-dimensional freehand ultrasound system [153] to monitor AVFs by modelling haemodynamic changes in a patient-specific AVF computational fluid dynamics (CFD) [191]. In particular, the shape of the anastomosis was found to impact flow profiles [37]. While others sought to make use of various metrics based on the calculation of wall shear stress (WSS) to quantify flow behaviours with AVF patency rates none of these have been able to reliably predict AVF failure [39], [120], [137], [153] especially for low and oscillatory flow [35], [103]. We therefore considered a new type of metric for identification of disease initiation, by analysing the pressure drop within an AVF, which is commonly associated with overall resistance and flow instabilities, as discussed in Section 2.6 [34], [88], [107].

The use of a new, CFD-calculated metric, resistance, derived from the pressure difference and flow rate within an AVF, presents potential to characterise AVF conditions and identify access dysfunction. It is crucial to model this with a patient-specific information to capture the effects of the pressure drop due to the geometrical configuration accurately, as discussed in Chapter 4. Such a metric can be measured non-invasively using imaging obtained with a freehand ultrasound tracking system previously described [153], coupled with CFD modelling [191], [192], [208]. This allows the identification of stenoses requiring treatment and allow the

5. CFD-derived resistance in problematic AVFs identification

successful continuation of the treatment. These CFD-derived parameters thus present a novel method of detecting conditions conducive to IH in patient geometries.

The aim of the study is to determine if CFD-derived resistance could be an early indicator of a problematic AVF. We further expand on the use of a previously described technique on tracking geometric and hemodynamic alterations [191] that enabled creation of CFD models for individual AVF based on real geometries, thus allowing for calculation of resistance.

5.2 Patient selection

A retrospective study was conducted on seventeen patients (mean age 70.2, range 60-80, 14 males, 3 female) who were treated with an interwoven nitinol stent (Abbott Vascular, Santa Clara, CA, USA) in their radiocephalic AVF at the Prince of Wales Hospital, Sydney, Australia. The interwoven nitinol stent resists kink formation when external forces are applied. This approach used to treat juxta-anastomotic stenosis shows more promising 1-year primary and assisted primary patency [209] as compared to other common treatments such as balloon angioplasty [210], [211].

This study was approved by the South Eastern Sydney Local Health District Human Research Ethics Committee (2018/ETH00577). The seventeen patients were selected from a larger group of patient (N = 42) who have been treated with the interwoven nitinol stent, documented in [209], in accordance to their consent to participate in our study. Consent was obtained for all patients, prior to study participation, in accordance with the ethical standards. These patients have radiocephalic AVF and have undergone dialysis. Patients with an arteriovenous graft, a brachial-cephalic AVF, or an AVF not used for dialysis were excluded from this study. Patients were assessed at a multidisciplinary renal vascular access clinic [164]. Table 11 outlines the baseline clinical characteristic of the seventeen study patients.

5. CFD-derived resistance in problematic AVFs identification

Table 11: Baseline clinical characteristic. Continuous data are presented as mean with standard deviation (\pm) (range). Categorical data are presented as the number (percentage).

Variables	All patients (N = 17)
Age, y	70.2 \pm 7.2 (60 - 80)
Gender (male)	14 (82)
Diabetes	13 (76)
Smoking	3 (18)
Hypertension	16 (94)
High cholesterol	11 (65)
Ischaemic heart disease	6 (35)
Cerebral vascular accident	0 (0)
Peripheral vascular disease	1 (6)
Cause of renal failure	
Unknown	1 (6)
Diabetes	12 (71)
Glomerulonephritis	1 (6)
Hypertension	2 (12)
Lithium induced	1 (6)

5.3 Statistical analysis

Statistical analyses were conducted in R (Version 1.2, RStudio, Inc., Boston, MA). Continuous data are presented as mean with standard deviation (\pm) or median (range). Categorical data are presented as number or percentage. Threshold for statistical significance was $P < 0.05$, with the estimates presented with a 95% confidence level estimate. Correlation between resistance and diameter at PV and PA were evaluated using Pearson product-moment correlation [212]. The correlation coefficient can be interpreted as shown in Table 12: Interpretation of correlation coefficient [212].

Table 12: Interpretation of correlation coefficient [212]

Range of correlation coefficient	Interpretation
0.0 – 0.1	Negligible correlation
0.1 – 0.39	Weak correlation
0.40 – 0.69	Moderate correlation
0.70 – 0.89	Strong correlation
0.90 – 1.00	Very strong correlation

5.4 CFD-derived resistance

Six patients had 3D-ultrasound image acquisition before and at various points after stent implantation (pre- and post-intervention) based on an informal schedule. Data for eleven patients was acquired after stent implantation, again at various time points, representing the group of patients with AVF geometries that had no issues with regards to juxta-anastomotic stenosis after being treated.

The same patient-specific CFD modelling pipeline outlined in Chapter 3 was used for each patient case. Patient geometry was acquire via the ultrasound scanning system [153] before simulating flow phenomena of each AVF with CFD modelling using patient-specific boundary conditions (Section 3.4.1).

Given the variability of patients' AVFs, resistance was calculated individually for respective scans (Chapter 3, Section 3.6). Centrelines from each geometry were generated and voxel edges sampled at a 1 mm distance by adopting the skeletonization algorithm, to reduce the 3-D binary volume to a single line, followed by a smooth curve fitting algorithm in Simpleware SCANIP (Synopsis Inc., CA, USA). The pressure values of each face on the wall were averaged to the closest nodes of the centrelines, allowing a circumferential averaged pressure to be obtained in 1mm increments from the anastomosis.

Pressure differences were calculated:

- First, from the anastomosis to 50 mm of the PV segment and 35 mm of the main inflow PA segment; this is the common region for juxta-anastomotic stent deployment of the AVF. Resistance, R at the PV and PA in each segment with Eq. 20 to determine the geometrical resistance of the vessel.
- Second, calculating the change in R with Eq. 21 at a 1 mm interval throughout the entire segment enabled interrogation of the entire AVF.

5.5 Resistance at different AVF segment

CFD-derived resistance was calculated at the PV and PA of the seventeen patients who have undergone a surgical intervention to address stenosed vessel at the juxta-anastomotic region. A number of examinations (referred as “scans”) were conducted for the seventeen patients at different time points. To quantify the resistance trend associated to the anastomosis stenosis treatment, scans from six patients taken before and after the intervention, and another eleven patients taken post-intervention, were analysed.

The range of resistance for the six patients who had scans pre- and post-intervention at PV and PA are as shown in Figure 38. At the PV, resistance ranges from 4.4 - 68.8 mmHg/l/min before intervention, and 0.4 – 3.4 mmHg/l/min after intervention. The average resistance values before intervention were 24.3 mmHg/l/min and 2.0 mmHg/l/min. At the PA, resistance ranges from 0.17 – 10.8 mmHg/l/min before intervention, and 2.1 – 10.0 mmHg/l/min afterward. The average resistance before intervention was 3.2 mmHg/l/min and 5.2 mmHg/l/min.

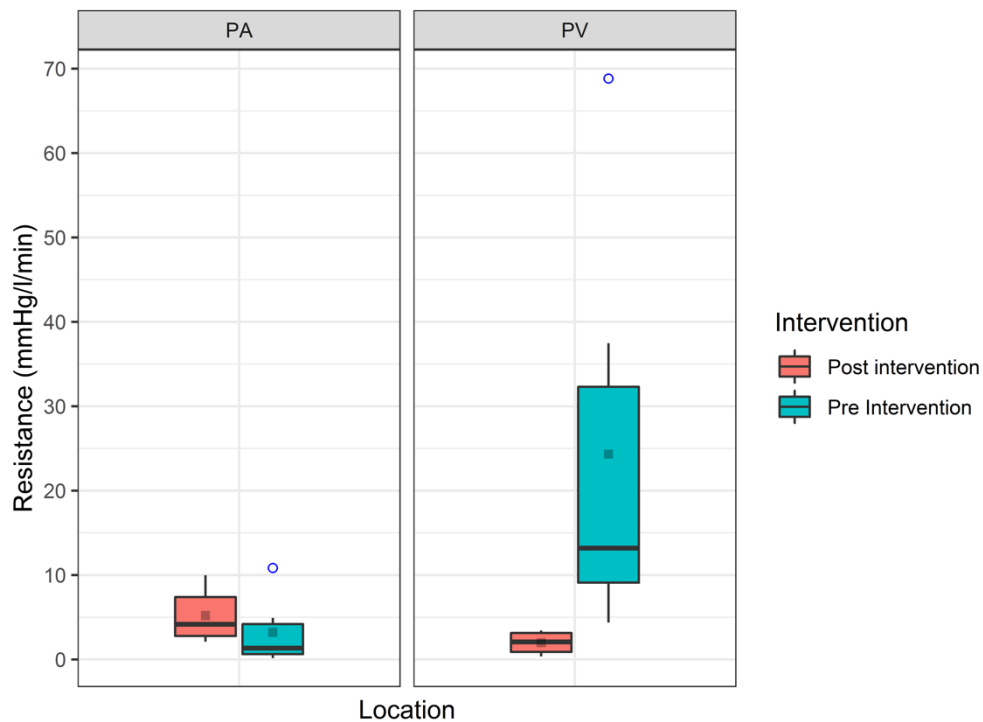


Figure 38: Boxplot representation and comparison of resistance range for the six patients with a pre- and post-intervention scan. Shaded (grey) squared points represent mean values. Outliers are represented with blue circles.

5.5.1 Vein segment (PV)

Resistance at the PV of patients with a scan before and after the intervention are presented in Table 13. Results of scans of the other eleven patients were conducted after intervention and are shown in Table 15.

All R values of the six patients decrease post intervention, with an average decrease of 77% (21 – 99%). The average diameter for each patient was calculated by sampling at 1 mm intervals along the vessels. There is an average of 25% increase in the average PV diameter for the six patients examined (Table 14). All resistance values at in the PV segment of the treated patients remained low (mean resistance values of 2.3 mmHg/l/min), as shown in Table 15.

Table 13: Changes in resistance pre- and post-intervention at the PV

Patient	Pre- intervention Resistance (mmHg/l/min)	Post- intervention Resistance (mmHg/l/min)	Decrease in Resistance (%)
1	9.6	3.4	65
2	4.4	3.4	21
3	16.8	2.5	85
4	68.8	1.7	98
5	8.9	0.6	93
6	37.5	0.4	99

5. CFD-derived resistance in problematic AVFs identification

Table 14: Changes in diameter pre- and post-intervention at the PV

Patient	Pre- intervention PV diameter (mm)	Post- intervention PV diameter (mm)	Change in diameter (%)
1	6.6	6.5	-2
2	6.3	6.5	+ 4
3	5.9	6.6	+ 12
4	4.6	5.7	+ 24
5	6.5	11.7	+ 81
6	5.0	6.7	+ 33

Table 15: Post intervention resistance values

Patient	Post intervention Resistance (mmHg/l/min)
7	2.5
8	0.6
9	7.9
10	1.1
11	2.0
12	1.9
13	0.8
14	5.8
15	0.8
16	0.8
17	3.1

5.5.2 Artery segment (PA)

Contrary to the PV segment, only two out of the six patients presented a drop in resistance post-intervention (Figure 39), with a 52% and 63% decrease in resistance values for Patient 4 and Patient 6. This was also reflected in the overall increase in resistance at the PA after intervention as shown in Figure 38. Although there is an increase in resistance at the PA for other patients, it is worth noting that these AVFs remained patent. The low resistance at the usable segment of the AVF, namely the PV, is shown to have more prominent association with intervention. The reasons for an increase in resistance after the treatment at the juxta-anastomotic region is the increase in brachial artery flow rate after intervention, causing larger pressure difference to drive the flow [209]. The resistance value at the PA all remained below 14 mmHg/l/min. No correlation was observed between the changes in resistance at the PA segment and patency rate.

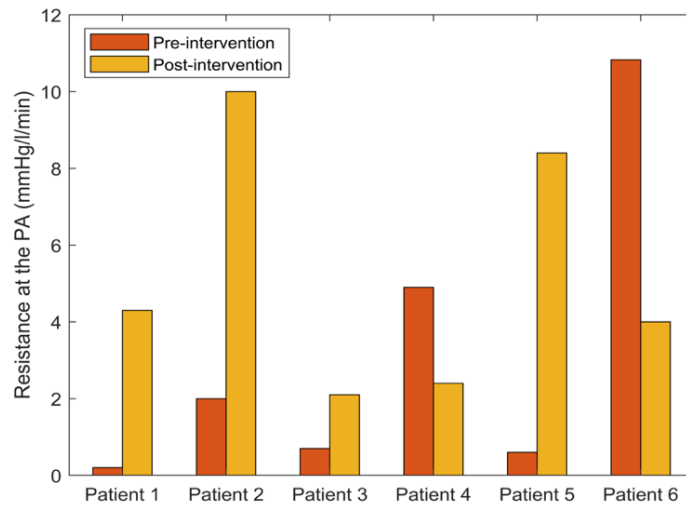


Figure 39: Changes of resistance at the PA pre- and post- intervention

5.6 Patients' clinical observation

In this section, naming of scans were designated “1” for the first patient, and “a” for the first scan. Patient 1 had a mature AVF used for dialysis (19 months old) where a slight narrowing was detected in the swing vein segment (Scan 1a), however no clinical identification of the need for treatment, even though resistance at the PV segment was reported at 9.4 mmHg/l/min. The patient then re-presented for Scan 1b 42 days later, showing an inward remodelling of the AVF with a reduced flow rate, with resistance at the PV reported at 9.6 mmHg/l/min. As a result, an endovascular intervention was performed with the placement of an interwoven nitinol stent in the juxta-anastomosis of the AVF. Scan 1c was then performed after the stent was implanted demonstrating patency of the juxta-anastomotic stent and a change in the geometry of the AVF, which saw resistance decrease in resistance to 3.4 mmHg/l/min. The fourth scan (Scan 1d), with resistance of 2.4 mmHg/l/min, was taken a year after the intervention and the AVF has remained patent since. Implantation of the juxta-anastomotic stent was associated with a decline in the resistance value in PV.

Patient 2 had a mature AVF (7 months old) with low flow rate issues with dialysing when scan 2a was performed. The issue of low flow rate remained three months after the first scan when Scan 2b was performed. An interwoven nitinol stent was implanted into the juxta-anastomotic segment. Scan 2c was performed 24 days post procedure and demonstrated a slight fall in the PV resistance. The patient remained with a patent and functional AVF, which was again observed at Scan 2d, 760 days after the first scan. Implantation of the juxta-anastomotic stent was associated with a decline in the PV resistance from 4.4 to 3.4 mmHg/l/min. Yet, an increase in resistance at the PA was, however, observed after the intervention from 2.0 mmHg/l/min to 10.0 mmHg/l/min, suggesting potential issues at the artery segment. The patient's death prevented the collection of further data.

5. CFD-derived resistance in problematic AVFs identification

Patient 3 presented with an AVF that failed to mature at 63 days post creation where Scan 3a was performed. A stent was thus implanted in the cannulation zone of the AVF, to facilitate dialysis. The patient returned at day 133 post creation (Scan 3b) with low flows in the AVF despite a patent stent. The resistance at the PV was 16.8 mmHg/l/min indicating the need for treatment. A new stenosis was observed in the swing vein and intervention to the swing vein was performed with implantation of an interwoven nitinol stent. The patient was then re-scanned at 35 days post stent implantation, with the scan demonstrating a resistance value of 2.5 mmHg/l/min. The AVF has remained patent since this scan. The effect of the first procedure showed an increase in R from 13.3 to 16.8 mmHg/l/min at the PV. The effect of the second procedure was an 85% decrease in R with implantation of the anastomotic stent.

Patient 4 presented with a mature AVF 145 days post creation. A narrowing was demonstrated on Scan 4a in the swing vein and intervention to the swing vein was undertaken with an interwoven nitinol stent implanted at the anastomosis. Resistance value was calculated to be 68.8 mmHg/l/min. The patient presented 137 days after the procedure with resistance values of 1.7mmHg/l/min.

Patient 5 presented with a mature AVF with arterial insufficiency. The first scan (Scan 5a) was taken prior to the surgical intervention. Scan 5a demonstrated a stenosis in the swing vein after which, intervention was performed to the swing vein and anastomosis comprising implantation of an interwoven nitinol stent. Scan 5b was performed five months after the stent procedure demonstrating patency of the AVF. Resistance at the PV decreased from 8.9 to 0.6 mmHg/l/min. The AVF has remained patent and has not required any further intervention.

Patient 6 presented with a mature AVF at which point Scan 6a was performed. The patient subsequently presented at day 134 post formation with dilation and insufficient flow in the AVF. Scan 6b was performed which demonstrated a stenosis in the swing vein of the AVF. A

5. CFD-derived resistance in problematic AVFs identification

juxta-anastomotic stent was implanted. Scan 6c was performed 43 days after the stent implantation and demonstrated patency of the AVF. The AVF has been patent since. The implantation of the interwoven stent was associated with a large decrease in resistance value from 37.5 to 0.4 mmHg/l/min.

Patient 7 to 17 presented with mature AVF, with an interwoven nitinol stent deployed prior to the scan. These cases had an average R value of 2.5 mmHg/l/min. Patient 9, of exception, had a higher resistance value of 7.9 mmHg/l/min, noting a notably high value compared to the other resistance values presented followed by a surgical intervention at the juxta-anastomotic swing segment. The relatively higher resistance at the PV of Patient 9 was an indication that surgery was required to maintain the AVF, with a stent being inserted again at the vein segment, resulting in a decrease in resistance to 1.9mmHg/l/min with the scan taken 29 days after the mentioned procedure.

5.7 Identifying stenosis region at the PV segment

Resistance at the PV is shown to have stronger association with AVF patency as shown in Section 5.4. The change in resistance per 1 mm interval at the PV was analysed along the entire length of the vein segment. The result of each CFD simulation were packaged in a way that allows rapid visualisation of geometry and stenosis region, by examining any increment of resistance from consecutive nodes, from the anastomosis. The maximum change in resistance per unit length coincides with the stenotic region of each the vessels as shown in the following sub-sections (Section 5.7.1 and Section 5.7.2)

5.7.1 Case Study I: Patient 1

Calculating the change in resistance with Eq. 21 at a 1mm intervals along the entire segment enabled detailed interrogation of the entire AVF. Patient 1 had undergone a stent deployment to treat a stenosis found at the anastomotic region. Based on Figure 40 (a), the peak change in resistance was observed at 0 – 10 mm from the anastomosis, at the stenosis region indicated in Figure 40 (b), Scan 1a. Inward remodelling persisted along the PV segment, with three peak resistance values shown in Figure 40 (a), and the maximum in resistance observed at around 10 – 20mm from the anastomosis. A gradual change in resistance was observed for Scans 1c and 1d, suggesting that there was no stenosis at the usable segment of the AVF. The AVF remained patent 15 months after Scan 1d was taken. The angiography images taken before and after the surgical procedure is as shown in Figure 40 (f) and Figure 40 (g).

5. CFD-derived resistance in problematic AVFs identification

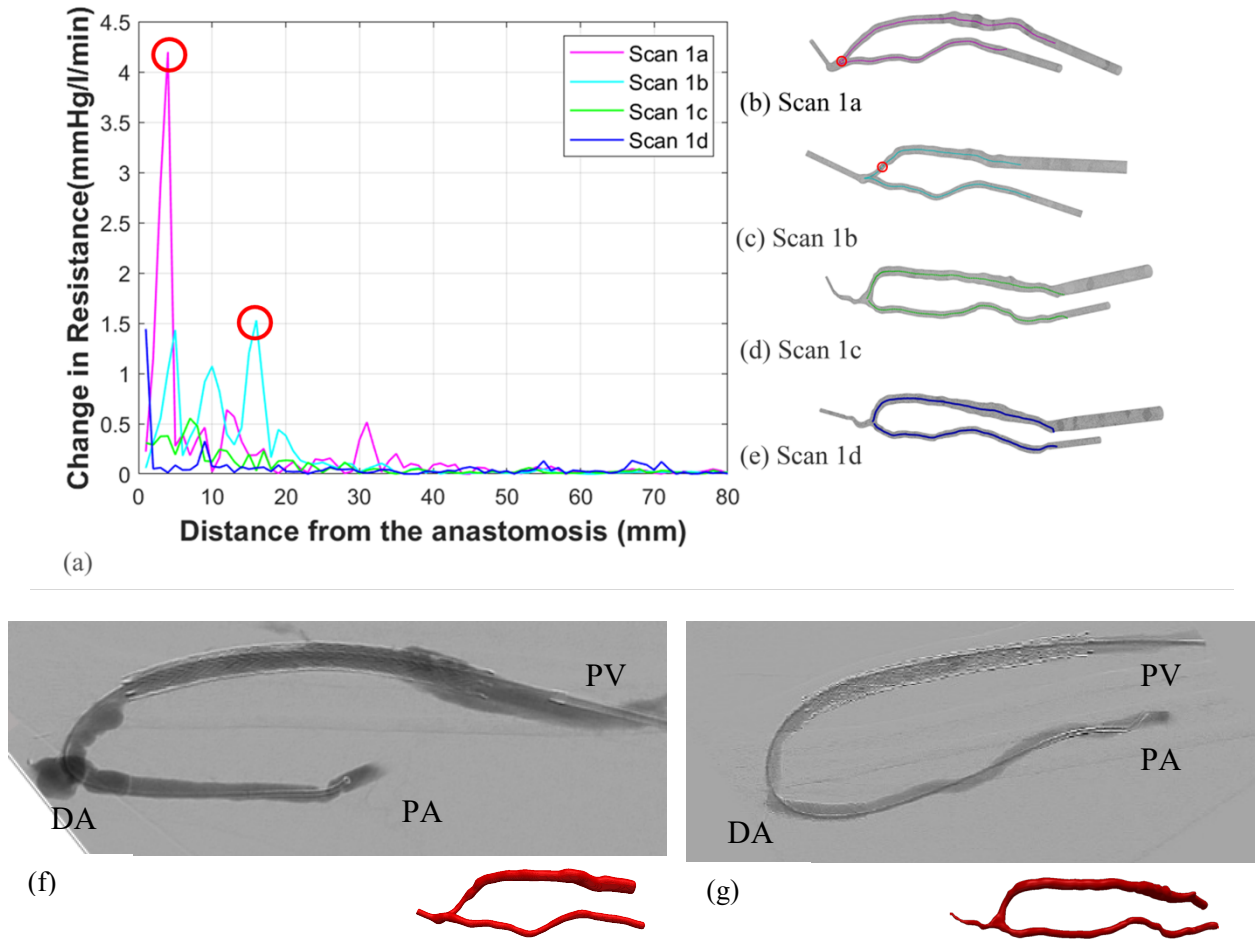


Figure 40: (a) Changes of R at 1mm interval along the PV of the AVF. Red circles represents the maximum change in R , coinciding with the stenosis region observed in each scan. (b) Scan 1a was taken 684 days post creation, (c) Scan 1b was taken 726 days post creation, and approximately 42 days from Scan 1a, (d) Scan 1c, 1160 days post creation, and approximately 434 days from the Scan 1b, e) Scan 1d, 42 months post creation, and approximately 112 days from Scan 1c. There was also an intervention between Scan 1b and 1c. (f) Angiography image before stent deployment, comparable to Scan 1b, (g) Angiography image after stent deployment, comparable to scan 1c. The three-dimensional geometry for these two scans are shown in the bottom right of the angiography images.

5.7.2 Case Study II: Patient 4

As reported in Table 13, there is a 98% decrease in resistance value from pre-intervention (Scan 4a) to post-intervention (Scan 4b) from 68.8 to 1.7 mmHg/l/min. This is associated with treatment at the juxta-anastomotic narrowing observed at the swing segment of the juxta-anastomotic vein. The sudden change in resistance also represents the increase in pressure, drawing a correlation with stenosis formation. From Scan 4b, Figure 42 (c), however, a severe narrowing was observed at the proximal cephalic vein, where the patient underwent subsequent angioplasty. Angiography images that are comparable to the three-dimensional AVF model, shown in Figure 41.

The resistance trend along the AVF was investigated to capture the whole picture of Patient 4's AVF condition. The maximum value of resistance was observed between 10 – 20 mm from the anastomosis, coinciding with the stenosis region seen in the geometry of Scan 4a. In Scan 4b, the peak location that coincides with stenosis region appeared to be beyond the juxta-anastomotic regions (> 50 mm from the anastomosis) seen in Figure 42. Resistance peaked between 50 – 60mm from the anastomosis where the narrowing was observed in the geometry of Scan 4b. A gradual resistance trend was observed in Scan 4c, where resistance values remained below 5mmHg/l/min, and there was no sudden increase in resistance observed. The AVF has remained patent since this intervention, with four additional scans taken on days 5, 68, 152 and 971 post procedure.

5. CFD-derived resistance in problematic AVFs identification

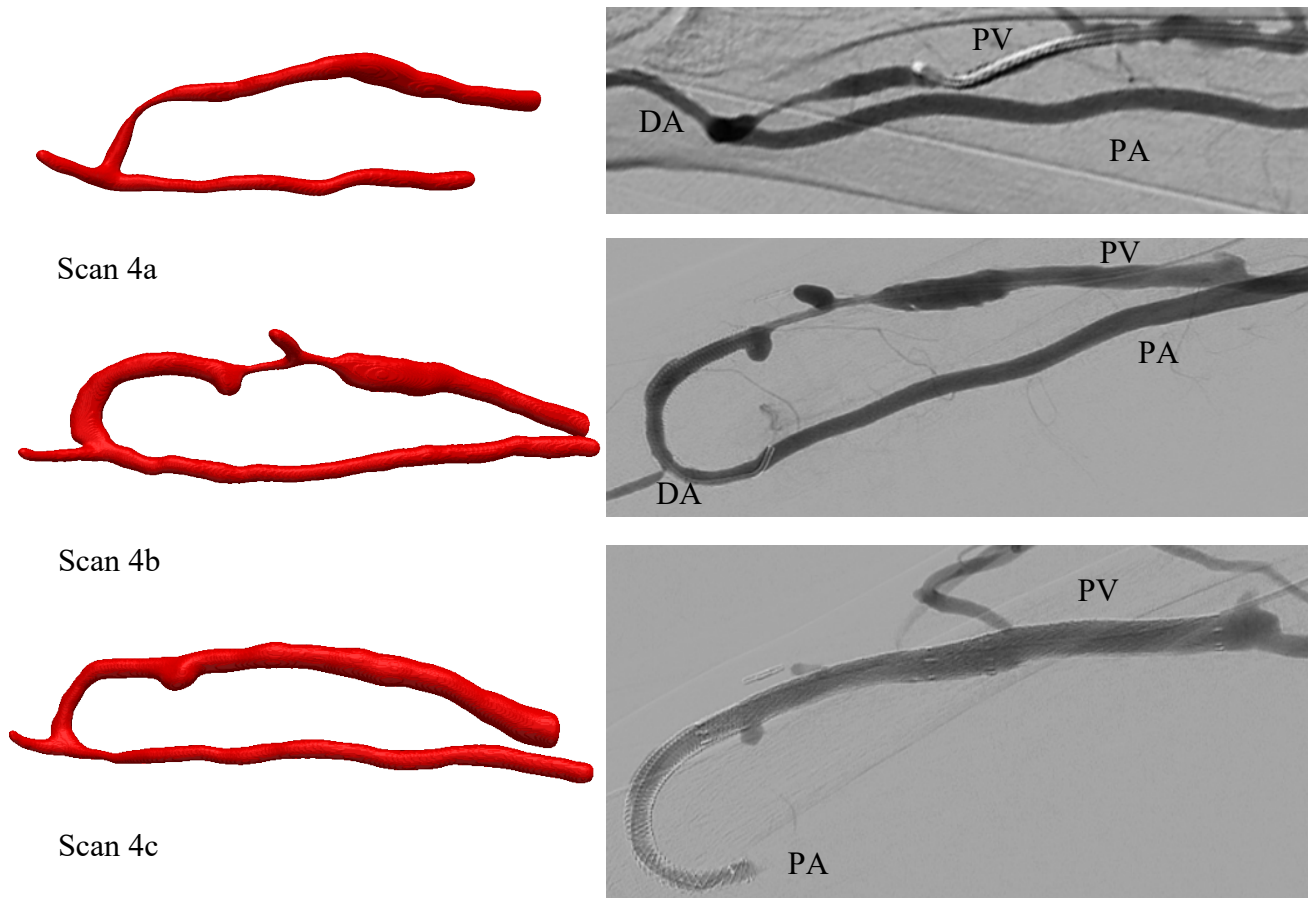


Figure 41: **(right)** Angiography images of Scan 4a, Scan 4b and Scan 4c that are comparable to the **(left)** three-dimensional AVF geometries.

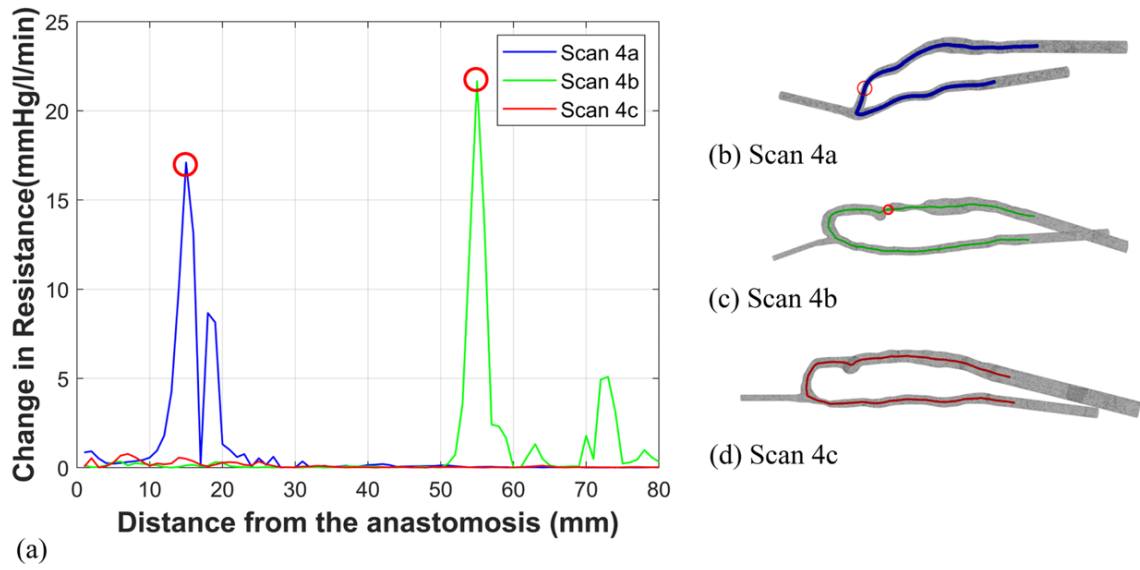


Figure 42: (a) Changes of R at 1mm interval along the PV of the AVF. The red circle shows the maximum change in R , that correlates with the stenosis region shown in respective geometries. Scan 4a was taken before the interwoven nitinol stent was deployed. Scan 4b was taken 4.5 month after the mentioned intervention. Scan 4c was taken one week after Scan 4b was taken.

5.8 Using resistance to predict the need for surgical intervention

Clinicians become aware of access dysfunction when they encountered issues during cannulation and dialysis. Balloon angioplasty or stent deployment are performed on diseased stenosed sections of the fistula circuit to enlarge the vessel lumen. However, repeat interventions are commonly required for restenosis.

Patient 8 provides an example where more complicated problems arose after treatment. The patient presented with a mature AVF which had previously required inflow intervention. Scan 8a was taken when the AVF had developed low flow. An interwoven nitinol stent was subsequently deployed to treat the stenosis. Although the issue on juxta-anastomotic stenosis was treated, the patient required further assistance as issues with dialysis persisted.

Changes to resistance were observed beyond the juxta-anastomotic stent segment, at approximately 80 mm from both PA and PV. The value of resistance at PV remained low (below 5 mmHg/l/min), but resistance at the PA was 59.5 mmHg/l/min (Figure 43). The high resistance at the PA, beyond the juxta-anastomotic segment (at 80 mm from the anastomosis), indicated the need of an intervention at the PA rather than the anastomotic PV segment. This high resistance value was associated with the narrowed region in the PA, with balloon angioplasty performed to the artery segment of the AVF after Scan 8a. Scan 8b was then carried out and resistance value was recorded to be 15.6 mmHg/l/min. Although there was a notable decrease in resistance after the intervention at the PA, the resistance value remained higher than average. AVF continued to have problems at the inflow artery with a further balloon angioplasty procedure conducted after. Given the high resistance observed at PA, treatment at the PA would have been more effective than at the juxta-anastomotic vein. No further patency information is available as Patient 8 underwent a kidney transplant.

5. CFD-derived resistance in problematic AVFs identification

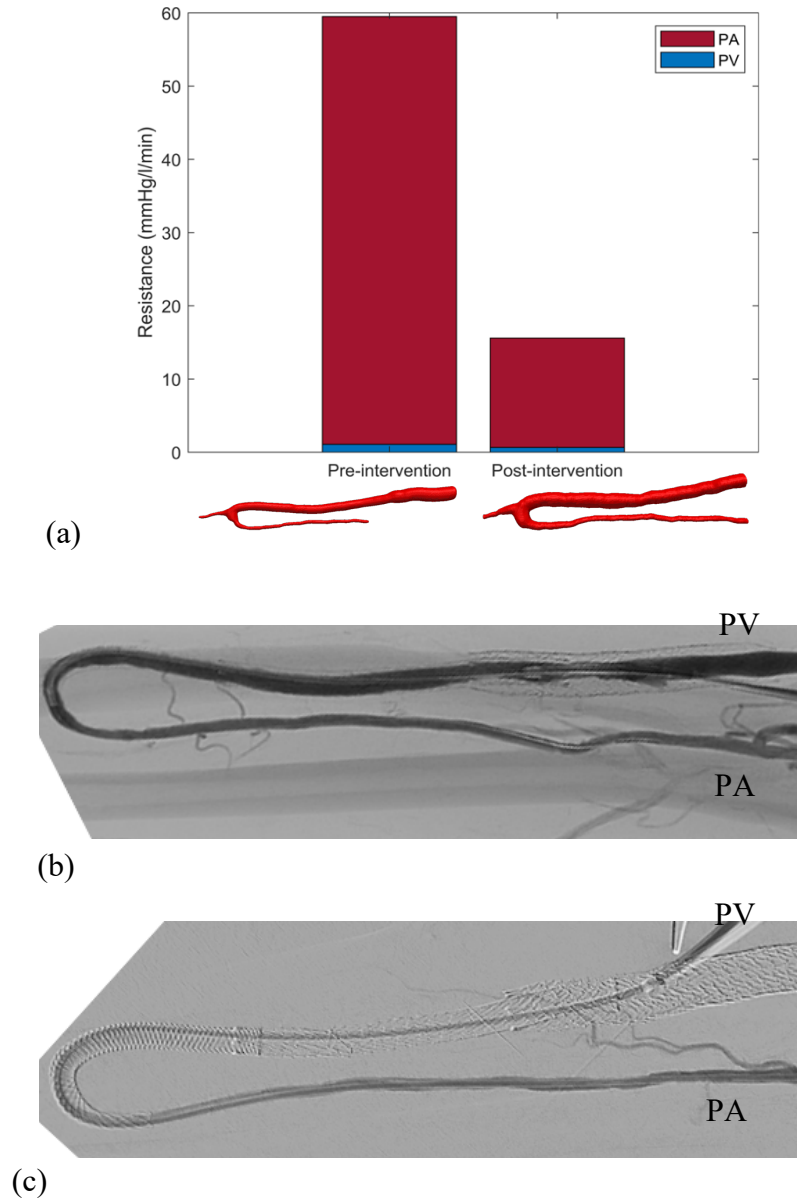


Figure 43: (a) R in the PA and PV of Patient 8. The geometry that associates to the pre- (Scan 8a) and post-intervention (Scan 8b) scans are shown below respective bar charts. (b) Angiography image that is comparable to Scan 8a and (c) Scan 8b

5.9 Clinical relevance

Given that vascular access is a lifeline for patients with ESRD who require dialysis, multiple methods such as physical examinations, surveillance, intra-access flow measurements and medical imaging are used to diagnose dysfunctional access before it leads to occlusion [213]. Among these, medical imaging such as ultrasound is most commonly used to examine blood flow rates, vessel diameter [213] and the change in velocity (peak systolic velocity) [214] to provide an indication of stenosis. The drawback, however, is the limitation of two-dimensional ultrasound images and heavy dependency on the sonographer's clinical expertise for the interpretation of standard sonographic criteria.

Patients with dysfunctional AVFs were found to have higher resistance values, and an overall decrease of resistance was observed after an intervention. Furthermore, there is a stronger negative association ($r = -0.9$) between resistance and the average diameter of the PV before

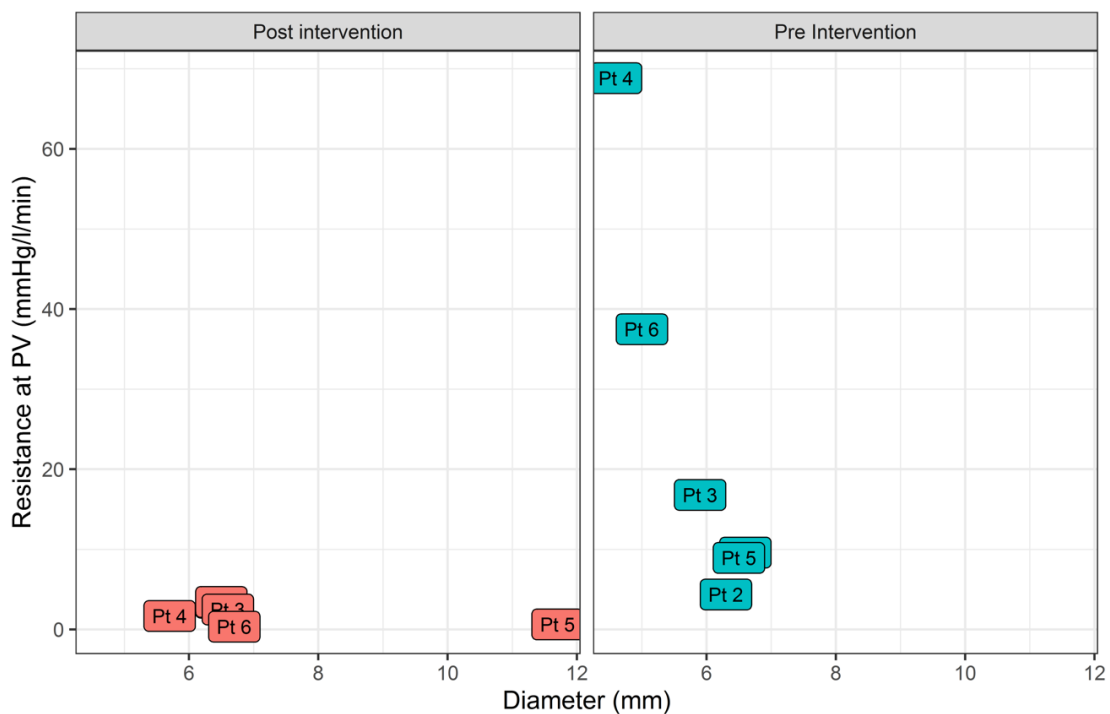


Figure 44: The relationship of resistance and average diameter of PV for the six patients pre- and post-intervention. Pt represents "patient" ID. Overlap labels for post-intervention scans are Pt 1, Pt 2, Pt 3; Overlap labels for pre-intervention scans is Pt 1.

5. CFD-derived resistance in problematic AVFs identification

intervention as compared to after intervention ($r = -0.5$), as shown in Figure 44, suggesting resistance as a better predictor of problematic AVF.

With the knowledge of the correlation observed between resistance at the PV and the AVF condition, this study sets a foundation for future prospective investigation. The technique can be incorporated with the regular AVF surveillance that is necessary for all ESRD patients. Clinicians then should be alerted when a scan returns a higher-than-average resistance value through the systematic approach of a multidisciplinary centre. The same patient is then to be observed clearly in case of an intervention. This enable clinicians and nurses to monitor closely patients who have a high resistance value instead of having to evaluate all the other comorbidities or to be caught off-guard by an emergency intervention. Furthermore, this three-dimensional ultrasound data acquisition and stenosis location identification technique provides a clearer picture of problematic vessels of the PV and PA along the circuit. The novel approach of determining patient-specific resistance through CFD modelling has the potential to reduce the number of surgical procedures required, each of which have associated risks. The cost and effort associated with this technique is also lower in comparison to other routine surveillance measures. Further assessment of the suitability of this predictor is detailed in Chapter 6.

5.9.1 Incorporating other technologies to complement the current model

Another emerging tool for medical education and training is augmented reality (AR), where computer-generated objects is integrated into the real world virtually [215]. AR has also shown potential in medical and patient education to help patients and clinician to make informed decisions [216]. In terms of the context of AVF care, good cannulation techniques and practices were shown to be crucial in maintaining AVF survival [217]. Despite challenges in AR development, the greater accessibility, user-friendliness, and ability to access multiple modes for cannulation training outweighs the challenges themselves.

There is a need to assist with training of dialysis nurses so that they gain appropriate cannulation expertise. A smartphone application, called FistulaFlow, accessible at <https://www.vfdunsw.com/fistula-scans>, was developed for this purpose [218]. The system outlined in Chapter 3 enabled data acquisition and processing of patient-specific AVF physiology with specific blood flow behaviour corresponding to a particular patient. This information can be subsequently linked to an AR application for anatomical animation and simulated results. These data were stored in an accessible website database providing greater accessibility, thereby improving patient education and nurse training. Patient-specific AVF flow patterns (generated from the CFD results) can be viewed easily by scanning a designated QR code for each patient's scans, as shown in a web database (Figure 45).

5. CFD-derived resistance in problematic AVFs identification

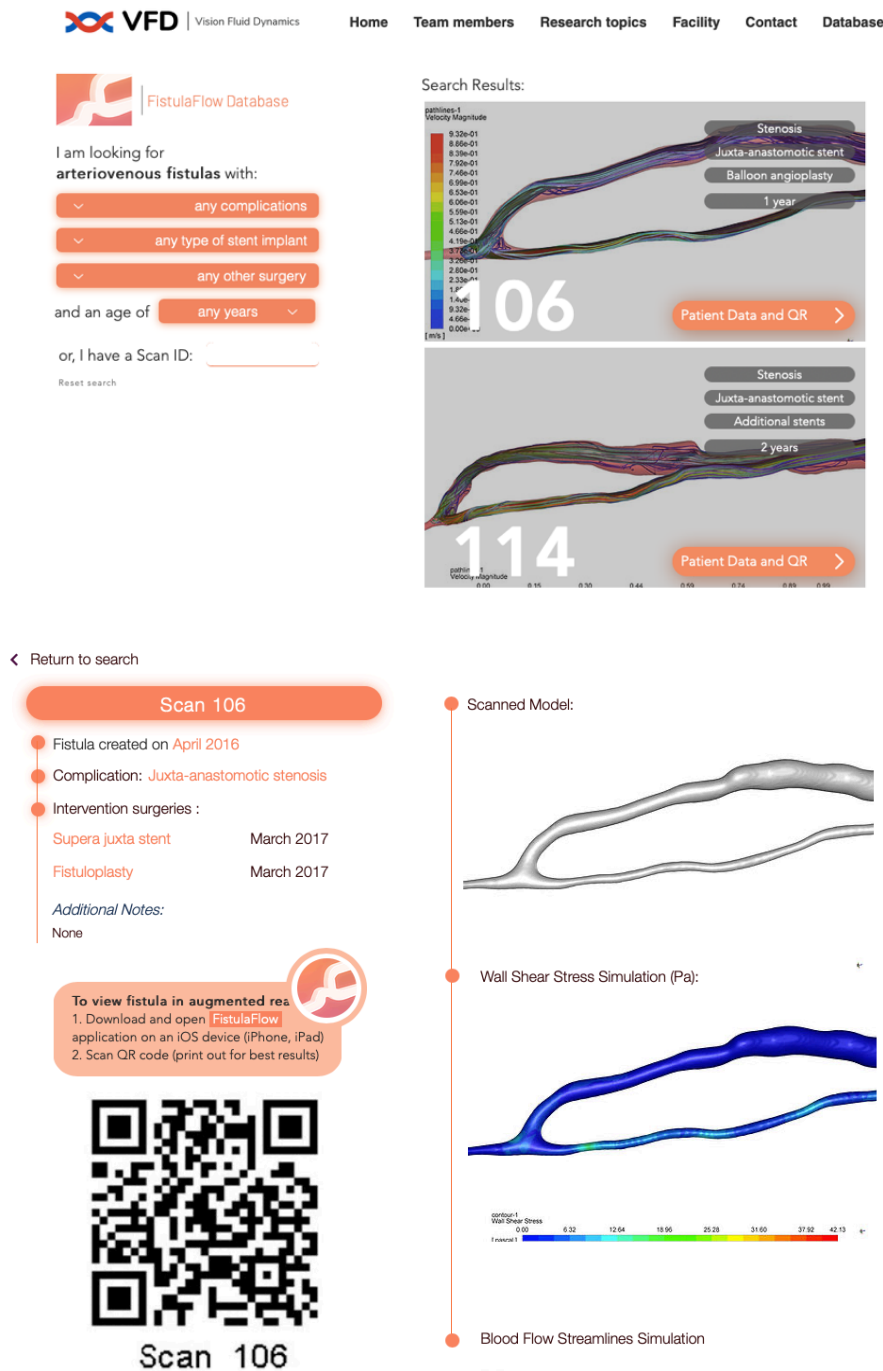


Figure 45: **(top)** Web database for the FistulaFlow application, accessible at <https://www.vfdunsw.com/fistula-scans> **(bottom)**. Example patient scan, information, CFD results and QR code for the FistulaFlow mobile application.

5. CFD-derived resistance in problematic AVFs identification

The mobile application can be downloaded to any smart device with a camera that allows QR code detection. This permits display of the patient anatomy and flow data in a real environment at any time (Figure 46). Besides providing better spatial awareness with regards to the cannulation zone of the AVF for nurses, the FistulaFlow mobile application platform also enables visualisation of the anatomy to identify potential problems for surgical intervention among vascular surgeons, and better self-care practices among the patients and their families.

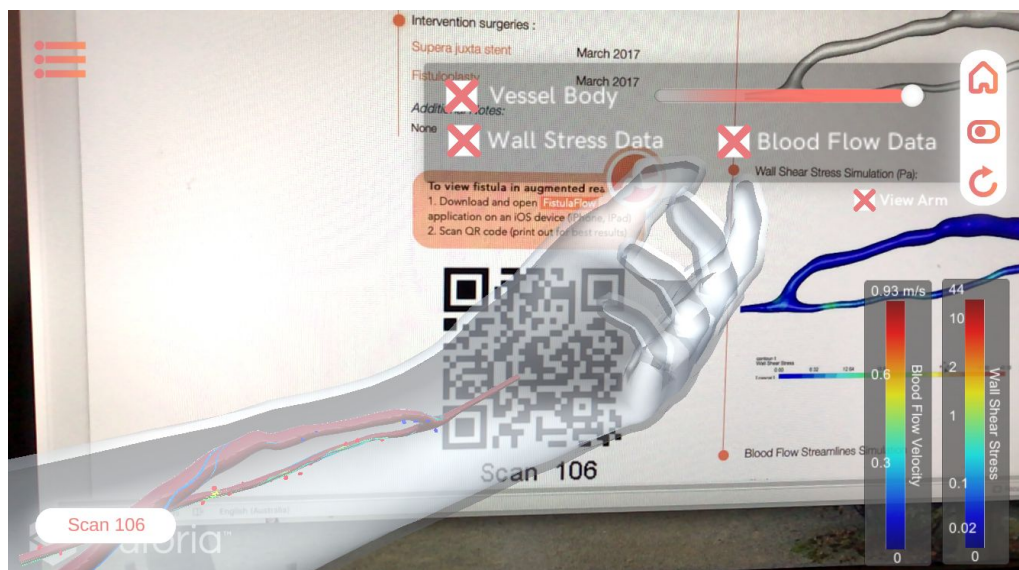


Figure 46: The user interface of the FistulaFlow mobile application platform in augmented reality: (**top right**) one can select or deselect any data of interest available; (**bottom left**) the patient ID, geometry and blood flow pattern specific to the AVF; (**bottom right**) Legend of blood flow velocity and wall shear stress [218].

5.10 Limitation

We recognise the limitations of the data size to this study – It was conducted at a single centre, with a retrospective design and has limited sample size. The patient population was a group undergoing juxta-anastomotic stenting, a procedure that showed promising outcome for its one-year primary patency rate [209], [219]. The reason for this choice was the ability to directly compare between problematic and healthy AVFs with this specific treatment. This also allowed verification of the CFD-derived resistance in its ability to detect problematic AVFs. The next chapter will discuss trends observed in patients with any intervention, and not limited to this treatment. Additional studies with multiple centres and prospective designs would give further weight to our findings that resistance measures are a useful tool to detect dialysis access circuit stenosis.

5.11 Conclusion

Results showed a 76% (21 – 99%) decrease in resistance at the PV, recorded after the juxta-anastomotic stenosis treatment. All resistance values in the PV segment of the treated patients remained low, post intervention. No correlation was reported between patency rate and resistance at the artery segment.

We observed a more prominent change in resistance values at the PV segment, compared to the PA segment, after surgical treatment, suggesting the association of resistance at the PV with the need for intervention. However, if the resistance is abnormally high regardless of the segment, the AVF should be examined, as there is a high likelihood that an intervention required. Furthermore, the overall resistance values along the entire AVF circuit provide a complete picture of the trend and status of patency. With the additional information, clinicians can be notified when a scan returns a higher-than-average resistance value, minimising the number of emergency intervention and thus improving the overall healthcare ecosystem.

CFD-derived resistance can be a promising metric to identify problematic AVFs and stenosis location. The development of this research has the objective to provide better care, identification of stenosis and disease diagnosis, especially for patients in remote areas who face immense challenges in accessing the right treatment [220]. The prospects of this technique are promising, by making use of the current data and in further refinement of the system to be more accessible and adaptable.

Chapter 6

Assessment of the suitability of CFD-derived resistance as a clinical indicator for AVF failure

The relationship between resistance and the likelihood of an intervention is further analysed in this chapter, using additional patient data that are not limited to the juxta-anastomotic stenosis treatment. A multilevel binary logistic regression was modelled with the eligible dataset to determine the odds of an intervention for a given resistance. The threshold for statistical significance was $P < 0.05$, with a 95% confidence level. This chapter serves as an exploratory analysis into the trends of resistance, and the chances of a required intervention and the clinical practicality of using resistance as a predictor beyond a specific patient group. Findings in this chapter were presented at the 26th Congress of Biomechanics at Milan, Italy in July 2021 [221].

6.1 Background

Stenosis, a narrowing of the vessel lumen as a result of intimal hyperplasia, is a common phenomenon seen in patients with an AVF, which reduces the ability of the patient to undergo haemodialysis [19], [22]. Physical examination such as inspection, palpation and auscultation [222], [223] are coupled with clinical imaging techniques such as angiography and ultrasound examinations to identify problematic AVFs. More recently, visualisation of the AVF, enabled by CFD modelling, found that disturbed, multidirectional and transitional turbulent-linked blood flow [35], [90], [102] were present in the AVF, especially at the anastomotic region, downstream of the PV segment. Different haemodynamic wall shear stress (WSS) parameters were used and correlated with AVF problems, but no significant association was identified between these parameters and stenosis prediction [39]. Therefore, there remains a need for identification of factors that may be used to predict the development of a stenosis and likelihood of an intervention.

In Chapter 5, the correlation of resistance at the PV segment with AVF patency rate was established by outlining patient cases in successful treatments, where stenosis was addressed at the juxta-anastomotic region. In the current chapter, all patient cases, including patients with a healthy AVF (no record of intervention, or healthy after an intervention), or requiring any sort of intervention to treat inflow or outflow stenosis (not limited to the juxta-anastomotic region) were investigated by a series of statistical models to evaluate the association between resistance and intervention.

6.2 Methods

6.2.1 Data Selection

A retrospective study of 46 patients (mean age 66.1, range 34 - 95, 33 males, 13 females), with a total of 83 examinations were used for this analysis. The selection criteria for this study are as follows:

1. Patients with radiocephalic AVF who underwent dialysis at the Prince of Wales Hospital Sydney Australia.
2. Patients with an arteriovenous graft, a brachial-cephalic AVF, or an AVF not used for dialysis were excluded from this study.
3. All patients were over 18 years of age.
4. All patient data was systematically reviewed to identify if an intervention was performed within the three months from when an examination was conducted.
5. Intervention was performed at the vein segment (PV) of the AVF.

The clinical characteristics for these patients are as shown in Table 16.

6.2.2 Patients' AVF geometry acquisition and data processing

Similar pipeline processes to those detailed in Chapter 3 were used to obtain the AVF geometry and CFD model for each patient. Average pressure changes from the anastomosis to 7.5 cm of the PV segment were calculated for the final (fourth) cycle once the simulation of four cardiac cycle was completed for all cases.

6. Assessment of resistance as a clinical indicator for AVF failure

Table 16: Baseline clinical characteristic for all patients examined

Variables	All patients (N = 46)
Age, y	66.1 \pm 11.8 (34.0 – 95.0)
Gender (male)	33 (72%)
Diabetes	27 (59%)
Smoking	15 (33%)
Hypertension	42 (91%)
High cholesterol	30 (65%)
Ischaemic heart disease	18 (39%)
Cerebral vascular accident	6 (13%)
Peripheral vascular disease	6 (13%)
Cause of renal failure	
Unknown	1 (2%)
Diabetes	24 (52%)
Glomerulonephritis	9 (20%)
Polycystic kidney disease	6 (13%)
Hypertension	5 (11%)
Lithium induced	1 (2%)

6.2.3 Definitions

The terms used throughout this chapter are defined as follows:

- A “scan” refers to an examination on the patient when patient geometry was acquired and modelled.
- “An intervention” is when a patient requires any surgical procedures such as balloon angioplasty, stent implantation or both, performed within three months from when the scan was taken.
- “Without intervention”, or “No intervention” is referred to a patient that did not require an intervention within the three months from when a scan was performed.
- “Resistance” used in this chapter refers to the calculated ratio of pressure to flow rate (Chapter 3, Section 3.6) and does not represent the peripheral or systemic vascular resistance in the circulatory system.

6.3 Statistical Analysis

Subjects are divided into two groups, those with intervention and those without intervention.

A multilevel binary logistic regression model (mixed-effect model) was fitted to estimate the odds or probability of an outcome (also referred as “intervention”). Then, the receiver operating characteristic (ROC) curve was used to estimate the diagnostic ability of the model.

6.3.1 The multilevel logistic regression model

A logistic regression model can be used to estimate the probability of an outcome of a binary response (“1” or “0”), that is whether or not a given patient will need to undergo an intervention within the next three months. Hence, the likelihood of having an intervention of a binary outcome is represented with a logistic function [224], [225].

For a logistic distribution, $E(Y|x)$ denotes the conditional probability of Y, given x, and the logistic regression model used is given as follows [224], [225],

$$E(Y|x) = \frac{\exp(\beta_0 + \beta_1 x)}{1 + \exp(\beta_0 + \beta_1 x)} \quad \text{Eq. 24}$$

The logit transformation of Eq. 24 is given as:

$$\text{logit} = g(x) = \ln \left[\frac{E(Y|x)}{1 - E(Y|x)} \right] = \beta_0 + \beta_1 x \quad \text{Eq. 25}$$

6. Assessment of resistance as a clinical indicator for AVF failure

Given that there were repeated observations of the same patients in this dataset, the assumption of independence and the outcome to be continuous of a linear model were not adhered to here [226]. For this reason, a multilevel regression model (mixed model) was adopted to provide flexibility to assess repeated, clustered or correlated data, such as clinical data used in this thesis [224], [227]–[231]. The association of an intervention of a particular AVF for a given resistance value was calculated based on all patient data collected.

The multilevel logistic regression (mixed-effect binomial logistic regression) model considers a fixed effect, that is resistance, and the random effect, that is the patient that is associated to a particular patient (cluster), illustrated in Figure 47.

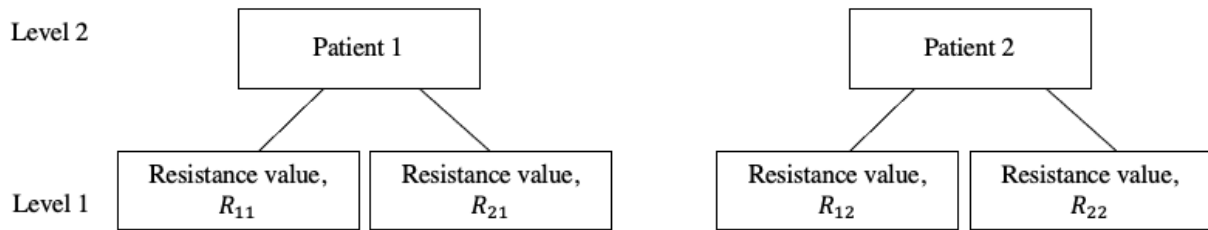


Figure 47: Illustration of the relationship between Level 1 predictor (fixed effect), that is resistance and the cluster (random effect), that is the different patient. A patient can have multiple resistance values based on the scan taken. Graphical illustration reproduced from [231].

The multilevel regression model used in this thesis is given as [224], [225]:

$$E(Y_{ij}|R_{ij}) = \frac{\exp(\beta_{0j} + \beta_1 R_{ij})}{1 + \exp(\beta_{0j} + \beta_1 R_{ij})} \quad \text{Eq. 26}$$

where

$$\beta_{0j} = \gamma_{00} + \mu_{0j} \quad \text{Eq. 27}$$

6. Assessment of resistance as a clinical indicator for AVF failure

By combining Eq. 25 – Eq. 27, the logit transformation of this multilevel regression model is given as,

$$\text{logit}_{ij} = \gamma_{00} + \mu_{0j} + \beta_1 R_{ij} \quad \text{Eq. 28}$$

where

subscript i refers to observation of individual resistance values (level 1)

subscript j refers to the cluster, that is the individual patients (level 2)

$Y_{ij} = 1$ denotes the conditional probability that the patients will need to undergo an intervention i.e the outcome of the i^{th} observation for the j^{th} individual (cluster)

R_{ij} denotes the observed value of the predictor variable, resistance

γ_{00} denotes the overall intercept

$u_{0j} \sim N(0, \sigma_{0j}^2)$ denotes the random effect, where σ_{0j}^2 denotes the variance of the random effect, that is the deviation of the j^{th} group (cluster) from the fixed intercept in a normal distribution

The `glmer` function was used under the `lme4` package in R [232]. Logit link function was used to evaluate the binary outcome of this model in a linearised scale, of a probability of an outcome to be between 0 and 1. The `glmer` function fits a generalised linear mixed-effects model with a response of the outcome, that is the intervention information. More details on this model can be found in Appendix 6A.

6.3.2 Receiver operating characteristic (ROC) analysis

The receiver operating characteristic (ROC) graph provides information about the performance and diagnostic ability of a model [233], [234] and is widely used in clinical data for trials and risk models to assess the ability to discriminate between the likelihood of a named outcome such as death or survival [235]–[238]. It illustrates the specificity and sensitivity of a diagnostic test across a spectrum of possible cut-off points [236]. In other words, it is a summary of the overall diagnostic accuracy.

The ROC analysis was conducted with the pROC package in R [233]. It is used to assess the trade-off between false positive, that is predicting that an individual will have an intervention, but they do not; and false negative, that is prediction that an individual will not have an intervention but they do. The y-axis of a ROC curve represents the sensitivity (true positive rate), that is predicting whether an individual will have an intervention, while true negative rates (specificity) or false positive rates ($1 - \text{specificity}$), are represented and shown on the x-axis of the ROC curve. The 2 x 2 confusion matrix of a generic classifier table and its definitions can be found in Appendix 6B.

The area under curve (AUC) is a measure of discrimination of a particular classification [234]. The AUC and ROC analyses are insensitive to an unbalanced dataset for two groups (or classes), like most clinical data. This enables ranking of a randomly given observation based on the ordering of the predicted probability, and the ability of the classifier to separate the two classes, in this case whether an intervention will be required. The AUC values range from 0.5 to 1, where a value of 1 indicates a perfectly accurate outcome, and 0.5, represented by the diagonal line of the ROC graph, indicates random discrimination. The general rules to assess the ROC graph based on the AUC values are shown in Table 17 [239].

6. Assessment of resistance as a clinical indicator for AVF failure

Table 17: General guideline in assessing the diagnostic ability of a test based on the AUC values in a ROC graph

$ROC = 0.5$	No discrimination (diagonal line observe in the ROC graph)
$0.5 < ROC < 0.7$	Poor discrimination
$0.7 < ROC < 0.8$	Acceptable discrimination
$0.8 < ROC < 0.9$	Excellent discrimination
$ROC \geq 0.9$	Outstanding discrimination

6.4 Resistance range

The boxplot, as shown in Figure 48 outlines the overall statistical distribution of data from all patient scans, at both segments of the AVF (PV and PA). A systematic review of intervention information was obtained for each patient based on the selection criteria outlined in Section 6.2.1. A patient who had an intervention was classified and labelled as “1”, and “0” represents patients who did not require an intervention. Descriptive statistics of resistance values based on the two groups are outlined in Table 18.

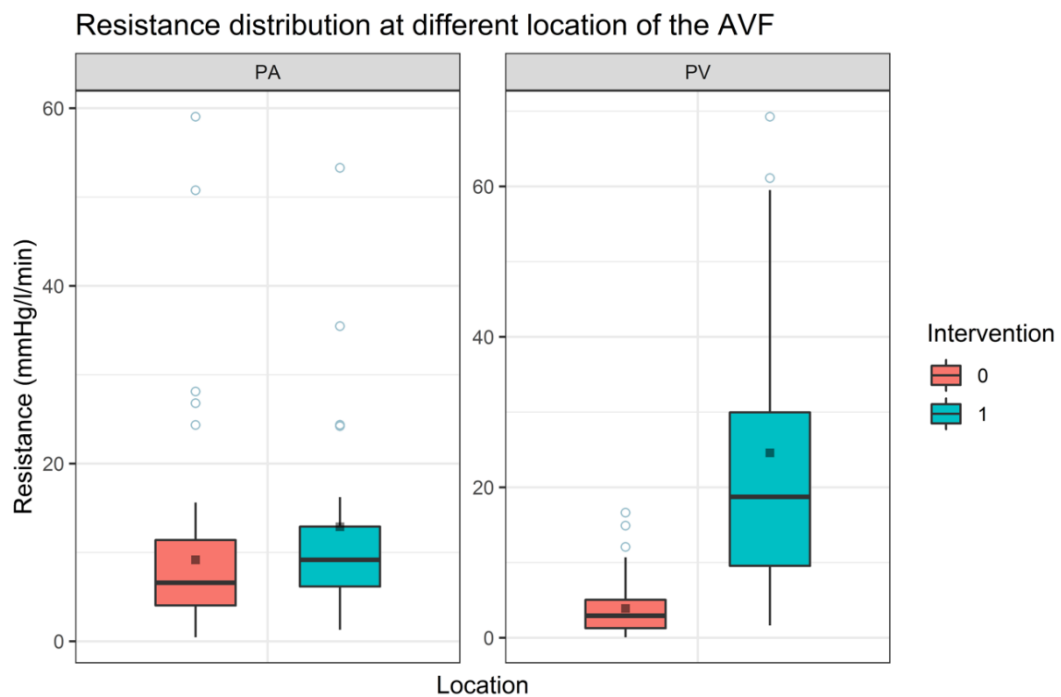


Figure 48: The range of resistance with patients of with intervention (labelled as "1") and without an intervention (labelled as "0") at PA and PV of the AVF. Shaded (grey) squared points represent mean values. Outliers are labelled as blue circles outside of the range of the boxplot.

6. Assessment of resistance as a clinical indicator for AVF failure

Table 18: Descriptive statistics of the resistance data at the PA and PV for the two different groups (intervention and no intervention). Units: mmHg/l/min

Location	PA		PV	
Group	No	Intervention	No	Intervention
	(“0”)	(“1”)	(“0”)	(“1”)
Interquartile range	7.4	6.8	3.8	20.4
Lower quartile	4.0	6.2	1.3	9.6
Upper quartile	11.4	12.9	5.0	30.0
Median	6.6	9.2	2.9	18.8
Mean	9.2	12.9	3.9	24.6
Maximum	59.0	53.3	16.6	69.3
Minimum	0.5	1.3	0.1	1.6

6.4.1 Vein segment (PV)

At PV, the two groups (with or without intervention) have a distinct resistance range given that the median and interquartile range do not overlap (Figure 48). This supports findings in Chapter 5, where changes in resistance at the vein segment (PV) played a more influential role in determining AVF patency for patients who had undergone juxta-anastomotic stent for stenosis treatment. The Welch two sample t-test [240] of these two groups gave a *P*-value of 0.00014 (less than 0.05), deeming the difference between the two groups to be statistically significant.

6.4.1.1 Group Classification: Intervention (“1”)

The interquartile range of patients who lie within the group of patient resistance values at the PV segment for the group of patients with an intervention is 20.4 mmHg/l/min, with a lower quartile value of 9.6 mmHg/l/min and upper quartile value of 30.0 mmHg/l/min. The median, which is the midpoint of the data is 18.8 mmHg/l/min. The maximum value, excluding outliers is 69.3 mmHg/l/min. The maximum and minimum resistance values of this group of patients are 69.3 and 1.6 mmHg/l/min respectively. The mean resistance value of this group is 24.6 ± 19.5 mmHg/l/min.

6.4.1.2 Group Classification: No Intervention (“0”)

The interquartile range of patient resistance values who lie within the group of patients without an intervention is 3.9 mmHg/l/min, with a lower quartile value of 1.3 mmHg/l/min and upper quartile value of 5.0 mmHg/l/min. The median value is 2.9 mmHg/l/min. The maximum and minimum resistance values of this group of patients are 16.6 and 0.1 mmHg/l/min respectively. The mean value is 3.9 ± 3.6 mmHg/l/min. The overall data for this group ranges from 0.1 – 10.7 mmHg/l/min. As compared to the group outlined in Section 6.4.1.1, the group with no intervention shows a less disperse dataset and a smaller range of resistance values.

6.4.2 Artery segment (PA)

The Welch two sample t-test for the two groups (with or without intervention) resulted in a *P*-value of 0.25, more than 0.05, leading to conclude that the difference between the two groups is statistically insignificant. Minimal association can be drawn between resistance at the artery segment (PA), and the chances of intervention.

6.4.2.1 Group Classification: Intervention (“1”)

This group had an intervention within three months from when the scan was performed. The interquartile range of this group's resistance values is 6.8 mmHg/l/min, with a lower quartile

value of 6.2mmHg/l/min and upper quartile value of 12.9 mmHg/l/min. The range of this dataset is 1.3 – 53.3 mmHg/l/min, with several outliers as indicated in Figure 48.

6.4.2.2 Group Classification: No Intervention (“0”)

The interquartile range of this group (located at the PA, and had no intervention performed) is 7.4 mmHg/l/min, with a lower quartile of 4.0 mmHg/l/min and upper quartile of 11.4 mmHg/l/min. The range of this data is 0.5 – 59 mmHg/l/min. Similar to the previous group, there were some outliers.

6.4.3 Outliers

Statistically, outliers are identified as datapoints with values that are 1.5 times the interquartile range, from the lower and upper quartile. Two outliers were identified in the group of patients who had an intervention, and three outliers were identified in the group of patients without an intervention at the PV segment (Figure 48).

Two (ID 4 and ID 62) out of the three outliers in the no-intervention group had an intervention one month prior to when the examination was done. Patient ID 4 had a stenting procedure three weeks prior to the previous scan, while Patient ID 62 had a balloon angioplasty performed four weeks before the scan. There was a likelihood that the vessels were still adapting post-surgery [241] as three other scans of Patient ID 4 showed subsequent decrease of resistance to within the range. Although demonstrating a higher-than-average resistance at the PV, no issues were reported on ID 77.

With regards to the intervention group, the two outliers were from the same patient (ID 8), both outside the resistance range of the average patient in the group. In the context of this study, any patients above the benchmark resistance value were concluded to have a risk and thus required intervention.

6.5 Association of resistance with an outcome (intervention)

The distribution of the data for the resistance calculated at both PA and PV is illustrated on a marginal distribution plot in Figure 49. The histogram along the horizontal axis corresponds to the resistance at the PA, while the histogram along the vertical axis corresponds to the resistance at the PV.

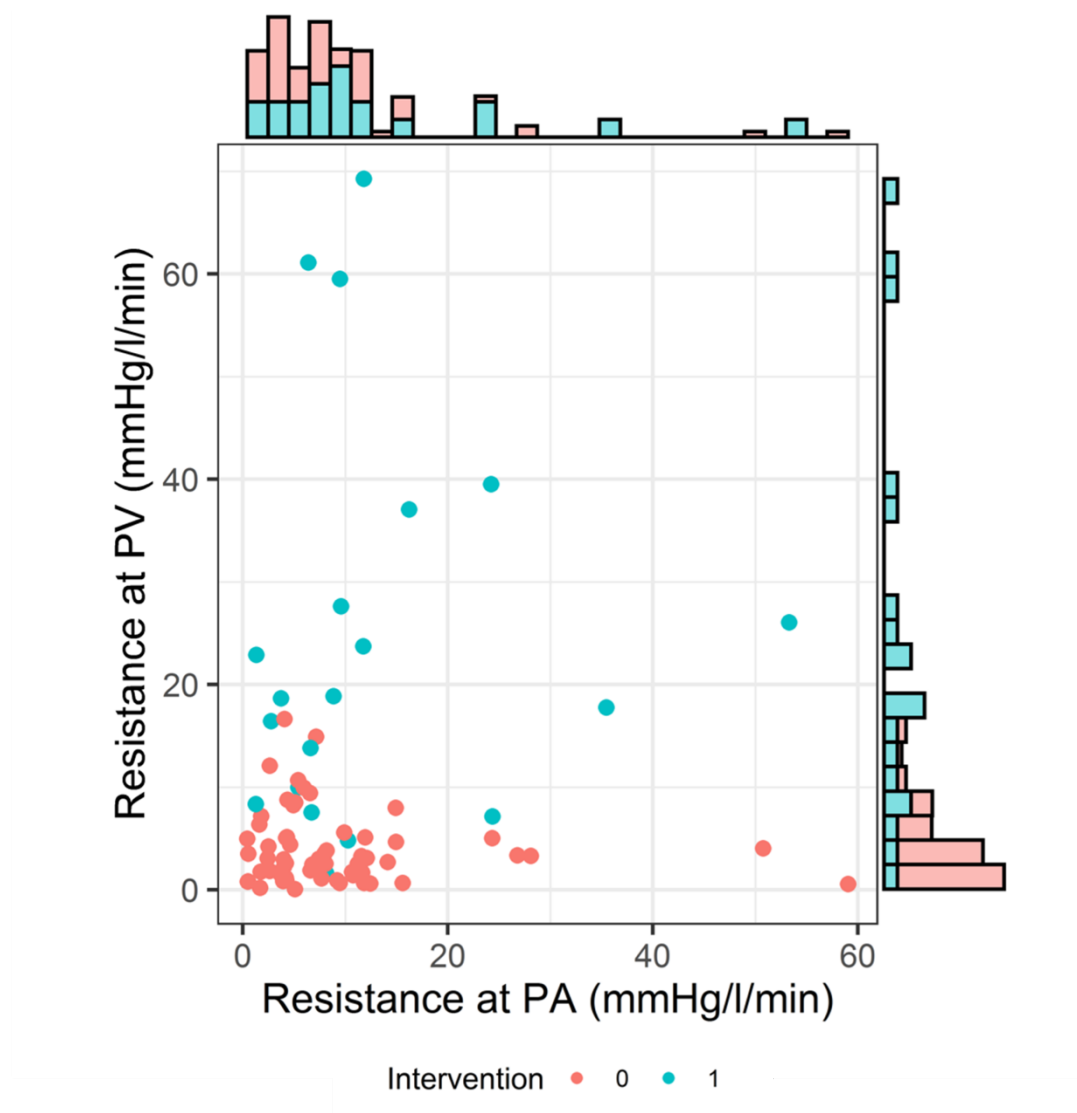


Figure 49: Marginal distribution plot of resistance calculated for eligible patient data. The intervention group are distinguished by colour: with an intervention denoted as “1”, and without intervention denoted as “0”. The histogram on the top corresponds to the frequency distribution of resistance at the PA, while the histogram on the right corresponds to the frequency distribution of resistance at the PV.

6. Assessment of resistance as a clinical indicator for AVF failure

At the PV, 94% of patients who did not have an intervention (59 out of 63) were shown to have resistance of less than 10mmHg/l/min, while 6% have resistance of more than 10 mmHg/l/min. Furthermore, as observed in the histogram of the marginal distribution plot (Figure 49) the patients with no AVF-related issues were found to be on the lower spectrum (of the vertical axis) as opposed to patients who had an intervention. For the group of patients who had an intervention, 70% had resistance of more than 10 mmHg/l/min, while 30% had resistance values below that.

At the PA, there were no definitive trends for patients with or without an intervention and without an intervention. 60% of patients from the group that had an intervention recorded a resistance of less than 10, while 40% of patients found to have a resistance more than 10 mmHg/l/min. On the other hand, 70% of the patients without an intervention recorded a resistance of less than 10mmHg/l/min, while 30% presented otherwise.

Based on Figure 49, patients with higher resistance at the PV were found to be associated with the “intervention” group as compared to patients with a higher resistance at the PA. If closer attention was paid to the lower half of the spectrum of the vertical axis (i.e. Resistance at PV < 10 mmHg/l/min) in the scatter plot, the majority of patients were found to not have an intervention, However, this patient group was shown to have resistance that spreads across the horizontal axis, with resistance at the PA to range between 0 – 60 mmHg/l/min. In other words, a lower PV value was demonstrated to be a common factor in this classified group, regardless of what the resistance value is at the PA.

Resistance at the PV segment of the two groups (with or without intervention) show distinctions based on the statistical description, illustrated in boxplots (Figure 48) and the marginal distribution graph (Figure 49). This data will hence form the basis of the multilevel regression model to estimate the association between resistance and the likelihood of an

6. Assessment of resistance as a clinical indicator for AVF failure

intervention. Estimates from the fixed effect of this multilevel binary logistic regression model are outlined in Table 19 which includes the association between resistance and the risk of an outcome. The intercept, β_0 represents the estimated mean outcome without a predictor, or the baseline logit, which was -4.54. The coefficient estimates, β_1 was 0.35, representing the relationship between the predictor variable, resistance, and the outcome. Exponentially, the odds of an outcome is 1.42. The variance estimates from the random effect, σ_{0j}^2 , was 1.30. Each cluster deviates with a variance of 1.30 from the mean estimate of the random intercept.

Table 19: Estimates from the multilevel logistic regression model, the effects of the fixed effect on the multilevel logistic regression model. Odds ratio is represented in exponential term.

Predictors	Coefficient	Standard error	Odds Ratio	P-value
(Intercept)	-4.54	1.45	0.01	0.002
Resistance	0.35	0.12	1.42	0.004

The logistic regression fitted curve for the multilevel binary logistic regression model based on this dataset was shown in Figure 50. Patient examination data that fulfills the selection criteria and is usable for this thesis is represented with the coloured bars shown along the x-axis of the plot of Figure 50. The fitted logistic regression curve also showed good correlation with our observation in the clinic patients scans, denoted with the pink rugs shown along the x-axis. Most clinical data for resistance that ranges from 0 – 10 mmHg/l/min consists of patients who did not have an intervention. As for patients with resistance that ranges from 10 – 20 mmHg/l/min, there are a mix of patients who require or did not require an intervention, seen in the division of the coloured bars that represents the group with an intervention (turquoise bars) and without and intervention (pink bars). The mixed clinical observations are attributed to the uncertainties seen for prediction within this resistance range, denoted by the larger shadowed region which represents the confidence interval.

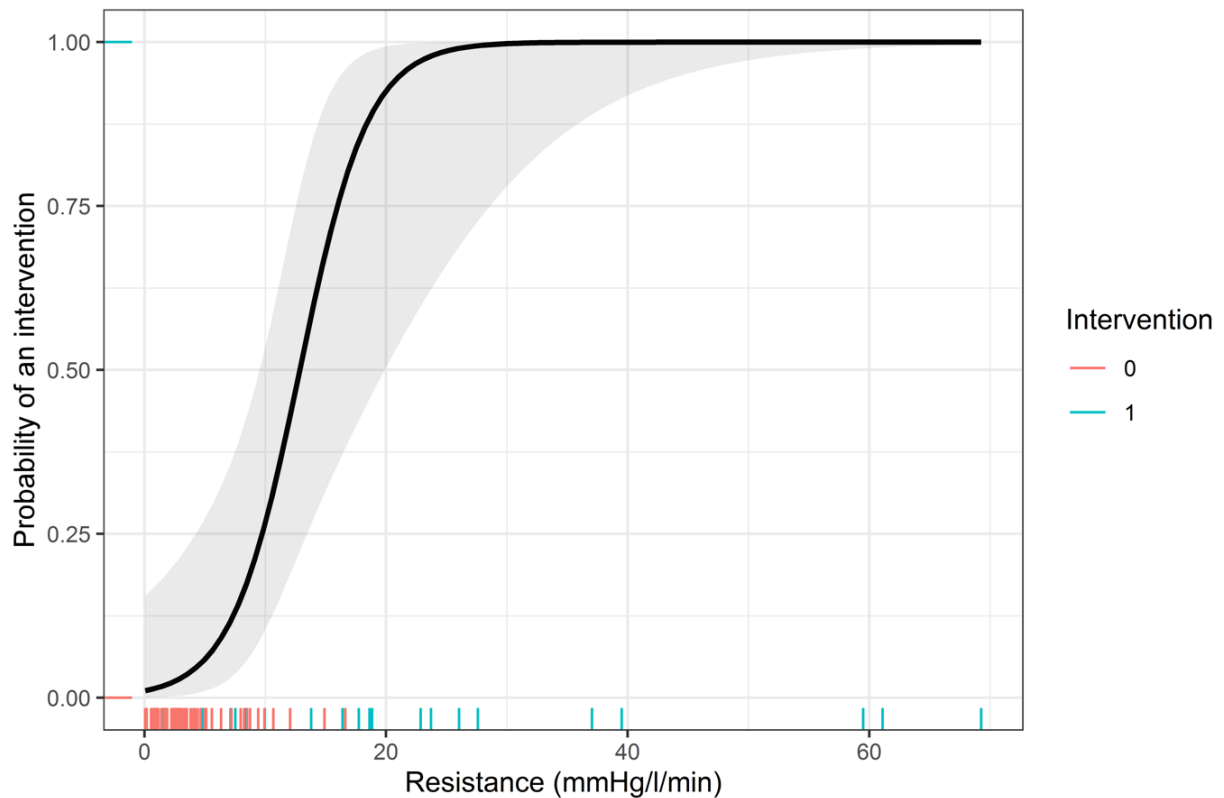


Figure 50: The logistic regression fitted curves the represents the fitted probability of an intervention for a given resistance of a mixed-effects logistic regression model. The shaded area depicts the uncertainty in that prediction based on the confidence interval limit. The rugs represents the dataset collected, and intervention, “1” and no intervention “0” group are distinguished by colour, per the legend.

Table 20 indicates the probability of an intervention based on a given resistance at the PV. For the resistance range of 0 – 10 mmHg/l/min, there is a 25% chance that the AVF will need an intervention. The risk of an intervention increases exponentially from 10 – 20 mmHg/l/min, with a probability of $25\% \leq P \leq 90\%$. The confidence interval, largest at 15 – 30 mmHg/l/min indicates the uncertainty of the estimates in this region, and that the probability of an intervention might vary for different patients. An AVF that has a resistance of beyond 20 mmHg/l/min has a very high likelihood of an intervention, with a probability of more than 90%. Table 20 summarizes findings from the multilevel logistic regression model.

6. Assessment of resistance as a clinical indicator for AVF failure

Table 20: Summary results from the multilevel binary logistic regression model

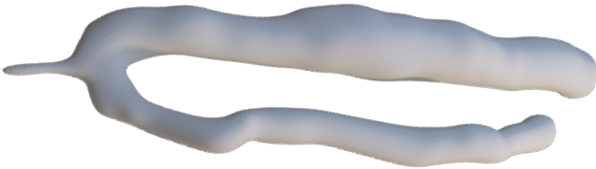

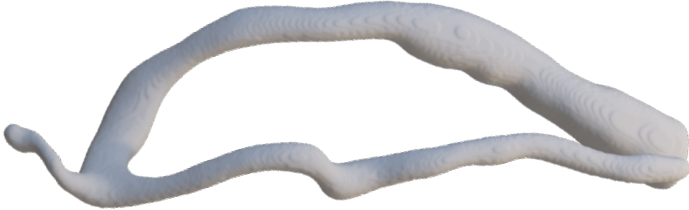


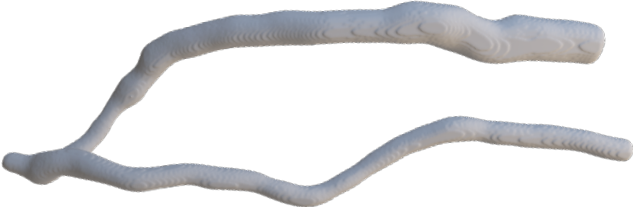
Resistance range	Likelihood of an intervention	Category
0 – 10 mmHg/l/min	25%	Low
10 – 20 mmHg/l/min	25 – 90 %	Medium/High
> 20 mmHg/l/min	90%	High

6.5.1 AVF geometrical configuration

Geometries of AVFs (Geometries A – F) that are identified as outliers based on clinical observations, that is patients who had an intervention, but have a range of resistance of 0 – 10 mmHg/l/min are tabulated in Table 21. Geometries of AVFs (Geometries I – V) for patients who do not require an intervention but have resistance that ranges from 10 – 20 mmHg/l/min are tabulated in Table 22. The ones (Geometries 1 – 5) who had an intervention and have resistance values that ranges from 10 – 20 mmHg/l/min are tabulated in Table 23. There was a mix of AVFs with acute and obtuse anastomotic angles, and high vein to artery diameter ratio for geometries included in Table 21 and Table 22. An acute anastomotic angle is a common observation for AVF geometries of patients requiring an intervention, where resistance in the range of 10 – 20 mmHg/l/min, as seen in Table 23. This is expected because an acute anastomotic angle was previously found to increase flow disturbance at the region [39]. Given a substantial proportion of patients (four out of the six patients shown in Table 21) who had an intervention and showed resistance values of more than 5 mmHg/l/min, a more systematic approach of determining the cut-off point for resistance based on different thresholds was deemed necessary and will be further expounded in Section 6.6.

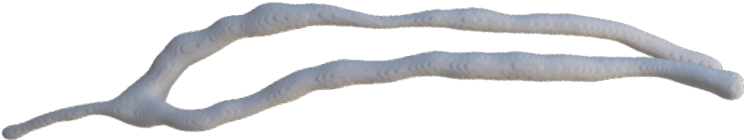

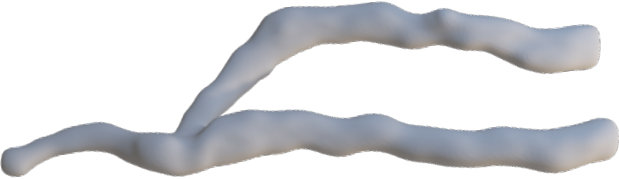

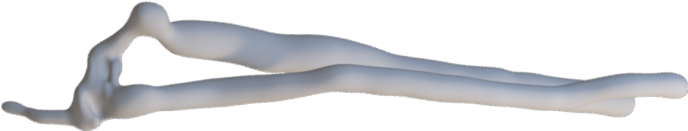
6. Assessment of resistance as a clinical indicator for AVF failure

Table 21: Outliers- AVF that had an intervention and have a resistance in the range of 0 -10 mmHg/l/min

	AVF Geometry	Resistance at PV (mmHg/l/min)
A		1.6
B		4.8
C		7.1
D		7.5
E		8.3
F		10.0

6. Assessment of resistance as a clinical indicator for AVF failure



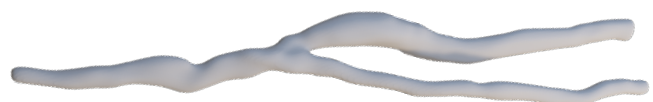
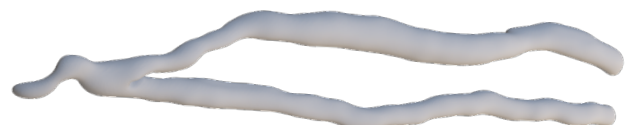
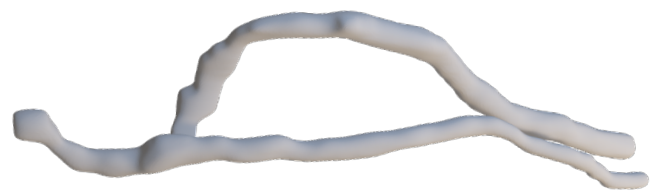
Table 22: Outliers: AVF that had no intervention and are in the range of 10- 20 mmHg/l/min

AVF Geometry	Resistance at PV (mmHg/l/min)
I	9.9
	
II	10.7
	
III	12.1 *
	
IV	14.9 *
	
V	16.6 *
	

* are identified outliers in the boxplot (Figure 48), in which the range of R is 1.5 times the IQR

6. Assessment of resistance as a clinical indicator for AVF failure

Table 23: AVF that had an intervention and are within the resistance range of 10-20 mmHg/l/min

	AVF Geometry	Resistance (mmHg/l/min)
1		13.8
2		16.4
3		17.8
4		18.6
5		18.9

6.6 Diagnostic ability of the model

The ROC curve (Figure 51) illustrates the ability of a multilevel regression risk model (Section 6.4), to discriminate between an intervention or no need of an intervention by providing a binary decision for each probability classification. The AUC for this model is 0.921, with a 95% confidence interval of sensitivity found to be (0.844 – 0.999). This suggests that there is a 92.1% (84.4% - 99.9%) chance that the resistance can correctly discriminate the chances of an intervention for a patient.

A resistance of 6.7 mmHg/l/min was the optimum cut-off point shown in Figure 51, with a sensitivity of 90% and specificity of 83%. There is a 90% chance that the prediction for an intervention at the particular resistance is a true positive, and a 17% chance that it is a false positive (predicted to have an intervention, but no intervention is required). Whilst the true positive rates and false positives rates are important for clinicians, the false negatives rate are equally essential. Clinicians will have to bear more cost with false negatives as compared to false positives, as the likelihood of an emergency intervention is higher for a false negative outcome.

The sensitivity, specificity, false negative rates, and false positive rates based on the threshold of different resistance values were examined, as tabulated in Table 24. The probability of an intervention increases with the increase in resistance. True positive rates decrease with an increase in resistance, while true negative rates increase with an increase in resistance. When resistance increases, the ability to discriminate a true positive of an outcome (an intervention) decrease, that is the likelihood of a correct discriminate of a true negative (no intervention) is higher. On the contrary, the likelihood of an accurate discriminate for a true positive (an intervention) is higher with the increase in resistance.

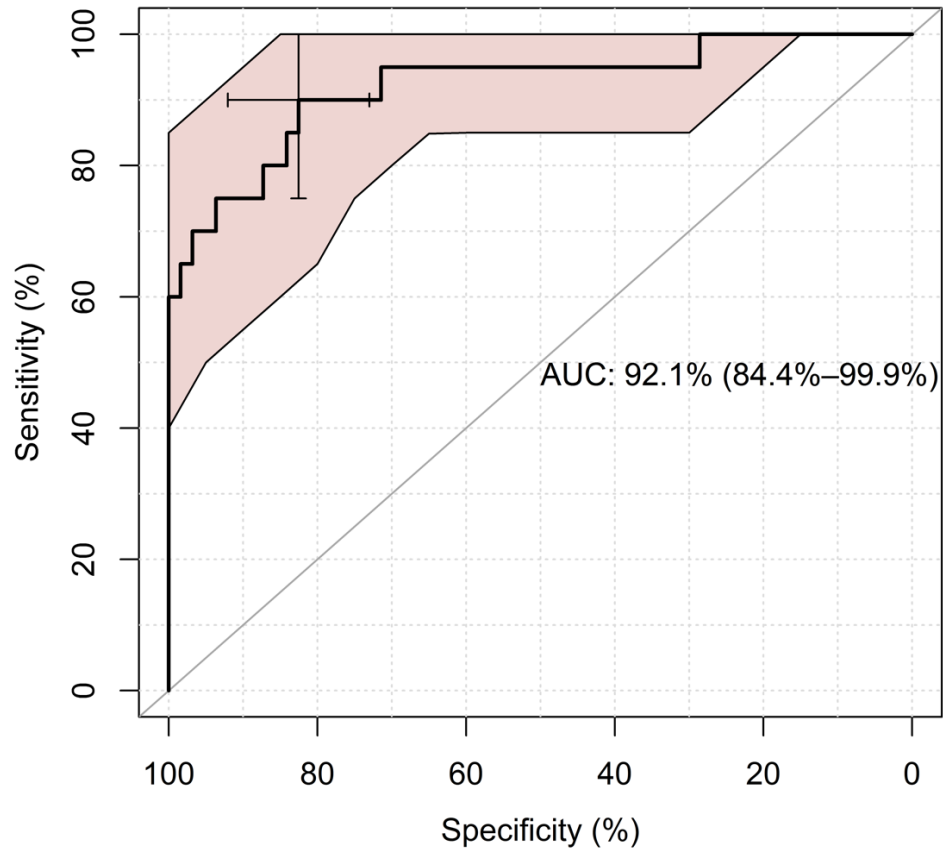


Figure 51: The ROC graph used to illustrate the diagnostic ability of the multilevel regression model. The AUC of this ROC curve is 92.1%, with a 95% confidence interval of sensitivity of 84.4 % to 99.9%. The threshold that has optimum sensitivity (90%) and specificity (83%) is when resistance is at 6.7 mmHg/l/min (labelled with the black cross)

6. Assessment of resistance as a clinical indicator for AVF failure

Table 24: True positive rates (sensitivity), true negative rates (specificity), false negative rates (1- sensitivity) and false positive rates (1- specificity) of different resistance with confidence interval in bracket if applicable

Threshold	Sensitivity	False negative rates	Specificity	False positive rates
resistance value	(%)	(%)	(%)	(%)
(mmHg/l/min)				
2.5	95	5	41	59
	(85 – 100)		(29 – 54)	
5.0	90	10	73	27
	(75 – 100)		(62 – 83)	
6.5	90	10	83	17
	(75 – 100)		(73 - 92)	
7.5	85	15	84	16
	(65 – 100)		(75 – 92)	
10.0	70	30	94	6
	(50-90)		(87 – 98)	
15.0	65	35	98	2
	(45 – 85)		(95 -100)	
20.0	45	55	100	0
	(25 – 65)			
30.0	25	75	100	0
	(5 – 45)			
40.0	15	85	100	0
	(0 – 30)			

6.7 Clinical relevance

Using CFD-derived resistance values to predict AVF failure shows potential for clinical use. The streamlined, non-invasive process of visualising AVF geometry and deriving resistance values will enable clinicians to identify dysfunctional AVF that affect the patient's dialysis circuit. There is potential to enhance pre-surgical planning using additional information on an AVF (three-dimensional geometries and AVF status). Thus, resistance values derived from CFD modelling serve as a single static value and show strong correlation with not only the probability of an intervention, but also AVF patency information.

6.7.1 Comparison of individualised resistance values and the effect of different individuals

The degree of dependency of observations within a cluster can be measured by calculating the intraclass correlation (ICC) Eq. 29 [231], [242]:

$$ICC = \frac{\sigma_{0j}^2}{\sigma_{0j}^2 + \left(\frac{\pi^2}{3}\right)} \quad \text{Eq. 29}$$

where

σ_{0j}^2 refers to variance estimate for random effect

$\left(\frac{\pi^2}{3}\right)$ refers to the standard logistic distribution, the assumed level-1 variance component

ICC ranges from 0 to 1, with 0 indicating total independence of cluster, that is, there is no intra-cluster variation and the chances of an intervention do not differ from one patient to another; and 1 is total interdependence of residuals, that is, the chances of an outcome only vary intra-cluster (no inter-cluster variation), where a patient will either have an intervention or do not have one, regardless of the observation. The ICC for this model is 0.28, indicating that there is

6. Assessment of resistance as a clinical indicator for AVF failure

a 28% chance of intervention between patients, and 72% chance of intervention or not regardless of patients. The relatively low ICC value indicates the low dependency of observation within a cluster, suggesting a stronger effect of an outcome due to the difference in resistance rather than different cluster (individuals).

In order to better measure the impact of the cluster (individuals) in the model, a comparative analysis of variance in outcome between clusters (individuals) and variance of outcome due to the differences in resistance was conducted. The variance of the random effect for this model is 1.30 based on the random effects as per Section 6.5. This is an estimation of how far below and above the chosen individual lies from the average curve. To visualise the effects of this variance, hypothetical patients were randomly generated from R. Random variables were produced from the normal distribution, $X \sim N(0, \sigma_{0j})$, where σ_{0j} is 1.14, representing the standard deviation of the random effect. Eighty hypothetical individuals were generated, with a variance of random effect that ranges from 3.04 to 3.77. Each hypothetical individual has a different intercept, β_{0j} , by varying variance of random effect, μ_{0j} (hypothetical patients) from Figure 52.

The relationship between resistance and the probability of an intervention for a given individual's random effect are represented by the blue lines shown in Figure 52. Given that the variance is relatively small, predictions made from the variance of hypothetical patients tend towards the average fitted prediction, shown by black line in Figure 52. The small variability between patients also suggests that resistance at the PV segment is a dominant predictor regardless of the patients. For instance, for two individuals with a given resistance at the PV, the variability in likelihood of an outcome (intervention) is small. Therefore, regardless of the individuals existing risk factors or prior surgical interventions, one could deduce the probability of an outcome with the individual's resistance value.

6. Assessment of resistance as a clinical indicator for AVF failure

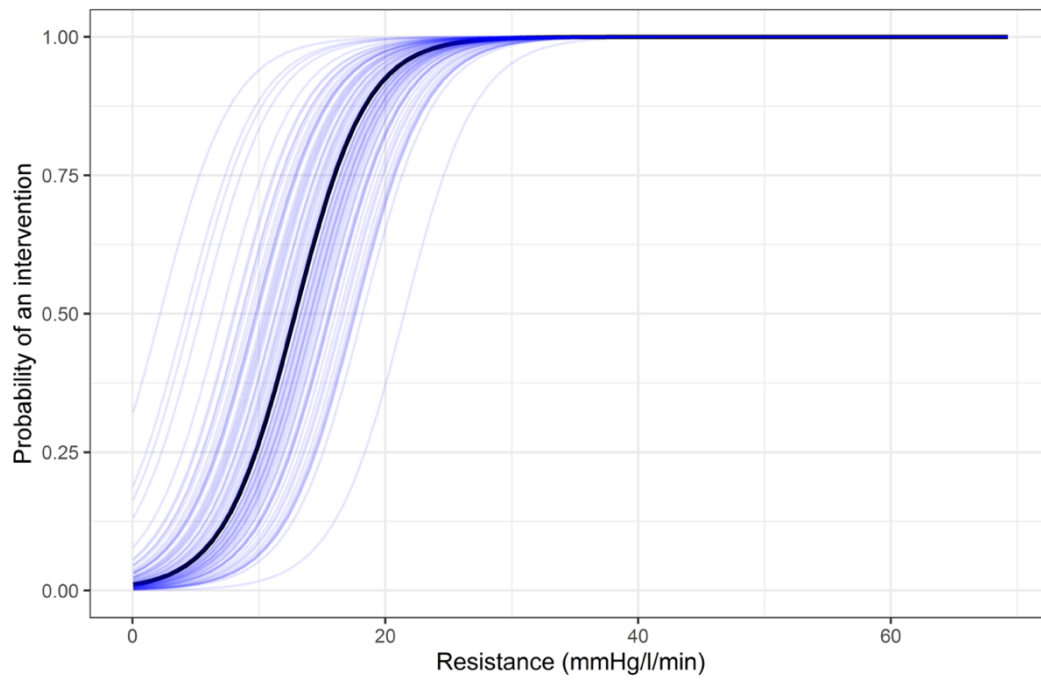


Figure 52: Association of resistance and the fitted probability curve for randomly generated variance of hypothetical individuals. Blue lines represent the fitted curve produced from the randomly generated hypothetical patients, and the black lines represent the average fitted prediction curve from our dataset.

6.7.2 Other comorbidities

The relationship of other predictors (comorbidities) and the probability of an intervention of these patients was examined with the multilevel regression model. A similar approach was adopted, where the other variables were set as fixed effects, and the patient ID was the random effect. Data that are not continuous were converted to binary data for this modelling. Other comorbidities were not statistically significant, with a P -value of more than 0.05 for all of these variables as shown in Table 25. Resistance at the PV segment was shown to be the dominant predictor as compared to the rest, as outlined in the previous sections, with a P -value of 0.004, indicating statistical significance.

Table 25: Relationship of other variables and the probability of an intervention

Variables	P -values	Estimates
Resistance (PA)	0.21	0.03
Age	0.33	0.03
Diabetes	0.52	0.36
Smoking	0.96	0.03
HTN	0.96	-0.06
High Cholesterol	0.69	0.23
CVA	0.43	0.54
PVD	0.96	0.05

6. Assessment of resistance as a clinical indicator for AVF failure

An assessment of several continuous variables, namely the patient's age and resistance at the PA segment was conducted with the core predictor, resistance at the PV segments. The ROC analysis showed that age of the patient and resistance at the PA segment appear to have poor diagnostic ability, seen in Figure 53, with an AUC of 0.576 and 0.606 respectively.

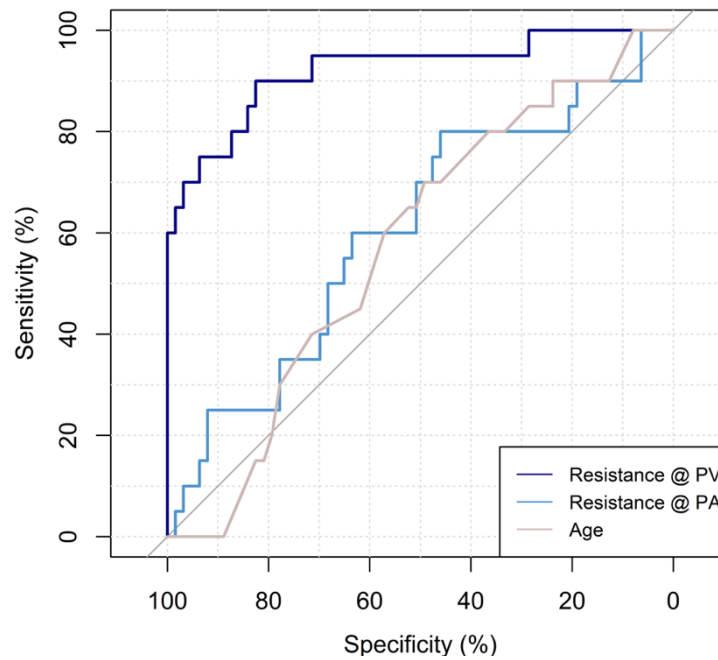


Figure 53: ROC graphs of continuous variables such as resistance at the artery segment and age of the patient

6.8 Limitation and future recommendations

We acknowledge the limitations of this study to only one single research centre with a limited patient sample size. Future studies that cover a larger demographic would add more value to this work and reduce selection bias and overfitting of data. Furthermore, a larger dataset with more dialysis centres will enable a more versatile and adaptable model that can be used independently in different centres prospectively. Besides, the use of CFD-derived resistance as a predictive indicator for AVF failure considers the association between resistance and an intervention, regardless of the time when the AVF was created or the amount of time until an intervention happens. Further analysis considering the longevity of an AVF by conducting different longitudinal studies would be able to quantify the relationship between resistance and intervention temporally. A Cox regression or survival model [243], [244] are potential models that can be used to model these with a study designed based on the mentioned hypothesis.

Although there are values in understanding the change of vasculature and activation of disease sites on a cell biological level, the time and cost required to conduct such studies has caused these work to be of less interest as compared to numerical studies [104]. Recently, a numerical study showed that the endothelial activation index, among other common indicators (time averaged wall shear stress, oscillatory shear index and relative reference time) showed potential in stenosis risk prediction [203]. Correlation of CFD-derived resistance can also be made with different parameters such as vascular function parameters (endothelial activation index) [203], blood flow sound frequency [147], or vascular wall motion pulses [245] given evidence of transitional and turbulent-like flow in an AVF [35], [163], [208] and cell-biological changes [22].

6.9 Conclusion

In this chapter, we evaluated the association between resistance and an outcome from dataset for any intervention types (not limited to juxta-anastomotic treatment), such as balloon angioplasty, proximal stent implantation and so on. The boxplot and marginal distribution graph were used to distinguish the distribution of resistance data for patient groups with and without an intervention, at the PA and PV. Resistance calculated at the PV segment showed outstanding positive correlation with AVF patency rate, with lower chances of intervention for patients with a low resistance. Additionally, the model has an outstanding discrimination with an AUC of 92.1% (84.4 – 99.9 %) from the ROC analysis. A cut-off point for resistance was also established from this dataset, where resistance at 6.7 mmHg/l/min yields a low probability of an intervention. Furthermore, CFD-derived resistance appeared to be a dominant predictor as compared to other comorbidities. In summary, CFD-based resistance showed promising potential as a clinical indicator for AVF failure where clinicians could potentially deduce the likelihood of an intervention for a patient by assessing the resistance values, regardless of the existing patient risk factors.

Chapter 7

Conclusion

Predictors of AVF failure are not well understood in current literature; this thesis aims to contribute to knowledge and practice by using AVF geometry and CFD modelling to analyse resistance in individuals as a clinical indicator for AVF failure. This chapter will also discuss the contributions of this work into future research and clinical applications.

7.1 Discussion

Early failure of AVF has been widely investigated (as compared to late AVF failure), mainly assessing the relationship between WSS and failure of AVF maturation [246]. The primary cause of late AVF failure is venous stenosis, which often occurs due to a lack of surveillance leading to inability to identify and treat the stenosis in a timely manner [247]. Hence, regular monitoring is important in prevention of access dysfunction and reduction of mortality, as it enables interventions to be implemented earlier [213].

Currently, physical examinations are the most common approach taken by both experienced and amateur nephrologists to identify vascular access dysfunction [222]. Different types of physical examinations yield different conclusions; for instance, with swelling, the location of the swelling suggests there is stenosis at the particular location; palpation and systolic-only thrills suggest outflow stenosis; and auscultation or high-pitched systolic bruit suggest stenosis [223]. Conclusions drawn through physical examinations are, however, subjective and largely dependent on the expertise of physicians. The findings in this thesis hold immense potential to add value to clinicians by complementing standard ways to investigate stenosis among haemodialysis patients.

Non-invasiveness, repeatability, and convenience in AVF data acquisition as outlined in this thesis enables rapid examination and monitoring of AVF vessels for identification of diseased AVFs. The regular patient monitoring at Prince of Wales Hospital, Sydney Australia (until March 2020 when data collection was halted due to the COVID-19 pandemic) showed that 88% of the blood flow types in AVFs were retrograde with varying blood flow ratios between the PA and DA, ranging from 2.5 – 36.9% at the DA and 64.5 – 98.3% at the PA. The varying flow distributions from the arteries towards (retrograde), or away (antegrade) from the venous segments manifest the significance of patient-specific modelling for targeted patient

recommendation. AVF shunts, post creation, bypass other vascular beds due to blood perfusions, results in increased blood flow and is the reason a majority of the flow type observed in AVF is retrograde [21]. The direction of flow has been shown to relate to recirculation zones around different localised sites of the AVF and promotes IH development [138]. Given the specificity of AVF geometry, calculating resistance through CFD modelling is superior to using Hagen-Poiseuille law estimates, especially given the presence of transitional flow in an AVF [35], [163]. The sensitivity of boundary conditions in computational modelling, founded from the correct three-dimensional geometry emphasises the importance of patient-specific conditions that closely match clinical expectations.

CFD-derived resistance was examined in a group of patients ($N = 17$) who had undergone juxta-anastomotic treatment for stenosis. A promising relationship was observed between the patency status and low resistance value at the PV. These findings were corroborated by clinical observations from medical database, where our findings were indeed found to match data-derived clinical insights. A static resistance value corresponding to the patients' AVF condition was calculated by taking the ratio of pressure drop from the anastomosis to a particular length of the AVF and flow rate. The change in resistance calculated at 1 mm interval also enabled the identification of stenosed segment along the AVF.

The relationship between resistance values in a larger group of patients with a total of 83 datasets, not limited to the juxta-anastomotic treatment, was also examined. Patients were separated into two groups: patients who eventually required intervention, and patients who did not require intervention on the AVF within a specified time. Based on the analysis performed, patients who did not have an intervention were found to have lower resistance value at the PV. The ROC analysis also suggests an outstanding discrimination of an AUC of 92.1%, with a cut-off resistance of 6.7 mmHg/l/min. Resistance at the PV also appeared to be a dominant predictor as compared to other comorbidities. These base findings have paved a way for further

clinical studies to be designed on a prospective application of this study, to assist with rapid detection of vascular access dysfunction among haemodialysis patients. Clinicians can stay alert to abnormal resistance trends along the circuit of a patient's AVF.

Whilst there are merits to the non-invasive nature of this proposed diagnostic approach, there is also potential for clinical implementation by performing an in-vitro validation with catheterization and pressure pump of the dialysis machine. Conventional pressure measurements such as direct venous pressure measurements and static pressure measurements (usually measured during dialysis) are invasive, and affected by the cannulation needle and pulsatility along the extracorporeal circuit of the dialysis machine [248], [249]. Dynamic pressure measurements can be inaccurate in patients with high blood flow rates, often seen in an AVF [213]. Although static pressure measurement is the recommended technique for access surveillance, static intra-access pressure ratios have also been shown to record limited correlation with access blood flow, reported in a study with 96 subjects with AVFs [250]. A combination of different mechanisms will be required for accurate pressure measurements and to lessen the damping effect of pulsatility. This can be done by designing a venous air trap in the extracorporeal system before pressure measurements are taken [248]. Other measures that are key to avoiding circumstances where AVF are damaged (such as over-exertion of pressure) include appropriate training for dialysis nurses with the aid of simulation technologies.

The rapidly changing conditions of an AVF as a consequence of the complex haemodynamics in the AVF from the extracorporeal and vascular circuit mean that there are merits in examining each patient's condition specifically for targeted treatment. Drawing on existing literature, there are many studies on predicting failure of AVF to mature [101], [161], [251] as compared to regular monitoring of AVF health to be alerted of any late failure. Given that AVF is the lifeline of ESRD patient, it is equally essential to integrate regular monitoring and detection of stenosis as part of the patient's dialysis routine to monitor AVF health throughout the vessel's

lifetime. This thesis therefore provides a fundamental study into the possibility of CFD-derived resistance as a new clinical indicator of AVF failure throughout the patency of an AVF (during or after remodelling), supported with findings from both clinical and engineering data, along with statistical significance.

7.2 Key findings

The successful creation and maturation of AVFs is essential in the management of ESRD patients. The aim of this thesis is to investigate the suitability of resistance as a diagnostic marker for AVF failure by examining real-patient data. Measuring AVF patency and detection of stenosis locations have proven to be a challenge for clinicians, hence there is a pressing need to identify diagnostic indicators which will accurately and rapidly identify problematic AVFs both during AVF creation and in the post-remodelling period. This thesis elaborates on the potential for CFD-derived resistance values as a diagnostic indicator to predict AVF failure in an individualised patient approach. The key findings of this thesis are:

1. The acquisition and processing of three-dimensional real-patient AVF geometry were enabled through a three-dimensional ultrasound system and pipeline analysis. Information on patient geometry and flow data was obtained during regular clinical visits, where each session took less than 20 minutes. This was accomplished in conjunction with patients' regular dialysis and clinic visits. Additionally, the three-dimensional patients' geometry was also highly comparable to the angiography images of the patient.
2. Flow (CFD-derived) resistance was calculated through a pipeline analysis of three-dimensional geometry acquisition, visualisation and patient-specific CFD modelling, enabling patient-targeted identification of problematic AVFs.
3. Patient-specific boundary conditions have proven vital to ensure that the CFD results prediction matches closely with the patients' physiological conditions, to ensure patient-targeted recommendations. Estimating flow rates based on the Hagen-Poiseuille model was also shown to be less accurate, especially in stenosis regions with turbulent typed flow features.

4. Proof-of-concept assessment of a group of patients who underwent surgical intervention to treat juxta-anastomotic stenosis demonstrated that resistance can be a suitable identifier for problematic AVFs.
5. Decreased PV resistance was shown to correlate with AVF patency rates and successful treatment of stenosis. Furthermore, analysis of patients pre- and post-surgery demonstrated that PV resistance may be a more reliable indicator than average PV diameter.
6. The three-dimensional AVF conceptualisation also enabled interrogation of the entire AVF circuit so that stenosis locations could be identified along the different segments (PV and PA). This will be extremely useful for regular surveillance in AVF care and may provide additional information for surgeons in terms of pre-operative planning.
7. In the analysis of a wider group of patients, PV resistance continued to be a more effective predictor of AVF failure than PA resistance and other patient's risk factors such as age, smoking, diabetes, hypertension, high cholesterol, CVA, and PVD. AUC of the ROC analysis was reported to be 92.1%, indicating a high discrimination ability of the diagnostic model.
8. Patient risk factors, including prior surgical interventions, continues to be a helpful prognosticator for future surgical intervention, however PV resistance was shown to be a more reliable single indicator of the need for future surgical intervention.
9. An individualised patient-specific approach to clinical care has shown proven key to improving and maintaining AVF health. The findings in this thesis reveal the potential for non-invasive measurement of haemodynamic variables such as AVF pressure and flow, which in turns helps clinicians detect problematic AVFs and optimises surgical management.

7.3 Future directions

Effective communication and collaboration between clinicians and engineers may improve management and outcomes for patients with ESRD. Clinicians collected patient data which was correlated with the three-dimensional patient-specific CFD models; this was then used to identify and visualise disease sites, predict AVF failure and need for surgical intervention, as shown in Figure 54.

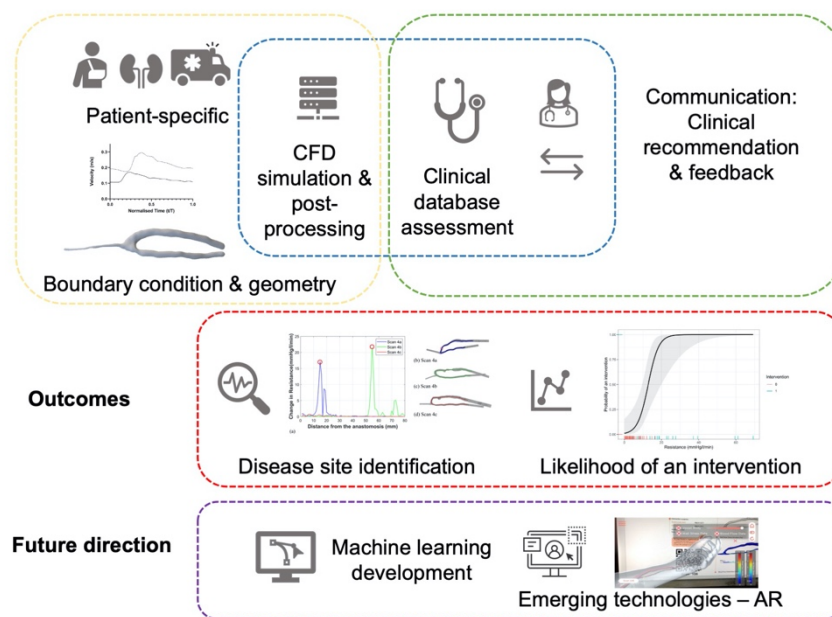


Figure 54: Connection of different parts of the system, distinguishable by the coloured boxes: AVF data acquisition, CFD modelling and post-processing (yellow) along with clinical database validation (blue) and regular communication with clinicians (green). This is followed by the visualisation of data to identify disease sites and likelihood of an intervention (red), which is the outcome of this thesis. The future direction toward a predictive clinical model will be achievable with more dataset and by incorporating emerging technologies (purple).

Further research encompassing more dialysis centres and patient populations of varying demographic will allow generalisability and improve predictive value of this model, with the aim to eventually apply this model prospectively. Furthermore, increasing the size of datasets would allow training and application of a neural network. The integration of machine learning and augmented reality into engineering and medicine also carries significant potential into preventing adverse outcomes, and increasing accuracy of diagnosis, therefore improving patient care.

Bibliography

- [1] N. Aslam, J. Bernardini, L. Fried, R. Burr, and B. Piraino, “Comparison of infectious complications between incident hemodialysis and peritoneal dialysis patients.,” *Clin. J. Am. Soc. Nephrol.*, vol. 1, no. 6, pp. 1226–1233, 2006, doi: 10.2215/CJN.01230406.
- [2] E. Lacson and S. M. Brunelli, “Hemodialysis treatment time: A fresh perspective,” *Clin. J. Am. Soc. Nephrol.*, vol. 6, no. 10, pp. 2522–2530, 2011, doi: 10.2215/CJN.00970211.
- [3] A. T. Azar and B. Canaud, “Hemodialysis System,” in *Modelling and Control of Dialysis Systems: Volume 1: Modeling Techniques of Hemodialysis Systems*, A. T. Azar, Ed. Berlin, Heidelberg: Springer Berlin Heidelberg, 2013, pp. 99–166. doi: 10.1007/978-3-642-27458-9_3.
- [4] J. H. Lawson, L. E. Niklason, and P. Roy-Chaudhury, “Challenges and novel therapies for vascular access in haemodialysis,” *Nat. Rev. Nephrol.*, vol. 16, no. 10, pp. 586–602, 2020, doi: 10.1038/s41581-020-0333-2.
- [5] P. Ravani, S. C. Palmer, M. J. Oliver, R. R. Quinn, J. M. MacRae, D. J. Tai, N. I. Pannu, C. Thomas, B. R. Hemmelgarn, J. C. Craig, B. Manns, M. Tonelli, G. F. M. Strippoli, and M. T. James, “Associations between hemodialysis access type and clinical outcomes: A systematic review,” *J. Am. Soc. Nephrol.*, vol. 24, no. 3, pp. 465–473, 2013, doi: 10.1681/ASN.2012070643.
- [6] I. J. Arhuidese, M. A. Cooper, M. Rizwan, B. Nejm, and M. B. Malas, “Vascular access for hemodialysis in the elderly,” *J. Vasc. Surg.*, vol. 69, no. 2, pp. 517-525.e1, 2019, doi: 10.1016/j.jvs.2018.05.219.
- [7] L. Berardinelli, “Grafts and Graft Materials as Vascular Substitutes for Haemodialysis Access Construction,” *Eur. J. Vasc. Endovasc. Surg.*, vol. 32, no. 2, pp. 203–211, 2006, doi: 10.1016/j.ejvs.2006.01.001.
- [8] P. Ravani, R. Quinn, M. Oliver, B. Robinson, R. Pisoni, N. Pannu, J. MacRae, B. Manns, B. Hemmelgarn, M. James, M. Tonelli, and B. Gillespie, “Examining the association between hemodialysis access type and mortality: The role of access complications,” *Clin. J. Am. Soc. Nephrol.*, vol. 12, no. 6, pp. 955–964, 2017, doi: 10.2215/CJN.12181116.

- [9] M. Allon and M. L. Robbin, “Increasing arteriovenous fistulas in hemodialysis patients: Problems and solutions,” *Kidney Int.*, vol. 62, no. 4, pp. 1109–1124, 2002, doi: 10.1111/j.1523-1755.2002.kid551.x.
- [10] C. E. Lok, T. S. Huber, T. Lee, S. Shenoy, A. S. Yevzlin, K. Abreo, M. Allon, A. Asif, B. C. Astor, M. H. Glickman, J. Graham, L. M. Moist, D. K. Rajan, C. Roberts, T. J. Vachharajani, and R. P. Valentini, “KDOQI Clinical Practice Guideline for Vascular Access: 2019 Update,” *Am. J. Kidney Dis.*, vol. 75, no. 4, pp. S1–S164, 2020, doi: 10.1053/j.ajkd.2019.12.001.
- [11] C. E. Lok, “Fistula first initiative: Advantages and pitfalls,” *Clin. J. Am. Soc. Nephrol.*, vol. 2, no. 5, pp. 1043–1053, 2007, doi: 10.2215/CJN.01080307.
- [12] E. Chisci, L. M. Harris, F. Menici, P. Frosini, E. Romano, N. Troisi, L. Ercolini, and S. Michelagnoli, “Outcomes of three types of native arteriovenous fistula in a single center,” *J. Vasc. Access*, vol. 18, no. 5, pp. 379–383, 2017, doi: 10.5301/jva.5000742.
- [13] T. Lee, M. Mokrzycki, L. Moist, I. Maya, M. Vazquez, and C. E. Lok, “Standardized Definitions for Hemodialysis Vascular Access,” *Semin. Dial.*, vol. 24, no. 5, pp. 515–524, 2011, doi: 10.1111/j.1525-139X.2011.00969.x.
- [14] I. Van Tricht, D. De Wachter, J. Tordoir, and P. Verdonck, “Hemodynamics and complications encountered with arteriovenous fistulas and grafts as vascular access for hemodialysis: A review,” *Ann. Biomed. Eng.*, vol. 33, no. 9, pp. 1142–1157, 2005, doi: 10.1007/s10439-005-5367-X.
- [15] T. Wilmink, L. Hollingworth, S. Powers, C. Allen, and I. Dasgupta, “Natural History of Common Autologous Arteriovenous Fistulae: Consequences for Planning of Dialysis Access,” *Eur. J. Vasc. Endovasc. Surg.*, vol. 51, no. 1, pp. 134–140, 2016, doi: 10.1016/j.ejvs.2015.10.005.
- [16] K. R. Wedgwood, P. A. Wiggins, and P. J. Guillou, “A prospective study of end-to-side vs. side-to-side arteriovenous fistulas for haemodialysis,” *Br. J. Surg.*, vol. 71, no. 8, pp. 640–642, 2005, doi: 10.1002/bjs.1800710831.
- [17] L. C. Bylsma, S. M. Gage, H. Reichert, S. L. M. Dahl, and J. H. Lawson, “Arteriovenous Fistulae for Haemodialysis: A Systematic Review and Meta-analysis of Efficacy and Safety Outcomes,” *Eur. J. Vasc. Endovasc. Surg.*, vol. 54, no. 4, pp. 513–522, 2017, doi:

10.1016/j.ejvs.2017.06.024.

- [18] S. E. Wilson, *Vascular Access: Principles and Practice*, 5th ed. Philadelphia, United States: Lippincott Williams and Wilkins, 2009.
- [19] T. C. Rothuizen, C. Wong, P. H. A. Quax, A. J. Van Zonneveld, T. J. Rabelink, and J. I. Rotmans, “Arteriovenous access failure: More than just intimal hyperplasia?,” *Nephrol. Dial. Transplant.*, vol. 28, no. 5, pp. 1085–1092, 2013, doi: 10.1093/ndt/gft068.
- [20] T. C. Rothuizen, C. Wong, P. H. A. Quax, A. J. Van Zonneveld, T. J. Rabelink, and J. I. Rotmans, “Arteriovenous access failure: More than just intimal hyperplasia?,” *Nephrol. Dial. Transplant.*, vol. 28, no. 5, pp. 1085–1092, 2013, doi: 10.1093/ndt/gft068.
- [21] B. S. Dixon, “Why don’t fistulas mature?,” *Kidney Int.*, vol. 70, no. 8, pp. 1413–1422, 2006, doi: 10.1038/sj.ki.5001747.
- [22] P. Roy-Chaudhury, L. M. Spergel, A. Besarab, A. Asif, and P. Ravani, “Biology of arteriovenous fistula failure,” *J. Nephrol.*, vol. 20, no. 2, pp. 150–163, 2007.
- [23] A. Caroli *et al.*, “Validation of a patient-specific hemodynamic computational model for surgical planning of vascular access in hemodialysis patients,” *Kidney Int.*, vol. 84, no. 6, pp. 1237–1245, 2013, doi: 10.1038/ki.2013.188.
- [24] Z. J. Lo, W. M. Tay, Q. Lee, J. L. Chua, G. W. L. Tan, S. Chandrasekar, and S. Narayanan, “Predictors of radio-cephalic arteriovenous fistulae patency in an asian population,” *J. Vasc. Access*, vol. 17, no. 5, pp. 411–416, 2016, doi: 10.5301/jva.5000591.
- [25] “Chronic kidney disease,” *Australian Institute of Health and Welfare*, 2018. <https://www.aihw.gov.au/reports-statistics/health-conditions-disability-deaths/chronic-kidney-disease/overview>
- [26] A. Sequeira, M. Naljayan, and T. J. Vachharajani, “Vascular Access Guidelines: Summary, Rationale, and Controversies,” *Tech. Vasc. Interv. Radiol.*, vol. 20, no. 1, pp. 2–8, 2017, doi: 10.1053/j.tvir.2016.11.001.
- [27] R. Fitridge, M. Thompson., and M. Thompson, *Mechanisms of Vascular Disease A Reference Book for Vascular Specialists*. 2011.

- [28] C. E. Alpers, P. B. Imrey, K. L. Hudkins, T. A. Wietecha, M. Radeva, M. Allon, A. K. Cheung, L. M. Dember, P. Roy-Chaudhury, Y. T. Shiu, C. M. Terry, A. Farber, G. J. Beck, H. I. Feldman, J. W. Kusek, and J. Himmelfarb, “Histopathology of veins obtained at hemodialysis arteriovenous fistula creation surgery,” *J. Am. Soc. Nephrol.*, vol. 28, no. 10, pp. 3076–3088, 2017, doi: 10.1681/ASN.2016050598.
- [29] P. E. Miller, A. Tolwani, C. P. Luscry, M. H. Deierhoi, R. Bailey, D. T. Redden, and M. Allon, “Predictors of adequacy of arteriovenous fistulas in hemodialysis patients,” *Kidney Int.*, vol. 56, no. 1, pp. 275–280, 1999, doi: 10.1046/j.1523-1755.1999.00515.x.
- [30] F. Saucy, E. Haesler, C. Haller, S. Déglise, D. Teta, and J. M. Corpataux, “Is intra-operative blood flow predictive for early failure of radiocephalic arteriovenous fistula?,” *Nephrol. Dial. Transplant.*, vol. 25, no. 3, pp. 862–867, 2010, doi: 10.1093/ndt/gfp577.
- [31] S. Lehoux, Y. Castier, and A. Tedgui, “Molecular mechanisms of the vascular responses to haemodynamic forces,” *J. Intern. Med.*, vol. 259, no. 4, pp. 381–392, 2006, doi: 10.1111/j.1365-2796.2006.01624.x.
- [32] N. Baeyens, C. Bandyopadhyay, B. G. Coon, S. Yun, and M. A. Schwartz, “Endothelial fluid shear stress sensing in vascular health and disease,” vol. 126, no. 3, pp. 821–828, 2016, doi: 10.1172/JCI83083.evolved.
- [33] Z. Kharboutly, V. Deplano, E. Bertrand, and C. Legallais, “Numerical and experimental study of blood flow through a patient-specific arteriovenous fistula used for hemodialysis,” *Med. Eng. Phys.*, vol. 32, no. 2, pp. 111–118, Mar. 2010, doi: 10.1016/j.medengphy.2009.10.013.
- [34] L. D. Browne, P. Griffin, K. Bashar, S. R. Walsh, E. G. Kavanagh, and M. T. Walsh, “In Vivo Validation of the In Silico Predicted Pressure Drop Across an Arteriovenous Fistula,” *Ann. Biomed. Eng.*, vol. 43, no. 6, pp. 1275–1286, 2015, doi: 10.1007/s10439-015-1295-6.
- [35] M. Bozzetto, B. Ene-Iordache, and A. Remuzzi, “Transitional Flow in the Venous Side of Patient-Specific Arteriovenous Fistulae for Hemodialysis,” *Ann. Biomed. Eng.*, vol. 44, no. 8, pp. 2388–2401, 2016, doi: 10.1007/s10439-015-1525-y.
- [36] J. E. Carroll, E. S. Colley, S. D. Thomas, R. L. Varcoe, A. Simmons, and T. J. Barber, “Tracking geometric and hemodynamic alterations of an arteriovenous fistula through

- patient-specific modelling,” *Comput. Methods Programs Biomed.*, vol. 186, 2020, doi: 10.1016/j.cmpb.2019.105203.
- [37] J. Carroll, R. L. Varcoe, T. Barber, and A. Simmons, “Reduction in anastomotic flow disturbance within a modified end-to-side arteriovenous fistula configuration: Results of a computational flow dynamic model,” *Nephrology*, vol. 24, no. 2, pp. 245–251, 2019, doi: 10.1111/nep.13219.
 - [38] C. V. Cunnane, E. M. Cunnane, D. T. Moran, and M. T. Walsh, “The presence of helical flow can suppress areas of disturbed shear in parameterised models of an arteriovenous fistula,” *Int. j. numer. method. biomed. eng.*, vol. 35, no. 12, pp. 1–14, 2019, doi: 10.1002/cnm.3259.
 - [39] C. V. Cunnane, E. M. Cunnane, and M. T. Walsh, “A Review of the Hemodynamic Factors Believed to Contribute to Vascular Access Dysfunction,” *Cardiovasc. Eng. Technol.*, vol. 8, no. 3, pp. 280–294, 2017, doi: 10.1007/s13239-017-0307-0.
 - [40] J. M. MacRae, C. Dipchand, M. Oliver, L. Moist, C. Lok, E. Clark, S. Hiremath, J. Kappel, M. Kiaii, R. Luscombe, and L. M. Miller, “Arteriovenous access failure, stenosis, and thrombosis,” *Can. J. Kidney Heal. Dis.*, vol. 3, no. 1, 2016, doi: 10.1177/2054358116669126.
 - [41] M. Franzoni and M. T. Walsh, “Towards the Identification of Hemodynamic Parameters Involved in Arteriovenous Fistula Maturation and Failure: A Review,” *Cardiovasc. Eng. Technol.*, vol. 8, no. 3, pp. 342–356, 2017, doi: 10.1007/s13239-017-0322-1.
 - [42] S. Sivanesan, T. V. How, and A. Bakran, “Sites of stenosis in AV fistulae for haemodialysis access,” *Nephrol. Dial. Transplant.*, vol. 14, no. 1, pp. 118–120, 1999, doi: 10.1093/ndt/14.1.118.
 - [43] C. C. Haudenschild, “Morphology of intimal hyperplasia: Research initiatives in vascular surgery *,” *J. Vasc. Surg.*, vol. 10, no. 5, pp. 591–592, Nov. 1989, doi: 10.1016/0741-5214(89)90157-2.
 - [44] P. Roy-Chaudhury, L. Arend, J. Zhang, M. Krishnamoorthy, Y. Wang, R. Banerjee, A. Samaha, and R. Munda, “Neointimal Hyperplasia in Early Arteriovenous Fistula Failure,” *Am. J. Kidney Dis.*, vol. 50, no. 5, pp. 782–790, 2007, doi: 10.1053/j.ajkd.2007.07.019.

- [45] A. K. Cheung, P. B. Imrey, C. E. Alpers, M. L. Robbin, M. Radeva, B. Larive, Y. T. Shiu, M. Allon, L. M. Dember, T. Greene, J. Himmelfarb, P. Roy-Chaudhury, C. M. Terry, M. A. Vazquez, J. W. Kusek, and H. I. Feldman, “Intimal hyperplasia, stenosis, and arteriovenous fistula maturation failure in the hemodialysis fistula maturation study,” *J. Am. Soc. Nephrol.*, vol. 28, no. 10, pp. 3005–3013, 2017, doi: 10.1681/ASN.2016121355.
- [46] M. Tabbara, J. C. Duque, L. Martinez, L. A. Escobar, W. Wu, Y. Pan, N. Fernandez, O. C. Velazquez, E. A. Jaimes, L. H. Salman, and R. I. Vazquez-Padron, “Pre-existing and Postoperative Intimal Hyperplasia and Arteriovenous Fistula Outcomes,” *Am. J. Kidney Dis.*, vol. 68, no. 3, pp. 455–464, 2016, doi: <https://doi.org/10.1053/j.ajkd.2016.02.044>.
- [47] G. E. Smith, R. Gohil, and I. C. Chetter, “Factors affecting the patency of arteriovenous fistulas for dialysis access,” *J. Vasc. Surg.*, vol. 55, no. 3, pp. 849–855, 2012, doi: 10.1016/j.jvs.2011.07.095.
- [48] A. Farber *et al.*, “Multiple preoperative and intraoperative factors predict early fistula thrombosis in the Hemodialysis Fistula Maturation Study,” *J. Vasc. Surg.*, vol. 63, no. 1, pp. 163–170.e6, 2016, doi: 10.1016/j.jvs.2015.07.086.
- [49] H. I. Feldman, M. Joffe, S. E. Rosas, J. E. Burns, J. Knauss, and K. Brayman, “Predictors of Successful Arteriovenous Fistula Maturation,” *Am. J. Kidney Dis.*, vol. 42, no. 5, pp. 1000–1012, 2003, doi: 10.1016/j.ajkd.2003.07.003.
- [50] M. K. Lazarides, G. S. Georgiadis, G. A. Antoniou, and D. N. Staramos, “A meta-analysis of dialysis access outcome in elderly patients,” *J. Vasc. Surg.*, vol. 45, no. 2, 2007, doi: 10.1016/j.jvs.2006.10.035.
- [51] A. Brahmabhatt, A. Remuzzi, M. Franzoni, and S. Misra, “The molecular mechanisms of hemodialysis vascular access failure,” *Kidney Int.*, vol. 89, no. 2, pp. 303–316, 2016, doi: 10.1016/j.kint.2015.12.019.
- [52] M. T. Parisotto, V. U. Schoder, C. Miriunis, A. H. Grassmann, L. P. Scatizzi, P. Kaufmann, A. Stopper, and D. Marcelli, “Cannulation technique influences arteriovenous fistula and graft survival,” *Kidney Int.*, vol. 86, no. 4, pp. 790–797, 2014, doi: 10.1038/ki.2014.96.
- [53] H. C. Rayner, R. L. Pisoni, B. W. Gillespie, D. A. Goodkin, T. Akiba, T. Akizawa, A.

- Saito, E. W. Young, and F. K. Port, “Creation, cannulation and survival of arteriovenous fistulae: Data from the dialysis outcomes and practice patterns study,” *Kidney Int.*, vol. 63, no. 1, pp. 323–330, 2003, doi: 10.1046/j.1523-1755.2003.00724.x.
- [54] M. A. Hussain, P. Yu, S. Burke, D. Hentschel, M. Al-Omran, D. L. Bhatt, M. Belkin, and C. K. Ozaki, “Predictors of Radiocephalic Arteriovenous Fistula Outcomes: First Look into the PATENCY-1 and PATENCY-2 Randomized Controlled Trials,” *J. Vasc. Surg.*, vol. 74, no. 3, p. e43, 2021, doi: 10.1016/j.jvs.2021.06.072.
- [55] D. Fulker, A. Simmons, and T. Barber, “Computational Model of the Arterial and Venous Needle during Hemodialysis,” *J. Biomech. Eng.*, vol. 139, no. 1, pp. 1–7, 2017, doi: 10.1115/1.4034429.
- [56] D. Fulker, B. Ene-Iordache, and T. J. Barber, “High Resolution Computational Fluid Dynamic Simulation of Haemodialysis Cannulation in a Patient Specific Arteriovenous Fistula,” *J. Biomech. Eng.*, vol. 140, no. 3, p. 031011, 2018, doi: 10.1115/1.4038289.
- [57] C. E. Lok, M. Allon, L. Moist, M. J. Oliver, H. Shah, and D. Zimmerman, “Risk Equation Determining Unsuccessful Cannulation Events and Failure to Maturation in Arteriovenous Fistulas (REDUCE FTM I),” *J. Am. Soc. Nephrol.*, vol. 17, no. 11, pp. 3204–3212, 2006, doi: 10.1681/ASN.2006030190.
- [58] A. Masengu, A. P. Maxwell, and J. B. Hanko, “Investigating clinical predictors of arteriovenous fistula functional patency in a European cohort,” *Clin. Kidney J.*, vol. 9, no. 1, pp. 142–147, 2016, doi: 10.1093/ckj/sfv131.
- [59] M. P. Lilly, J. R. Lynch, J. B. Wish, E. D. Huff, S. C. Chen, N. C. Armistead, and W. M. McClellan, “Prevalence of arteriovenous fistulas in incident hemodialysis patients: Correlation with patient factors that may be associated with maturation failure,” *Am. J. Kidney Dis.*, vol. 59, no. 4, pp. 541–549, 2012, doi: 10.1053/j.ajkd.2011.11.038.
- [60] D. C. Bosanquet, J. Rubasingham, M. Imam, J. D. Woolgar, and C. G. Davies, “Predicting outcomes in native AV forearm radio-cephalic fistulae; the CAVeA2T2scoring system,” *J. Vasc. Access*, vol. 16, no. 1, pp. 19–25, 2015, doi: 10.5301/jva.5000305.
- [61] L. I. Martinez, V. Esteve, M. Yeste, V. Artigas, and S. Llagostera, “Clinical Utility of a New Predicting Score for Radiocephalic Arteriovenous Fistula Survival,” *Ann. Vasc.*

- Surg.*, vol. 41, no. February, pp. 56–61, 2017, doi: 10.1016/j.avsg.2016.09.022.
- [62] M. L. Robbin *et al.*, “Prediction of Arteriovenous Fistula Clinical Maturation from Postoperative Ultrasound Measurements: Findings from the Hemodialysis Fistula Maturation Study,” *J. Am. Soc. Nephrol.*, vol. 29, no. 11, pp. 2735–2744, 2018, doi: 10.1681/ASN.2017111225.
 - [63] B. M. Voorzaat, K. E. A. van der Bogt, C. J. Janmaat, J. van Schaik, F. W. Dekker, J. I. Rotmans, L. Vogt, L. Huisman, B. A. T. F. Gabreëls, F. T. J. Boereboom, I. M. van der Meer, R. G. S. van Eps, D. Eefting, M. C. Weijmer, R. C. van Nieuwenhuizen, A. Abrahams, and R. J. Toorop, “Arteriovenous Fistula Maturation Failure in a Large Cohort of Hemodialysis Patients in the Netherlands,” *World J. Surg.*, vol. 42, no. 6, pp. 1895–1903, 2018, doi: 10.1007/s00268-017-4382-z.
 - [64] L. Wolowczyk, A. J. Williams, K. L. Donovan, and C. P. Gibbons, “The snuffbox arteriovenous fistula for vascular access,” *Eur. J. Vasc. Endovasc. Surg.*, vol. 19, no. 1, pp. 70–76, 2000, doi: 10.1053/ejvs.1999.0969.
 - [65] A. Kordzadeh, A. Askari, M. Hoff, V. Smith, and Y. Panayiotopoulos, “The Impact of Patient Demographics, Anatomy, Comorbidities, and Peri-operative Planning on the Primary Functional Maturation of Autogenous Radiocephalic Arteriovenous Fistula,” *Eur. J. Vasc. Endovasc. Surg.*, vol. 53, no. 5, pp. 726–732, 2017, doi: 10.1016/j.ejvs.2017.01.015.
 - [66] S. K. Kakkos and I. A. Tsolakis, “Commentary on ‘The Impact of Patient Demographics, Anatomy, Comorbidities and Peri-operative Planning on the Primary Functional Maturation of Autogenous Radiocephalic Arteriovenous Fistula,’” *Eur. J. Vasc. Endovasc. Surg.*, vol. 53, no. 5, p. 733, 2017, doi: 10.1016/j.ejvs.2017.02.002.
 - [67] C. Glass, M. Johansson, W. DiGragio, and K. A. Illig, “A meta-analysis of preoperative duplex ultrasound vessel diameters for successful radiocephalic fistula placement,” *J. Vasc. Ultrasound*, vol. 33, no. 2, pp. 65–68, 2009, doi: 10.1177/154431670903300201.
 - [68] P. W. G. Brown, “Preoperative radiological assessment for vascular access,” *Eur. J. Vasc. Endovasc. Surg.*, vol. 31, no. 1, pp. 64–69, 2006, doi: 10.1016/j.ejvs.2005.10.002.
 - [69] T. K. Jemcov, “Morphologic and functional vessels characteristics assessed by ultrasonography for prediction of radiocephalic fistula maturation,” *J. Vasc. Access*, vol.

- 14, no. 4, pp. 356–363, 2013, doi: 10.5301/jva.5000163.
- [70] R. R. Mendes, M. A. Farber, W. A. Marston, L. C. Dinwiddie, B. A. Keagy, and S. J. Burnham, “Prediction of wrist arteriovenous fistula maturation with preoperative vein mapping with ultrasonography,” *J. Vasc. Surg.*, vol. 36, no. 3, pp. 460–463, 2002, doi: 10.1067/mva.2002.126544.
 - [71] L. Turmel-Rodrigues, “Stenosis and thrombosis in haemodialysis fistulae and grafts: The radiologist’s point of view,” *Nephrol. Dial. Transplant.*, vol. 19, no. 2, pp. 306–308, 2004, doi: 10.1093/ndt/gfg503.
 - [72] L. S. Lauvao, D. M. Ihnat, K. R. Goshima, L. A. Chavez, A. C. Gruessner, and J. L. Mills, “Vein diameter is the major predictor of fistula maturation,” *J. Vasc. Surg.*, vol. 49, no. 6, pp. 1499–1504, Jun. 2009, doi: 10.1016/j.jvs.2009.02.018.
 - [73] J. van der Linden, T. W. Lameris, A. H. van den Meiracker, A. A. E. A. de Smet, P. J. Blankestijn, and M. A. van den Dorpel, “Forearm Venous Distensibility Predicts Successful Arteriovenous Fistula,” *Am. J. Kidney Dis.*, vol. 47, no. 6, pp. 1013–1019, 2006, doi: 10.1053/j.ajkd.2006.01.033.
 - [74] M. F. Kheda, L. E. Brenner, M. J. Patel, J. J. Wynn, J. J. White, L. M. Prisant, S. A. Jones, and W. D. Paulson, “Influence of arterial elasticity and vessel dilatation on arteriovenous fistula maturation: A prospective cohort study,” *Nephrol. Dial. Transplant.*, vol. 25, no. 2, pp. 525–531, 2010, doi: 10.1093/ndt/gfp462.
 - [75] C. H. Lin, C. H. Chua, S. S. Chiang, J. Y. Liou, H. F. Hung, and C. H. Chang, “Correlation of intraoperative blood flow measurement with autogenous arteriovenous fistula outcome,” *J. Vasc. Surg.*, vol. 48, no. 1, pp. 167–172, 2008, doi: 10.1016/j.jvs.2008.02.069.
 - [76] A. Colombo, M. Provenzano, L. Rivoli, C. Donato, M. Capria, G. Leonardi, S. Chiarella, M. Andreucci, G. Fuiano, D. Bolignano, and G. Coppolino, “Utility of Blood Flow/Resistance Index Ratio (Qx) as a Marker of Stenosis and Future Thrombotic Events in Native Arteriovenous Fistulas,” *Front. Surg.*, vol. 7, 2021, doi: 10.3389/fsurg.2020.604347.
 - [77] M. Malovrh, “Native arteriovenous fistula: Preoperative evaluation,” *Am. J. Kidney Dis.*, vol. 39, no. 6, pp. 1218–1225, 2002, doi: 10.1053/ajkd.2002.33394.

- [78] K. Koseoglu, H. Akar, B. Cildag, Y. Ozsunar, and P. Gayret, “Resistive index measurement of native hemodialysis arteriovenous fistula feeding artery as a predictor for fistula dysfunction,” *ASAIO J.*, vol. 50, no. 6, pp. 577–580, 2004, doi: 10.1097/01.mat.0000145052.75525.77.
- [79] K. M. Saqr, S. Tupin, S. Rashad, T. Endo, K. Niizuma, T. Tominaga, and M. Ohta, “Physiologic blood flow is turbulent,” *Sci. Rep.*, vol. 10, no. 1, pp. 1–12, 2020, doi: 10.1038/s41598-020-72309-8.
- [80] S. P. Suter and R. Skalak, “The History of Poiseuille’s Law,” *Annu. Rev. Fluid Mech.*, vol. 25, pp. 1–19, 1953.
- [81] J. H. G. Helthuis, T. P. C. van Doormaal, S. Amin-Hanjani, X. J. Du, F. T. Charbel, B. Hillen, and A. van der Zwan, “A patient-specific cerebral blood flow model,” *J. Biomech.*, vol. 98, p. 109445, 2020, doi: 10.1016/j.jbiomech.2019.109445.
- [82] T. Suzuki, H. Takao, T. Suzuki, S. Hataoka, T. Kodama, K. Aoki, K. Otani, T. Ishibashi, H. Yamamoto, Y. Murayama, and M. Yamamoto, “Proposal of hematocrit-based non-Newtonian viscosity model and its significance in intracranial aneurysm blood flow simulation,” *J. Nonnewton. Fluid Mech.*, vol. 290, p. 104511, 2021, doi: <https://doi.org/10.1016/j.jnnfm.2021.104511>.
- [83] K. M. Saqr, O. Mansour, S. Tupin, T. Hassan, and M. Ohta, “Evidence for non-Newtonian behavior of intracranial blood flow from Doppler ultrasonography measurements,” *Med. Biol. Eng. Comput.*, vol. 57, no. 5, pp. 1029–1036, 2019, doi: 10.1007/s11517-018-1926-9.
- [84] R. Gerrah, S. J. Haller, and I. George, “Mechanical Concepts Applied in Congenital Heart Disease and Cardiac Surgery,” *Ann. Thorac. Surg.*, vol. 103, no. 6, pp. 2005–2014, 2017, doi: 10.1016/j.athoracsur.2017.01.068.
- [85] S. M. Kute and D. A. Vorp, “The effect of proximal artery flow on the hemodynamics at the distal anastomosis of a vascular bypass graft: Computational study,” *J. Biomech. Eng.*, vol. 123, no. 3, pp. 277–283, 2001, doi: 10.1115/1.1374203.
- [86] J.-M. Corpataux, E. Haesler, P. Silacci, H. B. Ris, and D. Hayoz, “Low-pressure environment and remodelling of the forearm vein in Brescia-Cimino haemodialysis access,” *Nephrol. Dial. Transplant*, vol. 17, no. 6, pp. 1057–1062, 2002, doi:

10.1093/ndt/17.6.1057.

- [87] X. Girerd, G. London, P. Boutouyrie, J.-J. Mourad, M. Safar, and S. Laurent, “Remodeling of the Radial Artery in Response to a Chronic Increase in Shear Stress,” *Hypertension*, vol. 27, no. 3, pp. 799–803, 1996.
- [88] L. Botti, K. Van Canneyt, R. Kaminsky, T. Claessens, R. N. Planken, P. Verdonck, A. Remuzzi, and L. Antiga, “Numerical Evaluation and Experimental Validation of Pressure Drops Across a Patient-Specific Model of Vascular Access for Hemodialysis,” *Cardiovasc. Eng. Technol.*, vol. 4, no. 4, pp. 485–499, 2013, doi: 10.1007/s13239-013-0162-6.
- [89] K. Sriram, M. Intaglietta, and D. M. Tartakovsky, “Non-Newtonian Flow of Blood in Arterioles: Consequences for Wall Shear Stress Measurements,” *Microcirculation*, vol. 21, no. 7, pp. 628–639, 2014, doi: <https://doi.org/10.1111/micc.12141>.
- [90] A. Remuzzi, B. Ene-Iordache, L. Mosconi, S. Bruno, A. Anghileri, L. Antiga, and G. Remuzzi, “Radial artery wall shear stress evaluation in patients with arteriovenous fistula for hemodialysis access,” *Biorheology*, vol. 40, pp. 423–430, 2003.
- [91] B. Ene-Iordache, L. Mosconi, L. Antiga, S. Bruno, A. Anghileri, G. Remuzzi, and A. Remuzzi, “Radial artery remodeling in response to shear stress increase within arteriovenous fistula for hemodialysis access,” *Endothel. J. Endothel. Cell Res.*, vol. 10, no. 2, pp. 95–102, 2003, doi: 10.1080/10623320303365.
- [92] A. Noordergraaf, P. D. Verdouw, and H. B. K. Boom, “The use of an analog computer in a circulation model,” *Prog. Cardiovasc. Dis.*, vol. 5, no. 5, pp. 419–439, 1963, doi: 10.1016/S0033-0620(63)80009-2.
- [93] O. Frank, *Die Grundform des arteriellen pulses: Mathematische Analyse. Erste Abhandlung*. 1899.
- [94] M. J. C. Van Gemert, C. M. A. Bruyninckx, and M. J. H. Baggen, “Shunt haemodynamics and extracorporeal dialysis: An electrical resistance network analysis,” *Phys. Med. Biol.*, vol. 29, no. 3, pp. 219–235, 1984, doi: 10.1088/0031-9155/29/3/002.
- [95] M. J. C. van Gemert and C. M. A. Bruyninckx, “Simulated hemodynamic comparison of arteriovenous fistulas,” *J. Vasc. Surg.*, vol. 6, no. 1, pp. 39–44, 1987, doi: 10.1067/mva.1987.avs0060039.

- [96] W. Huberts, E. M. H. Bosboom, and F. N. Van De Vosse, "A lumped model for blood flow and pressure in the systemic arteries based on an approximate velocity profile function," *Math. Biosci. Eng.*, vol. 6, no. 1, pp. 27–40, 2009, doi: 10.3934/mbe.2009.6.27.
- [97] W. Huberts, A. S. Bode, W. Kroon, R. N. Planken, J. H. M. M. Tordoir, F. N. van de Vosse, and E. M. H. H. Bosboom, "A pulse wave propagation model to support decision-making in vascular access planning in the clinic.," *Med. Eng. Phys.*, vol. 34, no. 2, pp. 233–248, Mar. 2012, doi: 10.1016/j.medengphy.2011.07.015.
- [98] W. Huberts, K. Van Canneyt, P. Segers, S. Eloot, J. H. M. Tordoir, P. Verdonck, F. N. van de Vosse, and E. M. H. Bosboom, "Experimental validation of a pulse wave propagation model for predicting hemodynamics after vascular access surgery," *J. Biomech.*, vol. 45, no. 9, pp. 1684–1691, 2012, doi: 10.1016/j.jbiomech.2012.03.028.
- [99] S. Manini, K. Passera, W. Huberts, L. Botti, L. Antiga, and A. Remuzzi, "Computational model for simulation of vascular adaptation following vascular access surgery in haemodialysis patients," *Comput. Methods Biomech. Biomed. Engin.*, vol. 17, no. 12, pp. 1358–1367, Jan. 2014, doi: 10.1080/10255842.2012.745857.
- [100] S. Manini, L. Antiga, L. Botti, and A. Remuzzi, "pyNS: An Open-Source Framework for 0D Haemodynamic Modelling," *Ann. Biomed. Eng.*, vol. 43, no. 6, pp. 1461–1473, 2015, doi: 10.1007/s10439-014-1234-y.
- [101] M. Bozzetto, S. Rota, V. Vigo, F. Casucci, C. Lomonte, W. Morale, M. Senatore, L. Tazza, M. Lodi, G. Remuzzi, and A. Remuzzi, "Clinical use of computational modeling for surgical planning of arteriovenous fistula for hemodialysis," *BMC Med. Inform. Decis. Mak.*, vol. 17, no. 1, pp. 1–9, 2017, doi: 10.1186/s12911-017-0420-x.
- [102] B. Ene-Iordache and A. Remuzzi, "Disturbed flow in radial-cephalic arteriovenous fistulae for haemodialysis: Low and oscillating shear stress locates the sites of stenosis," *Nephrol. Dial. Transplant.*, vol. 27, no. 1, pp. 358–368, 2012, doi: 10.1093/ndt/gfr342.
- [103] V. Peiffer, S. J. Sherwin, and P. D. Weinberg, "Computation in the rabbit aorta of a new metric - the transverse wall shear stress - to quantify the multidirectional character of disturbed blood flow," *J. Biomech.*, vol. 46, no. 15, pp. 2651–2658, 2013, doi: 10.1016/j.jbiomech.2013.08.003.

- [104] P. Roy-Chaudhury, T. C. Lee, and R. Munda, “Predicting dialysis vascular access blood flow and diameter: Too much, too little, or just right,” *Kidney Int.*, vol. 84, no. 6, pp. 1076–1078, 2013, doi: 10.1038/ki.2013.307.
- [105] A. K. Niemann, J. Udesen, S. Thrysoe, J. V Nygaard, E. T. Fründ, S. E. Petersen, and J. M. Hasenkam, “Can sites prone to flow induced vascular complications in a-v fistulas be assessed using computational fluid dynamics?,” *J. Biomech.*, vol. 43, no. 10, pp. 2002–2009, 2010, doi: 10.1016/j.jbiomech.2010.02.037.
- [106] K. Van Canneyt, T. Pourchez, S. Eloot, C. Guillame, A. Bonnet, P. Segers, and P. Verdonck, “Hemodynamic impact of anastomosis size and angle in side-to-end arteriovenous fistulae: A computer analysis,” *J. Vasc. Access*, vol. 11, no. 1, pp. 52–58, 2010, doi: 10.5301/JVA.2010.2870.
- [107] L. D. Browne, M. T. Walsh, and P. Griffin, “Experimental and Numerical Analysis of the Bulk Flow Parameters Within an Arteriovenous Fistula,” *Cardiovasc. Eng. Technol.*, vol. 6, no. 4, pp. 450–462, 2015, doi: 10.1007/s13239-015-0246-6.
- [108] Y. He, C. M. Terry, C. Nguyen, S. A. Berceli, Y.-T. E. Shiu, and A. K. Cheung, “Serial analysis of lumen geometry and hemodynamics in human arteriovenous fistula for hemodialysis using magnetic resonance imaging and computational fluid dynamics,” vol. 46, no. 1, pp. 165–169, 2014, doi: 10.1016/j.jbiomech.2012.09.005.Serial.
- [109] I. Decorato, A.-V. V. Salsac, C. Legallais, M. Alimohammadi, V. Diaz-Zuccarini, and Z. Kharboutly, “Influence of an Arterial Stenosis on the Hemodynamics Within an Arteriovenous Fistula (AVF): Comparison Before and After Balloon-Angioplasty,” *Cardiovasc. Eng. Technol.*, vol. 5, no. 3, pp. 233–243, 2014, doi: 10.1007/s13239-014-0185-7.
- [110] D. Jodko, D. Obidowski, P. Reorowicz, and K. Jóźwik, “Blood flows in end-to-end arteriovenous fistulas: Unsteady and steady state numerical investigations of three patient-specific cases,” *Biocybern. Biomed. Eng.*, vol. 37, no. 3, pp. 528–539, 2017, doi: 10.1016/j.bbe.2017.05.006.
- [111] B. Ene-Iordache, L. Cattaneo, G. Dubini, and A. Remuzzi, “Effect of anastomosis angle on the localization of disturbed flow in ‘side-to-end’ fistulae for haemodialysis access,” *Nephrol. Dial. Transplant.*, vol. 28, no. 4, pp. 997–1005, Apr. 2013, doi: 10.1093/ndt/gfs298.

- [112] J. E. Hull, B. V. Balakin, B. M. Kellerman, and D. K. Wrolstad, “Computational fluid dynamic evaluation of the side-to-side anastomosis for arteriovenous fistula,” *J. Vasc. Surg.*, vol. 58, no. 1, pp. 187–194, 2013, doi: 10.1016/j.jvs.2012.10.070.
- [113] M. Boghosian, K. Cassel, M. Hammes, B. Funaki, S. Kim, X. Qian, X. Wang, P. Dhar, and J. Hines, “Hemodynamics in the cephalic arch of a brachiocephalic fistula,” *Med. Eng. Phys.*, vol. 36, no. 7, pp. 822–830, 2014, doi: 10.1016/j.medengphy.2014.03.001.
- [114] S. M. Javid Mahmoudzadeh Akherat, K. Cassel, M. Boghosian, M. Hammes, and F. Coe, “A predictive framework to elucidate venous stenosis: CFD & shape optimization,” *Comput. Methods Appl. Mech. Eng.*, vol. 321, no. October, pp. 46–69, 2017, doi: 10.1016/j.cma.2017.03.036.
- [115] P. M. McGah, D. F. Leotta, K. W. Beach, and A. Aliseda, “Effects of wall distensibility in hemodynamic simulations of an arteriovenous fistula,” *Biomech. Model. Mechanobiol.*, vol. 13, no. 3, pp. 679–695, 2014, doi: 10.1007/s10237-013-0527-7.
- [116] M. Sigovan, V. Rayz, W. Gasper, H. F. Alley, C. D. Owens, D. Saloner, G. Warren, H. F. Alley, C. D. Owen, and D. Saloner, “Vascular Remodeling in Autogenous Arterio-Venous Fistulas by MRI and CFD,” *Ann. Biomed. Eng.*, vol. 4, no. 164, pp. 657–668, 2011, doi: 10.1126/scisignal.2001449.Engineering.
- [117] Y. He, C. M. Terry, C. Nguyen, S. A. Berceli, Y.-T. E. T. E. Shiu, and A. K. Cheung, “Serial analysis of lumen geometry and hemodynamics in human arteriovenous fistula for hemodialysis using magnetic resonance imaging and computational fluid dynamics,” *J. Biomech.*, vol. 46, no. 1, pp. 165–169, Jan. 2013, doi: 10.1016/j.jbiomech.2012.09.005.
- [118] E. Rajabi-Jagahrgh, M. K. Krishnamoorthy, P. Roy-Chaudhury, P. Succop, Y. Wang, A. Choe, and R. K. Banerjee, “Longitudinal assessment of hemodynamic endpoints in predicting arteriovenous fistula maturation,” *Semin. Dial.*, vol. 26, no. 2, pp. 208–215, 2013, doi: 10.1111/j.1525-139X.2012.01112.x.
- [119] E. Rajabi-Jagahrgh, M. K. Krishnamoorthy, Y. Wang, A. Choe, P. Roy-Chaudhury, and R. K. Banerjee, “Influence of temporal variation in wall shear stress on intima-media thickening in arteriovenous fistulae,” *Semin. Dial.*, vol. 26, no. 4, pp. 511–519, 2013, doi: 10.1111/sdi.12045.

- [120] E. Colley, A. Simmons, R. Varcoe, S. Thomas, and T. Barber, “Arteriovenous fistula maturation and the influence of fluid dynamics,” *Proc. Inst. Mech. Eng. Part H J. Eng. Med.*, 2020, doi: 10.1177/0954411920926077.
- [121] N. Baeyens and M. A. Schwartz, “Biomechanics of vascular mechanosensation and remodeling,” *Mol. Biol. Cell*, vol. 27, no. 1, pp. 7–11, 2016, doi: 10.1091/mbc.E14-11-1522.
- [122] M. K. Krishnamoorthy, R. K. Banerjee, Y. Wang, J. Zhang, A. S. Roy, S. F. Khoury, L. J. Arend, S. Rudich, and P. Roy-Chaudhury, “Hemodynamic wall shear stress profiles influence the magnitude and pattern of stenosis in a pig AV fistula,” *Kidney Int.*, vol. 74, no. 11, pp. 1410–1419, 2008, doi: 10.1038/ki.2008.379.
- [123] B. Staarmann, M. Smith, and C. J. Prestigiacomo, “Shear stress and aneurysms: A review,” *Neurosurg. Focus*, vol. 47, no. 1, pp. 1–6, 2019, doi: 10.3171/2019.4.FOCUS19225.
- [124] C. R. White, M. Haidekker, X. Bao, and J. A. Frangos, “Temporal Gradients in Shear, but Not Spatial Gradients, Stimulate Endothelial Cell Proliferation,” *Circulation*, vol. 103, no. 20, pp. 2508–2513, 2001.
- [125] P. M. McGah, D. F. Leotta, K. W. Beach, R. Eugene Zierler, and A. Aliseda, “Incomplete Restoration of Homeostatic Shear Stress Within Arteriovenous Fistulae,” *J. Biomech. Eng.*, vol. 135, no. 1, p. 011005, 2012, doi: 10.1115/1.4023133.
- [126] M. Hammes, M. Boghosian, K. Cassel, S. Watson, B. Funaki, T. Doshi, S. M. J. M. Akherat, J. Hines, and F. Coe, “Increased inlet blood flow velocity predicts low wall shear stress in the cephalic arch of patients with brachiocephalic fistula access,” *PLoS One*, vol. 11, no. 4, pp. 1–18, 2016, doi: 10.1371/journal.pone.0152873.
- [127] S.-W. Lee, L. Antiga, and D. A. Steinman, “Correlations among indicators of disturbed flow at the normal carotid bifurcation,” *J. Biomech. Eng.*, vol. 131, no. 6, p. 061013, 2009, doi: 10.1115/1.3127252.
- [128] V. Peiffer, S. J. Sherwin, and P. D. Weinberg, “Does low and oscillatory wall shear stress correlate spatially with early atherosclerosis? A systematic review,” *Cardiovasc. Res.*, vol. 99, no. 2, pp. 242–250, 2013, doi: 10.1093/cvr/cvt044.
- [129] J. Suo, J. N. Oshinski, and D. P. Giddens, “Blood flow patterns in the proximal human

- coronary arteries: relationship to atherosclerotic plaque occurrence.,” *Mol. Cell. Biomech.*, vol. 5, no. 1, pp. 9–18, 2008.
- [130] H. Zhu, J. Zhang, J. Shih, D. S. Long, F. Lopez-bertoni, R. John, N. Maeda, and M. H. Friedman, “Differences in Aortic Arch Geometry, Hemodynamics, and Plaque Patterns between C57BL/6 and 129/SvEv Mice,” *J. Biomech. Eng.*, vol. 131, no. 12, pp. 1–19, 2009, doi: 10.1115/1.4000168.Differences.
- [131] H. Samady, P. Eshtehardi, M. C. McDaniel, J. Suo, S. S. Dhawan, C. Maynard, L. H. Timmins, A. A. Quyyumi, and D. P. Giddens, “Coronary artery wall shear stress is associated with progression and transformation of atherosclerotic plaque and arterial remodeling in patients with coronary artery disease,” *Circulation*, vol. 124, no. 7, pp. 779–788, 2011, doi: 10.1161/CIRCULATIONAHA.111.021824.
- [132] A. K. Joshi, R. L. Leask, J. G. Myers, M. Ojha, J. Butany, and C. R. Ethier, “Intimal thickness is not associated with wall shear stress patterns in the human right coronary artery,” *Arterioscler. Thromb. Vasc. Biol.*, vol. 24, no. 12, pp. 2408–2413, 2004, doi: 10.1161/01.ATV.0000147118.97474.4b.
- [133] Y. Mohamied, E. M. Rowland, E. L. Bailey, S. J. Sherwin, M. A. Schwartz, and P. D. Weinberg, “Change of Direction in the Biomechanics of Atherosclerosis,” *Ann. Biomed. Eng.*, vol. 43, no. 1, pp. 16–25, 2014, doi: 10.1007/s10439-014-1095-4.
- [134] Y. Mohamied, S. J. Sherwin, and P. D. Weinberg, “Understanding the fluid mechanics behind transverse wall shear stress,” *J. Biomech.*, vol. 50, pp. 102–109, 2017, doi: 10.1016/j.jbiomech.2016.11.035.
- [135] D. N. Ku, D. P. Giddens, C. K. Zarins, and S. Glagov, “Pulsatile flow and atherosclerosis in the human carotid bifurcation. Positive correlation between plaque location and low oscillating shear stress,” *Arteriosclerosis*, vol. 5, no. 3, pp. 293–302, 1985, doi: 10.1161/01.ATV.5.3.293.
- [136] B. Ene-Iordache, C. Semperboni, G. Dubini, and A. Remuzzi, “Disturbed flow in a patient-specific arteriovenous fistula for hemodialysis: Multidirectional and reciprocating near-wall flow patterns,” *J. Biomech.*, vol. 48, no. 10, pp. 2195–2200, 2015, doi: 10.1016/j.jbiomech.2015.04.013.
- [137] L. D. Browne, K. Bashar, P. Griffin, E. G. Kavanagh, S. R. Walsh, and M. T. Walsh,

- “The role of shear stress in arteriovenous fistula maturation and failure: A systematic review,” *PLoS One*, vol. 10, no. 12, pp. 1–24, 2015, doi: 10.1371/journal.pone.0145795.
- [138] A. Remuzzi and B. Ene-Iordache, “Novel paradigms for dialysis vascular access: Upstream hemodynamics and vascular remodeling in dialysis access stenosis,” *Clin. J. Am. Soc. Nephrol.*, vol. 8, no. 12, pp. 2186–2193, 2013, doi: 10.2215/CJN.03450413.
- [139] S. Sivanesan, T. V. How, and A. Bakran, “Characterizing flow distributions in AV fistulae for haemodialysis access,” *Nephrol. Dial. Transplant.*, vol. 13, no. 12, pp. 3108–3110, 1998, doi: 10.1093/ndt/13.12.3108.
- [140] J. Carroll, R. L. Varcoe, T. Barber, and A. Simmons, “Reduction in anastomotic flow disturbance within a modified end-to-side arteriovenous fistula configuration: Results of a computational flow dynamic model,” *Nephrology (Carlton)*, vol. 24, no. 2, pp. 245–251, Jan. 2019, doi: 10.1111/nep.13219.
- [141] C. Wang, H. Lu, M. A. Schwartz, and M. Alexander Schwartz, “A novel in vitro flow system for changing flow direction on endothelial cells,” *J. Biomech. Eng.*, vol. 45, no. 7, pp. 1212–1218, 2012, doi: 10.1016/j.jbiomech.2012.01.045.
- [142] C. Wang, B. M. Baker, C. S. Chen, and M. A. Schwartz, “Endothelial cell sensing of flow direction,” *Arterioscler. Thromb. Vasc. Biol.*, vol. 33, no. 9, pp. 2130–2136, 2013, doi: 10.1161/ATVBAHA.113.301826.
- [143] I. Decorato, Z. Kharboutly, T. Vassallo, J. Penrose, C. Legallais, and A. Salsac, “Numerical simulation of the fluid structure interactions in a compliant patient-specific arteriovenous fistula,” *Int. j. numer. method. biomed. eng.*, vol. 30, no. 2, pp. 143–159, 2014.
- [144] D. M. Hoganson, C. J. Hinkel, X. Chen, R. K. Agarwal, and S. Shenoy, “Validation of computational fluid dynamics-based analysis to evaluate hemodynamic significance of access stenosis,” *J. Vasc. Access*, vol. 15, no. 5, pp. 409–414, 2014, doi: 10.5301/jva.5000226.
- [145] R. E. Feaver, B. D. Gelfand, and B. R. Blackman, “Human haemodynamic frequency harmonics regulate the inflammatory phenotype of vascular endothelial cells,” *Nat. Commun.*, vol. 4, pp. 1–11, 2013, doi: 10.1038/ncomms2530.
- [146] M. Grochowina, L. Leniowska, and A. Gala-Błądzińska, “The prototype device for non-

- invasive diagnosis of arteriovenous fistula condition using machine learning methods,” *Sci. Rep.*, vol. 10, no. 1, pp. 1–11, 2020, doi: 10.1038/s41598-020-72336-5.
- [147] H. Y. Wang, C. H. Wu, C. Y. Chen, and B. S. Lin, “Novel noninvasive approach for detecting arteriovenous fistula stenosis,” *IEEE Trans. Biomed. Eng.*, vol. 61, no. 6, pp. 1851–1857, 2014, doi: 10.1109/TBME.2014.2308906.
- [148] K. Ota, Y. Nishiura, S. Ishihara, H. Adachi, T. Yamamoto, and T. Hamano, “Evaluation of hemodialysis arteriovenous bruit by deep learning,” *Sensors (Switzerland)*, vol. 20, no. 17, pp. 1–17, 2020, doi: 10.3390/s20174852.
- [149] C.-H. Chen, T.-H. Tao, Y.-H. Chou, Y.-W. Chuang, T.-B. Chen, D. Using, P. Radar, and L. Classification, “Arteriovenous Fistula Flow Dysfunction Surveillance: Early Detection Using Pulse Radar Sensor and Machine Learning Classification,” *Biosensors*, vol. 11, no. 9, 2021, doi: 10.3390/bios11090297.
- [150] L. Suqin, Z. Mingli, S. Shiteng, M. Honglan, Z. Lan, N. Qihong, and L. Qing, “Assessment of the Hemodynamics of Autogenous Arteriovenous Fistulas With 4D Phase Contrast-Based Flow Quantification MRI in Dialysis Patients,” *J. Magn. Reson. Imaging*, vol. 51, no. 4, pp. 1272–1280, 2020, doi: 10.1002/jmri.26936.
- [151] Y. He, Y. T. Shiu, D. B. Pike, P. Roy-Chaudhury, A. K. Cheung, and S. A. Berceli, “Comparison of hemodialysis arteriovenous fistula blood flow rates measured by Doppler ultrasound and phase-contrast magnetic resonance imaging,” *J. Vasc. Surg.*, vol. 68, no. 6, pp. 1848–1857.e2, 2018, doi: 10.1016/j.jvs.2018.02.043.
- [152] J. De Ruijter, J. J. M. Muijsers, F. N. Van de Vosse, M. R. H. M. Van Sambeek, and R. G. P. Lopata, “A generalized approach for automatic 3-D geometry assessment of blood vessels in transverse ultrasound images using convolutional neural networks,” *IEEE Trans. Ultrason. Ferroelectr. Freq. Control*, vol. 3010, no. c, pp. 1–10, 2021, doi: 10.1109/TUFFC.2021.3090461.
- [153] E. Colley, J. Carroll, S. Thomas, R. L. Varcoe, A. Simmons, and T. J. Barber, “A Methodology for Non-Invasive 3D Surveillance of Arteriovenous Fistulae Using Freehand Ultrasound,” *IEEE Trans. Biomed. Eng.*, vol. 65, no. 8, pp. 1885–1891, 2018, doi: 10.1109/TBME.2017.2782781.
- [154] G. Biglino, C. Capelli, D. Koniordou, D. Robertshaw, L. K. Leaver, S. Schievano, A.

- M. Taylor, and J. Wray, “Use of 3D models of congenital heart disease as an education tool for cardiac nurses,” *Congenit. Heart Dis.*, vol. 12, no. 1, pp. 113–118, 2017, doi: 10.1111/chd.12414.
- [155] J. P. Costello, L. J. Olivieri, A. Krieger, O. Thabit, M. B. Marshall, S. J. Yoo, P. C. Kim, R. A. Jonas, and D. S. Nath, “Utilizing Three-Dimensional Printing Technology to Assess the Feasibility of High-Fidelity Synthetic Ventricular Septal Defect Models for Simulation in Medical Education,” *World J. Pediatr. Congenit. Hear. Surg.*, vol. 5, no. 3, pp. 421–426, 2014, doi: 10.1177/2150135114528721.
- [156] J. Coles-Black, T. Barber, D. Bolton, and J. Chuen, “A systematic review of three-dimensional printed template-assisted physician-modified stent grafts for fenestrated endovascular aneurysm repair,” *J. Vasc. Surg.*, vol. 74, no. 1, pp. 296–306.e1, 2021, doi: 10.1016/j.jvs.2020.08.158.
- [157] R. N. Uppot, B. Laguna, C. J. McCarthy, G. De Novi, A. Phelps, E. Siegel, and J. Courtier, “Implementing virtual and augmented reality tools for radiology education and training, communication, and clinical care,” *Radiology*, vol. 291, no. 3, pp. 570–580, 2019, doi: 10.1148/radiol.2019182210.
- [158] S. Chidambaram, V. Stifano, M. Demetres, M. Teyssandier, M. C. Palumbo, A. Redaelli, A. Olivi, M. L. J. Apuzzo, and S. C. Pannullo, “Applications of augmented reality in the neurosurgical operating room: A systematic review of the literature,” *J. Clin. Neurosci.*, vol. 91, pp. 43–61, 2021, doi: 10.1016/j.jocn.2021.06.032.
- [159] W. J. Peterson, J. Barker, and M. Allon, “Disparities in fistula maturation persist despite preoperative vascular mapping,” *Clin. J. Am. Soc. Nephrol.*, vol. 3, no. 2, pp. 437–441, 2008, doi: 10.2215/CJN.03480807.
- [160] P. D. Lawton, J. Cunningham, N. Hadlow, Y. Zhao, and M. D. Jose, “Chronic kidney disease in the Top End of the Northern Territory of Australia, 2002–2011: A retrospective cohort study using existing laboratory data,” *BMC Nephrol.*, vol. 16, no. 1, pp. 1–9, 2015, doi: 10.1186/s12882-015-0166-6.
- [161] D. G. McGrogan, A. P. Maxwell, A. Z. Khawaja, and N. G. Inston, “Current tools for prediction of arteriovenous fistula outcomes,” *Clin. Kidney J.*, vol. 8, no. 3, pp. 282–289, 2015, doi: 10.1093/ckj/sfv019.

- [162] J. E. Carroll, “A Clinical Role for Fluid Arteriovenous Fistulae,” 2018.
- [163] S. Gunasekera, O. Ng, S. Thomas, R. Varcoe, C. de Silva, and T. Barber, “Tomographic PIV analysis of physiological flow conditions in a patient-specific arteriovenous fistula,” *Exp. Fluids*, vol. 61, no. 12, pp. 1–14, 2020, doi: 10.1007/s00348-020-03085-4.
- [164] S. D. Thomas, E. C. Ip, N. Katib, D. Pugh, A. Lennox, Z. Endre, E. Tan, C. Ellery, and R. L. Varcoe, “A comprehensive renal vascular access clinic results in improved patient outcomes and reduced costs,” *ANZ J. Surg.*, vol. 88, no. 3, pp. 185–190, 2018, doi: 10.1111/ans.13794.
- [165] J. E. Carroll, “A Clinical Role for Fluid Dynamics Modelling of Arteriovenous Fistulae,” University of New South Wales, 2018.
- [166] C. M. Moran and A. J. W. Thomson, “Preclinical Ultrasound Imaging—A Review of Techniques and Imaging Applications,” *Front. Phys.*, vol. 8, no. May, 2020, doi: 10.3389/fphy.2020.00124.
- [167] M. Yamamoto, J. Carrillo, A. Insunza, G. Mari, Y. Ville, and V. Y. Yamamoto M, Carrillo J, Insunza A, Mari G, “Error introduced into velocity measurements by inappropriate Doppler angle assignment [1],” *Ultrasound Obs. Gynecol.*, vol. 28, no. 6, pp. 853–854, 2006, doi: 10.1002/uog.3847.
- [168] K. Logason, T. Bärnin, M. L. Jonsson, A. Boström, H. G. Hårdemark, and S. Karacagil, “The importance of Doppler angle of insonation on differentiation between 50-69% and 70-99% carotid artery stenosis,” *Eur. J. Vasc. Endovasc. Surg.*, vol. 21, no. 4, pp. 311–313, 2001, doi: 10.1053/ejvs.2001.1331.
- [169] P. Bjerregaard and I. Gussak, “Naming of the waves in the ECG with a brief account of their genesis,” *Circulation*, vol. 100, no. 25, pp. 1937–1942, 1999, doi: 10.1161/01.CIR.100.25.e148.
- [170] G. Alfonsi, “Reynolds-averaged Navier-Stokes equations for turbulence modeling,” *Appl. Mech. Rev.*, vol. 62, no. 4, pp. 1–20, 2009, doi: 10.1115/1.3124648.
- [171] A. Remuzzi and M. Bozzetto, “Biological and Physical Factors Involved in the Maturation of Arteriovenous Fistula for Hemodialysis,” *Cardiovasc. Eng. Technol.*, vol. 8, no. 3, pp. 273–279, 2017, doi: 10.1007/s13239-017-0323-0.

- [172] F. R. Menter, “Two-equation eddy-viscosity turbulence models for engineering applications,” *AIAA J.*, vol. 32, no. 8, pp. 1598–1605, 1994, doi: 10.2514/3.12149.
- [173] F. P. P. Tan, G. Soloperto, S. Bashford, N. B. Wood, S. Thom, A. Hughes, and X. Y. Xu, “Analysis of flow disturbance in a stenosed carotid artery bifurcation using two-equation transitional and turbulence models,” *J. Biomech. Eng.*, vol. 130, no. 6, pp. 1–12, 2008, doi: 10.1115/1.2978992.
- [174] L. Goubergrits, J. Osman, R. Mevert, U. Kertzsch, K. Pöthkow, and H.-C. Hege, “Turbulence in blood damage modeling,” *Int. J. Artif. Organs*, vol. 39, no. 4, pp. 160–165, 2016.
- [175] F. P. P. Tan, G. Soloperto, S. Bashford, N. B. Wood, S. Thom, A. Hughes, and X. Y. Xu, “Analysis of Flow Disturbance in a Stenosed Carotid Artery Bifurcation Using Two-Equation Transitional and Turbulence Models,” *J. Biomech. Eng.*, vol. 130, no. 6, pp. 1–12, 2008, doi: 10.1115/1.2978992.
- [176] J. Cutnell and K. Johnson, *Physics*. 1998.
- [177] E. Nader, S. Skinner, M. Romana, R. Fort, N. Lemonne, N. Guillot, A. Gauthier, S. Antoine-Jonville, C. Renoux, M. D. Hardy-Dessources, E. Stauffer, P. Joly, Y. Bertrand, and P. Connes, “Blood rheology: Key parameters, impact on blood flow, role in sickle cell disease and effects of exercise,” *Front. Physiol.*, vol. 10, no. OCT, pp. 1–14, 2019, doi: 10.3389/fphys.2019.01329.
- [178] P. R. S. Vijayaratnam, C. C. O’Brien, J. A. Reizes, T. J. Barber, and E. R. Edelman, “The impact of blood rheology on drug transport in stented arteries: Steady simulations,” *PLoS One*, vol. 10, no. 6, pp. 1–19, 2015, doi: 10.1371/journal.pone.0128178.
- [179] P. J. Carreau, “Rheological Equations from Molecular Network Theories,” *Trans. Soc. Rheol.*, vol. 16, no. 1, pp. 99–127, Mar. 1972, doi: 10.1122/1.549276.
- [180] Y. I. Cho and K. R. Kenney, “Effects of the non-Newtonian viscosity of blood on flows in a diseased arterial vessel. Part 1: Steady flows,” *Biorheology*, vol. 28, no. 3–4, pp. 241–262, 1991, doi: 10.3233/BIR-1991-283-415.
- [181] A. D. Caballero and S. Laín, “A Review on Computational Fluid Dynamics Modelling in Human Thoracic Aorta,” *Cardiovasc. Eng. Technol.*, vol. 4, no. 2, pp. 103–130, 2013, doi: 10.1007/s13239-013-0146-6.

- [182] L. Grechy, F. Iori, R. W. Corbett, S. Shurey, W. Gedroyc, N. Duncan, C. G. Caro, and P. E. Vincent, “Suppressing unsteady flow in arterio-venous fistulae,” *Phys. Fluids*, vol. 29, no. 10, 2017, doi: 10.1063/1.5004190.
- [183] V. B. Kolachalama, A. R. Tzafriri, D. Y. Arifin, and E. R. Edelman, “Luminal flow patterns dictate arterial drug deposition in stent-based delivery,” *J. Control. Release*, vol. 133, no. 1, pp. 24–30, 2009, doi: 10.1016/j.jconrel.2008.09.075.
- [184] P. M. McGah, D. F. Leotta, and K. W. Beach, “Effects of Wall Distensibility on the Numerical Simulation of Arteriovenous Fistulae,” pp. 1–2, 2013, doi: 10.1115/SBC2013-14183.
- [185] L. Antiga, M. Piccinelli, L. Botti, B. Ene-Iordache, A. Remuzzi, and D. a. Steinman, “An image-based modeling framework for patient-specific computational hemodynamics,” *Med. Biol. Eng. Comput.*, vol. 46, pp. 1097–1112, 2008, doi: 10.1007/s11517-008-0420-1.
- [186] T. J. Pedley, “Mathematical modelling of arterial fluid dynamics,” *J. Eng. Math.*, vol. 47, no. 3–4, pp. 419–444, 2003, doi: 10.1023/B:ENGI.00000007978.33352.59.
- [187] H. (Deceased) Schlichting and K. Gersten, *Boundary-Layer Theory*. 2016.
- [188] M. Spiegel, T. Redel, J. J. Zhang, T. Struffert, J. Hornegger, R. G. Grossman, A. Doerfler, and C. Karmonik, “Tetrahedral vs. polyhedral mesh size evaluation on flow velocity and wall shear stress for cerebral hemodynamic simulation,” *Comput. Methods Biomech. Biomed. Engin.*, vol. 14, no. 1, pp. 9–22, 2011, doi: 10.1080/10255842.2010.518565.
- [189] P. J. Roache, “Quantification of Uncertainty in Computational Fluid Dynamics,” vol. 29, pp. 123–160, 1997.
- [190] X. J. He and D. N. Ku, “Pulsatile flow in the human left coronary artery bifurcation: average conditions,” *J. Biomech. Eng.*, vol. 118, no. 1, pp. 74–82, 1996, doi: 10.1115/1.2795948.
- [191] J. E. Carroll, E. S. Colley, S. D. Thomas, R. L. Varcoe, A. Simmons, and T. J. Barber, “Tracking geometric and hemodynamic alterations of an arteriovenous fistula through patient-specific modelling,” *Comput. Methods Programs Biomed.*, vol. 186, p. 105203, Apr. 2020, doi: 10.1016/j.cmpb.2019.105203.

- [192] O. Ng, S. Gunasekera, S. Thomas, R. Varcoe, and T. Barber, “A clinical predictive indicator for arteriovenous fistula (AVF) failure,” *Proc. 22nd Australas. Fluid Mech. Conf. AFMC2020*, no. December, pp. 7–10, 2020, doi: 10.14264/d3dc63e.
- [193] D. Santoro, F. Benedetto, P. Mondello, N. Pipitò, D. Barillà, F. Spinelli, C. A. Ricciardi, V. Cernaro, and M. Buemi, “Vascular access for hemodialysis: Current perspectives,” *Int. J. Nephrol. Renovasc. Dis.*, vol. 7, pp. 281–294, 2014, doi: 10.2147/IJNRD.S46643.
- [194] C. S. Bavare, J. Bismuth, H. F. El-Sayed, T. T. Huynh, E. K. Peden, M. G. Davies, A. B. Lumsden, and J. J. Naoum, “Volume flow measurements in arteriovenous dialysis access in patients with and without steal syndrome,” *Int. J. Vasc. Med.*, vol. 2013, 2013, doi: 10.1155/2013/328601.
- [195] P. Wiese and B. Nonnast-Daniel, “Colour doppler ultrasound in dialysis access,” *Nephrol. Dial. Transplant.*, vol. 19, no. 8, pp. 1956–1963, 2004, doi: 10.1093/ndt/gfh244.
- [196] C. A. Schinstock, R. C. Albright, A. W. Williams, J. J. Dillon, E. J. Bergstralh, B. M. Jenson, J. T. McCarthy, and K. A. Nath, “Outcomes of arteriovenous fistula creation after the fistula first initiative,” *Clin. J. Am. Soc. Nephrol.*, vol. 6, no. 8, pp. 1996–2002, 2011, doi: 10.2215/CJN.11251210.
- [197] S. Sivanesan, T. V. How, and A. Bakran, “Characterizing flow distributions in AV fistulae for haemodialysis access,” *Nephrol. Dial. Transplant.*, vol. 13, no. 12, pp. 3108–10, 1998, doi: 10.1093/ndt/13.12.3108.
- [198] G. Xiong, C. Figueroa, N. Xiao, and C. Taylor, “Simulation of blood flow in deformable vessels using subject-specific geometry and spatially varying wall properties,” *Int. J. Numer. Method Biomed. Eng.*, vol. 27, pp. 1000–1016, 2011, doi: 10.1002/cnm.1404.
- [199] N. Varble, S. Day, D. Phillips, D. Mix, K. Schwarz, K. A. Illig, and A. Chandra, “In vitro hemodynamic model of the arm arteriovenous circulation to study hemodynamics of native arteriovenous fistula and the distal revascularization and interval ligation procedure,” *J. Vasc. Surg.*, vol. 59, no. 5, pp. 1410–1417, 2014, doi: 10.1016/j.jvs.2013.04.055.
- [200] J. R. Womersley, “Methods for the calculation of velocity, rate of flow and viscous drag in arteries when the pressure gradient is known,” *J. Physiol.*, vol. 127, no. 3, pp. 553–

- 563, 1955, doi: 10.1113/jphysiol.1955.sp005276.
- [201] M. Bozzetto, P. Brambilla, S. Rota, B. Ene-Iordache, S. Sironi, G. Remuzzi, and A. Remuzzi, “Toward longitudinal studies of hemodynamically induced vessel wall remodeling,” *Int. J. Artif. Organs*, vol. 41, no. 11, pp. 714–722, 2018, doi: 10.1177/0391398818784207.
 - [202] J. B. Naidich, A. Weiss, E. P. Molmenti, J. J. Naidich, and J. S. Pellerito, “An Interesting Observation Regarding Retrograde Vertebral Artery Flow in Patients With Dialysis Access Fistulas,” *J. Ultrasound Med.*, vol. 38, no. 10, pp. 2703–2707, 2019, doi: 10.1002/jum.14975.
 - [203] A. Fuchs, N. Berg, and L. P. Wittberg, “Stenosis indicators applied to patient-specific renal arteries without and with stenosis,” *Fluids*, vol. 4, no. 1, 2019, doi: 10.3390/fluids4010026.
 - [204] I. Decorato, Z. Kharboutly, C. Legallais, and a. V Salsac, “Numerical study of the influence of wall compliance on the haemodynamics in a patient-specific arteriovenous fistula,” *Comput. Methods Biomech. Biomed. Engin.*, vol. 30, no. 2, pp. 143–159, 2014, doi: 10.1080/10255842.2011.593762.
 - [205] S. Pirola, Z. Cheng, O. A. Jarral, D. P. O’Regan, J. R. Pepper, T. Athanasiou, and X. Y. Xu, “On the choice of outlet boundary conditions for patient-specific analysis of aortic flow using computational fluid dynamics,” *J. Biomech.*, vol. 60, pp. 15–21, 2017, doi: 10.1016/j.jbiomech.2017.06.005.
 - [206] S. Mascia, S. Spiezia, A. Assanti, L. De Nicola, G. Stanzione, V. Bertino, and P. Zamboli, “Ischemic steal syndrome in a hemodialysis patient: The roles of Doppler ultrasonography and dynamic Doppler studies in diagnosis and treatment selection,” *J. Ultrasound*, vol. 13, no. 3, pp. 104–106, 2010, doi: 10.1016/j.jus.2010.09.003.
 - [207] J. W. Hirshfeld and A. S. Nathan, “Deriving Function From Structure: Applying Hagen-Poiseuille to Coronary Arteries,” *JACC Cardiovasc. Interv.*, vol. 13, no. 4, pp. 498–501, 2019, doi: 10.1016/j.jcin.2019.11.031.
 - [208] S. Gunasekera, O. Ng, S. Thomas, R. Varcoe, C. De, and T. Barber, “A numerical investigation of a stented arteriovenous fistula,” in *Proceedings of the 22nd Australasian Fluid Mechanics Conference AFMC2020*, 2020, no. December, pp. 7–10. doi:

10.14264/160df47.

- [209] S. D. Thomas, S. Peden, P. Crowe, and R. L. Varcoe, “Interwoven Nitinol Stents to Treat Radiocephalic Anastomotic Arteriovenous Fistula Stenosis,” *J. Endovasc. Ther.*, vol. 26, no. 3, pp. 394–401, 2019, doi: 10.1177/1526602819842851.
- [210] T. W. I. Clark, D. A. Hirsch, K. J. Jindal, P. J. Veugelers, and J. LeBlanc, “Outcome and prognostic factors of restenosis after percutaneous treatment of native hemodialysis fistulas,” *J. Vasc. Interv. Radiol.*, vol. 13, no. 1, pp. 51–59, Jan. 2002, doi: 10.1016/s1051-0443(07)60009-8.
- [211] A. Cohen, A. Korzets, H. Neyman, Y. Ori, S. Baytner, A. Belenky, M. Knieznik, G. N. Bachar, and E. Atar, “Endovascular Interventions of Juxtaanastomotic Stenoses and Thromboses of Hemodialysis Arteriovenous Fistulas,” *J. Vasc. Interv. Radiol.*, vol. 20, no. 1, pp. 66–70, 2009, doi: 10.1016/j.jvir.2008.10.009.
- [212] P. Schober and L. A. Schwarte, “Correlation coefficients: Appropriate use and interpretation,” *Anesth. Analg.*, vol. 126, no. 5, pp. 1763–1768, 2018, doi: 10.1213/ANE.0000000000002864.
- [213] N. Koirala, E. Anvari, and G. McLennan, “Monitoring and Surveillance of Hemodialysis Access,” *Semin. Intervent. Radiol.*, vol. 33, no. 1, pp. 25–30, 2016, doi: 10.1055/s-0036-1572548.
- [214] K. Wo, B. J. Morrison, and R. N. Harada, “Developing Duplex Ultrasound Criteria for Diagnosis of Arteriovenous Fistula Stenosis,” *Ann. Vasc. Surg.*, vol. 38, no. December 2008, pp. 99–104, 2017, doi: 10.1016/j.avsg.2016.04.013.
- [215] C. Kamphuis, E. Barsom, M. Schijven, and N. Christoph, “Augmented reality in medical education?,” *Perspect. Med. Educ.*, vol. 3, no. 4, pp. 300–311, 2014, doi: 10.1007/s40037-013-0107-7.
- [216] M. Kljun, V. Geroimenko, and K. Čopič Pucihar, *Augmented Reality in Education: Current Status and Advancement of the Field*. 2020. doi: 10.1007/978-3-030-42156-4_1.
- [217] M. T. Parisotto, V. U. Schoder, C. Miriunis, A. H. Grassmann, L. P. Scatizzi, P. Kaufmann, A. Stopper, and D. Marcelli, “Cannulation technique influences arteriovenous fistula and graft survival,” *Kidney Int.*, vol. 86, no. 4, pp. 790–797, 2014,

- doi: 10.1038/ki.2014.96.
- [218] V. Lun, “Design and Development of an educational AVF database and augmented reality application,” University of New South Wales, 2021.
 - [219] J. Swinnen, K. Lean Tan, R. Allen, D. Burgess, and I. V. Mohan, “Juxta-anastomotic stenting with aggressive angioplasty will salvage the native radiocephalic fistula for dialysis,” *J. Vasc. Surg.*, vol. 61, no. 2, pp. 436–442, 2015, doi: 10.1016/j.jvs.2014.05.097.
 - [220] N. J. Scholes-Robertson, M. Howell, T. Gutman, A. Baumgart, V. SInka, D. J. Tunnicliffe, S. May, R. Chalmers, J. Craig, and A. Tong, “Patients’ and caregivers’ perspectives on access to kidney replacement therapy in rural communities: systematic review of qualitative studies,” *BMJ Open*, vol. 10, no. 9, p. e037529, 2020, doi: 10.1136/bmjopen-2020-037529.
 - [221] O. Ng, S. Gunasekera, S. Thomas, R. Varcoe, and T. Barber, “CFD-Derived Resistance as a clinical indicator for problematic AVF,” in *26th Congress of Biomechanics*, 2021, vol. 65, no. 8, p. 2021.
 - [222] C. Leon and A. Asif, “Physical examination of arteriovenous fistulae by a renal fellow: Does it compare favorably to an experienced interventionalist?,” *Semin. Dial.*, vol. 21, no. 6, pp. 557–560, 2008, doi: 10.1111/j.1525-139X.2008.00477.x.
 - [223] K. Abreo, B. M. Amin, and A. P. Abreo, “Physical examination of the hemodialysis arteriovenous fistula to detect early dysfunction,” *J. Vasc. Access*, vol. 20, no. 1, pp. 7–11, 2019, doi: 10.1177/1129729818768183.
 - [224] D. W. Hosmer, S. Jr., Lemeshow, and R. Sturdivant, “Introduction to the Logistic Regression Model,” in *Applied Logistic Regression*, John Wiley & Sons, Ltd, 2013, pp. 1–33. doi: <https://doi.org/10.1002/9781118548387.ch1>.
 - [225] D. W. Hosmer and S. Lemeshow, *Applied logistic regression*. John Wiley and Sons, 2000.
 - [226] I. B. Society, “A Random-Effects Ordinal Regression Model for Multilevel Analysis Author (s): Donald Hedeker and Robert D . Gibbons Published by : International Biometric Society Stable URL : <http://www.jstor.org/stable/2533433>,” *Society*, vol. 50, no. 4, pp. 933–944, 2010.

- [227] A. Cnaan, N. M. Laird, and P. Slasor, “Mixed Models: Using the General Linear Mixed Model to Analyse Unbalanced Repeated Measures and Longitudinal Data,” *Tutorials Biostat.*, vol. 2, pp. 127–158, 2005, doi: 10.1002/0470023724.ch1c(i).
- [228] H. Singmann and D. Kellen, “An introduction to mixed models for experimental psychology,” *New Methods Cogn. Psychol.*, pp. 4–31, 2019, doi: 10.4324/9780429318405-2.
- [229] R. Bono, R. Alarcón, and M. J. Blanca, “Report Quality of Generalized Linear Mixed Models in Psychology: A Systematic Review,” *Front. Psychol.*, vol. 12, no. April, pp. 1–15, 2021, doi: 10.3389/fpsyg.2021.666182.
- [230] E. Lanzarone, A. Finotello, B. Pane, G. Pratesi, D. Palombo, M. Conti, and G. Spinella, “Prediction model of isolated iliac and abdominal aneurysms,” *Eur. J. Clin. Invest.*, vol. 51, no. 7, pp. 1–13, 2021, doi: 10.1111/eci.13517.
- [231] N. Sommet and D. Morselli, “Keep calm and learn multilevel logistic modeling: A simplified three-step procedure using stata, R, Mplus, and SPSS,” *Int. Rev. Soc. Psychol.*, vol. 30, no. 1, pp. 203–218, 2017, doi: 10.5334/irsp.90.
- [232] D. Bates, M. Mächler, B. M. Bolker, and S. C. Walker, “Fitting linear mixed-effects models using lme4,” *J. Stat. Softw.*, vol. 67, no. 1, 2015, doi: 10.18637/jss.v067.i01.
- [233] T. Fawcett, “An introduction to ROC analysis,” *Pattern Recognit. Lett.*, vol. 27, no. 8, pp. 861–874, 2006, doi: 10.1016/j.patrec.2005.10.010.
- [234] J. N. Mandrekar, “Receiver operating characteristic curve in diagnostic test assessment,” *J. Thorac. Oncol.*, vol. 5, no. 9, pp. 1315–1316, 2010, doi: 10.1097/JTO.0b013e3181ec173d.
- [235] V. R. Kumar and G. M. Antony, “A Review of Methods and Applications of the ROC Curve in Clinical Trials,” *Ther. Innov. Regul. Sci.*, vol. 44, no. 6, pp. 659–671, 2010, doi: 10.1177/009286151004400602.
- [236] G. L. Grunkemeier and R. Jin, “Receiver operating characteristic curve analysis of clinical risk models,” *Ann. Thorac. Surg.*, vol. 72, no. 2, pp. 323–326, 2001, doi: 10.1016/S0003-4975(01)02870-3.
- [237] J. Y. Verbakel, E. W. Steyerberg, H. Uno, B. De Cock, L. Wynants, G. S. Collins, and B. Van Calster, “ROC curves for clinical prediction models part 1. ROC plots showed

- no added value above the AUC when evaluating the performance of clinical prediction models,” *J. Clin. Epidemiol.*, vol. 126, pp. 207–216, 2020, doi: 10.1016/j.jclinepi.2020.01.028.
- [238] N. A. Obuchowski, M. L. Lieber, and F. H. Wians, “ROC curves in Clinical Chemistry: Uses, misuses, and possible solutions,” *Clin. Chem.*, vol. 50, no. 7, pp. 1118–1125, 2004, doi: 10.1373/clinchem.2004.031823.
- [239] D. W. Hosmer, S. Jr., Lemeshow, and R. Sturdivant, “Assessing the Fit of the Model,” in *Applied Logistic Regression*, John Wiley & Sons, Ltd, 2013, pp. 153–225. doi: <https://doi.org/10.1002/9781118548387.ch5>.
- [240] B. L. Welch, “The signifiacnce of the difference between two means when the population variances are unequal,” *Biometrika*, vol. 29, no. 3–4, pp. 350–362, 1938.
- [241] R. Stolic, “Most important chronic complications of arteriovenous fistulas for hemodialysis,” *Med. Princ. Pract.*, vol. 22, no. 3, pp. 220–228, 2013, doi: 10.1159/000343669.
- [242] S. Nakagawa and H. Schielzeth, “A general and simple method for obtaining R² from generalized linear mixed-effects models,” *Methods Ecol. Evol.*, vol. 4, no. 2, pp. 133–142, 2013, doi: 10.1111/j.2041-210x.2012.00261.x.
- [243] D. R. Cox, “Regression Models and Life-Tables,” *J. R. Stat. Soc. Ser. B*, vol. 34, no. 2, pp. 187–202, 1972, doi: 10.1111/j.2517-6161.1972.tb00899.x.
- [244] D. R. Cox and D. Oakes, *Analysis of Survival Data*, 1st ed. 1984. doi: <https://doi.org/10.1201/9781315137438>.
- [245] D. Using, P. Radar, and L. Classification, “Arteriovenous Fistula Flow Dysfunction Surveillance: Early Detection Using Pulse Radar Sensor and Machine Learning Classification,” 2021.
- [246] A. Remuzzi, M. Bozzetto, and P. Brambilla, “Is shear stress the key factor for AVF maturation?,” *J. Vasc. Access*, vol. 18, no. Suppl 1, pp. S10--S14, 2017, doi: 10.5301/jva.5000686.
- [247] C. Mercado, L. Salman, G. Krishnamurthy, K. Choi, S. Artikov, I. Thomas, D. Merrill, and A. Asif, “Early and late fistula failure,” *Clin. Nephrol.*, vol. 69, no. 2, pp. 77–83, Feb. 2008, doi: 10.5414/cnp69077.

- [248] D. Fulker, G. Keshavarzi, A. Simmons, D. Pugh, and T. Barber, “Pulsatility produced by the hemodialysis roller pump as measured by doppler ultrasound,” *Artif. Organs*, vol. 39, no. 11, pp. 945–950, 2015, doi: 10.1111/aor.12469.
- [249] A. Besarab, S. Frinak, R. A. Sherman, J. Goldman, F. Dumler, M. V. Devita, T. Kapoian, F. Al-Saghir, and T. Lubkowski, “Simplified measurement of intra-access pressure,” *J. Am. Soc. Nephrol.*, vol. 9, no. 2, pp. 284–289, 1998, doi: 10.1097/00002480-199604000-00383.
- [250] L. M. Spergel, J. E. Holland, S. Z. Fadem, C. J. McAllister, and E. J. Peacock, “Static intra-access pressure ratio does not correlate with access blood flow: Rapid communication,” *Kidney Int.*, vol. 66, no. 4, pp. 1512–1516, 2004, doi: 10.1111/j.1523-1755.2004.00946.x.
- [251] D. C. Bosanquet, J. Rubasingham, M. Imam, J. D. Woolgar, and C. G. Davies, “Predicting outcomes in native AV forearm radio-cephalic fistulae; the CAVeA2T2 scoring system,” *J. Vasc. Access*, vol. 16, no. 1, pp. 19–25, 2015, doi: 10.5301/jva.5000305.
- [252] S. Bianconcini, “Asymptotic properties of adaptive maximum likelihood estimators in latent variable models,” *Bernoulli*, vol. 20, no. 3, pp. 1507–1531, 2014, doi: 10.3150/13-BEJ531.
- [253] B. M. Bolker, M. E. Brooks, C. J. Clark, S. W. Geange, J. R. Poulsen, M. H. H. Stevens, and J. S. S. White, “Generalized linear mixed models: a practical guide for ecology and evolution,” *Trends Ecol. Evol.*, vol. 24, no. 3, pp. 127–135, 2009, doi: 10.1016/j.tree.2008.10.008.
- [254] P. Kabaila and N. Ranathunga, *On Adaptive Gauss-Hermite Quadrature for Estimation in GLMM's*, vol. 1150 CCIS. Springer Singapore, 2019. doi: 10.1007/978-981-15-1960-4_9.

Appendices

Appendix 3A

The $k - \omega$ SST model used in this thesis is a two-equation eddy-viscosity model, combining the $k - \omega$ and the $k - \epsilon$ models [172]. The blending function, F_1 activates the $k - \omega$ near the wall, while the $k - \epsilon$ in the free stream region. Governing equations for the $k - \omega$ SST model is given as follow:

The two-equation model is given as

$$\frac{\partial \rho k}{\partial t} + \frac{\partial \rho u_j k}{\partial x_j} = P - \beta^* \rho \omega k + \frac{\partial}{\partial x_j} \left[(\mu + \sigma_\omega \mu_T) \frac{\partial k}{\partial x_j} \right] \quad \text{Eq. 30}$$

$$\begin{aligned} \frac{\partial \rho \omega}{\partial t} + \frac{\partial \rho u_j \omega}{\partial x_j} = & \frac{\gamma}{v_t} P - \beta \rho \omega^2 + \frac{\partial}{\partial x_j} \left[(\mu + \sigma_\omega \mu_T) \frac{\partial \omega}{\partial x_j} \right] \\ & + 2(1 - F_1) \rho \sigma_{\omega_2} \frac{1}{\omega} \frac{\partial k}{\partial x_j} \frac{\partial \omega}{\partial x_j} \end{aligned} \quad \text{Eq. 31}$$

where,

$$\tau_{ij} = \mu_j \left(\frac{\partial u_i}{\partial x_j} + \frac{\partial u_j}{\partial x_i} - \frac{2}{3} \frac{\partial u_k}{\partial x_k} \delta_{ij} \right) - \frac{2}{3} \rho k \delta_{ij} \quad \text{Eq. 32}$$

$$P = \min \left(\tau_{ij} \frac{\partial u_i}{\partial x_j}, 20 \beta^* \rho \omega k \right) \quad \text{Eq. 33}$$

Kinematic eddy viscosity is given as,

$$\mu_T = \frac{\rho a_1 k}{\max(a_1 \omega, S F_2)} \quad \text{Eq. 34}$$

where

$S = \sqrt{2 W_{ij} W_{ij}}$ is the vorticity magnitude with

$$W_{ij} = \frac{1}{2} \frac{\partial u_i}{\partial x_j} + \frac{\partial u_j}{\partial x_i} \quad \text{Eq. 35}$$

Turbulent kinematic viscosity is given as,

$$\nu_t = \frac{\mu_t}{\rho} \quad \text{Eq. 36}$$

Each of the constants is a blend of the first (Wilcox $k-\omega$) and second ($k-\epsilon$)

set F1, first blending function

$$\phi = F\phi_1 + (1 - F)\phi_2 \quad \text{Eq. 37}$$

$$F_1 = \tanh \left[\min \left[\max \left(\frac{2\sqrt{k}}{\beta^*\omega y}, \frac{500\nu}{y^2\omega}, \frac{4\sigma_{\omega 2}k}{CD_{k\omega}y^2} \right) \right]^4 \right] \quad \text{Eq. 38}$$

$CD_{k\omega}$ is the positive portion of the cross-diffusion term, given as:

$$CD_{k\omega} = \max \left(2\rho\sigma_{\omega 2} \left(\frac{1}{\omega} \right) \frac{\partial k}{\partial x_i} \frac{\partial \omega}{\partial x_i}, 10^{-20} \right) - \quad \text{Eq. 39}$$

F2, second blending function

$$F_2 = \tanh \left[\left[\max \left(\frac{2\sqrt{k}}{\beta^*\omega y}, \frac{500\nu}{d^2\omega} \right) \right]^2 \right] \quad \text{Eq. 40}$$

where ρ is density, μ is the molecular dynamic viscosity, d is the distance from the field point to the nearest wall, and

The constants are given as:

$$\begin{aligned} \sigma_{k1} &= 0.85 & \sigma_{\omega 1} &= 0.5 & \beta_1 &= 0.075 \\ \sigma_{k2} &= 1.0 & \sigma_{\omega 2} &= 0.856 & \beta_2 &= 0.0828 \\ \beta^* &= 0.09 & k &= 0.41 & a_1 &= 0.31 \\ \gamma_1 &= \frac{\beta_1}{\beta^*} - \frac{(\sigma_{\omega 1}k^2)}{\sqrt{\beta^*}} & \gamma_2 &= \frac{\beta_2}{\beta^*} - \frac{(\sigma_{\omega 2}k^2)}{\sqrt{\beta^*}} \end{aligned}$$

Appendix 6A

The following R code was used to model this in R-studio (Version 1.2, RStudio, Inc., Boston, MA) [232]:

```
glmer(Outcome ~ Resistance + (1|ID), family = binomial,  
      data = mydata, nAGQ = 30)
```

The intervention outcome is denoted by “0” and “1”, “0” representing no intervention performed, and “1” representing an intervention performed, which corresponds to the selection criteria. This is separated by “~”, followed by the fixed effect, that is the predictor, Resistance. Terms after the “+” notation represents the random effects, that is the clustered patients ID in this case. “1” in the term “(1 | ID)” represents the intercept from each cluster, denoted as ID. In other words, the intercept, β_{0j} is allowed to vary, but the slope, β_1 remains the same for each cluster.

“nAGQ” represents the adaptive Gauss-Hermite Quadrature, that is a generalised linear mixed model fitted by maximum likelihood with the adaptive Gauss-Hermite quadrature technique. This technique, although requires more time, has a more accurate estimation than Laplace as it incorporates data from the initial fit to increase the precision [252], [253]. This technique evaluates the integrand by identifying the optimal probability density function [253], [254].

Appendix 6B

Classifiers used typically are illustrated in the confusion matrix, used to visualise the performance algorithm used for ROC analysis in Figure 55.

		Actual condition	
		P	N
Predicted Condition	PP	TP	FP
	PN	FN	TN

where

P depicts the actual condition – positives

N depicts the actual condition – negatives

PP depicts the predicted condition – positives

PN depicts the predicted condition – negatives

TP depicts the true positives

FP depicts the false positives

FN depicts the false negatives

TN depicts the true negatives

Figure 55: The confusion matrix, visualising the performance algorithm used for the ROC analysis. Reprinted and adapted with permission [233].

The performance metrics calculated from the classifiers are,

True positive rates, TPR, that is the sensitivity,

$$TPR = \frac{TP}{TP + FN} = 1 - FN \quad \text{Eq. 41}$$

False negatives rates, FN,

$$FNR = \frac{FN}{TP + FN} = 1 - TP \quad \text{Eq. 42}$$

True negatives rates, TNR, that is the specificity/precision

$$TNR = \frac{TN}{TN + FP} = 1 - FP \quad \text{Eq. 43}$$

False positives rate, FP, that is 1 – specificity

$$FPR = \frac{FP}{TN + FP} = 1 - TN \quad \text{Eq. 44}$$